Forschungszentrum Karlsruhe
Technik und Umwelt

Wissenschaftliche Berichte
FZKA 5571

Pre-oxidised BWR Test CORA-28: Test Results

S. Hagen, P. Hofmann, V. Noack, L. Sepold, G. Schanz, G. Schumacher

Hauptabteilung Ingenieurtechnik
Institut für Materialforschung
Institut für Neutronenphysik und Reaktortechnik
Projekt Nukleare Sicherheitsforschung

Juni 1997

Forschungszentrum Karlsruhe
Technik und Umwelt
Wissenschaftliche Berichte

FZKA 5571

Pre-oxidised BWR Test CORA-28: Test Results

S. Hagen, P. Hofmann, V. Noack, L. Sepold,
G. Schanz, G. Schumacher

Hauptabteilung Ingenieurtechnik
Institut für Materialforschung
Institut für Neutronenphysik und Reaktortechnik
Projekt Nukleare Sicherheitsforschung

Forschungszentrum Karlsruhe GmbH, Karlsruhe
1997

Als Manuskript gedruckt
Forschungszentrum Karlsruhe GmbH
Postfach 3640, 76021 Karlsruhe

Mitglied der Hermann von Helmholtz-Gemeinschaft
Deutscher Forschungszentren (HGF)

ISSN 0947-8620

Abstract

Pre-oxidised BWR Test CORA-28: Test Results

The CORA out-of-pile experiments were part of the international Severe Fuel Damage (SFD) program. They were set up to provide information on the failure mechanisms of Light Water Reactor (LWR) fuel elements in the temperature range from 1200°C to 2400°C.

Most of the CORA experiments were performed with a cladding of as-received Zircaloy. To simulate the influence of the oxide layer developed during operation, test CORA-28 was performed with a pre-oxidised bundle. The pre-oxidation was performed in the CORA-facility and resulted in an oxide layer thickness of up to 55 μm.

Due to the axial temperature profile the oxide layer formed preferentially in the upper half of the bundle. Consequently, a different material behaviour was found in the upper and the lower part of the bundle. The negligible pre-oxidation of the lower part resulted in the same behaviour as of the unoxidised bundle.

In the upper part the following processes were found. The beginning of the temperature escalation was delayed by about 200 s and the rise of temperature amounted to a mean value of 3 K/s compared to about 10 K/s seen in a non pre-oxidised bundle. The basic damage mechanisms were the same, but the stronger pre-oxidation in the upper part of the bundle remarkably reduced the interaction between the liquefied absorber material and the Zircaloy of the channel box wall and by this also the interaction with the Zircaloy of the fuel rods. A higher portion of the channel box walls and of the cladding survived. The reduced chemical interaction resulted in a reduced melt formation and relocation of melt. Due to the decreased ability for wetting of oxidised surfaces by metallic melts a larger portion of melt relocated by slumping, instead of flowing down and "refreezing" on the rod surfaces.

Although the stainless steel tubes of the absorber, which contained the B_4C powder, were liquefied by chemical interactions, the remaining B_4C columns survived. In CORA-28 this B_4C columns remained up to an intact elevation of about 650 mm. A total of 104 g hydrogen was produced in the test.

Zusammenfassung

BWR Versuch CORA-28 mit voroxidiertem Bündel

Die CORA out-of-pile Experimente wurden im Rahmen des international geplanten "Severe Fuel Damage" Programms durchgeführt. Sie sollten Informationen über die Schadensmechanismen an Leichtwasser-Reaktoren (LWR) Brennelementen im Temperaturbereich von 1200°C bis 2400°C liefern.

Die meisten CORA-Experimente wurden mit unbehandelten Zircaloy-Hüllrohren durchgeführt. Um den Einfluß einer beim Reaktorbetrieb entstandenen Oxidschicht zu simulieren, erfolgte der Versuch CORA-28 mit einem voroxidierten Bündel. Die Voroxidation wurde in der CORA-Anlage durchgeführt und erreichte eine Oxidschichtdicke von bis zu 55 μm.

Entsprechend dem axialen Temperaturprofil entstand die Oxidschicht bevorzugt im oberen Bereich des Bündels. Daraus folgte ein unterschiedliches Verhalten im oberen und unteren Teil des Bündels. In der unteren Hälfte ergab sich das gleiche Verhalten wie beim unbehandelten Bündel.

Im oberen Bündelbereich fand man folgende Verhältnisse: Der Beginn der Temperatureskalation war um ca. 200 s verzögert. Die Temperaturanstiegsgeschwindigkeit betrug ca. 3 K/s gegenüber etwa 10 K/s beim nicht voroxidierten Bündel. Die grundsätzlichen Schadensmechanismen waren die gleichen, aber die stärkere Voroxidation des Zry in der oberen Hälfte des Bündels verringerte die Wechselwirkung zwischen dem Absorbermaterial und dem Zircaloy der Kanalwandung und damit auch die Reaktion mit dem Zircaloy der Brennstabhüllen. Die verringerte chemische Wechselwirkung resultierte in einer Reduktion der Schmelzmenge und der Verlagerung von Schmelze im Bündel. Durch das verschlechterte Benetzungsverhalten für metallische Schmelzen auf den anoxidierten Oberflächen, verringerte sich der Anteil der Schmelze, der sich durch Herabfließen und Erstarren auf der Staboberfläche anlagerte.

Obwohl die Edelstahlhüllen der Absorberstäbe durch die Wechselwirkung mit B_4C verflüssigt wurden, blieb ein großer Teil des B_4C im unteren Bereich als gesinterte Säule bestehen. Im Versuch CORA-28 überlebten diese Säulen bis zu einer Höhe von 650 mm. Insgesamt wurden während des Experiments 104 g Wasserstoff erzeugt.

Contents

1. Introduction

The TMI-2 accident has demonstrated that a severe fuel damage transient will not necessarily escalate to an uncontrolled core melt down accident if the design basis accident limits are exceeded. Therefore, comprehensive research programs have been initiated in various countries to investigate the relevant fuel rod bundle damage mechanisms that occur in an uncovered core, after an increase of temperature.

In the Federal Republic of Germany at the Kernforschungszentrum Karlsruhe (KfK) the Severe Fuel Damage (SFD) Program is now co-ordinated by the Project Nuclear Safety Research (PSF) as successor of Project Nuclear Safety (PNS) and LWR Safety Project Group (PRS). As part of this program, out-of-pile experiments (the CORA-Program) were conducted at the Hauptabteilung Ingenieurtechnik (HIT). These experiments had been designed to provide information on the behaviour of Light Water Reactor (LWR) fuel elements under severe fuel damage (SFD) conditions, up to meltdown. The results of the out-of-pile experiments can be used for the assessment of the SFD computer codes.

Within the frame work of international co-operation the out-of-pile experiments contribute complementary information to the results obtained from the limited number of inpile tests. The investigation of the basic phenomena of the damage process was supported by separate-effect tests.

The most important aspects concerning fuel rod failure and subsequent core degradation are the chemical interactions amongst the fuel element components in competition with the oxidation of the cladding in steam, which causes also the temperature escalation. Melt formation starts around 1200°C by chemical interactions of the Inconel spacer grids and absorber materials (Ag, In, Cd) for PWRs and B_4C/stainless steel for BWRs with the Zircaloy cladding. The dissolution of the UO_2 pellets by liquid Zircaloy starts far below the UO_2 melting point.

Melt relocation, blockage formation and finally fragmentation of fuel elements during reflooding characterise the degraded core and the potential of long-term coolability. Furthermore, the influence of internal pressure of the fuel rods (ballooning and bursting) and external pressure of the system (solid contact between pellets and cladding) on the bundle meltdown behaviour was investigated. Further on, the investigation of the influence of pre-oxidation, initial heat-up rate, steam availability, water level in the bundle and bundle size were included in the program. The damage behaviour of VVER fuel elements was the subject of the last two CORA-tests.

The tests performed in the CORA-facility are listed in the test matrix (Table 1). The original test matrix focussed on the behaviour of PWR fuel elements. In 1988, discussion showed that in most countries using nuclear energy, information on the behaviour of BWRs in severe accident conditions was needed. In consequence, five planned PWR experiments were replaced by BWR tests in the revised test matrix. Also the original sequence of tests was changed, as one can see from the test numbers.

In this report results of BWR test CORA-28 are being described. In most tests the Zry cladding was used in the as-received state. During normal operation, however, an oxide layer of about 50 μm is being formed dependent of operating time and conditions. In CORA-28, therefore, the influence of pre-oxidation of the Zry cladding on the damage behaviour of BWR bundles was to be investigated. The bundle was pre-oxidised in the CORA-facility up to about 55 μm oxide layer thickness. The conditions of pre-oxidation are given in Appendix B.

2. Description of the CORA test facility

The CORA out-of-pile facility was designed to investigate the behaviour of LWR fuel elements under severe fuel damage accident conditions. In the experiments the decay heat was simulated by electrical heating. Great emphasis was placed on the fact that the test bundles contained the original materials used in light-water reactor fuel elements so that the different material interactions could be investigated.

Pellets, cladding, grid spacers, absorber rods, and channel box walls were typical of those of the investigated LWRs with respect to their compositions and radial dimensions. In test CORA-28 the following BWR components were used: Original UO_2 pellets, Zry-4 cladding, Zry spacers, Zry channel box walls and B_4C absorber inside stainless steel tubes surrounded by the stainless steel of the blade.

Figure 1 gives a simplified flow diagram of the facility. The geometrical arrangement of the different CORA components is given in Figure 2. The central part of the facility was the fuel rod bundle. The bundle was enclosed in a Zry shroud with ZrO_2 fibre insulation. A high-temperature radiation shield surrounded the bundle and shroud assembly, leaving an annular space for the movement of the quench cylinder. The bundle was connected to the power supply system at the upper and lower ends.

Below the bundle was the quench unit with a water-filled quench cylinder, which can be moved along the bundle at a controlled speed. The cylinder was guided by three rods, which in addition connected the electric power to the bundle lower end.

The bundle upper end was fixed at the bundle head plate. The plate was connected to the surge condenser by a funnel-shaped tube. The surge condenser was double-walled, leaving access to the bundle end fittings above the bundle head funnel.

The steam was produced in the steam generator, superheated and guided to the lower end of the bundle. The steam not consumed within the bundle was condensed in two parallel condensers and the hydrogen produced was fed into the off-gas system after dilution by air to a low H_2 concentration.

Bundle design:

The bundle and its surroundings are shown in Figure 3 and 4. The bundle horizontal arrangement is given in Figure 5 and the bundle components in Figure 6a. Characteristic data of the bundle are presented in Tables 2, 3 and 4. The bundle consisted of 12 heated rods, 6 unheated rods, two channel box walls and the absorber blade, representing part of a BWR absorber fuel element arrangement.

The heated fuel rod simulator was sheathed with standard Zry4 cladding tube, containing UO_2 annular pellets with a central heater. The heater consisted of a 1024 mm long tungsten rod (6 mm diameter), the upper electrode (300 mm molybdenum; 689-770 mm copper) and the lower electrodes (300 mm molybdenum; 183-219 mm copper). The electrodes had a diameter of 9 mm. The electrodes were flame-sprayed with 0.2 mm thick layer of ZrO_2. Large flexible copper cables proved the connection to the electrical system. The resistance of the flexible cables to the points of voltage measurement for the determination of the power was less than 1 m Ω per rod (recommended value: 0.5 mΩ).

The resistivities R of tungsten, molybdenum and copper are given respectively in the following three equations:

$$R_W = 2.61 \cdot 10^{-2} + 2.63 \cdot 10^{-4} T_w + 2.20 \cdot 10^{-8} T^2_w$$

$$R_{Mo} = 2.29 \cdot 10^{-2} + 5.36 \cdot 10^{-5} T_{mo} + 1.38 \cdot 10^{-7} T^2_{Mo} - 2.22 \cdot 10^{-11} T^3_{Mo}$$

$$R_{Cu} = 7.89 \cdot 10^{-3} + 9.90 \cdot 10^{-5} T_{cu} - 5.49 \cdot 10^{-8} T^2_{Cu} + 3.16 \cdot 10^{-11} T^3_{Cu}$$

with T in [Kelvin] and R in [$\Omega mm^2/m$].

The unheated fuel rod simulators consisted of solid UO_2 pellets and Zry cladding. The unheated rods extended about to the -200 mm elevation, i.e. to about 20 mm above the initial water level of the quench cylinder (-220 mm). Zry-4 spacers were used at three elevations (-33 mm, 578 mm, 1167 mm) to maintain the positions of the rods.

The fuel rod simulators were screwed into the bundle head plate sealing it hermetically. The bundle head plate thus gave the fixed elevation for the axial thermal movement of the rods. The channel box walls were made of 1.2 mm thick Zry-4. The absorber blade contained stainless steel and B_4C and was made of original LWR-components.

To cool the bundle upper end, the heated rods (the copper electrode inside the Zry cladding) and the connectors for the pressure capillaries and the thermocouples of the unheated rods were surrounded by water. The water was cooled by a heat exchanger. Argon was blown against the lower surface of the plate to protect the sealing of the bundle head plate.

At the lower end the heated fuel rod simulators were cooled by the water of the quench cylinder. The initial water level was at the -220 mm elevation. The unheated rods were in contact with the water of the quench cylinder only by the thermocouple connection cables. The gross volume of water inside the quench cylinder (230 mm ID) was about 70 l.

The bundle was surrounded by a Zry-4 shroud of 1.2 mm thickness. The shroud conducted the steam flow through the bundle. The steam entered at an orientation of 180° into the lower end (0 mm elevation). To minimise the heat losses from the shroud, it was surrounded by a 19 mm (0.75 inch) thick insulating layer of ZrO_2 fibre. On account of the low heat conductivity and heat capacity of the ZrO_2 fibre, the shroud temperature could follow the bundle temperature closely during heatup. The shroud participated in the interaction with steam. The resulting oxidation energy contributed substantially to bundle heat-up.

The connection between steam inlet at 0 mm elevation and shroud was made by a stainless steel steam distribution tube. This tube extended down into the water of the quench cylinder thus forming a lower closure. The time history of the water level in the quench cylinder in all tests showed that there is no net condensation of steam into the quench cylinder.

At an elevation of 40 mm the steam distribution tube was connected to the shroud. From this elevation the shroud extended in vertical direction for 1195 mm and the insulation for 1070 mm. At eight elevations (190-890 mm) windows of 30x30 mm in the shroud and shroud insulation allowed bundle inspection by a video-system (Figure 6b).

The annuli between the shroud and the high-temperature shield on one hand and high-temperature shield and pressure containment on the other hand were closed at the upper end by fibre ceramic layers of 38 mm thickness.

High-temperature shield:

To keep the heat losses as low as possible, the bundle was surrounded by an additional high-temperature shield (HTS). The vertical and the horizontal cross-sections of the high temperature shield are given in Figures 3 and 4. The high temperature shield consisted mainly of ceramic fibre plates. The inner layer of plates consisted of ZrO_2, and the outer layer of Al_2O_3. The fibre ceramics were excellent insulators and had a low density which resulted in a low heat capacity. The thermal shock behaviour of the fibre ceramics was also extremely low.

The mechanical strength of the high-temperature shield was ensured by external walls of stainless steel (0.9 mm). The fibre ceramic plates were attached to the stainless steel cover by ceramic nails. The inner ZrO_2 layer was 38 mm thick, and the outer Al_2O_3 layer was 76 mm. They were separated by a gap of 23 mm. The distance from the inner insulation surface to the centre of the bundle was 153 mm.

The high-temperature shield was located within the pressure tube. In the pressure tube a large number of flanges allowed access to the bundle. Through these holes and their extensions in the temperature shield, the bundle could be inspected during the test with the help of the videoscope systems.

Heating system:

In CORA-28 12 rods out of 18 were heated. The rods could be connected to three independent power supply systems. In this test, the intended power input was the same for all rods. Since the voltages and currents of the individual rods were measured, the power input for each rod was determined. The power input was controlled by a computer. The time-dependent power history was programmed before the test. The power was controlled by measurement of the currents of the groups, and by setting the voltage necessary to obtain the desired power.

3. Test conduct

3.1 Pre-oxidation

CORA-28 should investigate the influence of pre-oxidation of a BWR type bundle. During normal operation in a BWR an oxide layer of about 50 μm is formed in dependence of operation time and conditions. Therefore pre-oxidation of test bundle CORA-28 was foreseen in the CORA-facility. A first pre-oxidation of about 4500 s at about 1050°C resulted in contrast to the pre-calculations about 20 μm oxide layer. A second pre-oxidation phase of 10000 s at 1100°C was necessary to reach the desired oxide layer. The axial distribution of the measured oxide layers of a Zry-4 test tube, which was situated inside the bundle during the pre-oxidation phases is given in Figure 8. Power input and temperature during the first pre-oxidation phase are given in Appendix B.

3.2 *Test conduct of main test*

In the CORA experiments the following phases for the test sequence were generally distinguished (Figure 9):

1. 0-3000 s: pre-heating
2. 3000-4800 s: transient
3. > 4800: cooldown.

To keep the videoscope windows clear a flow of 1.7 g/s argon was directed to the front of the windows. For the protection of the bundle head plate, 4.3 g/s of argon were used to purge the area below the plate. The 6 g/s flow set up for videoscopes and bundle head plate did not flow through the bundle and is marked with the label „videoscopes“ in the second graph of Figure 9. The boundary conditions during the test are given in detail in Figures 10 to 26. Figure 10 shows the argon flow within the facility. Both amounts contribute to the dilution of the hydrogen leaving the facility. Figure 11 presents the overpressure (1,2 bar, 2,2 bar absolute) of the system.

The flow of Argon through the bundle amounts to 8 g/s. The argon is preheated and is flowing through the steam superheater. 2 g/s of steam is added also through the superheater after 3300 s. During the preheat phase a constant electric power input supported the temperature increase in the insulation to a level high enough to avoid condensation.

During the transient phase the initial temperature increase of about 1 K/s was produced by raising the electric power input from 4.5 to 23 kW (Figure 9). The test was terminated by turning off the electric power at 4800 s (slow cooldown by heat losses). The steam input was stopped at the same time.

Figure 12 shows the total electric power input, which was produced by the voltage inputs for the three groups of rods (Figure 13) and the resulting total current (Figure 15). The total electric energy input was derived from the time integral of the power input (Figure 14).

The regular increase of the voltage in Figure 13 was disturbed at about 4400 s. The irregularities were produced by melt formation allowing an electric bypass to and through neighbouring unheated rods. In consequence a lower voltage input is necessary to reach the foreseen power input. This effect can more clearly be seen in Figure 18, showing the currents of the single rods. The resistance of the bundle, the three rod groups and the single rods are given in Figure 16, Figure 19 and Figure 20 to 22. At the beginning of melting the resistance was reduced due to the bypass effect instead of increased with the temperature of the tungsten heater rods. The tendency is typical for all measurements. The sharp spikes during power shutdown are artificial due to measurement of voltage and current not taken at exactly the same times.

In Figure 23 the water temperatures in the quench cylinder at - 250 mm and -300 mm (initial water level at - 220 mm) are given. The decrease of the temperature at -250 mm and the increase at -300 mm were caused by melt falling into the quench cylinder and disturbing the stratification of quench water temperatures highest at the top.

The temperatures measured at - 50 mm elevation (Figure 24) show partly the irregularities at about 4400 s caused by the melt produced in the upper part of the bundle. As shown in Figure 24 for azimuthal angles of 15° and 195° the temperatures were measured at the steam distribution tube and for angles of 165° and 345° at 15 mm inside the tube.

The temperature of the argon at the steam inlet was measured with two thermocouples (Figure 25). The resulting temperatures of the two thermocouples are practically the same. The slow increase of the steam inlet temperature was caused by the heatup of the walls of the connecting tube between superheater and the entrance of the bundle, due to the additional heat capacity of the steam.

Figure 26 demonstrates the axial asymmetry of the temperature at the bundle due to the more effective cooling by the quench water and the „cold" gases and steam entering at the lower end of the bundle. Given are temperatures at 50 mm below (- 50 mm) and 50 mm above (1050 mm) the tungsten rod (heated) region.

4. Temperature measurements

The temperatures in the bundle were measured by high-temperature thermocouples consisting of WRe5/WRe26 wires and HfO_2 insulating material. The sheath was made of tantalum and Zircaloy. Thermocouples labeled „Ker" were additionally shielded with a ZrO_2 sheath. The measurements taken in the high-temperature shield were performed with NiCrNi-thermocouples sheathed with stainless steel. Also the compensation cables were sheathed with stainless steel. The positions of the thermocouples in the bundle are given in Table 5 and Figure 27 and those in the high-temperature shield in Figures 51a and 51b.

The temperature measurements of the bundle are presented as functions of time in the following way: on one hand, the temperatures of the components (heated rods, unheated rods, channel box walls, absorber blade, etc.) are given in Figures 28 - 39, on the other hand - for comparison reasons - the temperature measurements of the different components are selected by identical axial elevations (Figures 40 - 47). The temperature measurements of the high-temperature shield are shown in Figures 52 - 70. A summary of the temperature measurements is given by the set of best-estimate temperatures in Figures 48 and 49.

4.1 Temperatures of the components

The temperature measurements sorted according to their positions at the different components are given in Figures 28 to 39. For all components of the bundle (Figure 28 to 31) the same axial profile was found. At the beginning of the power input (3000 s), the temperature of the gas entering the 0-mm elevation with a temperature of about 540 to 630 °C (Figure 25) was higher than the temperature of the bundle. In consequence at that time the gas was heating the bundle with maximum temperature at the lower end. With increasing bundle temperature, gas and steam acted as coolant. In consequence, the axial temperature maximum moved to the upper part. The maximum temperature was reached at the elevation 750 mm to 950 mm. From this region the temperature escalation extended to the lower and upper elevations. The temperature escalation due to the exothermal Zr/steam reaction worked to about 150 mm elevation at the lower end and 1250 mm at the upper end. The strong temperature increase on the channel box wall at 50 mm elevation was caused by relocating melt (Figure 30).

The temperature rise during the escalation in CORA-28 was less than in tests for PWR bundles. The reason is a smaller exothermal Zr/steam reaction at the BWR bundles. PWR-typical tests were run with 6 g steam/s and BWR-typical tests with 2 g steam/s. The lower reaction is reflected in lower hydrogen production in the BWR-typical tests. For instance in the PWR-type test CORA-29 /15/ the total hydrogen production was twice as large as in CORA-28.

The temperature of the shroud (Figure 36) showed the same axial behaviour at nearly the same level as those in the bundle. This fact was caused by the good insulation and low heat capacity of the shroud insulation. The Zry shroud took part in the exothermal reaction and thus contributed to the bundle heat-up.

The temperatures at the outside of the shroud insulation (Figure 37) exhibited a strong axial increase (from 200°C at 50 mm elevation to 1200°C at 950 mm elevation). There existed a strong radial temperature gradient within the shroud insulation, due to the low thermal conductivity of the ZrO_2 fibre.

The readings of Figure 38 were taken by thermocouples suspended from the "pertinax" bundle head plate into the coolant channels. The elevations 1471 mm and 1511 mm, given in Figure 39, correspond to the lower and upper surface of the bundle head plate. This figure shows that the maximum temperatures at the lower and upper surfaces of the bundle head plate were about 120°C and 70°C.

4.2 Temperatures measured at different elevations

The temperature as function of time measured at the different elevations is given in Figure 40 to 47. The elevation 1511 mm (Figure 40) corresponds to the upper surface of the bundle head plate, which was cooled by water. BKPL means that the thermocouple (TC) was attached to the surface of the bundle head plate and h and u, that the TC was attached to the heated (3.5) or unheated (2.4) fuel rod simulator. The maximum value measured at this elevation during the test was below 80°C. The highest temperatures were reached in the heated rods due to the heat conductivity in the central upper electrode. We have no explanation for the relative low values at the unheated rods.

The elevation 1491 mm represents the middle vertical height of the bundle head plate and elevation 1471 mm its lower surface. The middle of the bundle head plate reached about 90°C shortly after the end of the test. The maximum temperature at the lower surface of the bundle head plate varied between 120°C and 150°C. The higher temperature was measured with the thermocouple attached to the heated rod 3.5 (see Figure 5).

The temperatures measured between 1400 mm and 1150 mm are given in Figure 41. Above 1350 mm the maximum temperature stayed below about 200°C. This is due to the additional cooling of the bundle head plate by argon. At 1250 mm a maximum temperature of 1200°C was reached and at 1150 mm the maximum temperature amounted to about 1650°C.

Figures 42 to 45 show that between 950 mm and 350 mm a maximum temperature close to 2000°C was reached. At 1050 mm and 150 mm the maximum temperature amounted to above 1800°C. At 50 mm elevation the temperature stayed below 1000°C and did therefore not participate in the exothermic reaction. The steep increase in the channel box temperature was probably caused by melt relocation from the upper hotter part of the bundle. The axial temperature distribution has clearly moved to the upper part of the bundle.

At 0 mm elevation the preheated gas and steam entered into the bundle. (The tungsten heaters within the bundle were placed between 0 mm and 1000 mm elevation). The temperature of the gas at the steam inlet are given in the upper half of Figure 46. The increase of the temperature is caused by the introduction of steam at 3300 s. The heat capacity of the additional steam heated the walls of the connecting pipes so that the heat losses of the steam entering at 800°C were getting smaller. As a consequence, the steam temperature at the entrance of the bundle increased from 540°C to 630°C.

The temperatures measured at the spacers and in the neighbourhood of the bundle at -50 mm elevation are shown in the lower half of Figure 46. The large temperature spike was caused by relocating melt.

The comparison of the temperatures measured on different components at the same elevation show that the radial gradient inside the bundle could be neglected. The measurements taken at the same elevation have therefore been combined to give one representative temperature for the bundle at that elevation. Due to the failure of some thermocouples after the escalation these "estimated" temperatures are more reliable before this event. The results of this combination of measurements are given in Figure 48 as "best-estimated" temperatures of the bundle for different elevations as a function of time. In Figure 49 these values were rearranged as axial temperature distributions for different times within the test sequence.

Up to 3400 s the temperature in the bundle was mainly determined by the temperature of the inlet "gas" of about 550°C resulting in an axial temperature profile with the maximum at the lower end. With increasing power input and temperature level the gas was cooler than the bundle and so acted as coolant. The maximum of the temperature moved to the upper end of the bundle. At about 4200 s the axial temperature profile had its maximum between 850 mm and 950 mm and reached a level where the chemical heating of the exothermal Zry/steam reaction increased its contribution. The temperature escalation started first in this region and then moved to the 450-mm elevation in less than 100 s down and then with a lower velocity up to 1250 mm and down to 150 mm.

In Figure 50a the time histories of the bundle temperature and the measured hydrogen are compared. One can clearly recognise the relationship of the temperature escalation and the hydrogen production. Correlated to the H_2-production is the exothermic reaction energy of the Zr/steam interaction.

In Figure 72 the chemical power calculated from the measured total hydrogen of Figure 71 is compared to the electric power input. During its maximum the chemical power was 50% higher than the maximum of the electric power.

For comparison in Figure 50b the bundle temperature and hydrogen production is given in addition for the PWR-test CORA-29. In this test the preoxidation reached only about 10μm ZrO_2 in maximum. More important for this comparison may be the higher steam input of 6 g/s for the PWR-test compared to the 2 g/s for the BWR-test CORA-28. Also in this PWR test we got the correlation between temperature increase and hydrogen production. But the temperature escalation was stronger in agreement with the faster production of hydrogen, which is in total twice as large for the PWR-test.

4.3 Temperatures of the High-Temperature Shield

To reduce the radial heat losses, the insulated bundle was surrounded by the additional fibre insulation of the high-temperature shield (HTS). The position of thermocouples on the inner surface (153 mm radius), inside the insulation and on the outer surface (293 mm radius) are given in Figures 51a and 51b. Results of the measurement of temperatures at different locations are given in Figures 52 to 70.

The maximum temperature of the inner surface amounted from 200°C at -50 mm elevation to 950°C at 1150 mm elevation (Figure 52). The azimuthal variation of the temperature at the inner surface (153 mm) is shown in Figures 53 to 55. At 550 mm a variation of 200 K is measured (Figure 53); at 950 mm a maximum difference of 100 K was recorded and at 50 mm elevation the measurements of the maximum temperature agree within 20 K.

The temperatures measured at the inner surface of the HTS can be compared with the temperatures on the outside of the bundle insulation. At 950 mm a maximum temperature of 1150°C at 75° of the insulation outside can be compared with the temperature at the inner surface of the HTS of about 900°C (the azimuthal difference at this elevation amounts to 100 K). At 550 mm the maximum temperature of the outside insulation was about 1000 °C compared to 970°C on the inner HTS with a variation of 200 K. At 50 mm elevation about 200°C at the outer bundle insulation compared to about 250°C at the inner HTS surface with a variation of about 20°C. The lower temperature at the bundle insulation at this elevation, may be connected to the fact, that the bundle is immersed into the water of the quench cylinder, while the high-temperature shield (HTS) has no contact to the water of the quench cylinder.

The temperatures recorded within the insulation and on the pressure vessel are given in Figures 57 to 65. At a radius of 172 mm the maximum temperature varied between 120°C and 480°C. At 153 mm the maximum was reached at 4900 s, and at 172 mm the maximum was found at about 5500 s. For 192 mm radius the maximum temperatures were between 70°C and 240°C at elevations 50 mm to 950 mm and were reached at about 6500 s. At 255 mm radius the temperature stayed below 100°C and the maximum was not reached before 9000-12000 s.

At 293 mm radius, the outer surface of the insulation of the HTS, the temperature at 950 mm elevation (Figure 64) was with 110°C higher than at 255 mm radius. It is assumed that the insulation was heated at the upper elevation from the outside by convection or radiation from the upper uninsulated part of the bundle. The maximum temperature of the outer surface of the pressure vessel at 990 mm was below 70°C. The radial distribution of the temperatures at 950 mm, 550 mm and 50 mm are given in Figures 66 to 70. These figures clearly show the decrease of the temperature and delay in build-up of the maximum with increasing radius.

5. Failure of absorber blade and fuel rods

Information on the failure of the absorber blade could be gained from observation of irregularities of the absorber blade temperatures. In Figure 77a deviation from a smooth temperature reading can be seen at about 4330 s. The thermocouples for the measurement of temperature in the absorber blade were located inside the blade between the tubes filled with B_4C powder. The melt formation started at the contact of B_4C powder and surrounding ss tube. In agreement with the separate-effect tests the irregularities in the temperature traces pointed out that the interaction B_4C/ss starts between 1200°C and 1300°C.

The internal pressure was measured at four unheated and two heated rods, as shown in Figure 73. The sudden drop in the pressure difference of about 3 bar between internal rod and system pressure indicates the failure of the fuel rod simulators. The rods failled in the sequence 6.4, 4.2, 4.6, 7.1, 2.4, 3.5 in the period from 4340 s to 4485 s (Figure 74 and 76): I.e. the failure started with 3 unheated rods positioned adjacent to the channel box wall in a temperature range from 1370°C to 1400°C.

6. Hydrogen generation

The hydrogen produced during the test by the steam/zirconium reaction was measured with mass spectrometer systems installed at two positions, i.e. above the test section, and in the mixing chamber after the gas had passed the condenser (see Figure 1). The gas at the test section outlet could contain a high steam partial pressure and had therefore to be diluted by helium before it entered the analyser through a capillary tube. For this purpose a dilution chamber with flow meters was installed.

A schematic diagram of the probes, gas lines, and gas analysis system is provided in Figure 7. The off-gas mixture which contained hydrogen among other gases is transported to the spectrometer via capillary tubes. It was analysed by quadrupole mass spectrometers of the type Leibold PQ 100. The ion currents representing the concentration of the respective gases were determined. The production rate of a gas component was calculated with the ratio of the partial pressure of the particular gas to that of argon (carrier gas) and multiplied by the argon flow rate through the test bundle. The hydrogen generation rate was evaluated as follows:

$$R_m = 2 \bullet p_H F_{Ar} / (22.4 \bullet p_{Ar}) \quad [g/s]$$

with

R_m = mass production rate of hydrogen [g/s]

p_H = partial pressure of hydrogen

p_{Ar} = partial pressure of argon

F_{ar} = volumetric argon flow through mixing chamber [l/s].

Based on a calibration test with bundle CORA-7, in which a mixture of argon and 30% hydrogen was radially injected into the test section, the delay time of monitoring the gas was determined to be 80 s. This time was taken into account for the measured hydrogen production in all CORA experiments. The same calibration test, however, showed lower hydrogen production rates than would be expected from the injected gas flow. For this reason the measured data were corrected based on the actual gas concentration, i.e. on the gas input during the calibration test. A transfer function was determined and applied to the measured data. The result is a corrected curve that better represents the H_2 production rate in the test section.

The hydrogen production rate during test CORA-28 is given in Figure 71. The corrected data are based on the transfer function of the CORA-7 calibration test. The corrected curve shows a steeper profile. The small peaks in the corrected curve are a consequence of the correction method and should therefore not be taken into account. The maximum production rate of about 220 mg/s was reached at about 4700 s. The total hydrogen produced amounts to 104 g.

Production of energy is correlated with the formation of hydrogen in the exothermal Zircaloy/steam reaction. Using the corrected values of the measured hydrogen the resulting chemical power is shown in Figure 72. In the same figure the electric power input is given for comparison. The maximum value of the chemical power is 50% larger than the maximum of the electric power. Using the total amount of 104 g produced, the total oxidation energy was determined to 15,8 MJ. The total electric input amounted to 28.8 MJ (Figure 14). The exothermal energy corresponds to 55 % of the electric input, compared with nearly 100% in the PWR test CORA-29.

To calculate the percentage of Zr oxidation from the hydrogen production that bundle length is used, which had experienced temperature above 1700 K. For PWR bundle mass of cladding and shroud and for BWR bundle mass of cladding, shroud and channel box walls were taken into account. With these assumptions for CORA-28 we get a total Zr oxidation of 30% compared to 75% for CORA-29. The fraction of steam consumed in CORA-28 was 79% compared to 38% in CORA-29. The reason is the much higher steam input of 6 g/s in CORA-29 compared to 2 g/s in CORA-28.

7. Post-test appearance of the bundle

The post-test appearance of the bundle CORA-28 is presented in Figures 85-133. The state of the insulation can be seen in Figure 85, which gives the bundle at different orientations. These photographs show the bundle after the test, still in its test position. Only the surrounding high-temperature shield had been removed, to give access to the bundle. The pieces of insulation missing in the photographs were broken away after the test. The outer appearance of the ZrO_2 fibre boards in Figure 85 shows an overall smooth surface. In Figures 86 and 87, photographs of the inner surfaces of the fibre insulation show the areas of interaction between shroud and insulation. The strongest attack on the fibre boards was found at 120° and 300° orientation. This corresponds to the direction of the absorber channel. In this direction the melt from absorber blade and channel box walls had the easiest access to the shroud. In Figures 88 and 89 an overview of the shroud after removal of the insulation is given. The most destroyed area corresponds to areas with the strongest attack on the insulation (120° and 300°).

To recognise the details at the damage on the shroud in Figures 90 - 99 detail photographs at 120° and 300° orientation are given. The temperatures given on these figures show the axial profile of the maximum bundle temperature. Figures 100 to 104 show detail photographes of the windows in the shroud and a region where the shroud was destroyed, so that the view towards the bundle is possible.

In Figures 105 to 108 relocated melt "refrozen" in the lower end of the bundle (50 mm to -200 mm elevation) is shown. Figures 109 + 110 show the melt which had passed the bundle and relocated into the water of the quench cylinder on top of the so-called comb plate.

The damage of the bundle can best be comprehended by including the information from cross sections of the bundle. To enable the cutting of the cross sections a Lucite box was set around the bundle for encapsulation with epoxy resin. The lower end of this box was sealed, by a paraffin layer which was produced by "refreezing" paraffin floating on the water of the quench cylinder. Rütapax 0273 with the hardener LC (Bakelite GmbH, Iserlohn) was used as epoxy resin. This epoxy resin was chosen as its reaction time was long enough that the shrinkage effect was negligible. The hardening time was one week. The bundle was filled starting from the bottom through the steam inlet to avoid air entrainment. A saw with 2.3 mm thick diamond blade of 500 mm OD (mean diamond grain size 138 μm) was used to cut the bundle at 3200 rpm. The cross sections are presented in Figures 111 to 133. Horizontal cross sections are given in Figures 111 to 114, the vertical cross sections are presented in Figures 115 to 123. Finally, in Figures124 to 133 cross sections of the pre-oxidised test CORA-28 are compared to the normal tests CORA-16. A complete set of horizontal cross sections is given in the appendix (A33 - A41).

From the post-test photographs and the cross sections one can obtain the following information:

- Based on the temperature profile, damage of the bundle was found between about 150 mm and 1150 mm. In the cross sections at 142 mm and 1157 mm the shroud had kept its intact shape and no attack on the fuel rod simulators can be found. Only high deformations of the channel box walls can be recognised. From the absorber blade only remnants of the stainless steel tubes had survived at 142 mm. (The intact form can be seen in the cross section at 57 mm elevation.)
- The strong deformation of the oxidised shroud in the cross sections between 257 mm and 1057 mm show on the other hand the larger plasticity of oxidised Zry at high temperatures. The strongest attack on the shroud had developed on the walls adjacent to the absorber channel (120° - 300° direction).
- The damage within the bundle started at the absorber channel, as clearly can be seen from the cross sections. In the upper part of the bundle the absorber blade had completely disappeared and at 142 mm elevation, in the otherwise intact bundle, the absorber blade was strongly dissolved. Up to 657 mm only the sintered remnants of the B_4C rods had survived (Figure 124).
- The vertical cross sections show that these sintered rods form a stable configuration up to about 690 mm elevation (Figure 119).
  Above this elevation all absorber material had disappeared. This means that in a reactor large regions could be left without absorber. During reflood the consequences on the recriticality must be taken into account.
- The B_4C in contact with the stainless steel started the eutectic interactions. With the melt formation the contact between the materials increased and accelerated the liquefaction process of tube and blade wall. This process started in the upper part of the bundle at the axial temperature maximum. The liquefied material flew into the gap between absorber blade and channel box wall. The stainless steel melt started to attack the Zircaloy channel box wall by eutectic interaction. The

eutectic interaction liquefied the channel box wall far below the melting temperature of the Zircaloy and released the melt into the bundle. The melt flew down within the gap solidifying according to the axial temperature profile.

- The attack of absorber material on the channel box wall and the Zry cladding of the fuel rod simulator can clearly be seen in horizontal cross sections from 157 mm to 1057 mm.

- As CORA-28 should investigate the influence of pre-oxidation on the damage the behaviour of the bundle should be discussed in comparison to test CORA-16, which was performed without pre-oxidation (Figures 124 to 133).
  The preoxidation had to be performed within the facility. In consequence due to the axial temperature profile the preoxidation is strongly dependent on the elevation. As can be seen in Figure 8 the oxide layer varied from negligible values at the bottom to about 55 μm in the upper part of the bundle.

  The comparison of the cross sections CORA-28/CORA-16 show that the stronger preoxidation in the upper part of the bundle reduced the interaction between the B_4C/steel absorber melt and the Zircaloy of the channel box wall and the cladding of the fuel rod simulators. A larger part of the oxidised channel box wall remained in place. In the lower part, there was more or less the same material behaviour as in the non-oxidised BWR bundles. The comparison of the fuel rod simulators show the same tendency: the lower damage of the cladding for CORA-28 in the upper part of the bundle due to the reduced interaction. In general, the melt formation was reduced in CORA-28 compared with CORA-16.

8. Blockage formation and mass distribution

The relocation of molten material was also determined by measuring the axial distribution of the blocked area and bundle mass. These measurements were performed in connection with the epoxying process. As can be seen in Figure 80 the resin was poured into the Lucite mould from the bottom end. By weighing the resin left in the supply container after each step, i.e. when the resin level had raised in the bundle by 1 cm, the difference of mass allowed the calculation of the void volume of the bundle as a function of axial height. The filling process was slow enough so that the reading at the scale could have been taken for each cm.

The error of this measured mass distribution amounts to about 15%. (10% with respect of the measurement of 1 cm increments of the epoxy level and 5% due to the error of mass measurement.) The error, however, is alternating, i.e. epoxy not measured at one step is certainly included in the next reading at the scale. A filtering method using a Fourier transformation, where higher frequencies were cut off by a low pass filter, was performed to deal with these errors.

The data of the mass of resin as a function of elevation (g/cm) in Figure 81 demonstrate the scatter. The smoothed solid-line curve in Figure 81 was obtained from the data (crosses) by filtering. The axial distribution in Figure 81 is the distribution of the epoxy bundle fill-up, i.e. a complement to blockage in the bundle.

Using the density of the epoxy and the cross sectional area inside the Lucite mould the structural area of the bundle end state can be evaluated. Referred to the area of the shroud, it is given in Figure 83a as "relative blockage".

Blocked area (Cross section mould inside-cross section epoxy- cross-section of shroud remnants) referred to cross section of shroud inside.

As part of the shroud was removed together with the fibre insulation after the test, the remnants of the shroud which were present during the filling process were excluded in the evaluation by measuring their contribution to the cross section separately. The areas are given as percentages, where 100% means complete blockage.

To determine the axial mass distribution, the epoxy-filled bundle was cut into horizontal slices and these bundle segments were weighed. The distribution is shown in Figure 82. Knowing the axial epoxy distribution, the contribution of the resin was subtracted from the measured weight to give the mass distribution of the bundle. Also this distribution was corrected for the share of the shroud. The results are given in Figure 83b. These data represent the mass of the rods and spacer. In Figure 83 the measured curve is compared with the mass distribution of the intact bundle.

Specific mass = (Mass of weighed samples -epoxy mass -mass of shroud remnants) referred to the pertinent axial segment.

If one compares the uncertainty of the axial mass distribution with the axial volume distribution, one can see, that the method using the weighed samples is the more accurate. The uncertainty of the measurement of the filled-in epoxy mass contains the same absolute error. However, the relative error is only one fifth, because the epoxy resin is referred to a 5 cm block compared with the reference of 1 cm for the volume method. Because of the lower density of the epoxy resin in comparison with the density of the structural material the relative error is further reduced. On the other hand in the mass distribution the resolution is reduced.
The axial distribution of blocked area and mass in the bundles (Figure 83) are very similar and in accordance with the results from the cross section. Material was reduced in the region above 650 mm and between 300 mm and 500 mm and relocated to the lower part of the bundle. Less material is moved than in the other tests. Only a small blockage had formed with the maximum at 200 mm.

In Figure 84 the axial mass distribution is compared with the axial temperature distribution. One can recognise a strong relation between the axial temperature profile and the melt relocation. The melt relocation to lower elevations corresponds to the expansion of high temperatures to the low elevation. Melt relocation and axial temperature distribution are always strongly connected, i.e. the melt relocation is determined by the axial temperature distribution, but the axial temperature distribution on the other side is influenced by the melt relocation and the exothermal steam/Zircaloy reaction triggered by the heat transported with the melt.

9. Summary and discussion of major results

CORA-28 was a BWR-test which should investigate the influence of pre-oxidation, on the damage initiation and propagation. Due to the axial temperature profile in the CORA-facility during the pre-oxidation, the maximum oxide layer thickness had formed preferentially in the upper, hotter part of the bundle. Consequently, a modified material behaviour in the upper part of the bundle is to be seen.

In the lower part practically the same behaviour as of the unoxidised as-received bundle was noticed. The B_4C in contact to the stainless steel started the eutectic interactions. With the melt formation the contact between the materials increased and accelerated the liquefaction process of cladding tube and blade wall. This process started in the upper part of the bundle where the maximum temperature exists. The liquefied material flew into the gap between absorber blade and channel box wall. The stainless steel melt started to attack the Zircaloy channel box wall by eutectic interactions. The eutectic interactions liquefied the channel box wall far below the melting temperature of the Zircaloy and released the melt. The melt running down within the gap solidified due to the axial temperature gradient.

In the upper part the following processes can be found. The beginning of the temperature escalation was delayed by about 200 s and the rise of temperature was reduced to a mean value of about 3 K/s due to pre-oxidation. The basic damage mechanisms were the same, but stronger pre-oxidation in the upper part of the bundle reduced the interaction between the liquefied absorber material and the Zircaloy of the channel box walls. By this also the interaction with the Zircaloy cladding of the fuel rods is reduced. A larger portion of the channel box walls and of the cladding survived. The reduced chemical interactions resulted in a reduced melt formation and relocation in the bundle.

Although the stainless steel tubes of the absorber rods, which contain the B_4C powder, were liquefied by chemical interactions, the remaining declad B_4C columns survived by sintering. In CORA-28 this B_4C columns remained intact up to an elevation of about 650 mm. Besides those remnants in the case of the considered accident one has to take into account the question of re-criticality for the reactor with partly relocated absorber rods in the case of reflooding.

The total amount of hydrogen produced was 104 g. This corresponds to an oxidation energy of 15.8 MJ. The total electric input amounted to 28.8 MJ. With this the exothermal energy corresponded to 55% of the electric power input, compared with nearly 100% in the PWR test CORA-29.

Using the bundle length, that had experienced temperatures above 1430°C for the determination of the Zr oxidation, Zr oxidation in the test CORA-28 amounts to 30%, compared to PWR-test CORA-29 with 75%. The fraction of steam consumed in

CORA-28: 79% compared to 38% in CORA-29. (This is the result of the much higher steam input 6 g/s in CORA-29 compared to 2 g/s in CORA-28.)

10. References

1. J.M. Broughton; P. Kuan, D.A. Petti; "A Scenario of the Three Mile Island Unit 2 Accident", *Nuclear Technology*, Vol. 87, 34-53 (1989).
2. S. Hagen, K. Hain: "Out-of-pile Bundle Experiments on Severe Fuel Damage (CORA-Program)", *KfK* 3677 (1986).
3. S. Hagen, P. Hofmann, G. Schanz, L. Sepold; "Interactions in Zircaloy/UO_2 Fuel Rod Bundles with Inconel Spacers at Temperatures above 1200°C (CORA-2 and CORA-3)", *KfK* 4378 (1990).
4. S. Hagen, P. Hofmann, V. Noack, G. Schanz, G. Schumacher, L. Sepold; "Results of SFD Experiment CORA-13 (OECD International Standard Problem 31)" *KfK* 5054 (1993).
5. M. Firnhaber, K. Trambauer, S. Hagen, P. Hofmann, G. Schanz, L. Sepold:ISP-31, "CORA-13 Experiment on Severe Fuel Damage GRS-106", *KfK* 5287, NEA/CSNI/R (93) 17 (1993).
6. S. Hagen, P. Hofmann, V. Noack, G. Schanz, G. Schumacher, L. Sepold; "BWR Slow Heat-up Test CORA-31: Test Results", *KfK* 5383 (1994)
7. S. Hagen, P. Hofmann, V. Noack, G. Schanz, G. Schumacher, L. Sepold; "Dry Core BWR Test CORA-33: Test Results", *KfK* 5261 (1994).
8. S. Hagen, P. Hofmann, V. Noack, G. Schanz, G. Schumacher, L. Sepold; "Behaviour of a VVER Fuel Element Tested under Severe Accident Conditions in the CORA Facility (Test Results of Experiment CORA-W1)" *KfK* 5212 81994).
9. S. Hagen, P. Hofmann, V. Noack, G. Schanz, G. Schumacher, L. Sepold; "Behaviour of a VVER-1000 Fuel Element with Boron Carbide/Steel Absorber

Tested under Severe Fuel Damage Conditions in the CORA Facility (Results of Experiment CORA-W2)", *KfK* 5363 (1994).

10. J. Burbach; "Results of SEM/EDX Microrange Analyses of the PWR Fuel Element Meltdown Experiment CORA-13", *KfK* 5162 (1993).
11. J. Burbach; "Results of SEM/EDX Microrange Analyses of the BWR Fuel Element Meltdown Experiment CORA-16", *KfK* 5282 (1994).
12. S. Hagen, P. Hofmann, V. Noack, L. Sepold, G. Schanz, G. Schumacher;" Comparison of the Quench Experiments CORA-12, CORA-13, CORA-17", *FZKA* 5679, (1996).
13. S. Hagen, P. Hofmann, V. Noack, L. Sepold, G. Schanz, G. Schumacher; "Impact of absorber rod material on bundle degradation seen in CORA experiments", *FZKA* 5680 (1996).
14. S. Hagen, P. Hofmann, V. Noack, L. Sepold, G. Schanz, G. Schumacher; "Cold Lower End Test CORA-10: Test Results"; FZKA 5572 (1997)
15. S. Hagen, P. Hofmann, V. Noack, L. Sepold, G. Schanz, G. Schumacher; "Pre-oxidised PWR Test CORA-29: Test Results"; FZKA 5928 (1997)
16. S. Hagen, P. Hofmann, V. Noack, L. Sepold, G. Schanz, G. Schumacher; "Slow Heatup PWR Test CORA-30: Test Results" FZKA 5929 (1997)

11. Acknowledgements

The authors would like to express their thank to Dr. Larry Ott from ORNL, who has supported the planning, performance and evaluation of the test by his fruitful calculations with the ORNL BWR experiment-specific CORA-models.

At the Kernforschungszentrum Karlsruhe a variety of support needed for preparation, conduct, and evaluation of the experiment is hereby gratefully acknowledged.
The facility was designed by K. Hain and his team. The special bundle set up was designed by Mr. H. Junker. The test rods were assembled by Mr. E. Mackert, the test bundles by Messrs. H. Gießmann and R. Röder. The authors would like to thank Messrs. H. Benz, C. Grehl and H.J. Röhling for test preparations and conduct.

Mr. K. P. Wallenfels was responsible for arrangement of camera and video systems and for the preparation of temperature measurements. Messrs. R. Huber and H. Malauschek prepared and conducted the on-line measurements of the off-gas composition.

Finally we would like to express our gratitude to Mrs. U. Ivanitsch for the careful typing of this report.

List of tables

Table 1: CORA Test Matrix

Test No.	Max. Cladding Tempera-tures	Absorber Material	Other Test Conditions	Date of Test
2	≈ 2000°C	-	UO_2 refer., inconel spacer	Aug. 6, 1987
3	≈ 2400°C	-	UO_2 refer., high temperature	Dec. 3, 1987
5	≈ 2000°C	Ag, In, Cd	PWR-absorber	Febr. 26, 1988
12	≈ 2000°C	Ag, In, Cd	quenching	June 9, 1988
16	≈ 2000°C	B_4C	BWR-absorber	Nov. 24, 1988
15	≈ 2000°C	Ag, In, Cd	rods with internal pressure	March 2, 1989
17	≈ 2000°C	B_4C	quenching	June 29, 1989
9	≈ 2000°C	Ag, In, Cd	10 bar system pressure	Nov. 9, 1989
7	< 2000°C	Ag, In ,Cd	57-rod bundle, slow cooling	Febr. 22, 1990
18	< 2000°C	B_4C	59-rod bundle, slow cooling	June 21, 1990
13	≈ 2200°C	Ag, In, Cd	OECD/ISP; quench initiation at higher temperature	Nov. 15, 1990
10	≈ 2000°C	Ag, In, Cd	cold lower end 2 g/s steam flow rate	July 16, 1992
33	≈ 2000°C	B_4C	dry core conditions, no extra steam input	Oct. 1, 1992
W1	≈ 2000°C	-	WWER-test	Febr. 18, 1993
W2	≈ 2000°C	B_4C	WWER-test with absorber	April 21, 1993

Initial heat-up rate: ≈ 1,0 K/s; Steam flow rate, PWR: 6 g/s, BWR: 2 g/s; CORA 10: 2g/s; CORA W1 + W2: 4 g/s; quench rate (from the bottom) ≈ 1 cm/s

Table 2: Design characteristics of bundle CORA-28

Bundle type		BWR
Bundle size		18 rods
Number of heated rods		12
Number of unheated rods		6
Pitch		14.3 mm
Rod outside diameter		10.75 mm
Cladding material		Zircaloy-4
Cladding thickness		0.725 mm
Rod length	- heated rods elevation	1840 mm - 369 to 1471 mm
	- unheated rods elevation	1672 mm - 201 to 1471 mm
Heated pellet stack		0 to 1000 mm
Heater material		Tungsten (W)
Heater	- length	1000 mm
	- diameter	6 mm
Fuel pellets	- heated rods	UO_2 annular pellets
	- unheated rods	UO_2 full pellets
Pellet stack	- heated rods	0 to 1000 mm
	- unheated rods:	- 200 to 1300 mm
U-235 enrichment		0.2 %
Pellet outer diameter (nominal)		9.1 mm
Grid spacer	- material	Zircaloy -4
	- length	42 mm
	- location (upper end)	lower -33 mm center 578 mm top 1167 mm
Shroud	- material	Zircaloy -4
	- wall thickness	1.2 mm
	- outside dimensions	94.4 x 116 mm
	- elevation	40 - 1235 mm

Table 2 (continuation)

Shroud insulation	- material	ZrO_2 fibre
	- insulation thickness	19 mm
	- elevation	40 mm to 1070 mm
Mo electrode	- length	300 mm (upper and lower end, respectively)
	- diameter	8.6 mm
Cu electrode	- length	189 mm (lower end)
	- length	669 mm (upper end)
	- diameter	8.6 mm
Absorber rod	- number of rods	11
	- material	B_4C powder
	- cladding	Stainless steel
	- cladding OD	5.8 mm
	- cladding ID	4.6 mm
	- length	1600 mm
	- absorber material	-270 mm to +1300 mm
Absorber blade	- material	stainless steel
	- dimensions inside	76 x 6 mm
	- wall thickness	1 mm
Channel box wall	- material	Zircaloy -4
	- dimensions inside	13 x 92 mm
	- wall thickness	1.2 mm
Plenum Volume	- heated rods	$19.8 \cdot 10^{-6}$ m^3
	- unheated rods	39.0 10^{-6} m^3

Table 3: Total specific mass data of bundle CORA-28

Specific mass [kg/m]	
Tungsten heater elements	6.55
UO_2	8.65
Zircaloy in rods	2.70
Absorber, B_4C	0.311
Absorber rods , Stainless steel	0.852
Absorber blade, Stainless steel	1.293
Grid spacer	0.114
Zircaloy of channel box wall *	1.45
Zircaloy of shroud	2.90
Total zircaloy	7.05

* two walls inside the bundle

Table 4: Areas of bundle CORA-28

Cross section areas [m^2]	
Tungsten	$3.393\ 10^{-4}$
UO_2	$8.314\ 10^{-4}$
Zircaloy cladding	$4.110\ 10^{-4}$
Absorber, B_4C	$1.828\ 10^{-4}$
Absorber rods , Stainless steel	$1.08\ 10^{-4}$
Absorber blade, Stainless steel	$1.637\ 10^{-4}$
Zircaloy of channel box wall *	$2.21\ 10^{-4}$
Zircaloy of shroud	$4.41\ 10^{-4}$
Total area inside the shroud	$7.42\ 10^{-3}$

* two walls inside the bundle

Table 5: Position of Thermocouples

Positions of thermocouples in unheated rods (CORA 28)

Slot Number	Elevation [mm]	Rod Number
134	1511	2,4
135	1511	6,4
136	1471	2,4
137	1471	6,4
131	1350	6,2
101	1150	2,6
102	1050	6,4
103	950	4,2
104	850	4,6
105	750	2,4
221	550	2,4
222	550	2,6
223	450	4,6
224	350	4,2
231	150	6,4
232	50	6,2

Positions of thermocouples in absorber blade (CORA-28)

Slot Number	Elevation [mm]	Direction of TE
109	1350	300°
110	1250	120°
111	1150	120°
112	1050	120°
113	950	300°
114	850	300°
115	750	120°
228	550	120°
229	450	120°
230	350	300°
241	250	300°
242	150	120°
234	50	120°

Positions of thermocouples at heated rods (CORA-28)

Slot Number	Elevation [mm]	Rod Number
132	1511	3,5
133	1471	3,5
106	1150	1,7
107	950	3,5
108	750	5,3
225	550	5,3
226	350	3,5
227	150	1,7
233	50	7,1

Positions of thermocouples for gas (CORA 28)

Slot Number	Elevation [mm]	Direction of TE
116	1350	75°
117	1250	0°
138	1471	190°
139	1400	90°
141	1491	225°
142	1511	45°

Positions of thermocouples at the Channel Box Wall

Slot Number	Elevation [mm]	Direction of TE
118	1150	120°
119	950	300°
243	550	120°
244	150	300°
235	50	120°

Positions of thermocouples in ceramic tube(CORA-28)

Slot Number	Elevation [mm]	Direction of TE
120	950	120°
121	950	345°
122	750	165°
123	950	340°

Positions of thermocouples at the grid spacer (CORA-28)

Slot Number	Elevation [mm]	Direction of TE
124	1146	45°
125	1146	225°
245	557	45°
246	557	225°
236	-54	45°
237	-54	255°

Positions of thermocouples shroud outer surface

Slot Number	Elevation [mm]	Direction of TE
126	1150	75°
127	950	255°
128	750	165°
247	550	255°
248	350	255°
249	150	75°
238	50	75°

Positions of thermocouples in shroud insulation(CORA-28)

Slot Number	Elevation [mm]	Direction of TE
129	950	75°
130	750	255°
250	550	255°
251	450	255°
252	350	75°
253	150	75°
239	50	75°

Positions of thermocouples steam distribution tube

Slot Number	Elevation [mm]	Direction of TE
62	-300	180°
261	-250	60°
262	0	180°
263	0	180°
264	-50	15°
265	-50	195°
266	-50	165°
267	-50	345°

Table 6: Temperatures [°C] of test CORA-28 at 0 seconds for different components

	Components						
Elevation [mm]	Heated rod	Unheated rod	Absorber blade	Channel box wall	Shroud	Shroud isolation	**HTS 153 mm**
1511	34	21					
1471	76	68					
1350		80	127				
1250			174				79
1150	221	230	232	239	160		88
1050		264	248				84
950	241	294	253	297	271	118	78
850		226	254				78
750	276	261	250		245	119	76
650							74
550	330	280	289	308	299	99	73
450		273	308			99	69
350	299	367	321		314	119	66
250			340				62
150	332	411	394	389	314	89	64
50	363	460	405	456	292	47	70
-50							63

Table 7: Temperatures [°C] of test CORA-28 at 3000 seconds for different components

	Components						
Elevation [mm]	Heated rod	Unheated rod	Absorber blade	Channel box wall	Shroud	Shroud isolation	**HTS 153 mm**
1511	29	20					
1471	58	51					
1350		63	94				
1250			164				91
1150	267	273	265	275	195		103
1050		318	297				96
950	309	345	308	346	319	140	88
850		296	310				86
750	330	315	304		299	135	84
650							80
550	381	330	331	350	334	109	79
450		321	347			109	76
350	349	398	356		348	133	72
250			367				67
150	366	430	413	404	340	95	69
50	385	469	418	465	308	51	74
-50							67

Table 8: Best-estimate bundle temperatures of test CORA-28

	time, seconds											
elevation	3000	3200	3400	3600	3800	4000	4200	4400	4500	4600	4800	max.
0mm	540°c	540°C	560°C	570°C	580°C	595°C	610°C	615°C	620°C	620°C	620°C	630°C
50mm	460°C	490°C	530°C	570°C	590°C	610°C	640°C	670°C	695°C	715°C	795°C	800°C
150mm	420°C	470°C	540°C	610°C	660°C	720°C	790°C	860°C	790°C	1000°C	1440°C	1450°C
250 mm	400°C	450°C	530°C	620°C	720°C	800°C	900°C	980°C	1170°C	1460°C	1920°C	1920°C
350mm	380°C	425°C	520°C	650°C	780°C	890°C	1010°C	1165°C	1500°C	1830°C	1960°C	1960°C
450 mm	340°C	355°C	450°C	590°C	760°C	930°C	1000°C	1210°C	1700°C	1860°C	1930°C	1930°C
550mm	325°C	360°C	480°C	640°C	800°C	950°C	1100°C	1490°C	1700°C	1810°C	1930°C	1930°C
750 mm	325°c	360°C	480°C	640°C	790°C	950°C	1170°C	1500°C	1700°C	1810°C	1840°C	1840°C
850mm	300°C	320°C	420°C	475°C	750°C	965°C	1150°C	1450°C	1670°C	1810°C	1840°C	1840°C
950mm	320°C	370°C	500°C	625°C	800°C	950°C	1150°C	1450°C	1670°C	1780°C	1840°C	1840°C
1050mm	330°C	350°C	415°C	560°C	720°C	870°C	1025°C	1230°C	1430°C	1600°C	1770°C	1780°C
1150mm	265°C	290°C	370°C	475°C	600°C	710°C	820°C	930°C	1050°C	1380°C	1620°C	1620°C
1250mm	215°C	240°C	320°C	385°C	460°C	530°C	600°C	670°C	710°C	820°C	1070°C	1090°C
1350mm	90°C	90°C	110°C	160°C	190°C	210°C	205°C	215°C	220°C	220°C	225°C	235°C

Table 9: Distribution of void volumes in unheated and heated rods

Void volume of one unheated rod

	Elevation [mm]	Volume [cm^3]	Relative volume [cm^3/cm]
Dishing of uranium pellets; gap between pellet stack and cladding	-201 to 1315	4.083	0.027
Void volume above pellet stack	1315 to 1439	8.378	0.678
	1439 to 1456	0.711	0.419
	1456 to 1522	3.658	0.55
	1522 to 1531	0.387	0.43
	1531 to 1762	6.531	0.283
	1762 to 1764	0.084	0.419
System for pressure measurement		15.120	
Total void volume		38.952	

Void volume of one heated rod

	Elevation [mm]	Volume [cm^3]	Relative volume [cm^3/cm]
Void volume below pellet stack	-369 to -334	0.826	0.236
	-334 to 0	1.391	0.0417
Gap between pellet stack and cladding and between pellet stack and heater	0 to 1024	2.311	0.023
void above pellet stack	1024 to 1875	3.545	0.0417
	1875 to 1911	0.852	0.24
System for pressure measurement		10.860	
Total void volume		19.785	

Table 10: List of cross sections for test bundle CORA-28

Probe	Proben-länge	Axiale Lage unten	Axiale Lage oben	Bemerkungen
28-a	xx mm	-xx mm	-60 mm	Unteres Reststück
Schnitt	2 mm			Unterer Abstandshalter
28-01	13 mm	-58 mm	-45 mm	Querschnitt, oben poliert
Schnitt	2 mm			
28-b	98 mm	-43 mm	55 mm	1 Längsschnitt
Schnitt	2 mm			
28-c	83 mm	57 mm	140 mm	2 Längsschnitte, 28-c-2 poliert
Schnitt	2 mm			
28-02	13 mm	142 mm	155 mm	Querschnitt, 2teilig, oben poliert
Schnitt	2 mm			
28-d	98 mm	157 mm	255 mm	2 Längsschnitte, 28-d-2 poliert
Schnitt	2 mm			
28-e	83 mm	257 mm	340 mm	1 Längsschnitt
Schnitt	2 mm			
28-03	13 mm	342 mm	355 mm	Querschnitt, 2teilig, oben poliert
Schnitt	2 mm			
28-f	98 mm	357 mm	455 mm	Mittl. Abstandshalter
Schnitt	2 mm			
28-g	83 mm	457 mm	540 mm	1 Längsschnitt
Schnitt	2 mm			
28-04	13 mm	542 mm	555 mm	Querschnitt, 2teilig, oben poliert
Schnitt	2 mm			
28-h	98 mm	557 mm	655 mm	1 Längsschnitt
Schnitt	2 mm			
28-i	98 mm	657 mm	755 mm	1 Längsschnitt
Schnitt	2 mm			

Table 10: (continuation)

28-j	98 mm	757 mm	855 mm	Oberer Abst.halter
Schnitt	2 mm			
28-k	83 mm	857 mm	940 mm	
Schnitt	2 mm			
28-05	13 mm	942 mm	955 mm	Querschnitt, 2teilig, oben poliert
Schnitt	2 mm			
28-l	98 mm	957 mm	1055 mm	
Schnitt	2 mm			
28-m	98 mm	1057 mm	1155 mm	
Schnitt	2 mm			
28-n	98 mm	1157 mm	1255 mm	
Schnitt	2 mm			
28-o	xx mm	1257 mm	xxxx mm	Oberes Reststück

List of figures

Appendix A:

A10 : Temperatures of the spacers used in test, pre-heat phase

A11 : Temperatures measured with ceramic-protected TCs; pre-heat phase

A12 : Temperatures of the outer side of shroud, pre-heat phase

A13 : Temperatures of the shroudinsulation, pre-heat phase

A14 : Gas temperatures measured above the heated zone; pre-heat phase

A15 : Temperatures at elevations given, pre-heat phase (1511, 1471-1491 mm)

A16 : Temperatures at elevations given, pre-heat phase (1400-1250, 1150,1146 mm)

A17 : Temperatures at elevations given, pre-heat phase (1050, 950 mm)

A18 : Temperatures at elevations given, pre-heat phase (850 , 750 mm)

A19 : Temperatures at elevations given, pre-heat phase (450, 350 mm)

A20 : Temperatures at elevations given, pre-heat phase (150, 50 mm)

A21 : Temperatures at elevations given, pre-heat phase (0, -50, -54 mm)

A22 : Temperatures at elevations given, pre-heat phase (-250, -300 mm)

A23 : Pre-heating phase temperatures of HTS at 153 mm radius, inner surface, 345°

A24 : Pre-heating phase temperatures of HTS at 550 mm elevation, inner surface at 153 mm radius

A25 : Pre-heating phase temperatures of HTS at 950 mm elevation, inner surface at 153 mm radius

A26 : Pre-heating phase temperatures of HTS at 50 mm elevation, inner surface at 153 mm radius

A27 : Pre-heating phase temperatures of HTS at 153 mm radius, inner surface, 165°

A28 : Pre-heating phase temperatures in HT shield at 172 mm radius

A29 : Pre-heating phase temperatures in HT shield at 192 mm radius

Appendix B:

B12	:	Temperatures of the shroud insulation
B13	:	“Gas temperature“ measured above the shroud
B14	:	Temperatures in the upper part of the bundle
B15	:	Temperatures of the water in the quench cylinder
B16	:	Temperatures at -50 mm at the steam distribution tube
B17	:	Temperatures of inner surface at 153 mm radius
B18	:	Comparison of temperatures of inner surface at 153 mm radius

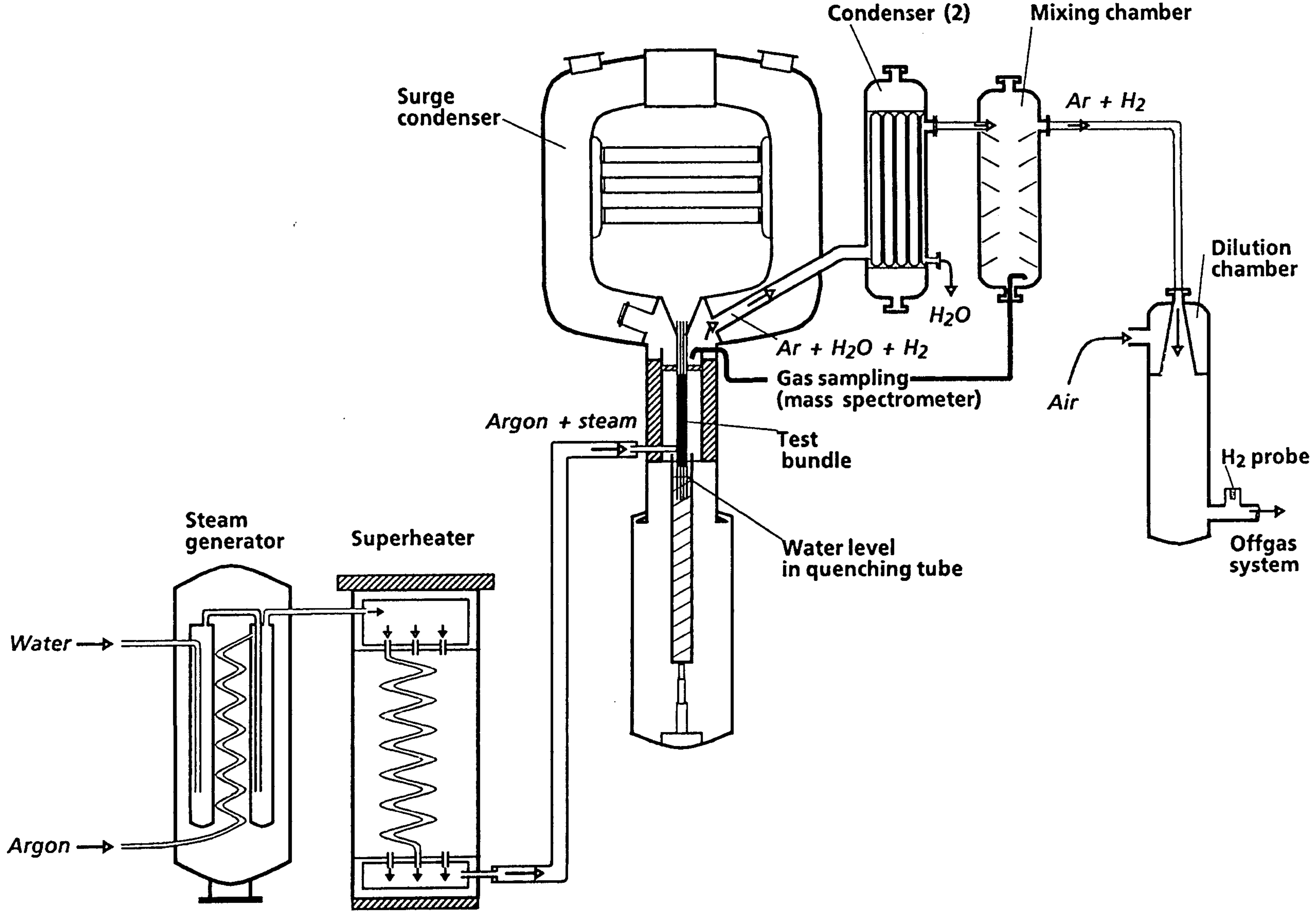

Fig. 1: SFD Test Facility (simplified flow diagram)

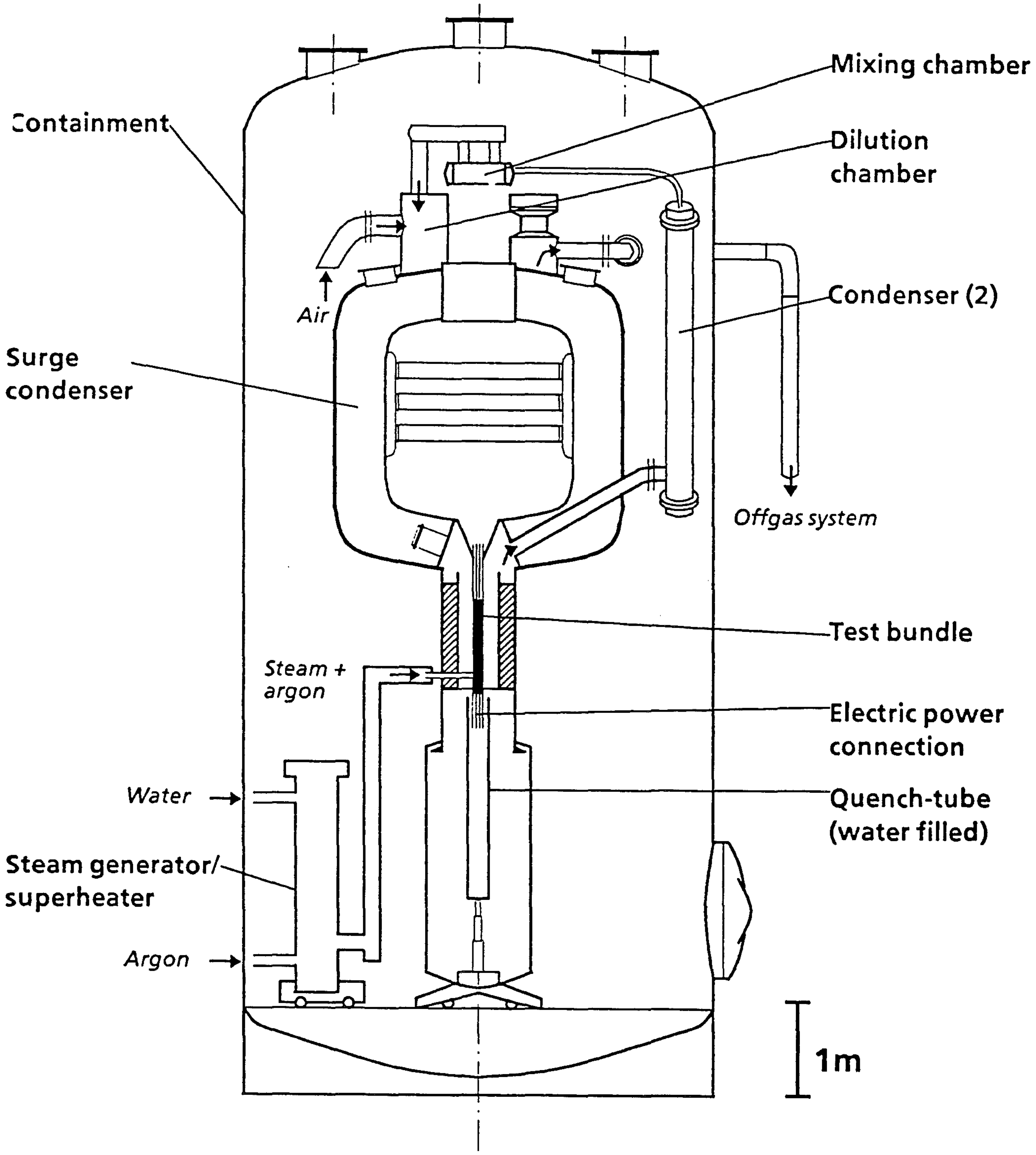

Fig. 2: SFD Test Facility CORA (Main Components)

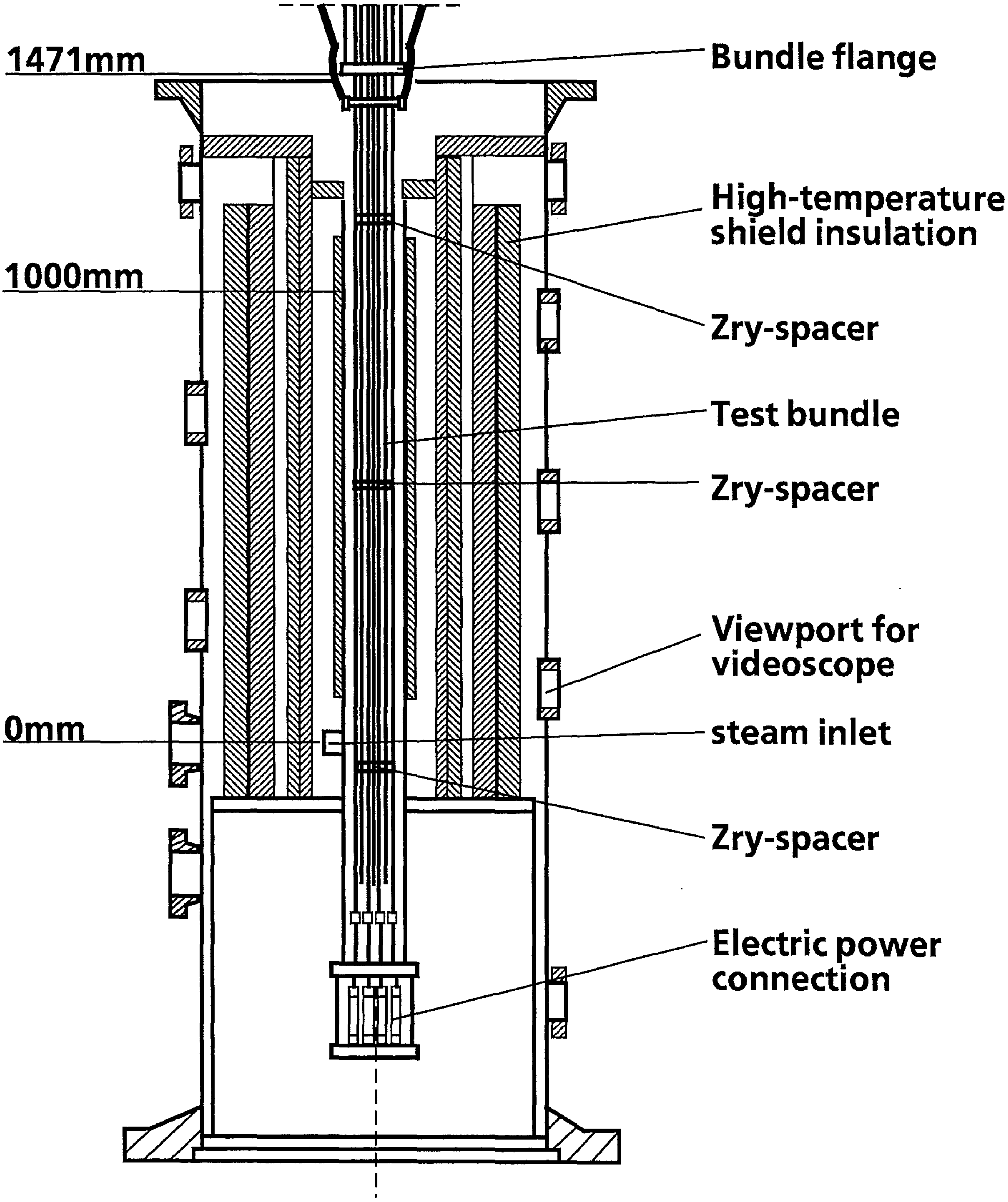

Fig. 3: CORA bundle arrangement

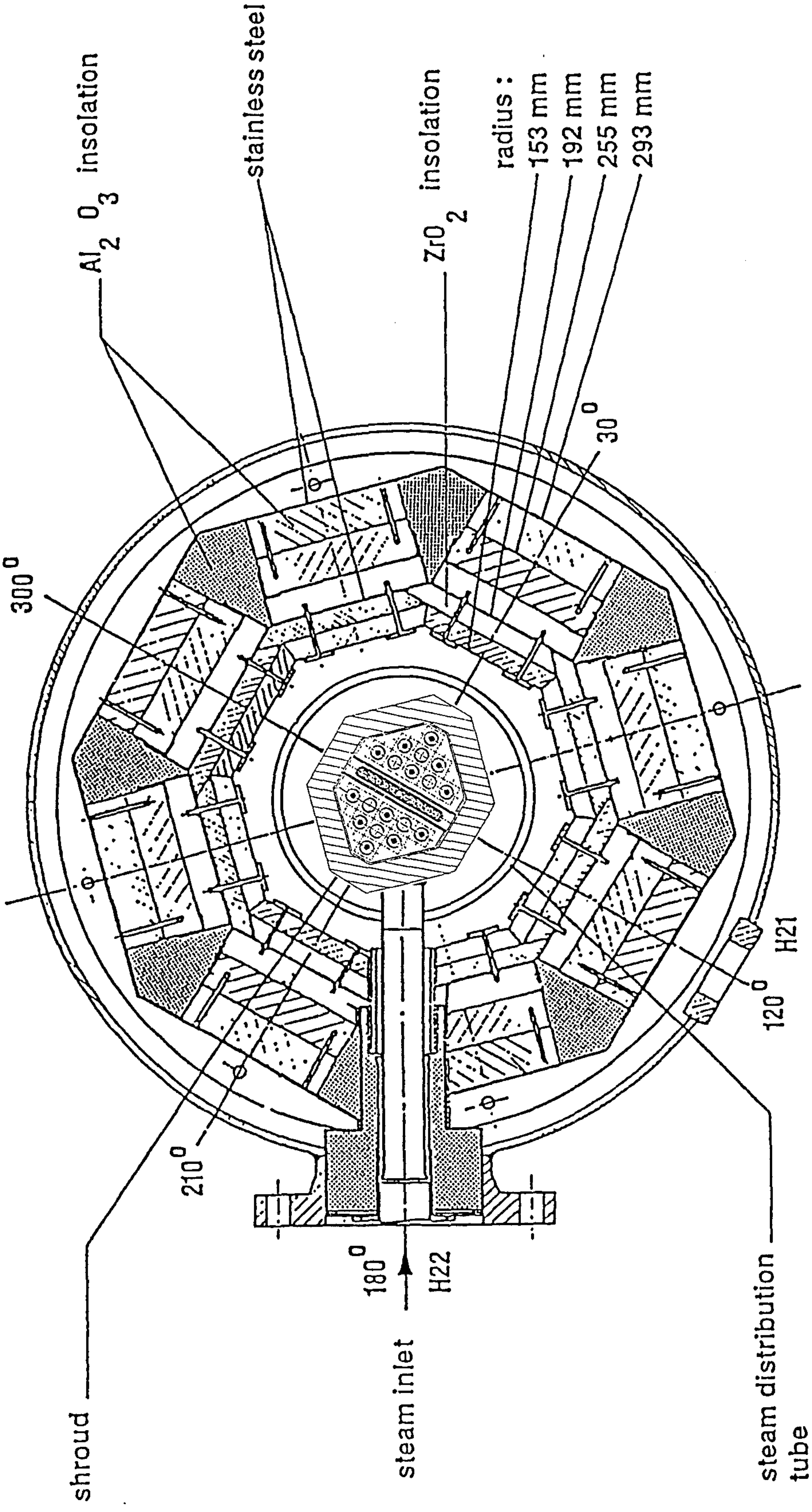

Fig. 4: Horizontal cross section of the high-temperature shield

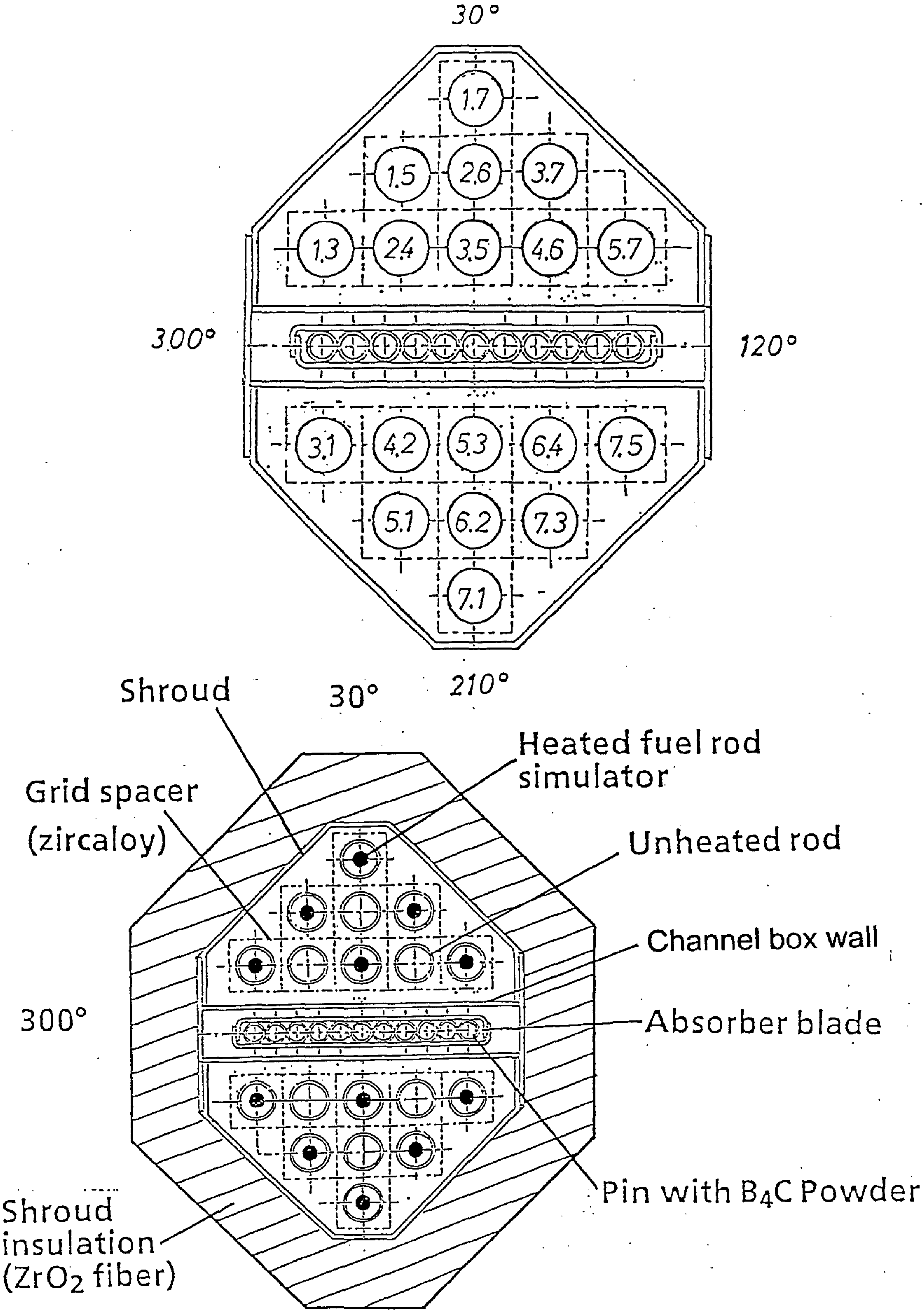

Fig. 5: Rod arrangement and test rod designation of bundle CORA-28

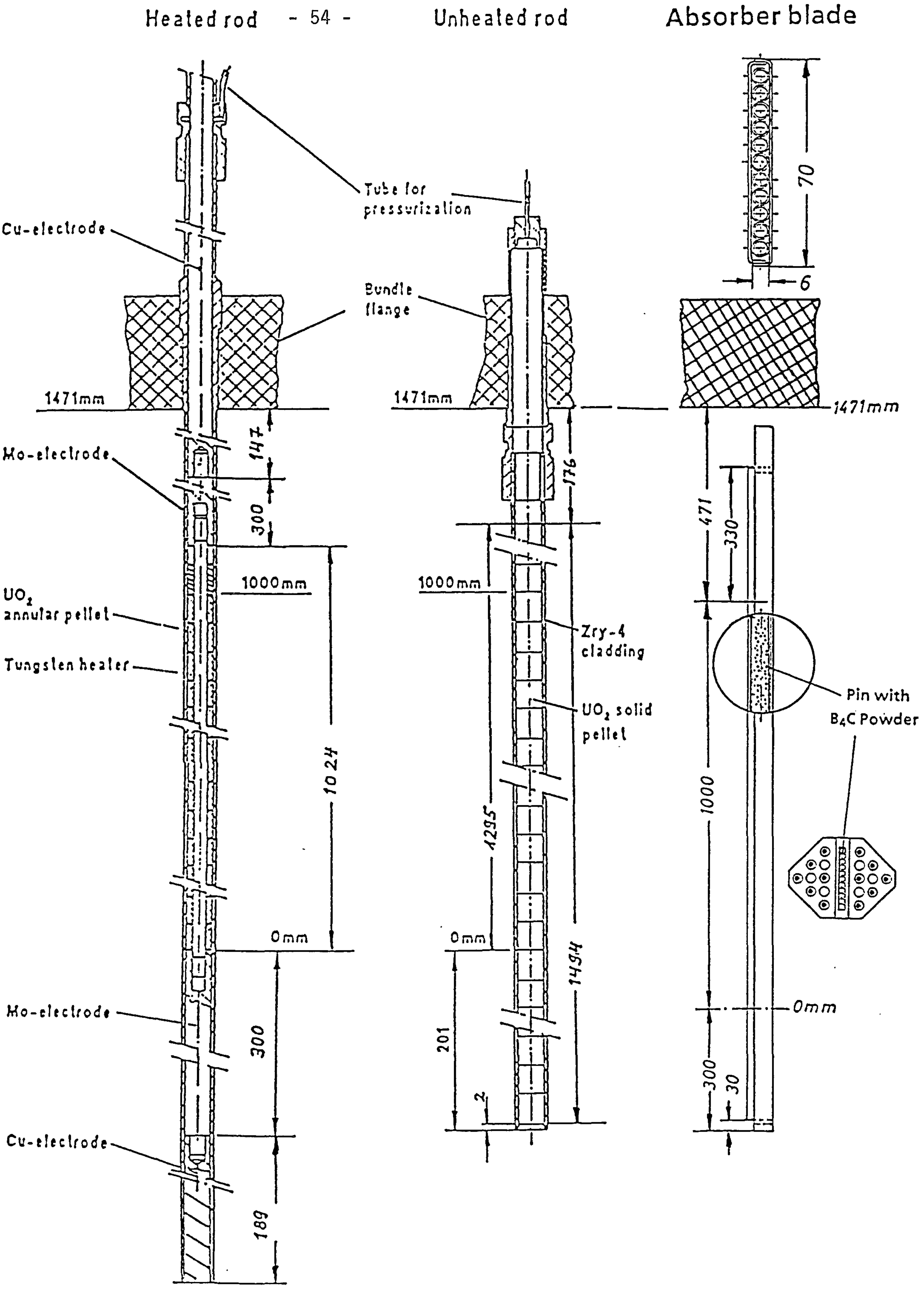

Fig. 6a: Rod types used in the CORA experiments

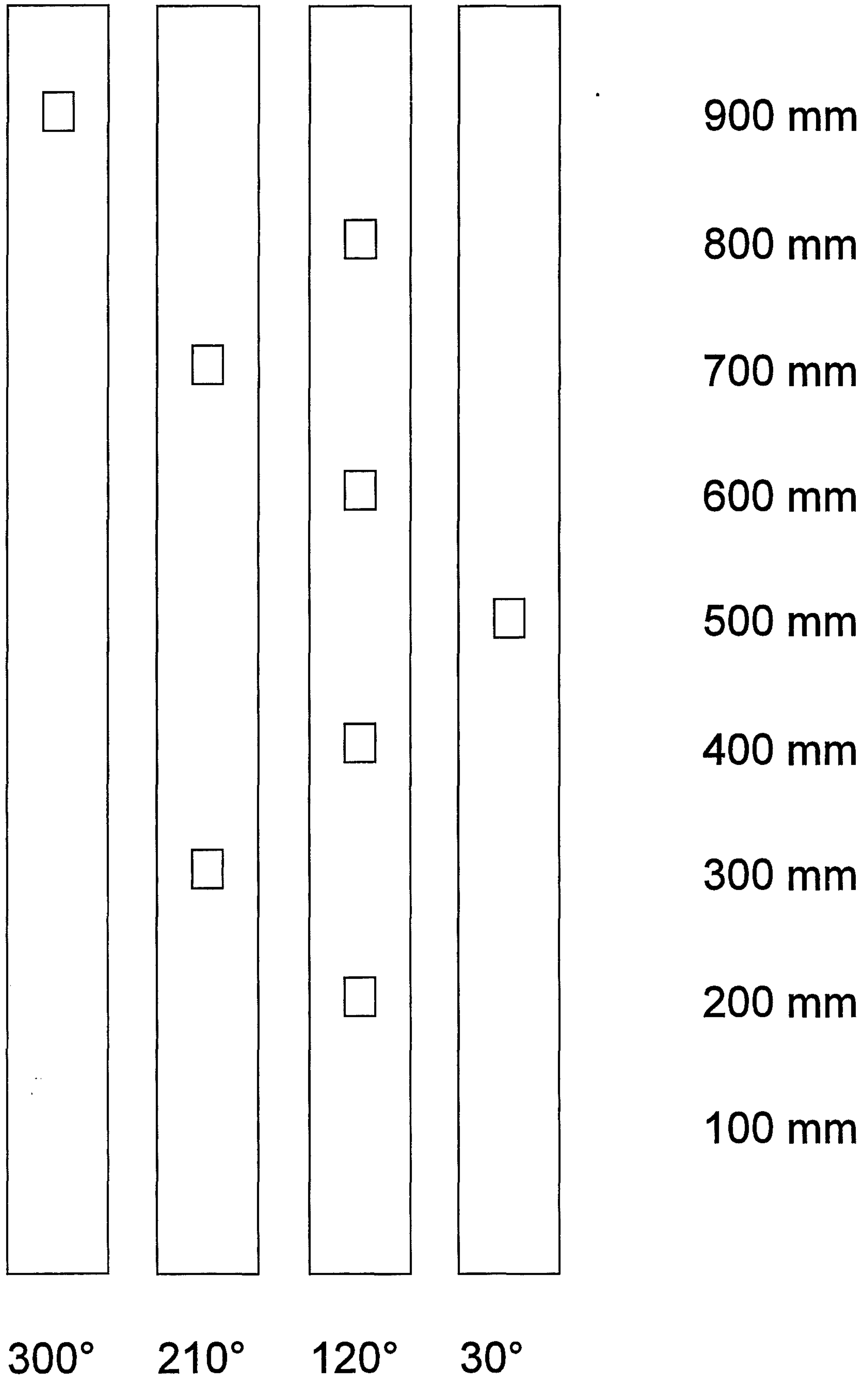

Fig. 6b: CORA-28; Position of windows in the shroud

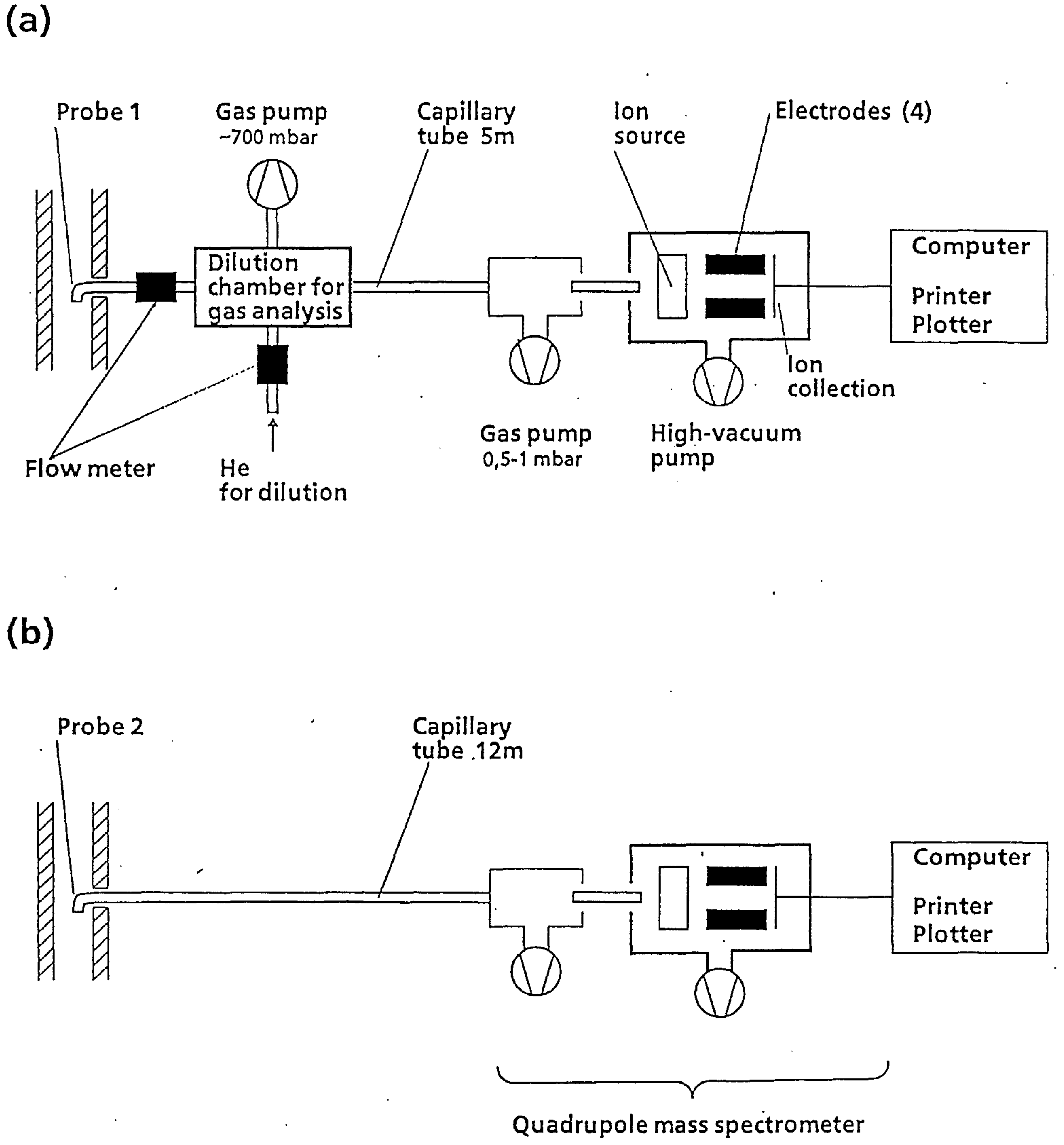

Location (a) : Outlet of test section

Location (b) : Mixing chamber

Fig. 7: Facility of hydrogen measurement

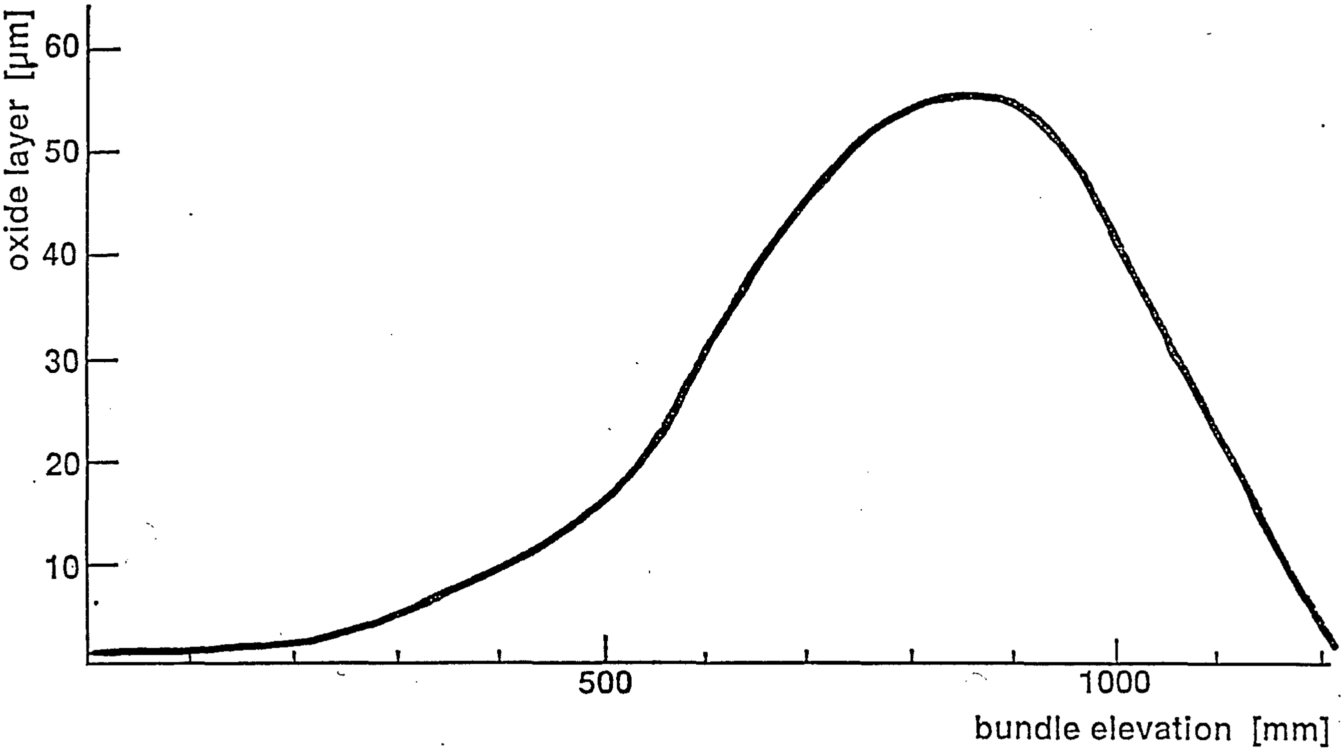

Fig. 8: CORA-28; Axial distribution of oxide layer after preoxidation

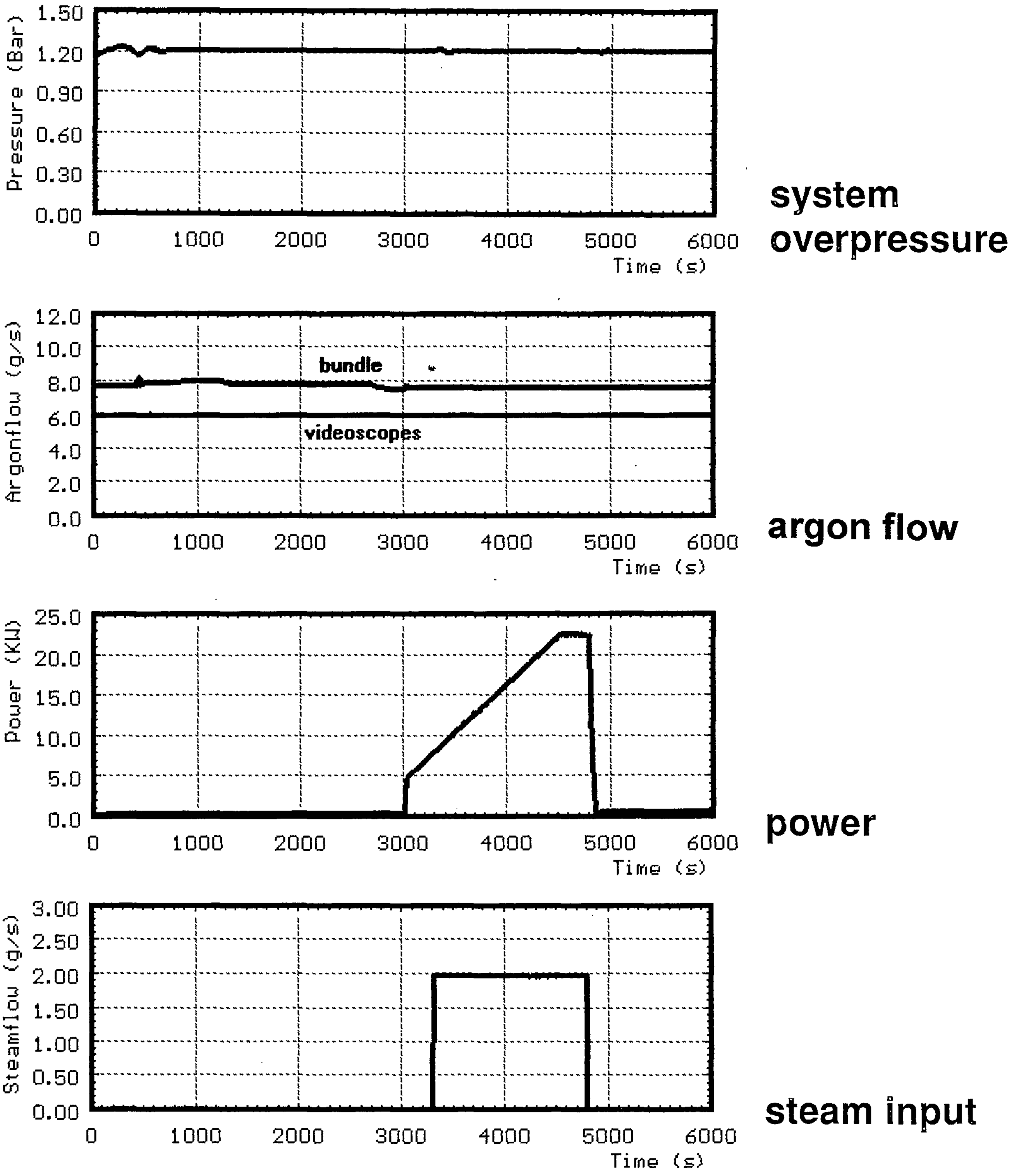

Fig. 9: CORA-28; System pressure, argon flow, steam input and power

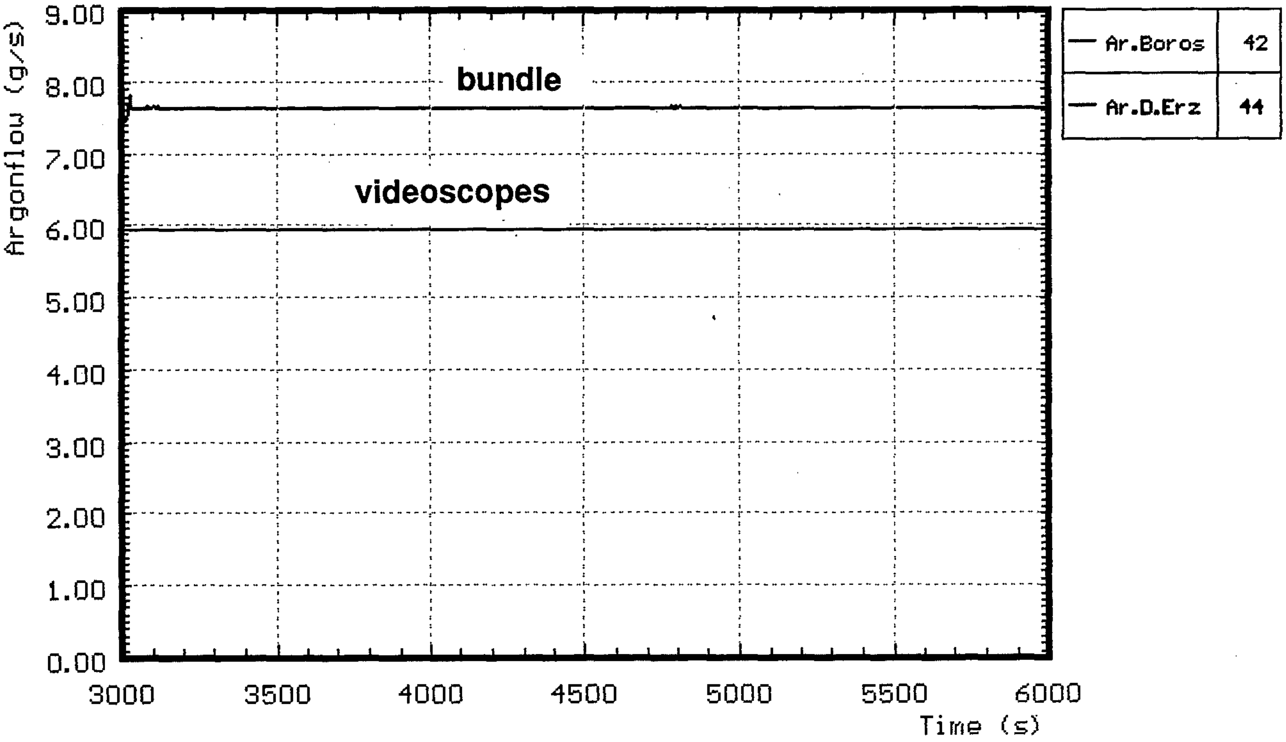

Fig. 10: CORA-28; Argon flow through bundle and videoscopes

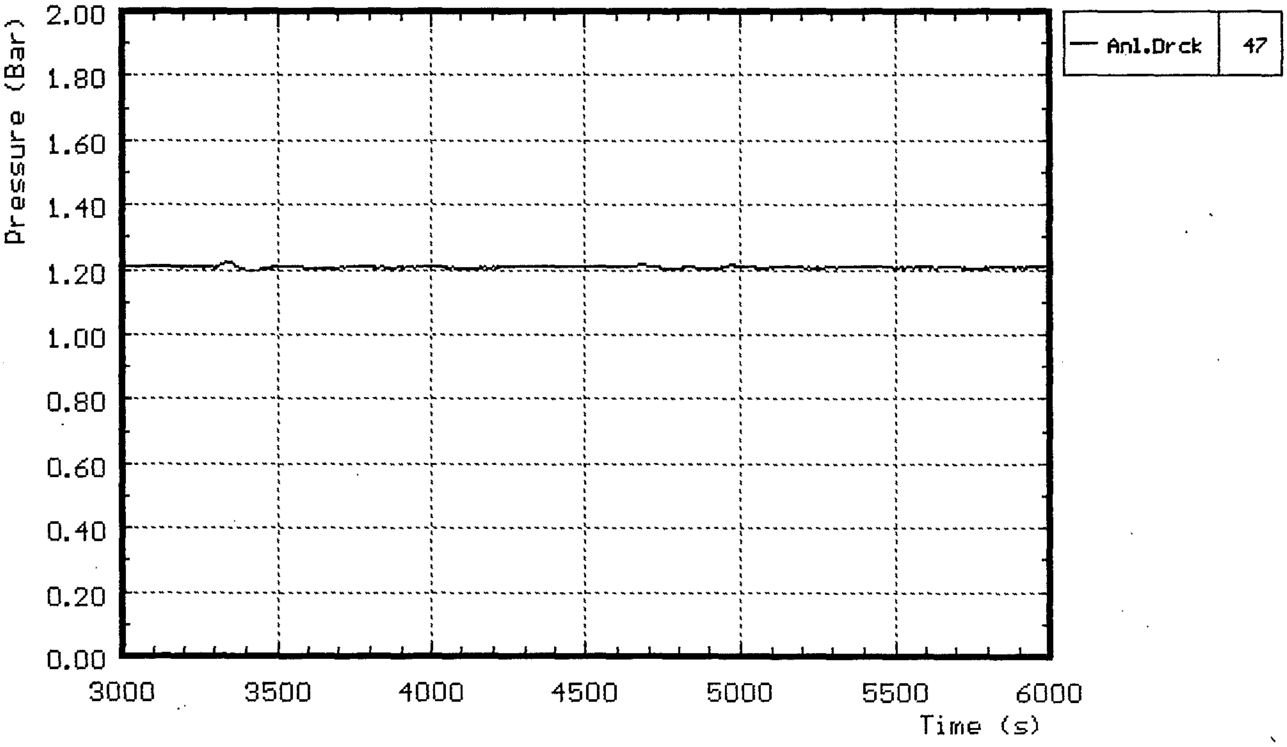

Fig. 11: CORA-28; System pressure (gauge)

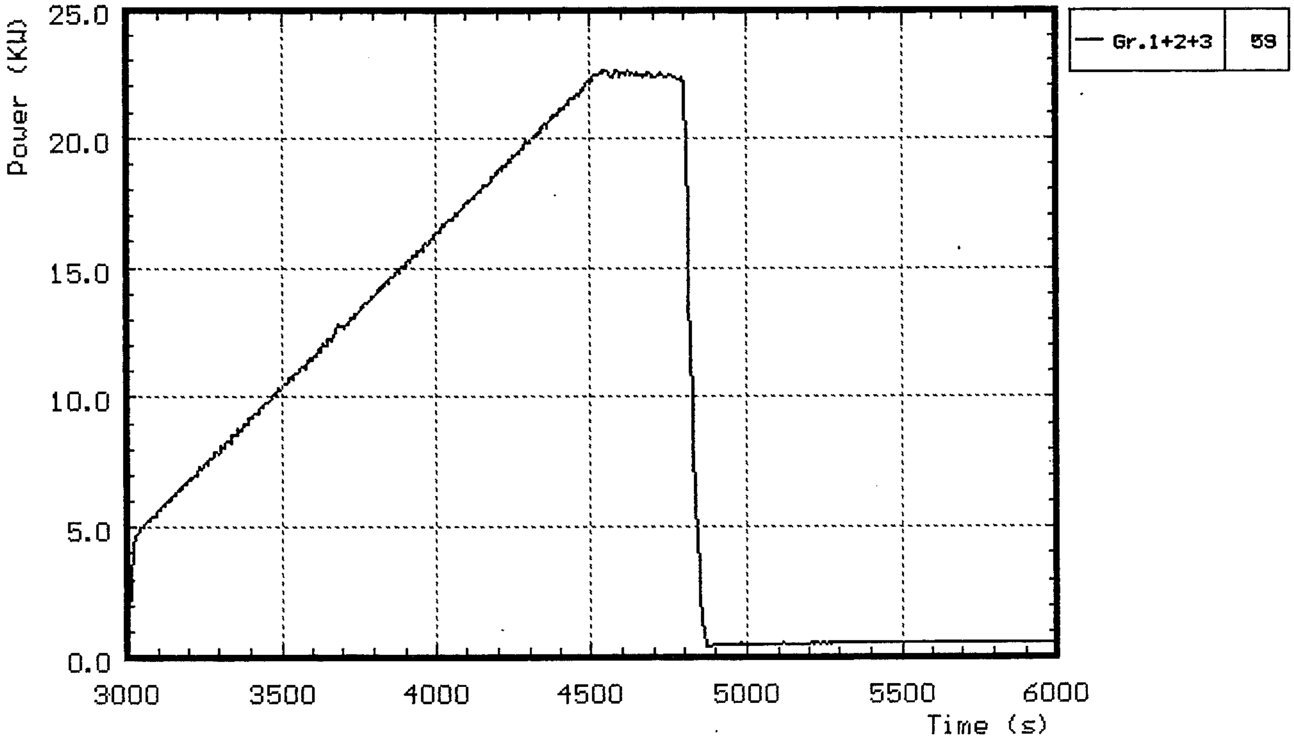

Fig. 12: CORA-28; Total electric power input

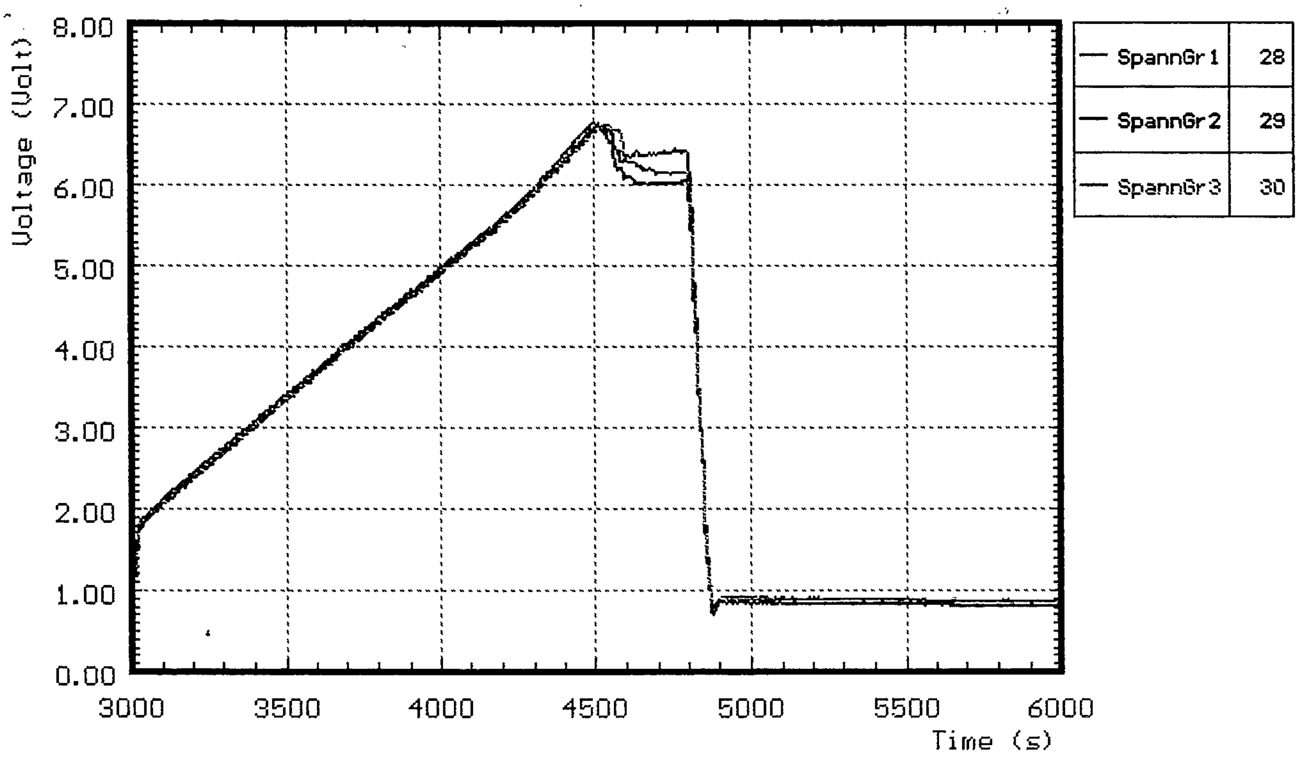

Fig. 13: CORA-28; Voltage input for the 3 rod groups

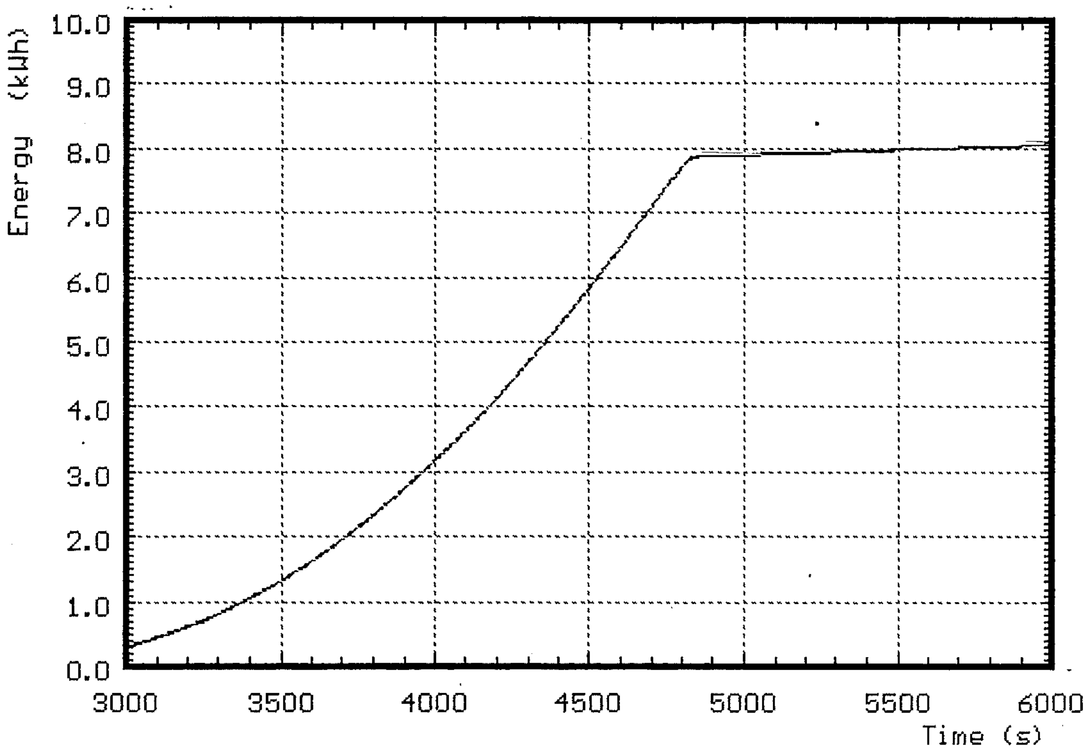

Fig. 14: CORA-28; Total electric energy input

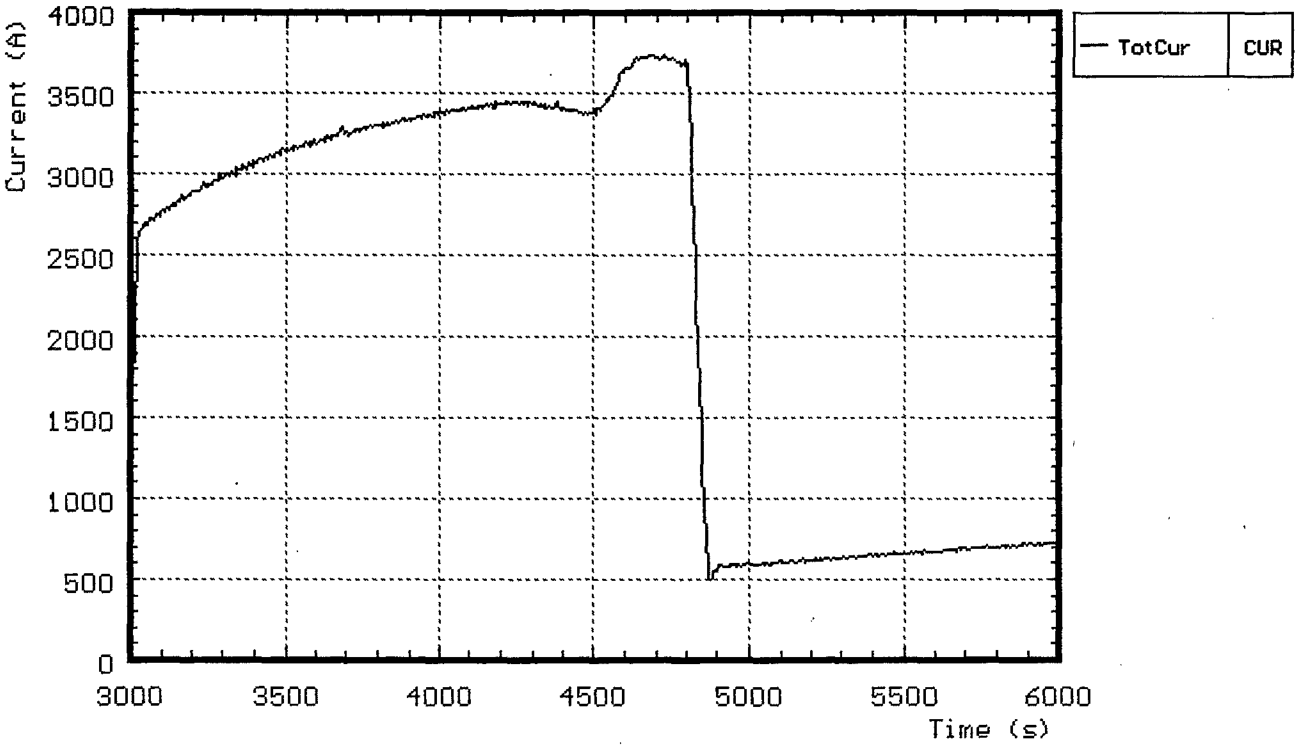

Fig. 15: CORA-28; Total current

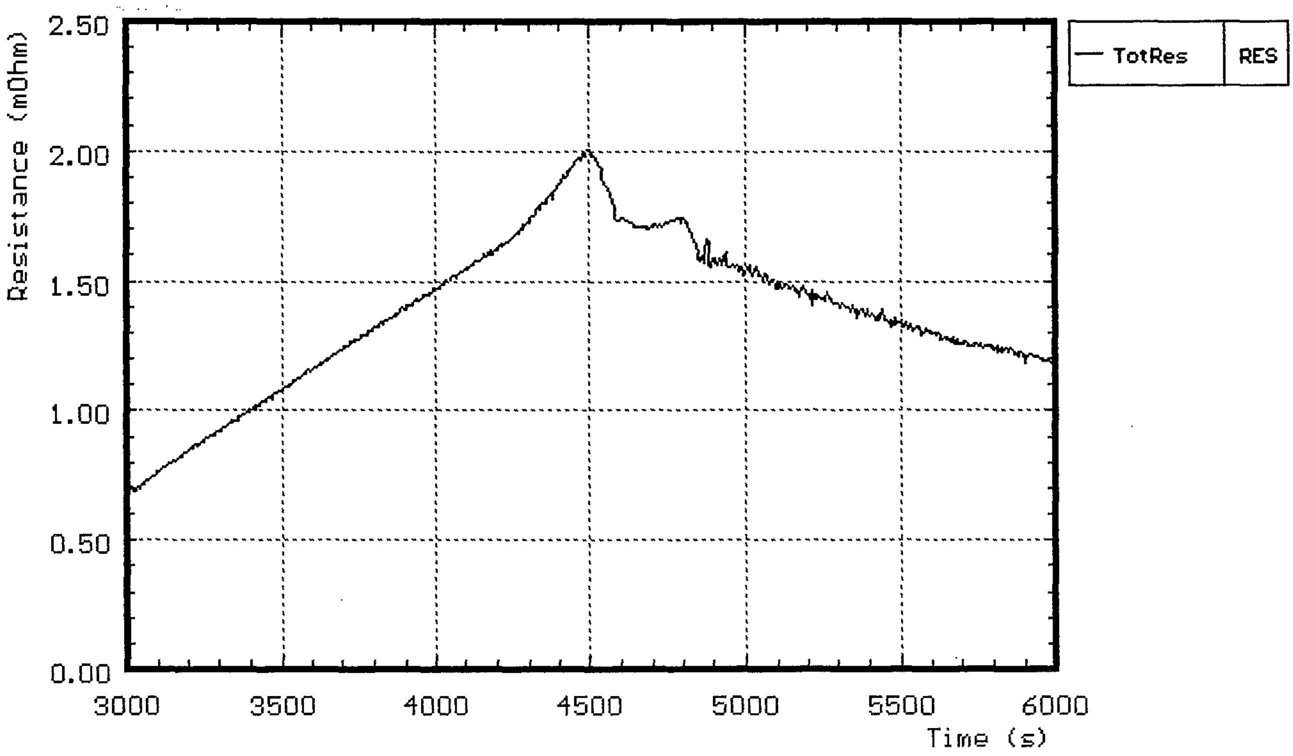

Fig. 16: CORA-28; Resistance of bundle (Voltage group 1/total current)

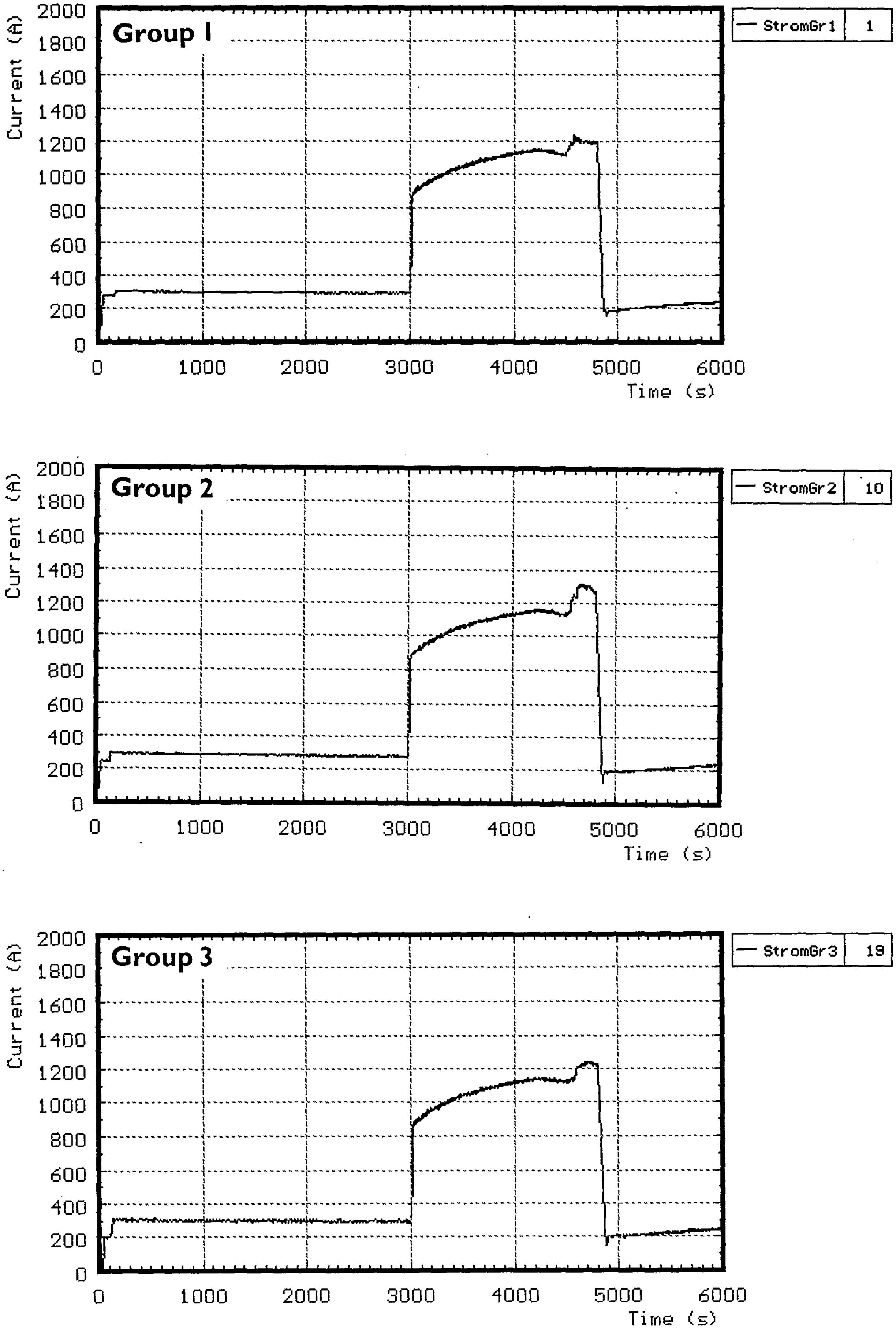

Fig. 17: CORA-28; Current of the rod groups

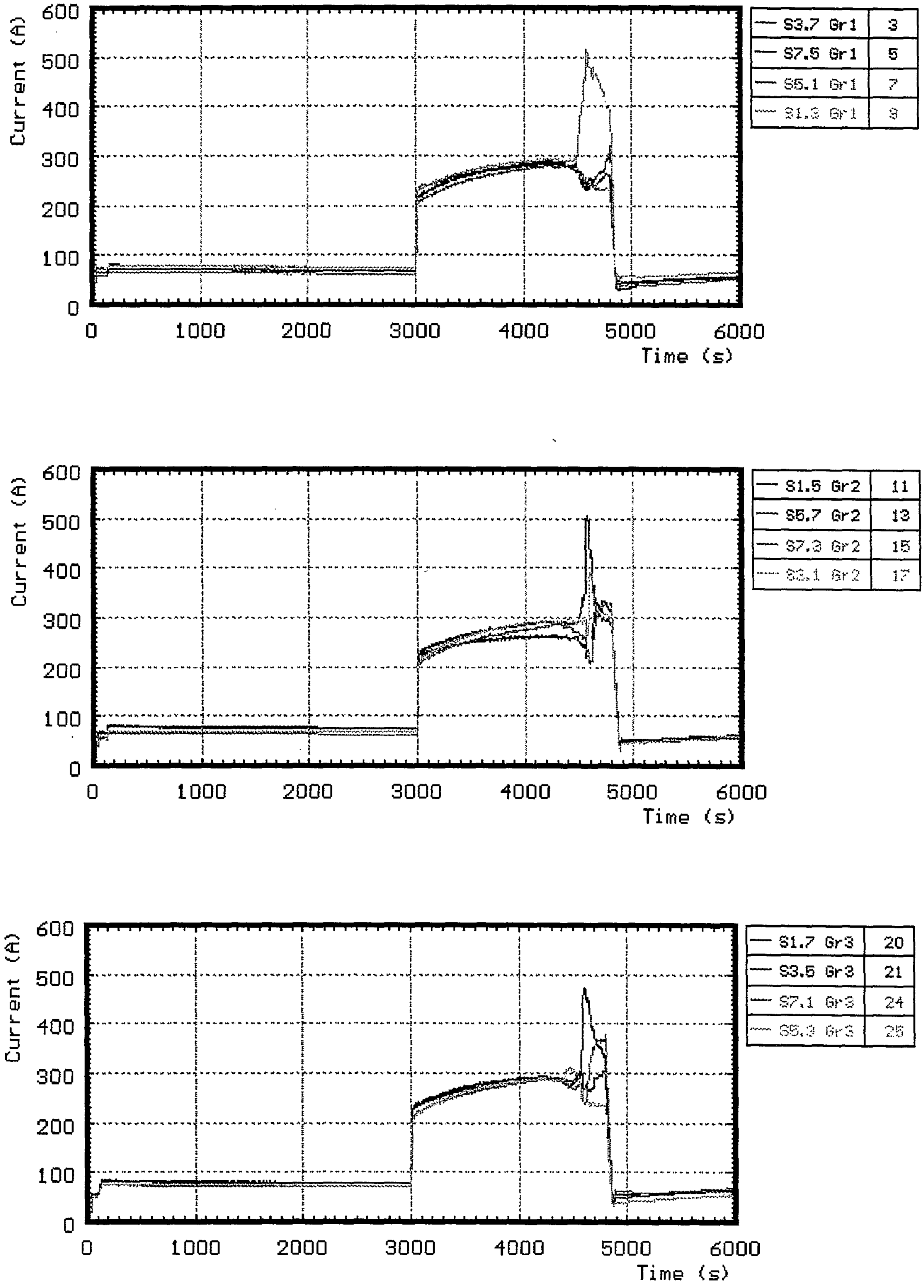

Fig. 18: CORA-28, Variation of currents within the rod groups

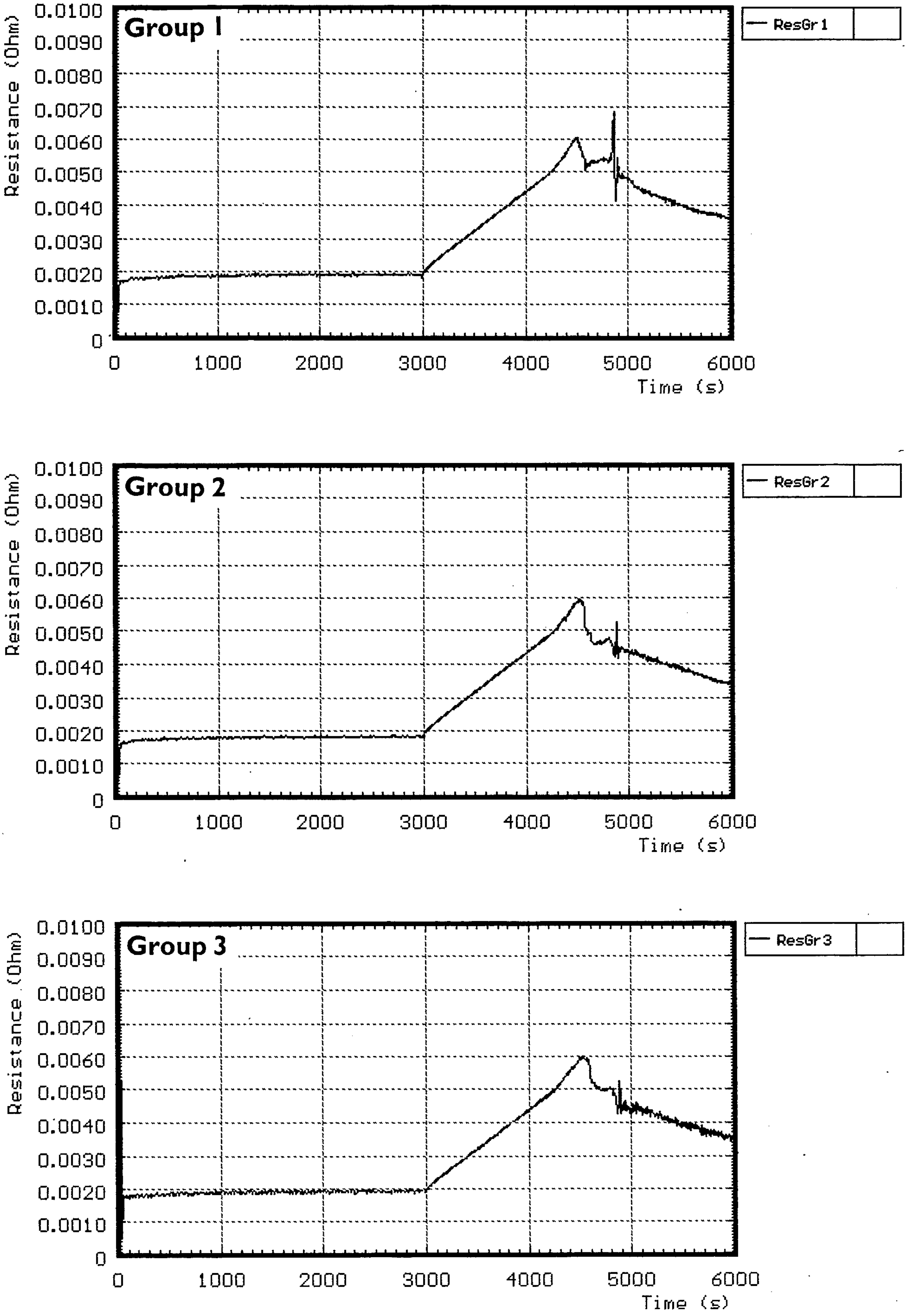

Fig. 19: CORA-28; Resistance of the rod groups

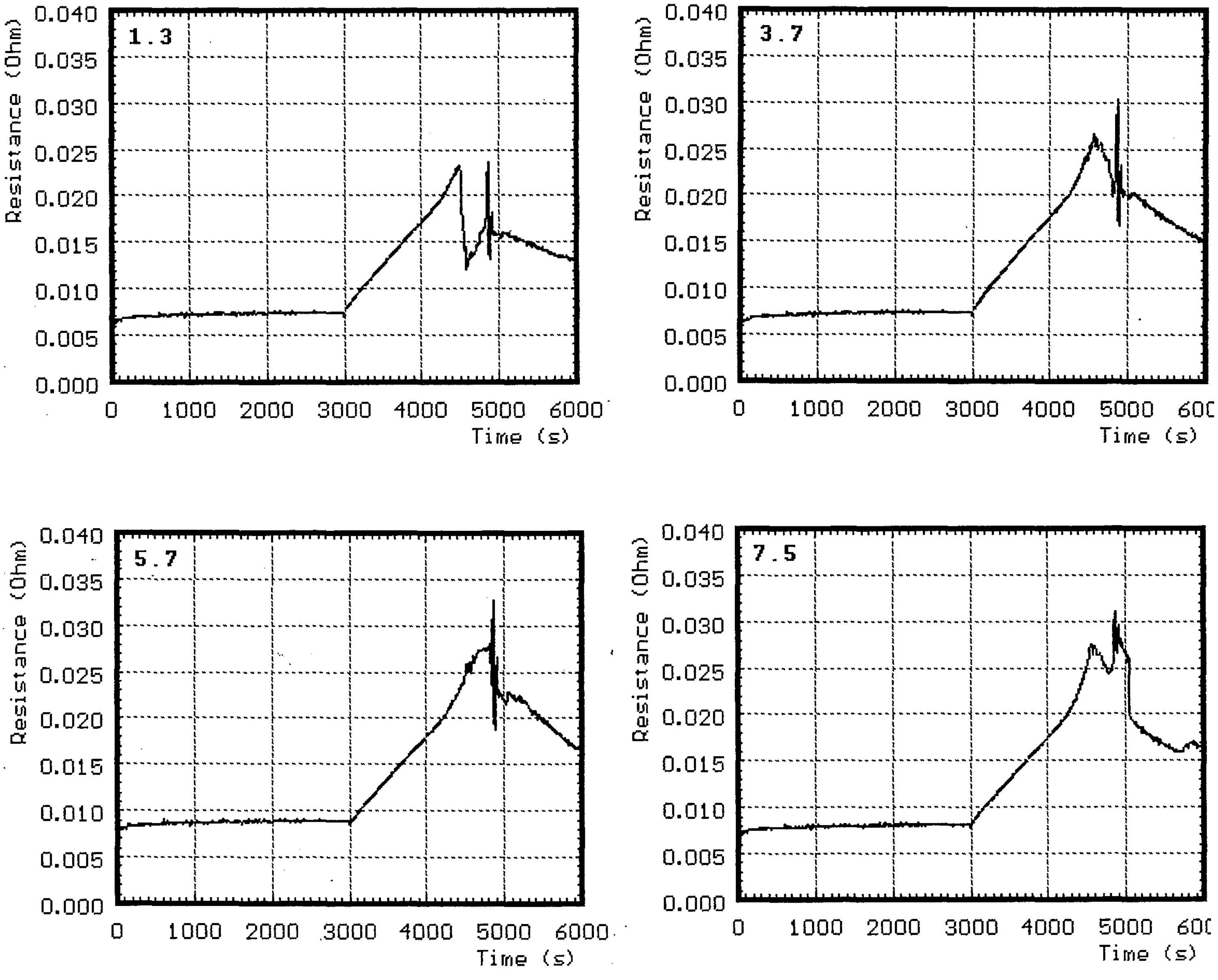

Fig. 20: CORA-28; Resistance of single rods: group 1

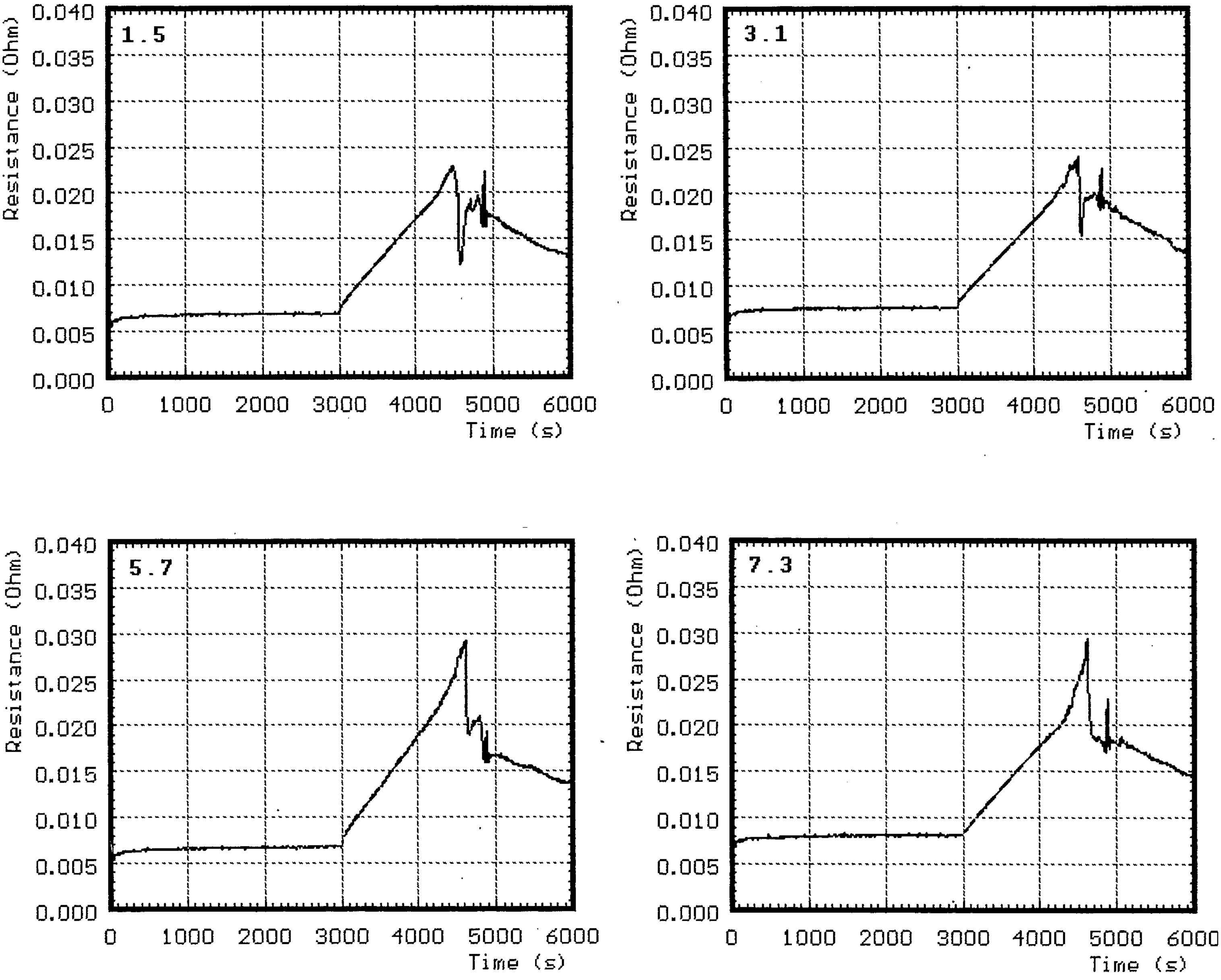

Fig. 21: CORA-28; Resistance of single rods: group 2

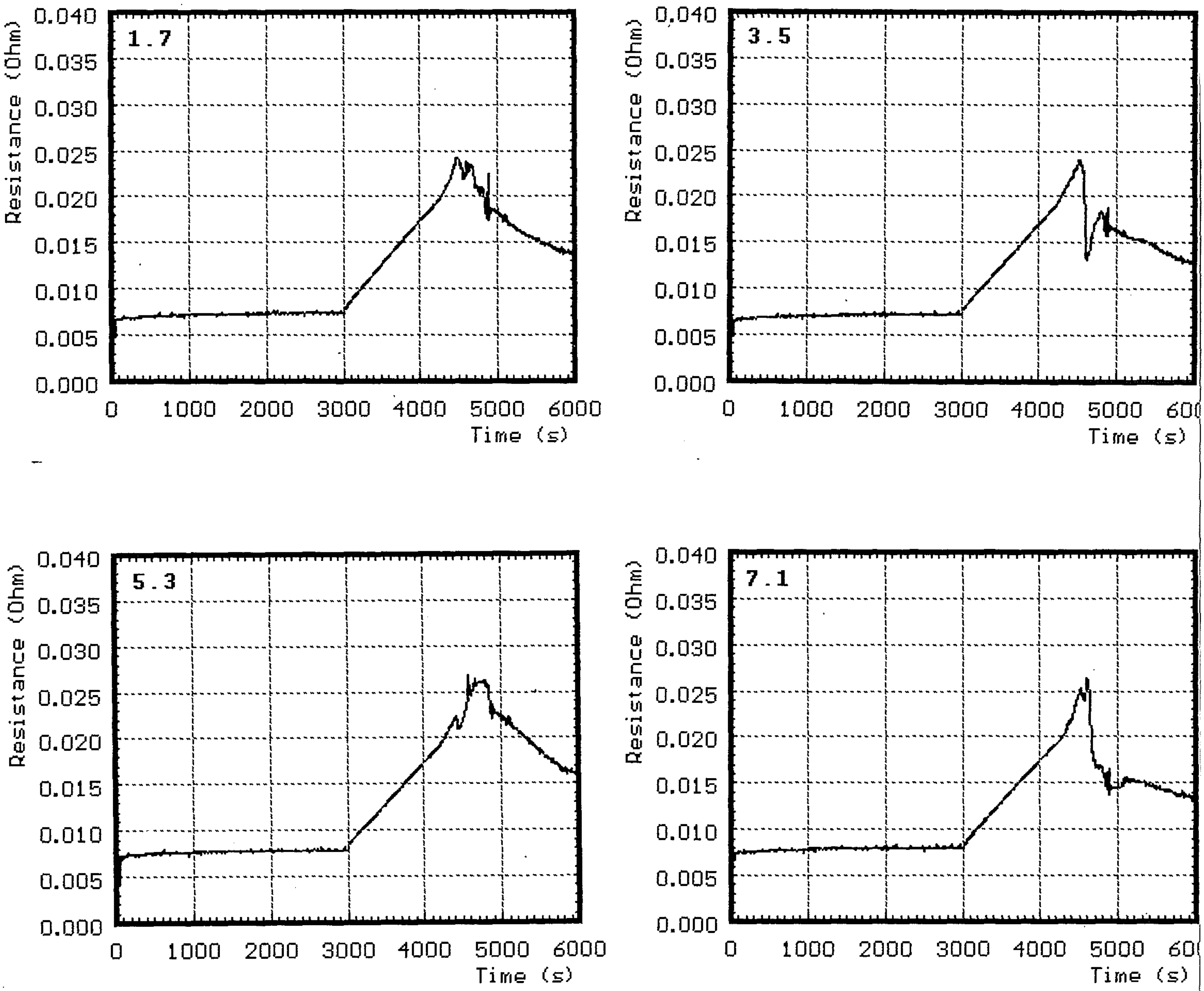

Fig. 22: CORA-28; Resistance of single rods: group 3

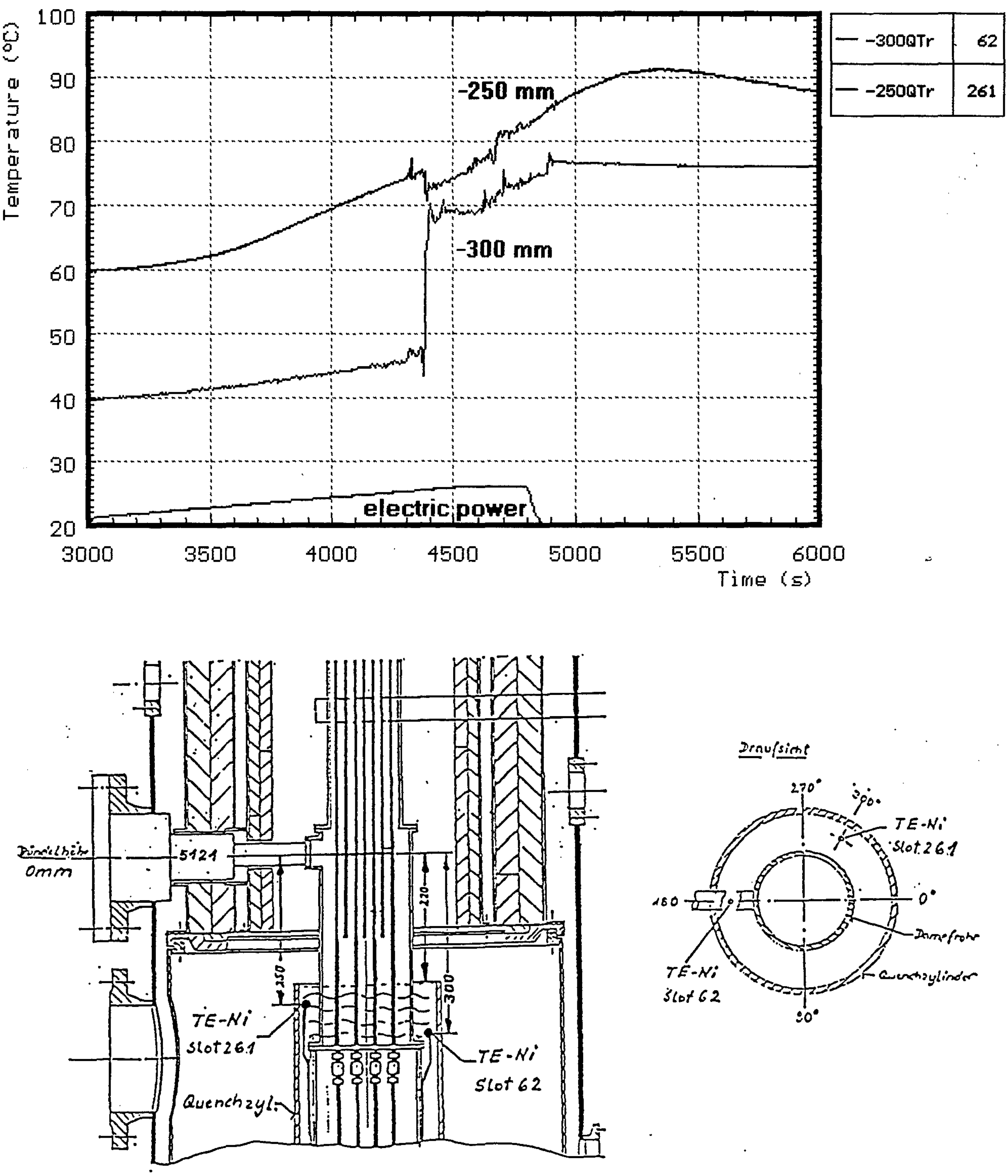

Fig. 23: CORA-28; Water temperature in the quench cylinder

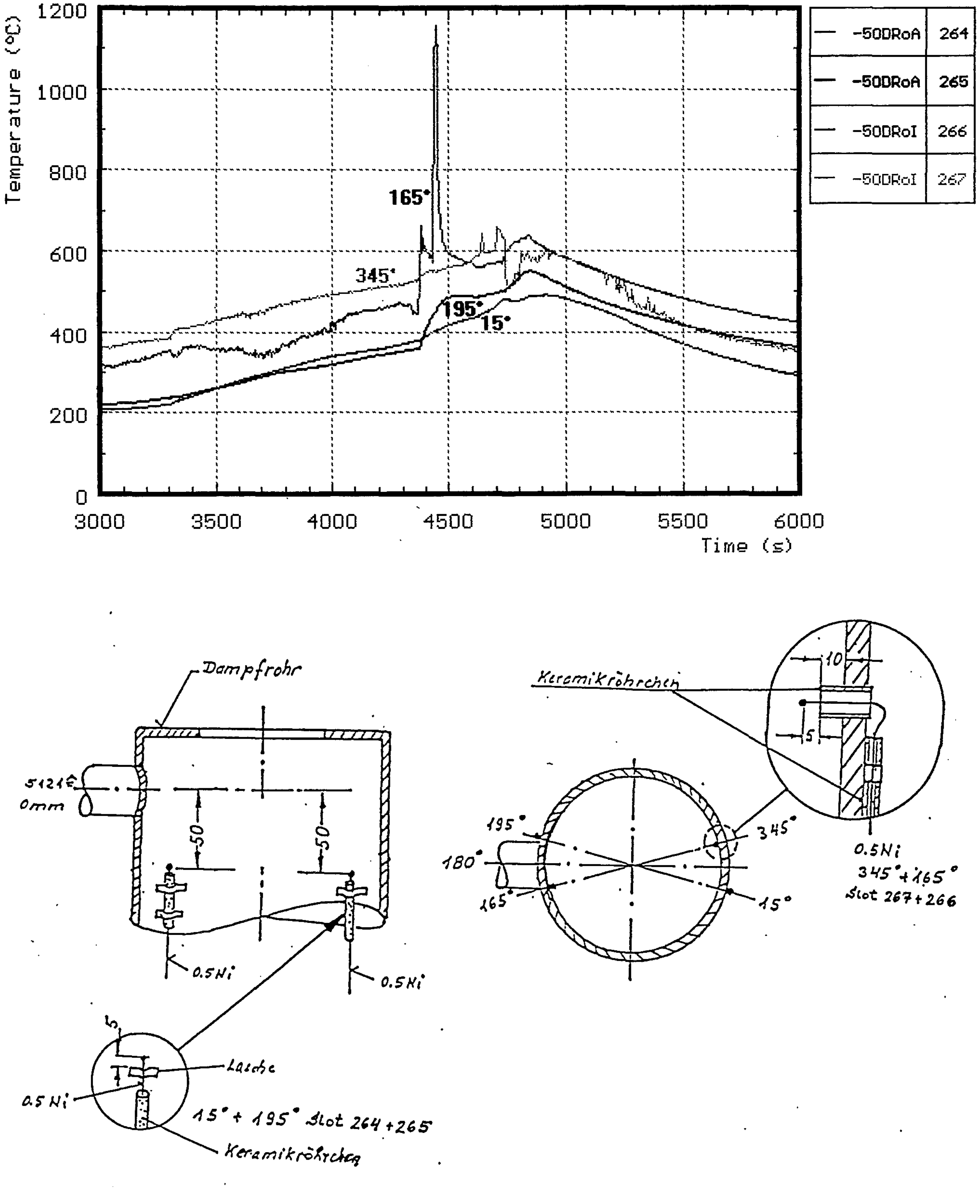

Fig. 24: CORA-28; Temperature in and on steam tube at -50mm elevation

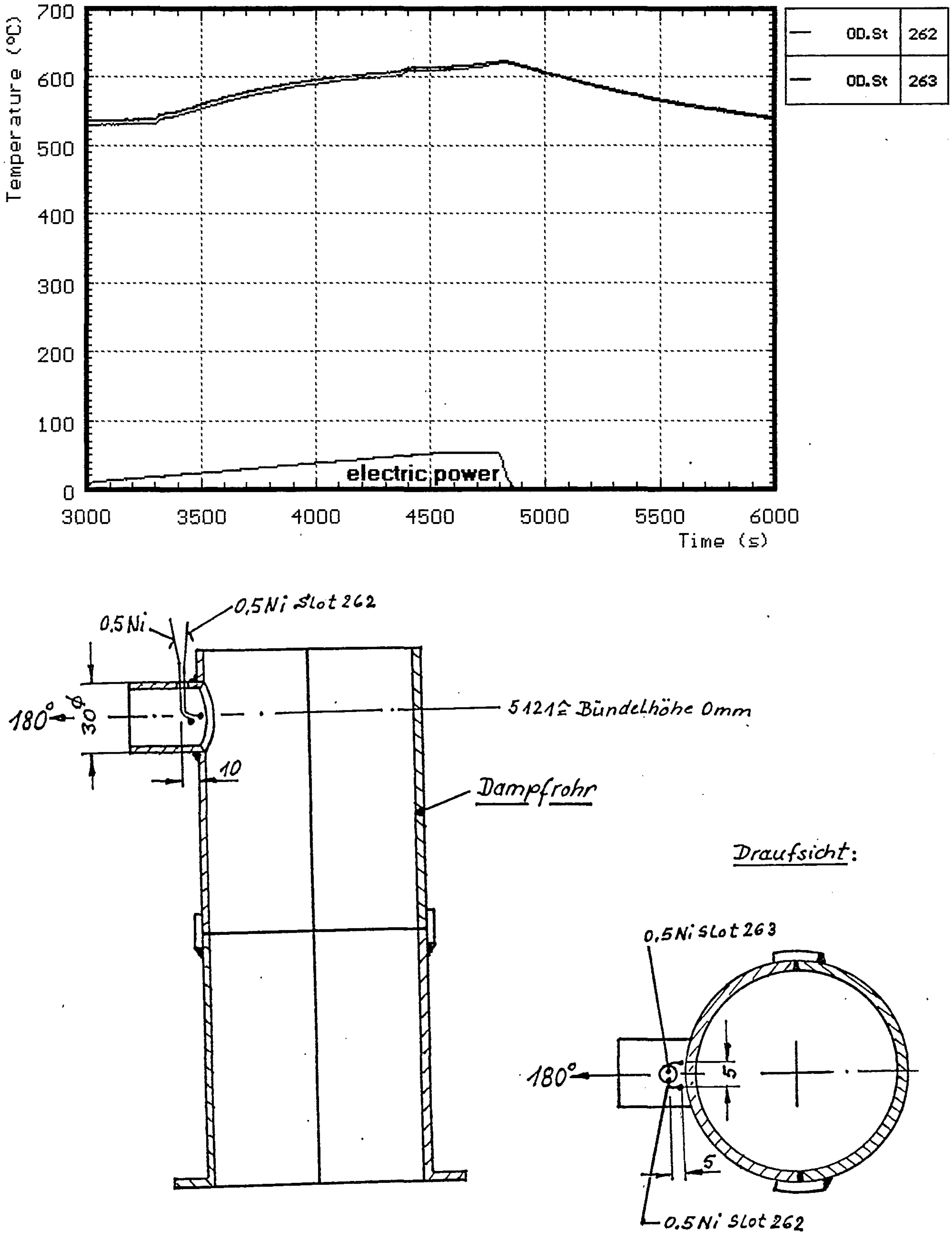

Fig. 25: CORA-28; Temperatures at steam inlet

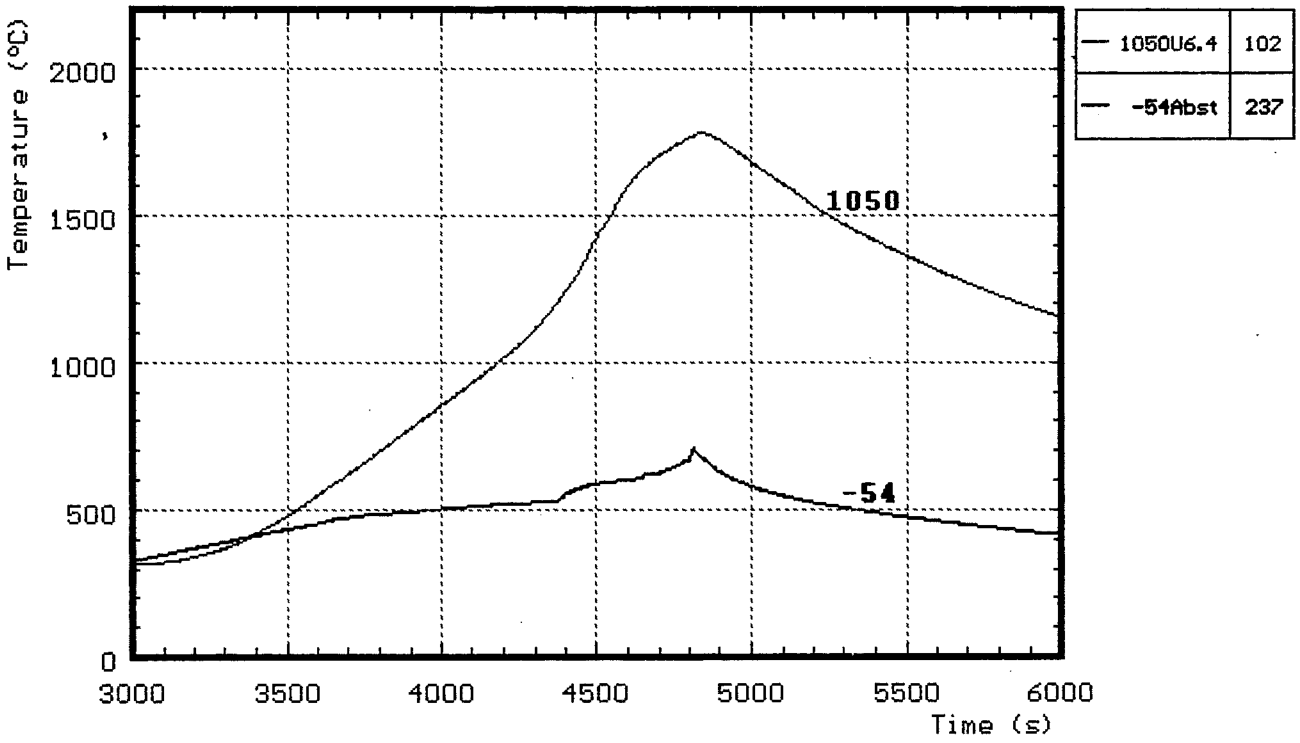

Fig. 26: CORA-28; Comparison of temperatures 50 mm above and below the heated region

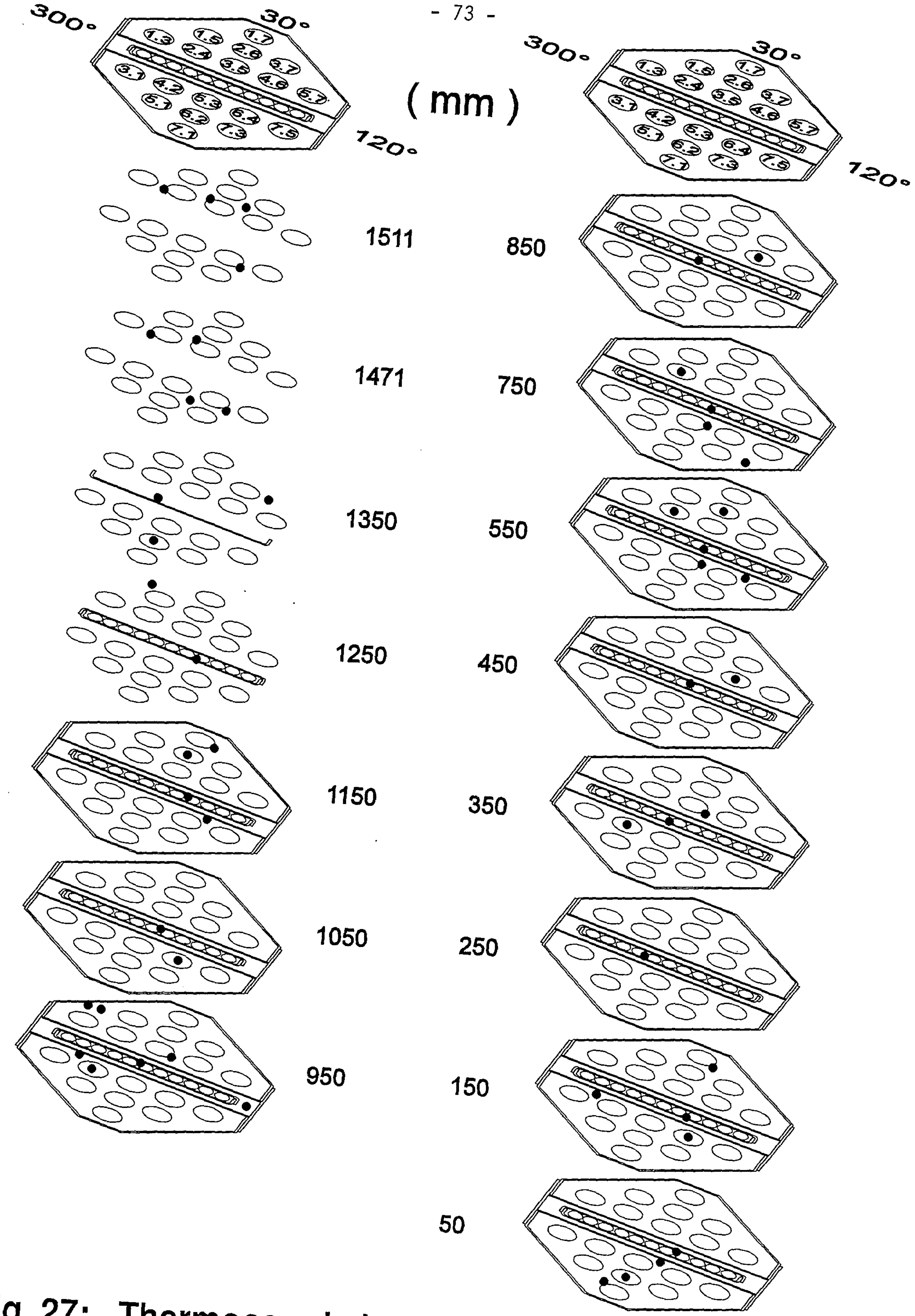

Fig. 27: Thermocouple locations within the bundle (CORA-28)

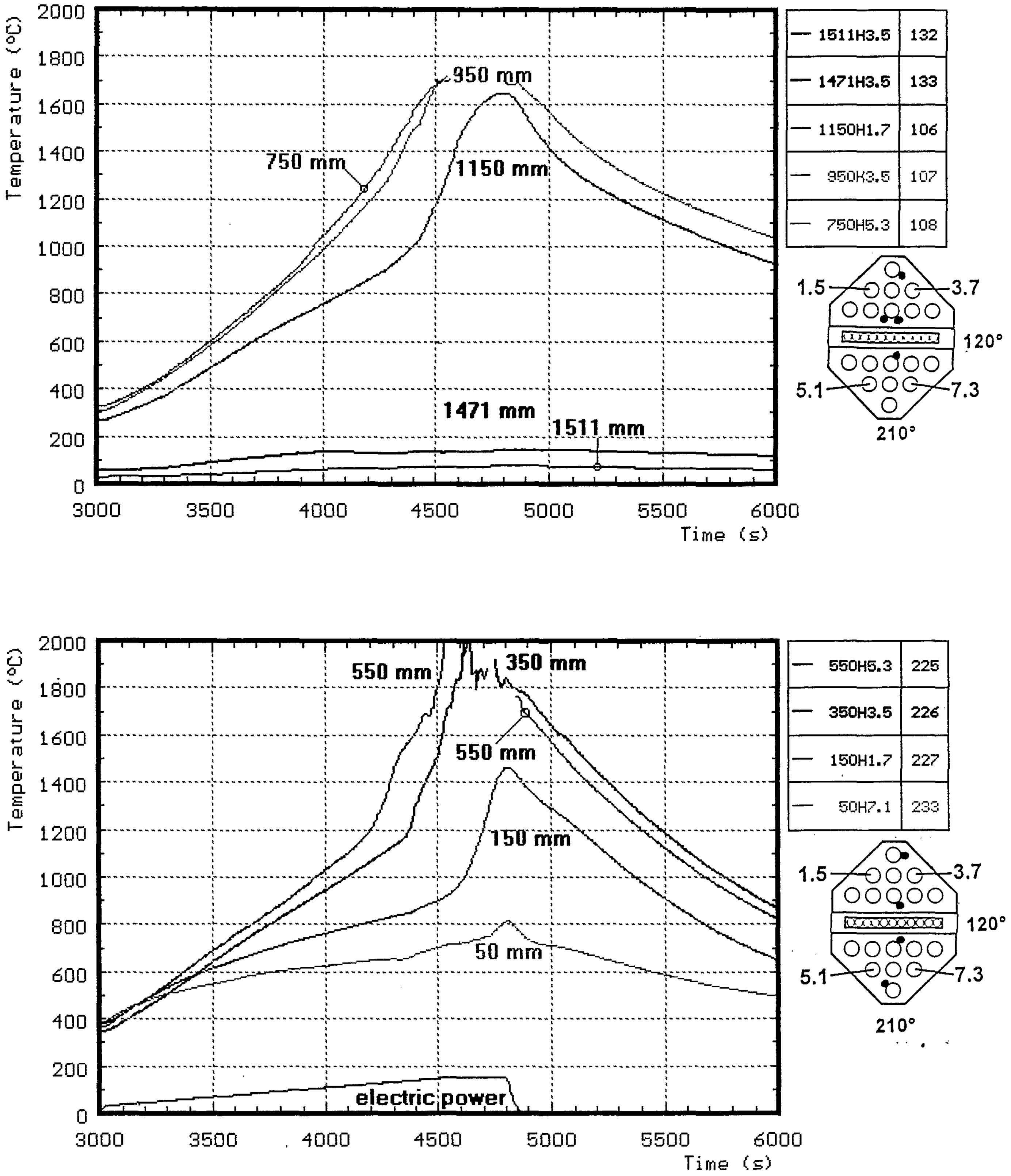

Fig. 28: CORA-28; Temperatures of heated rods

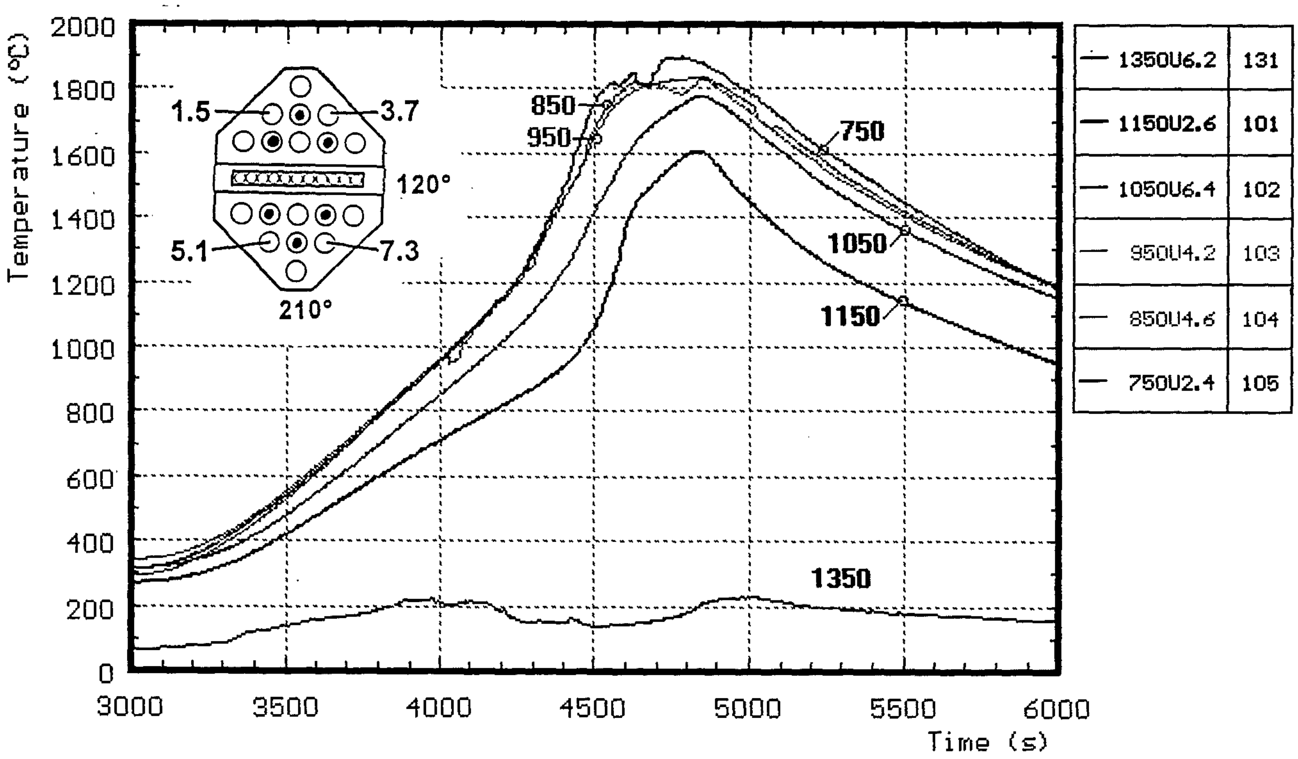

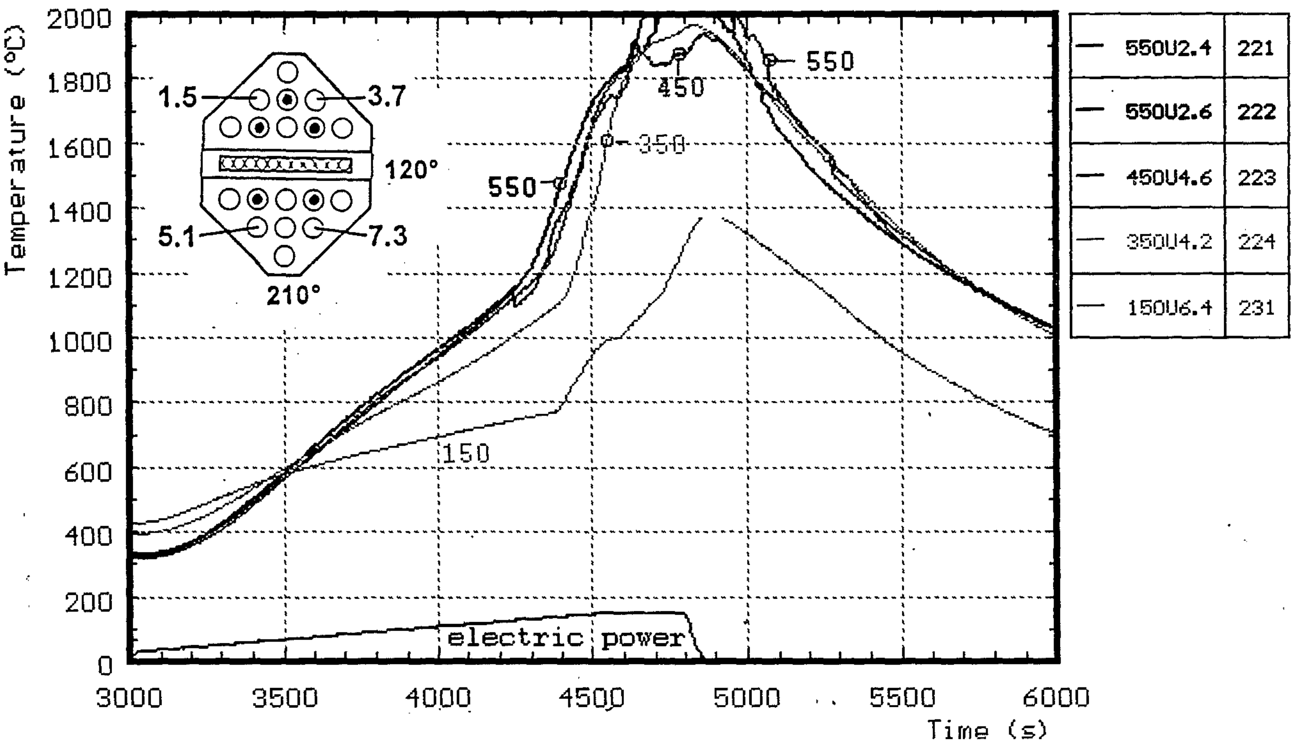

Fig. 29: CORA-28; Temperatures of unheated rods (TCs in central position)

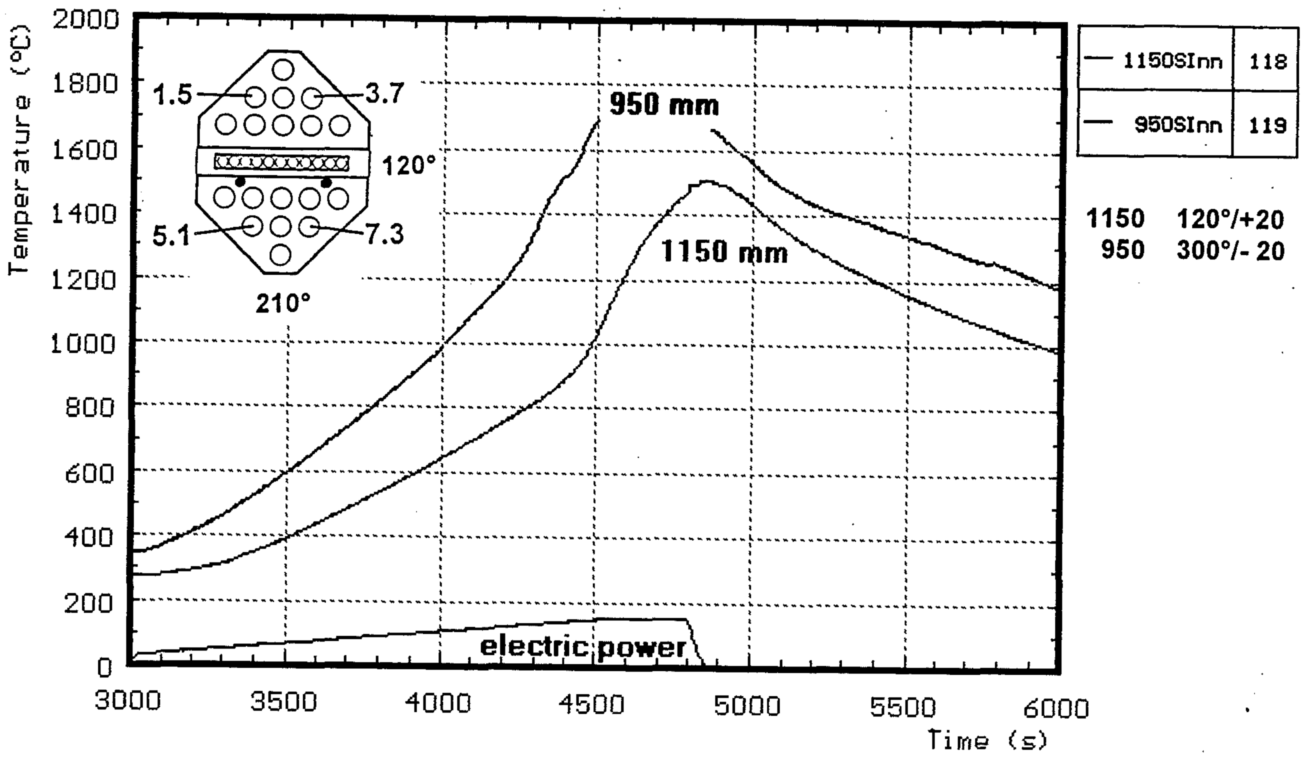

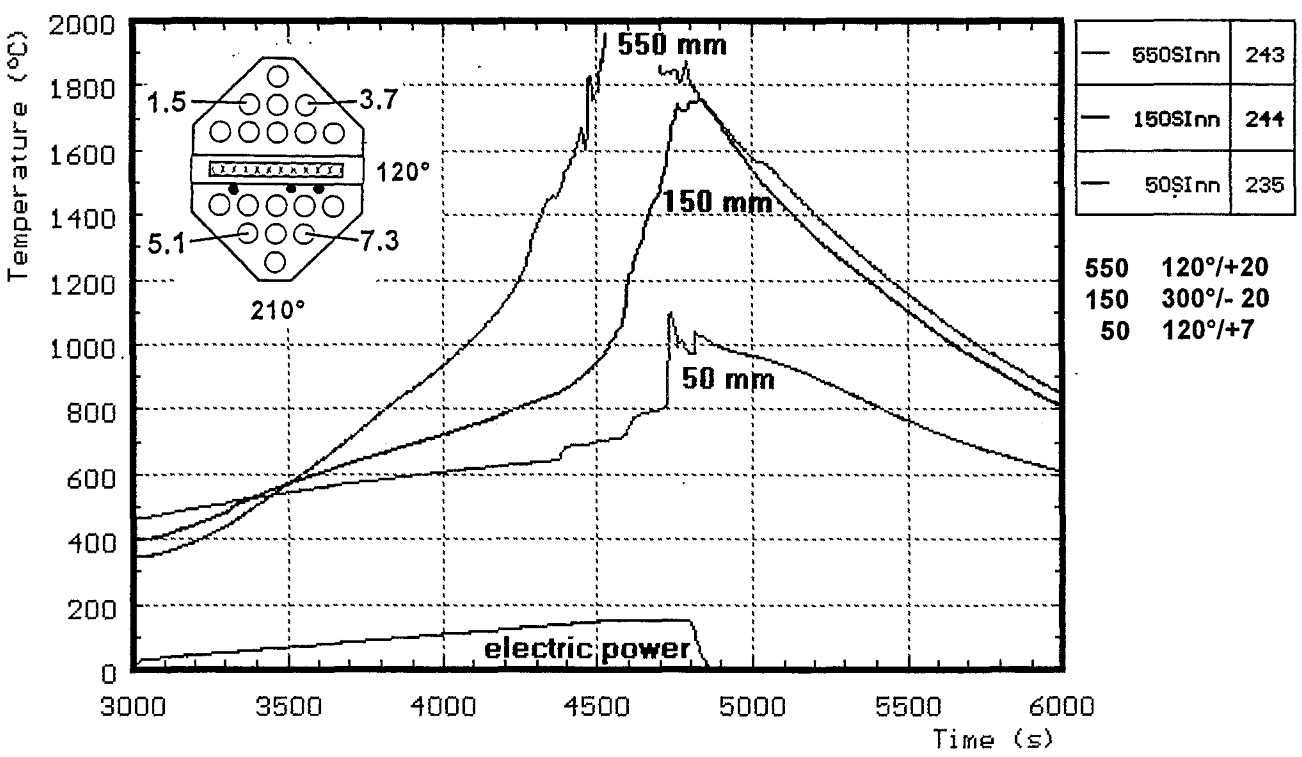

Fig. 30: CORA-28; Temperatures on the channel box wall

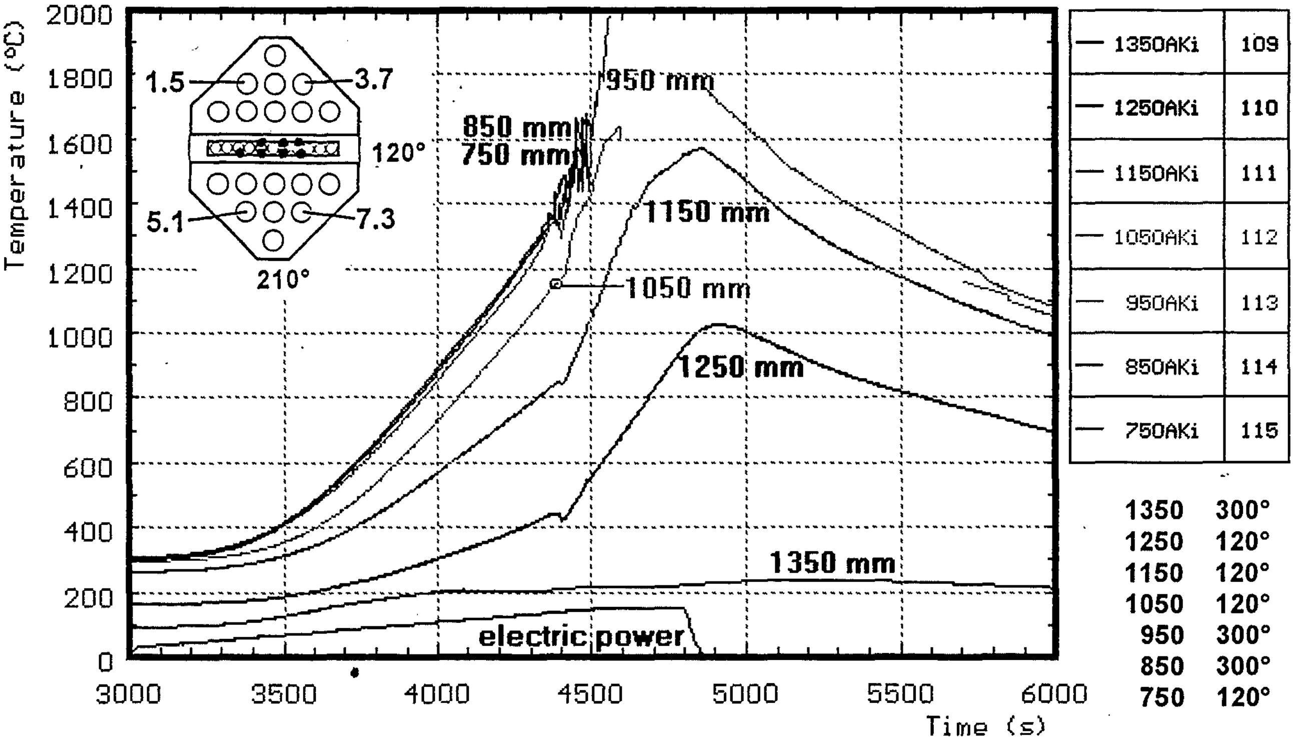

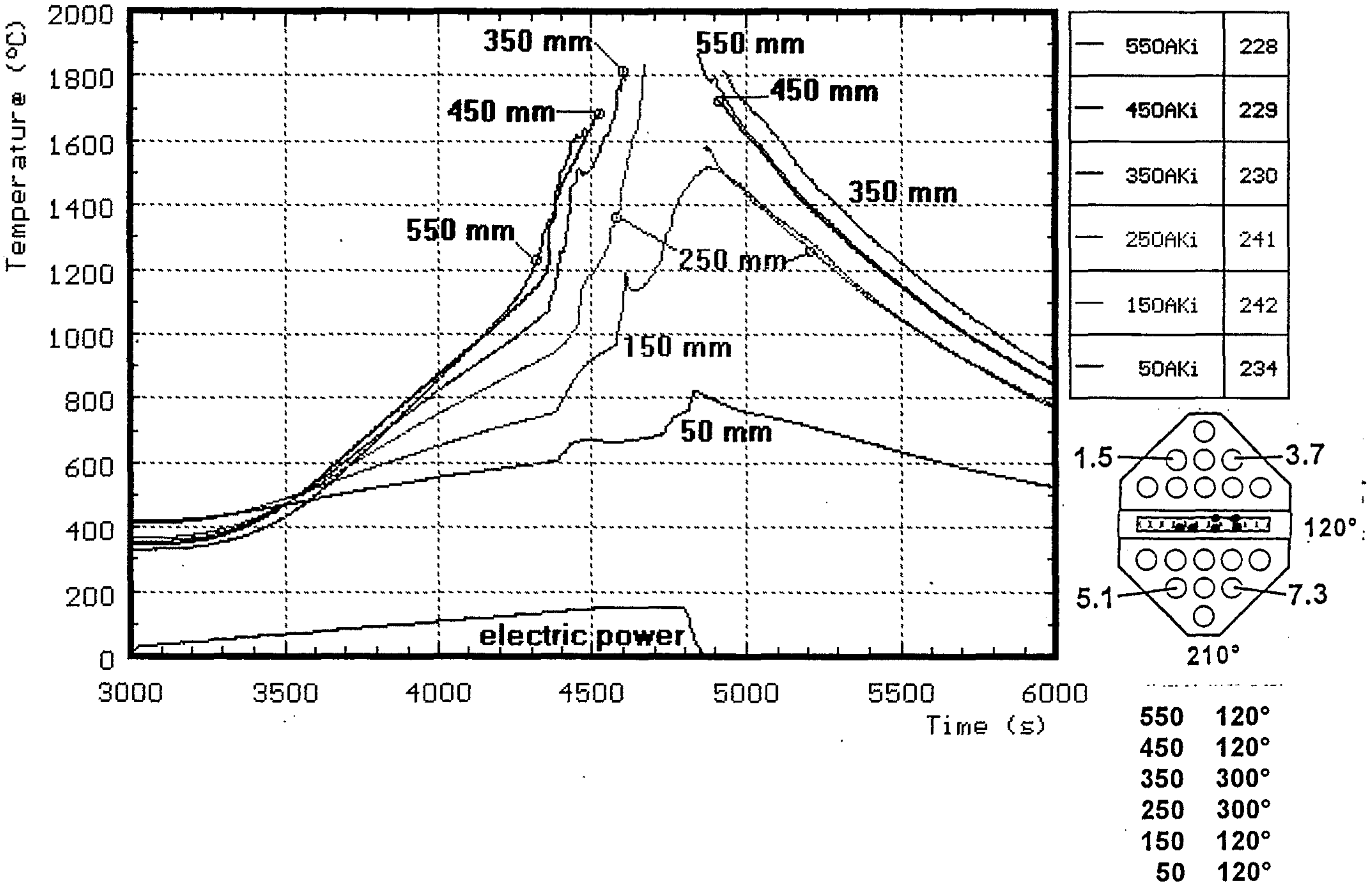

Fig. 31: CORA-28; Temperatures in the absorber blade

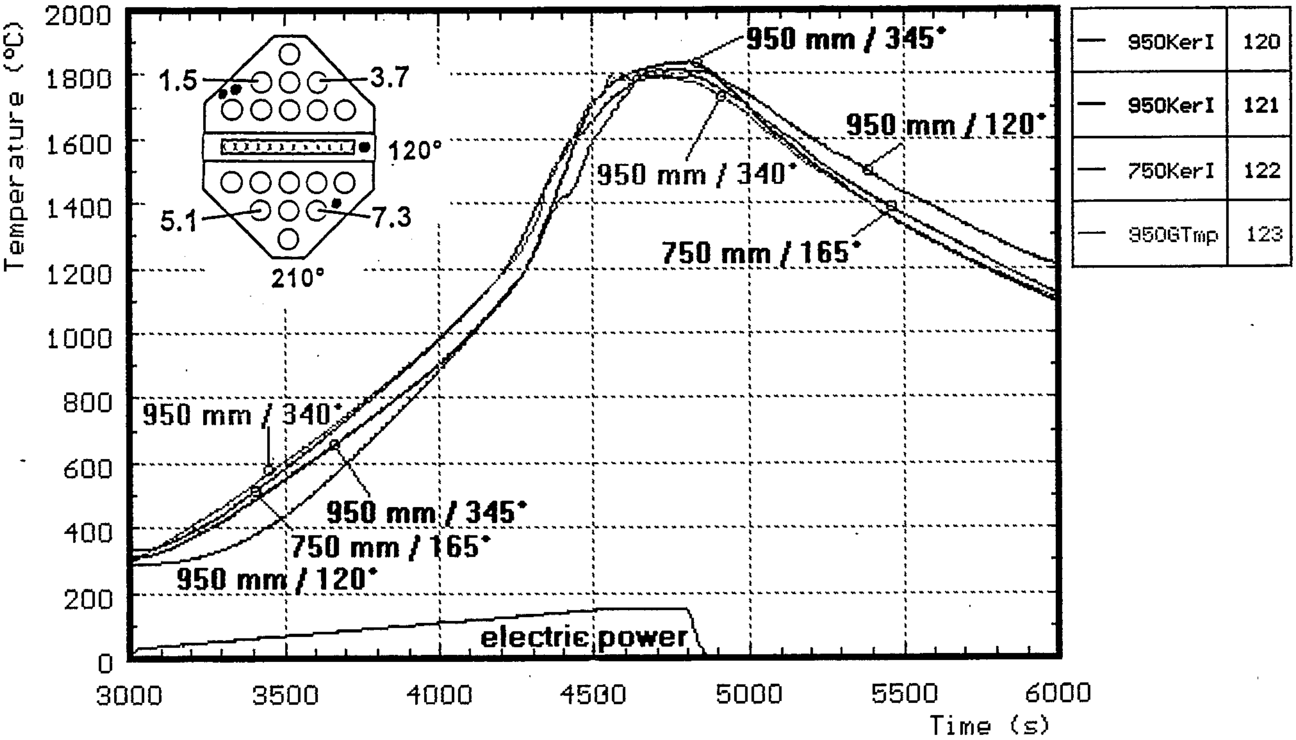

Fig. 32: CORA-28; Temperatures measured with ceramic protected TCs

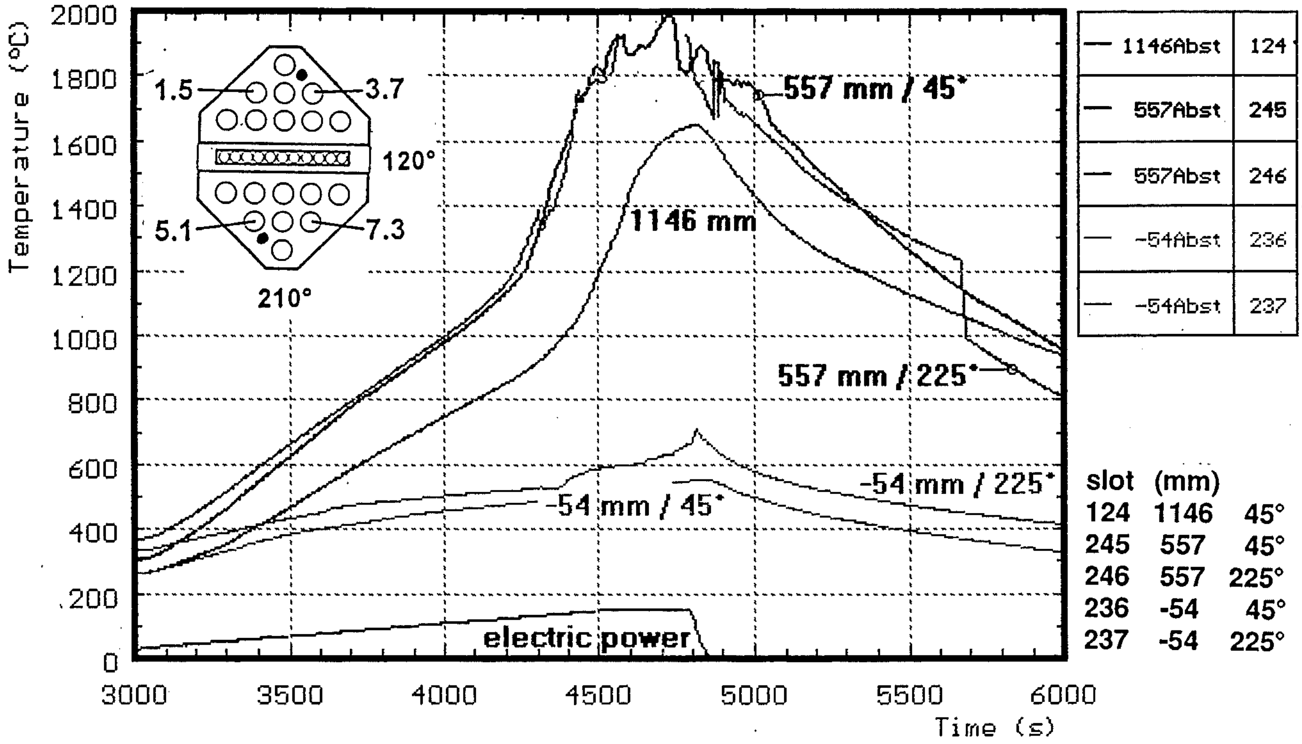

Fig. 33: CORA-28; Temperatures on the spacers used in test CORA-28

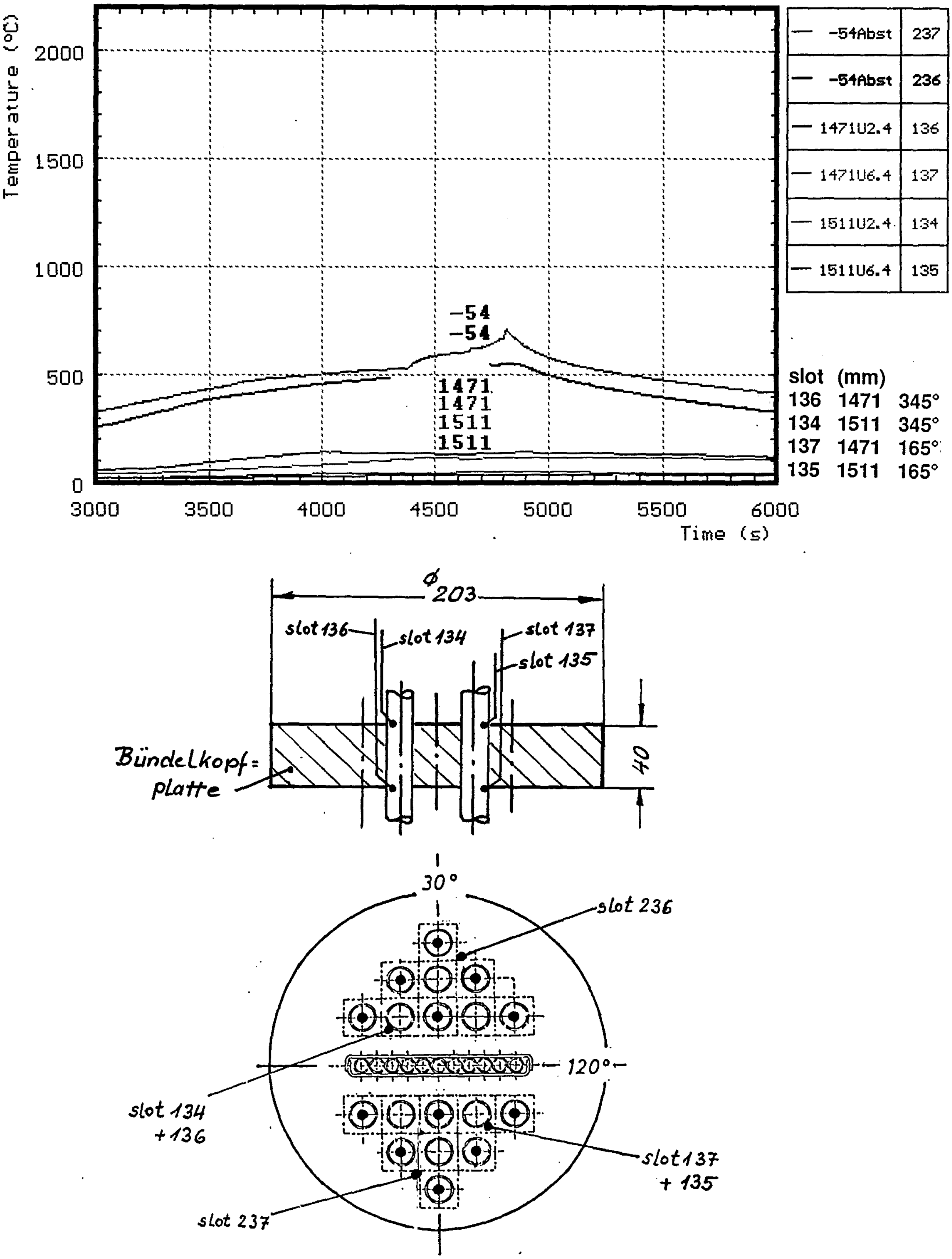

Fig. 34: CORA-28; Temperatures at the bundle head plate and of the lower spacer

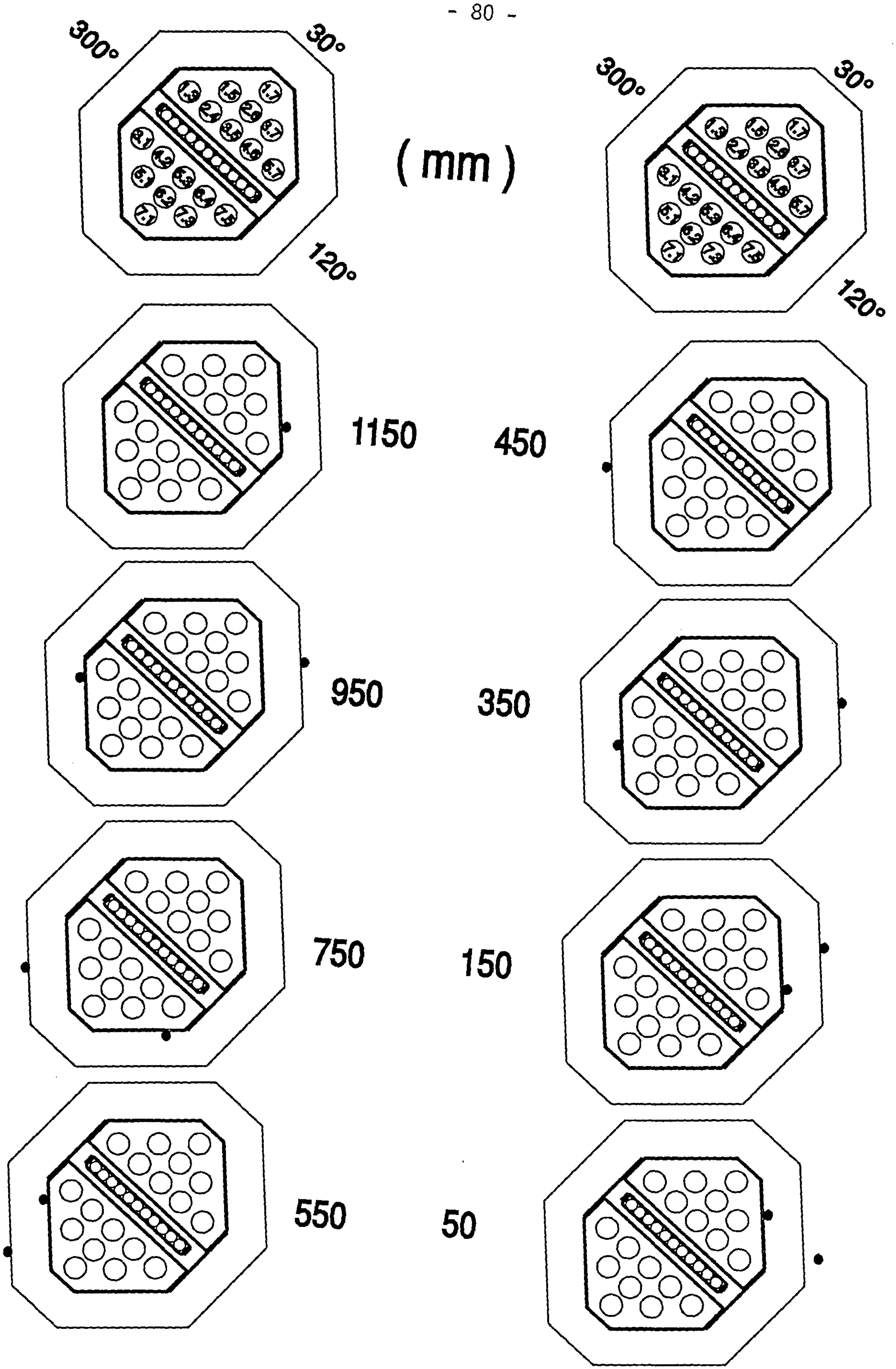

Fig. 35: Location of the thermocouples at shroud and shroud insulation (CORA-28)

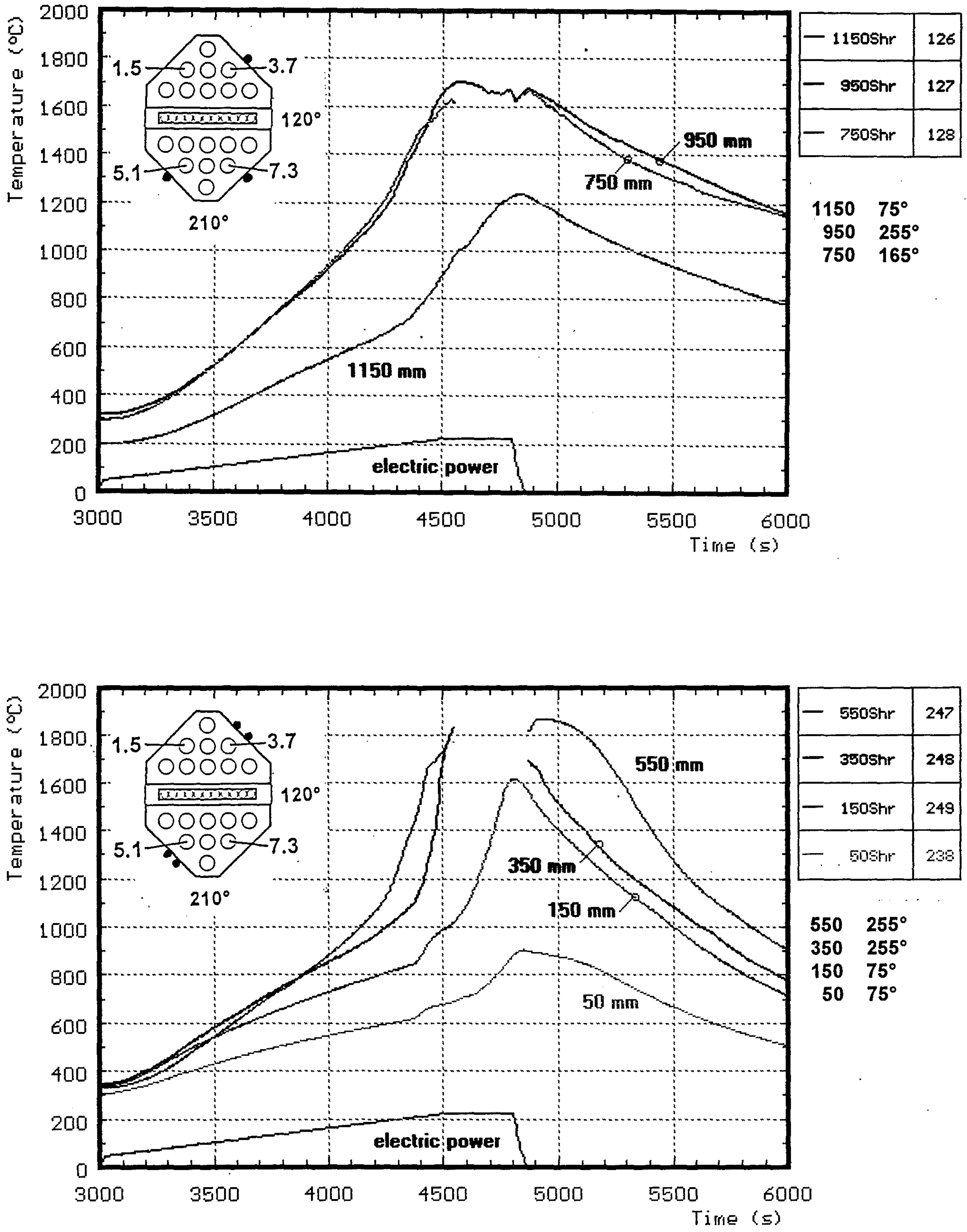

Fig. 36: CORA-28; Temperatures of the outer side of the shroud

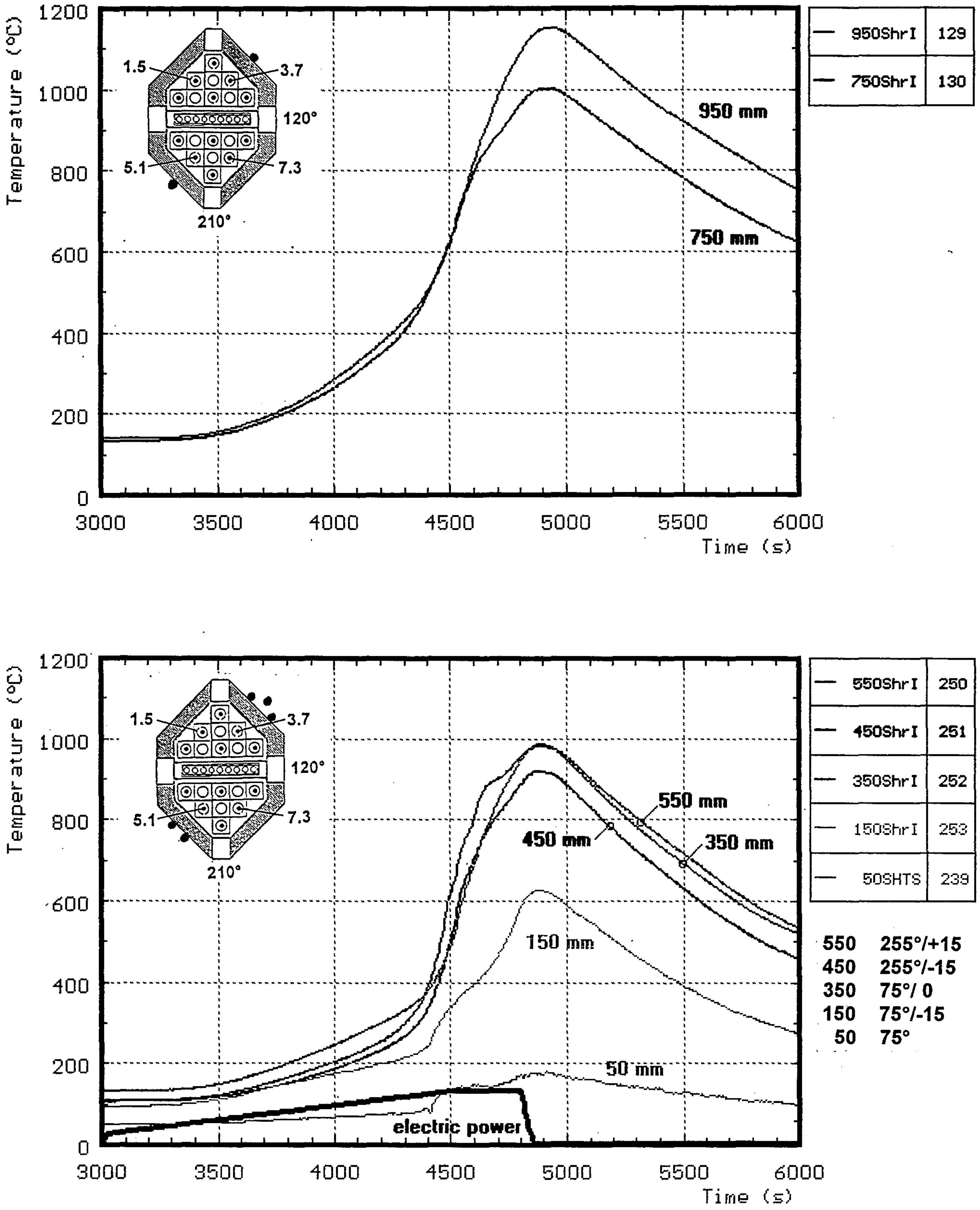

Fig. 37: CORA-28; Temperatures on the shroud insulation

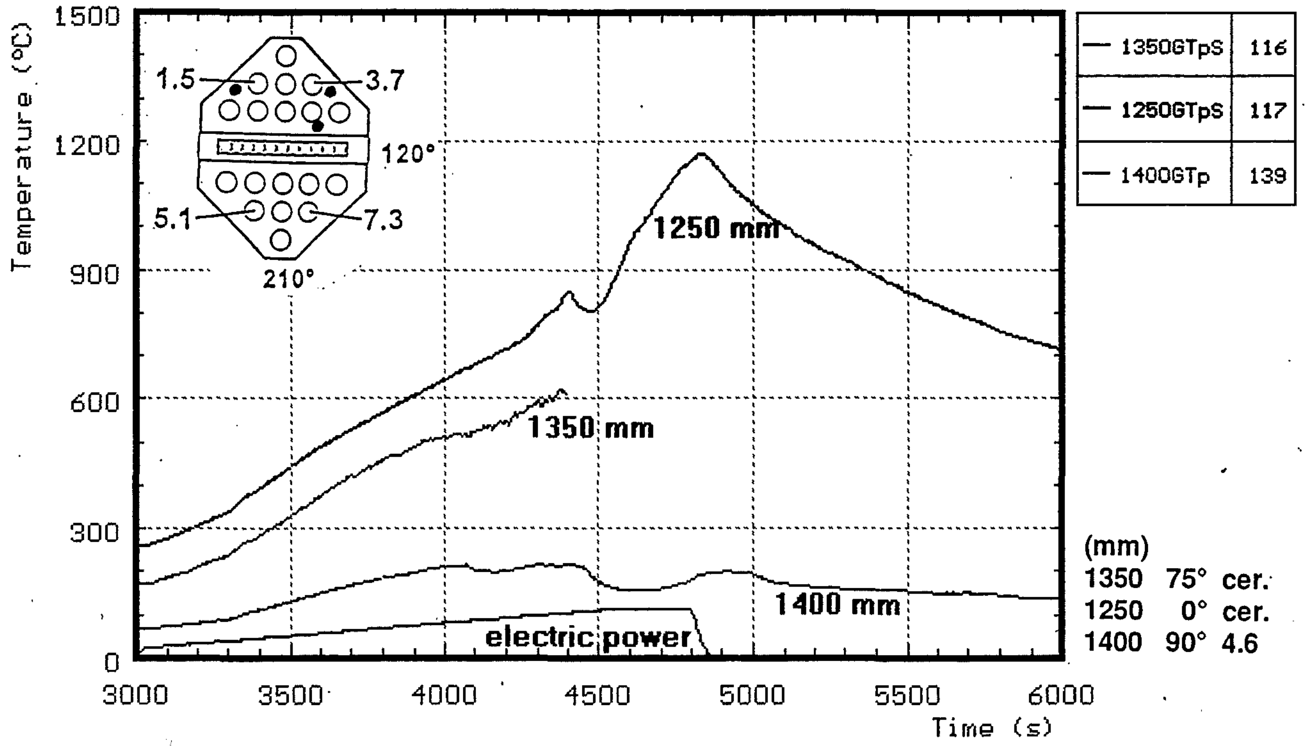

Fig. 38: CORA-28; Gas temperature above the heated zone

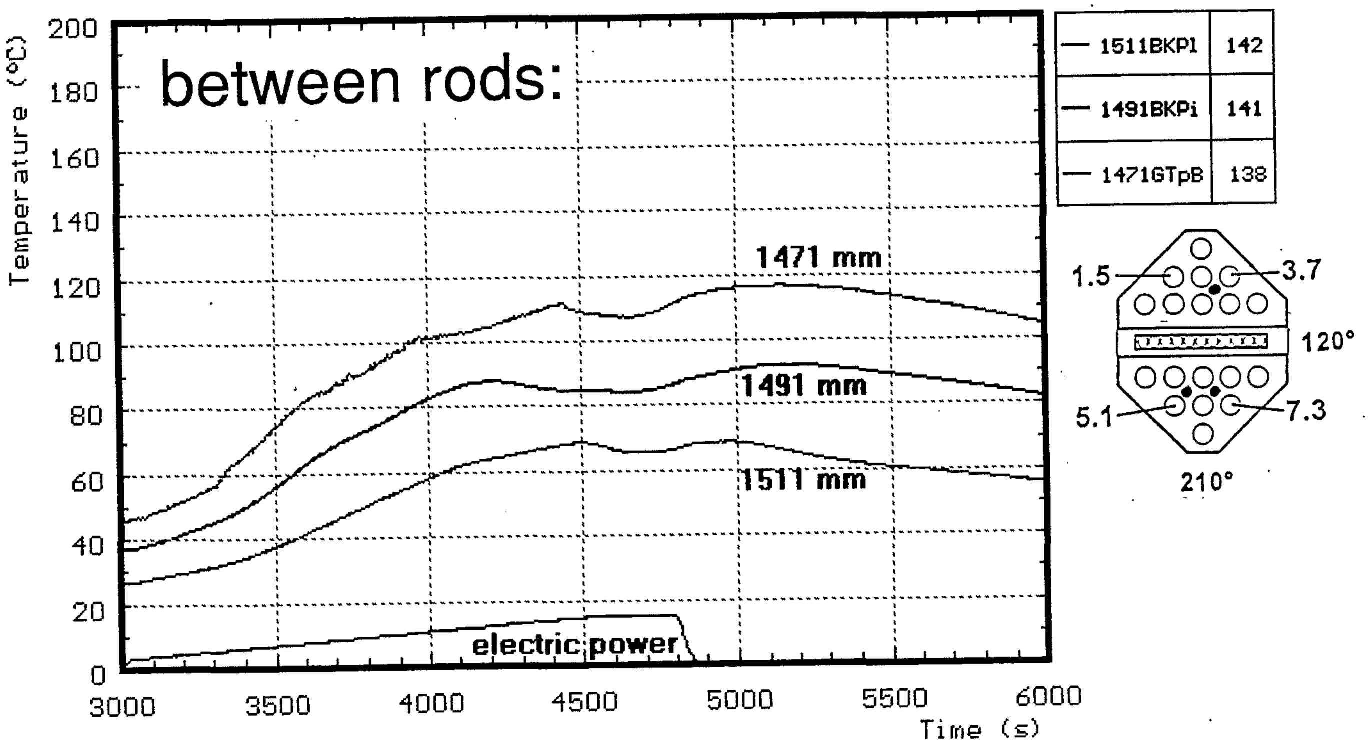

Fig. 39: CORA-28; Temperatures measured in and under the bundle head plate (1471, 1491, 1511 mm)

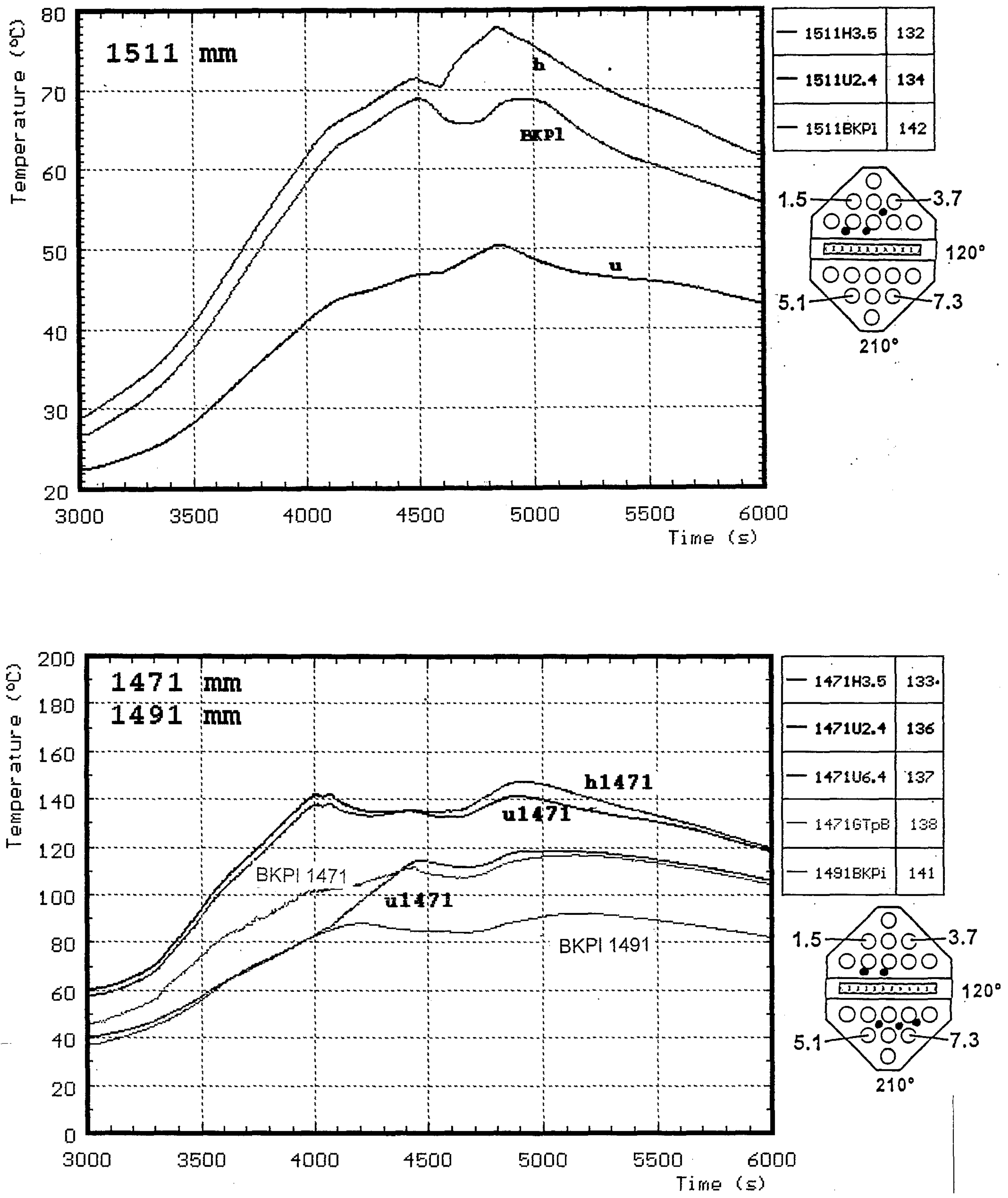

h: heated
u: unheated

BKPl : bundle heat plate

Fig. 40: CORA-28; Temperatures at elevations given (1511, 1491, 1471 mm)

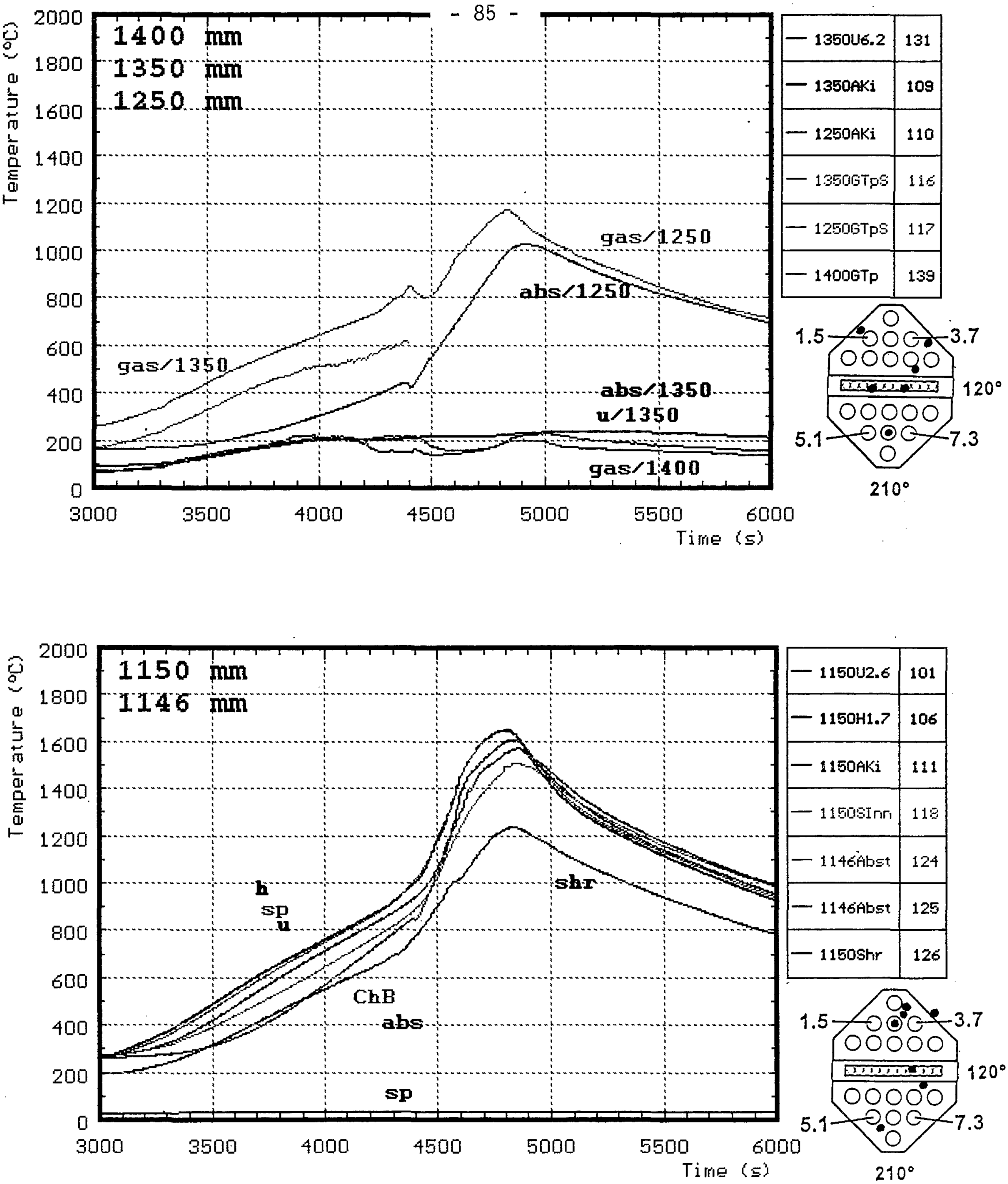

h:	heated rods	abs:	in absorberblade
u:	unheated rods	gas:	gas temperature
sp:	spacer	shr:	on shroud
ChB:	channel box wall		

Fig. 41: CORA-28; Temperatures at elevations given (1400 - 1146 mm)

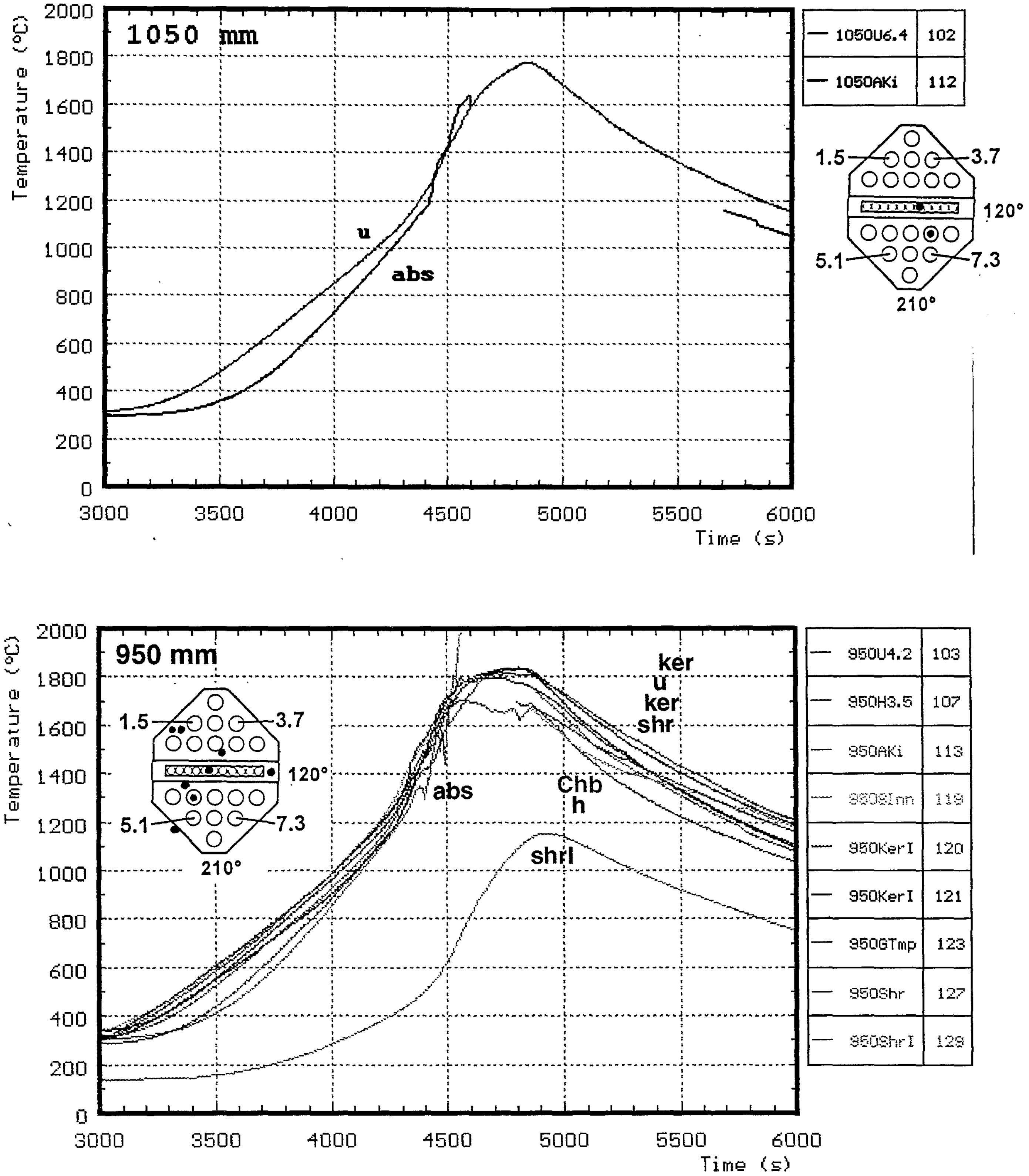

h : heated rods
u : unheated rods
shrl : shroud insolation
ChB : channel box wall

abs : in absorberblade
ker : ceramic protected termocouples
shr : on shroud

Fig. 42: CORA-28; Temperatures at elevations given (1050,950 mm)

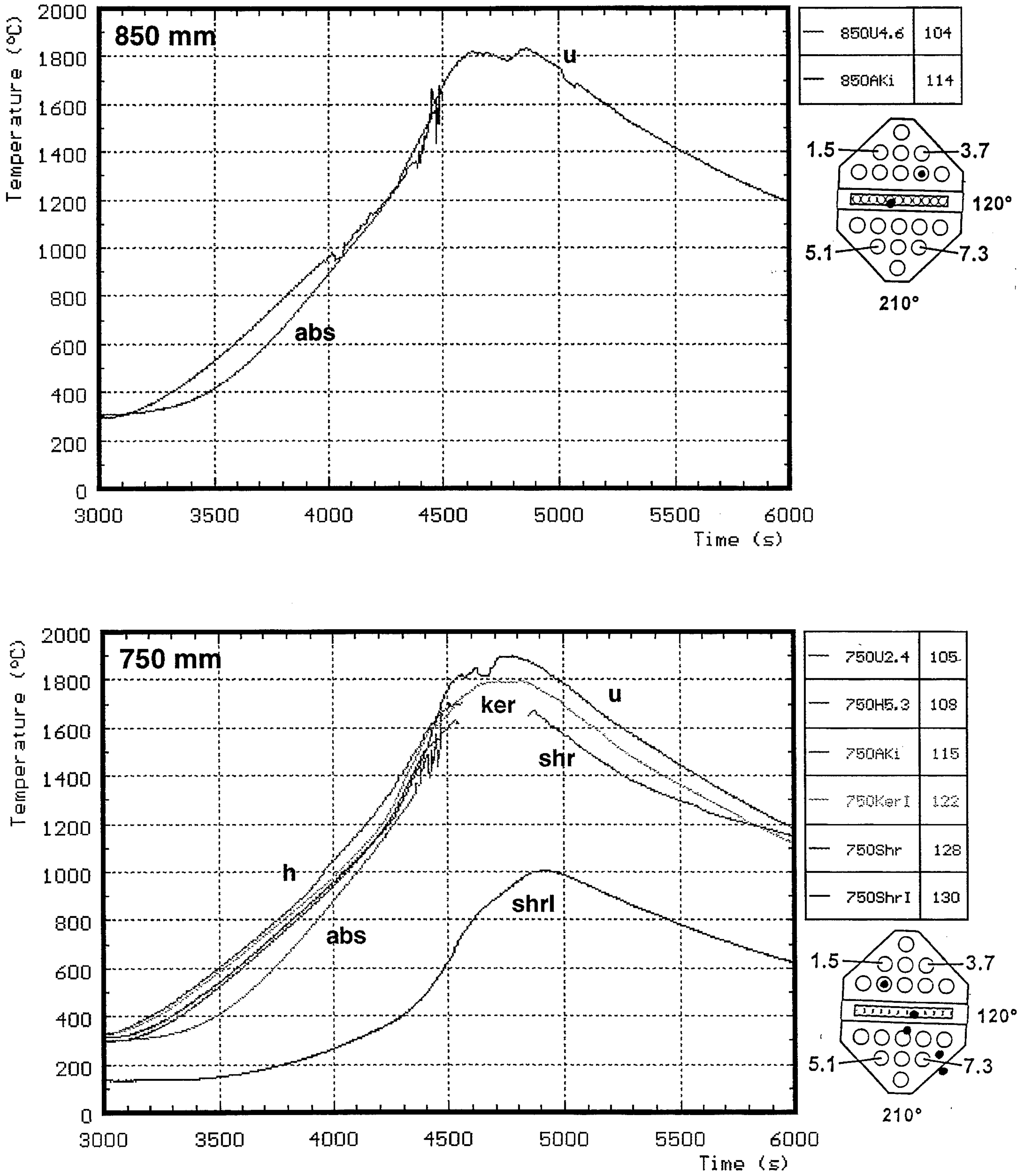

h: heated rod
u: unhated rod
shr: on shroud

shrl: shroud insulation
ker: ceramic protected thermocouples
abs: in absorberblade

Fig. 43: CORA-28; Temperatures at elevations given (850, 750 mm)

c28_043.cdr

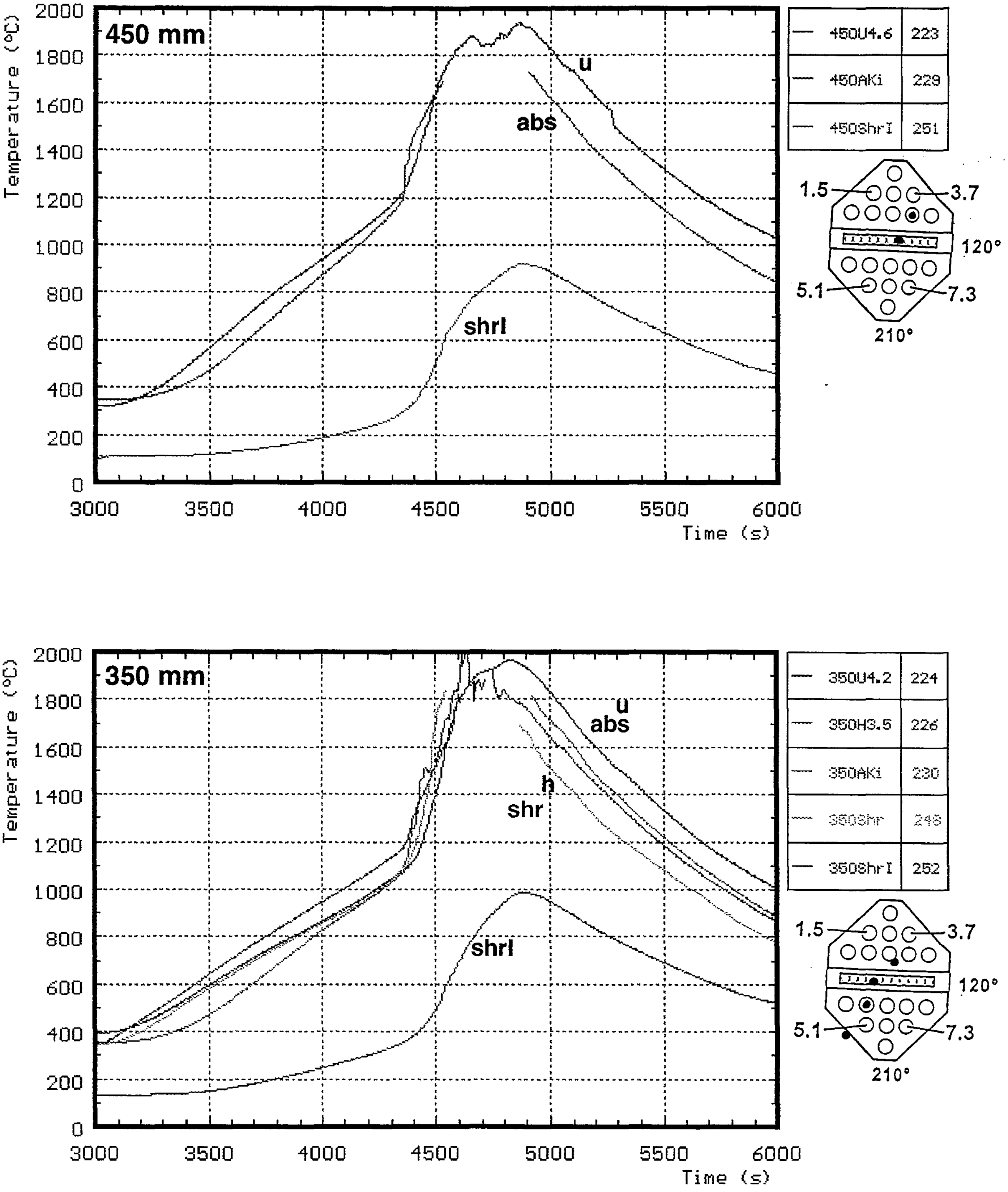

h: heated rod
u: unhated rod
shr: on shroud

shrl: shroud insulation
abs: in absorberblade

Fig. 44: CORA-28; Temperatures at elevations given (450, 350 mm)

c28_044.cdr

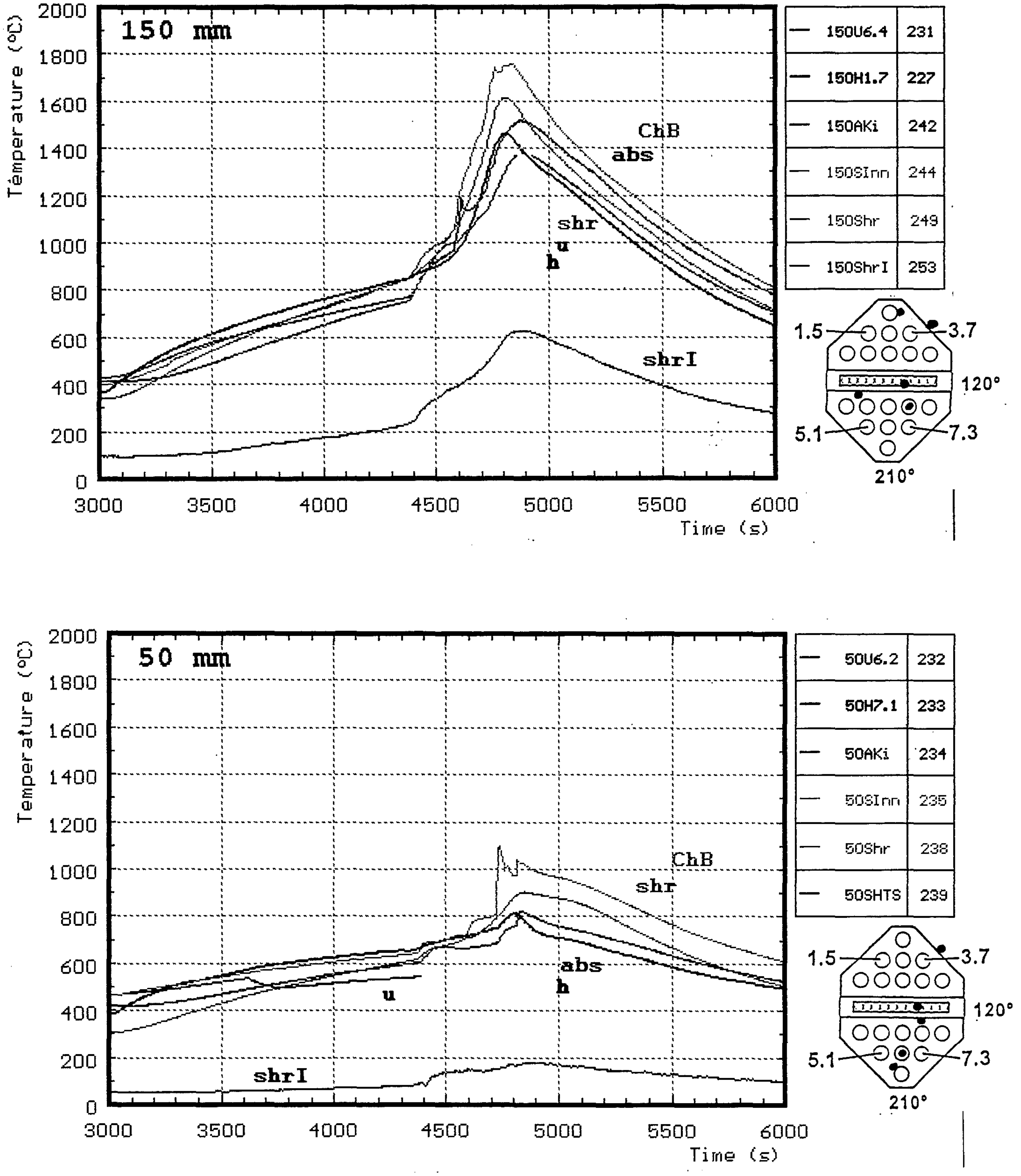

h : heated rods
u : unheated rods
shr : on shroud

shrI : shroud insolation
abs : in absorberblade
ChB : channel box wall

Fig. 45: CORA-28; Temperatures at elevations given (150, 50 mm)

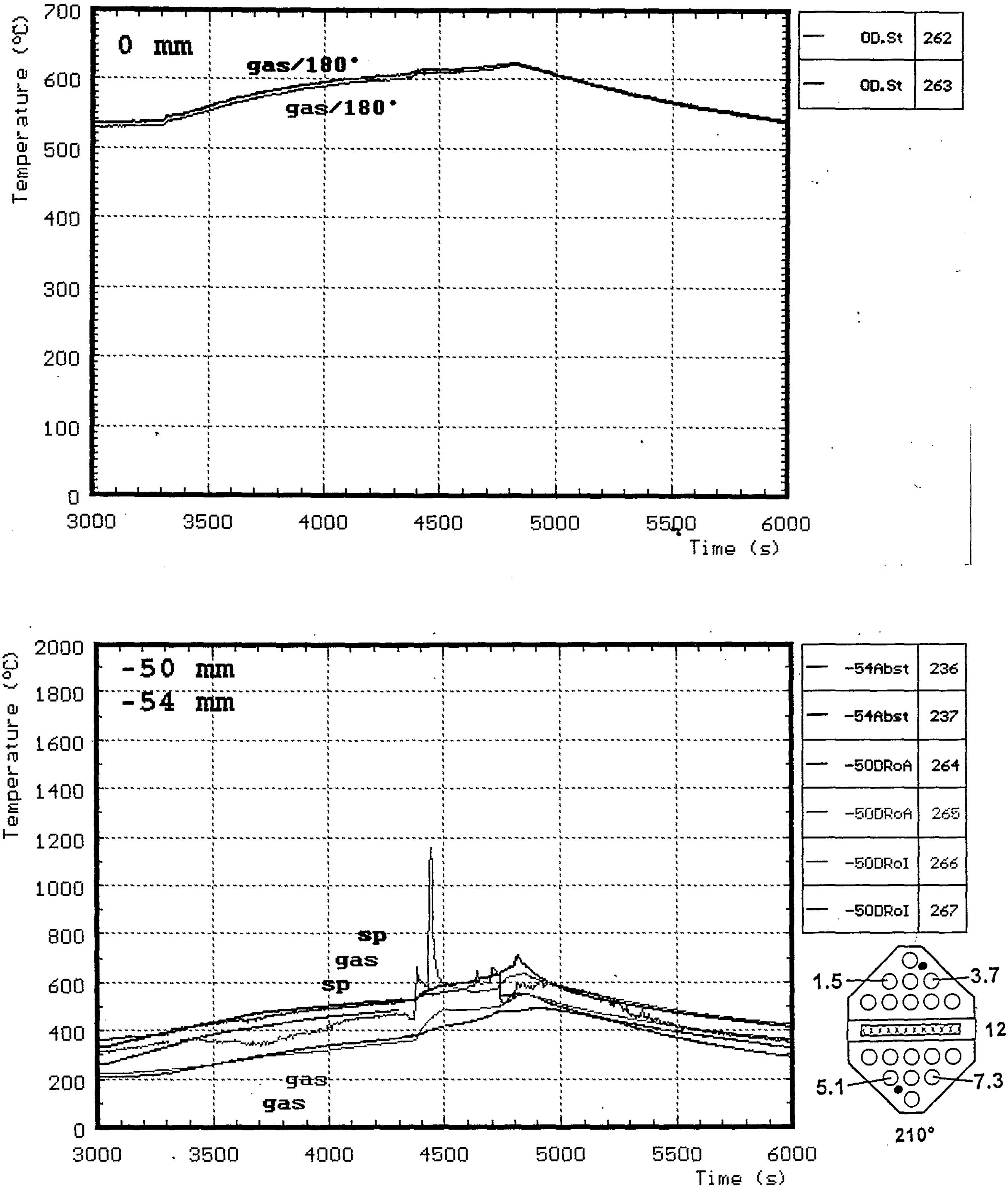

sp : spacer

gas : gas temperature

Fig. 46: CORA-28; Temperatures at elevations given (0, -50, -54 mm)

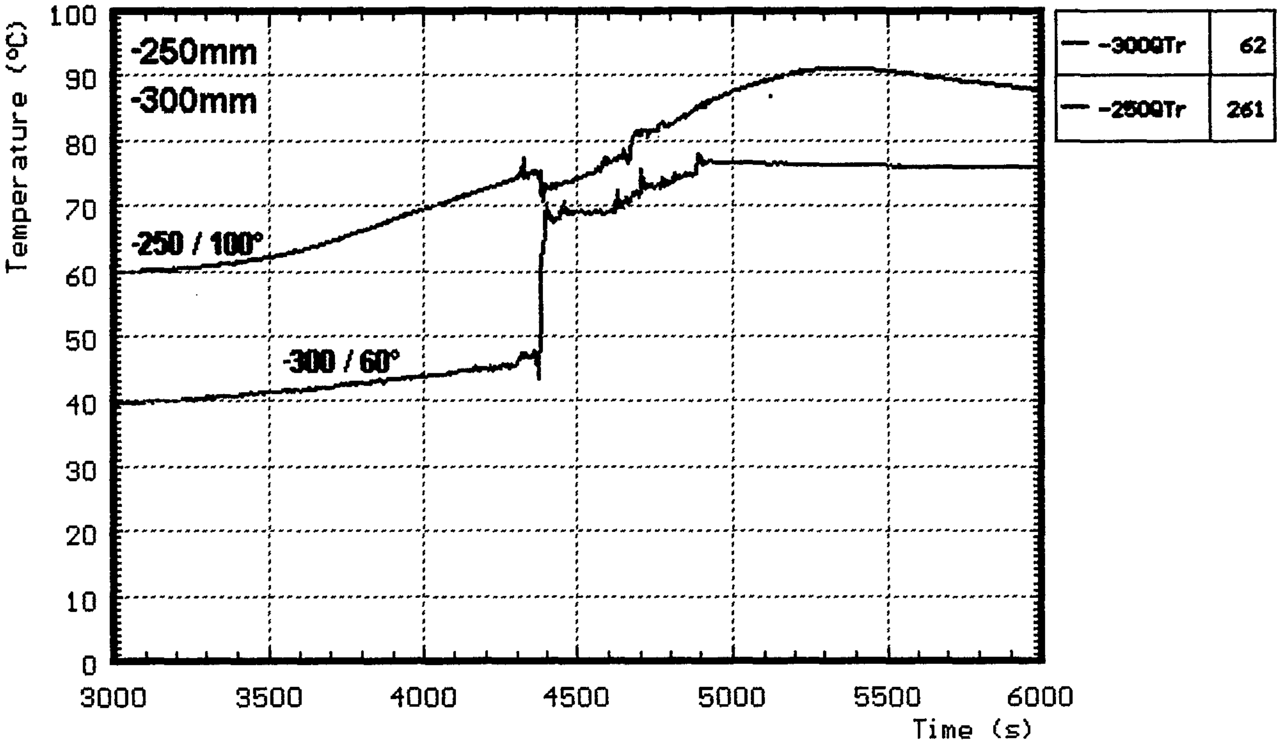

Fig. 47: CORA-28; Temperatures at elevations given (-250, -300 mm)

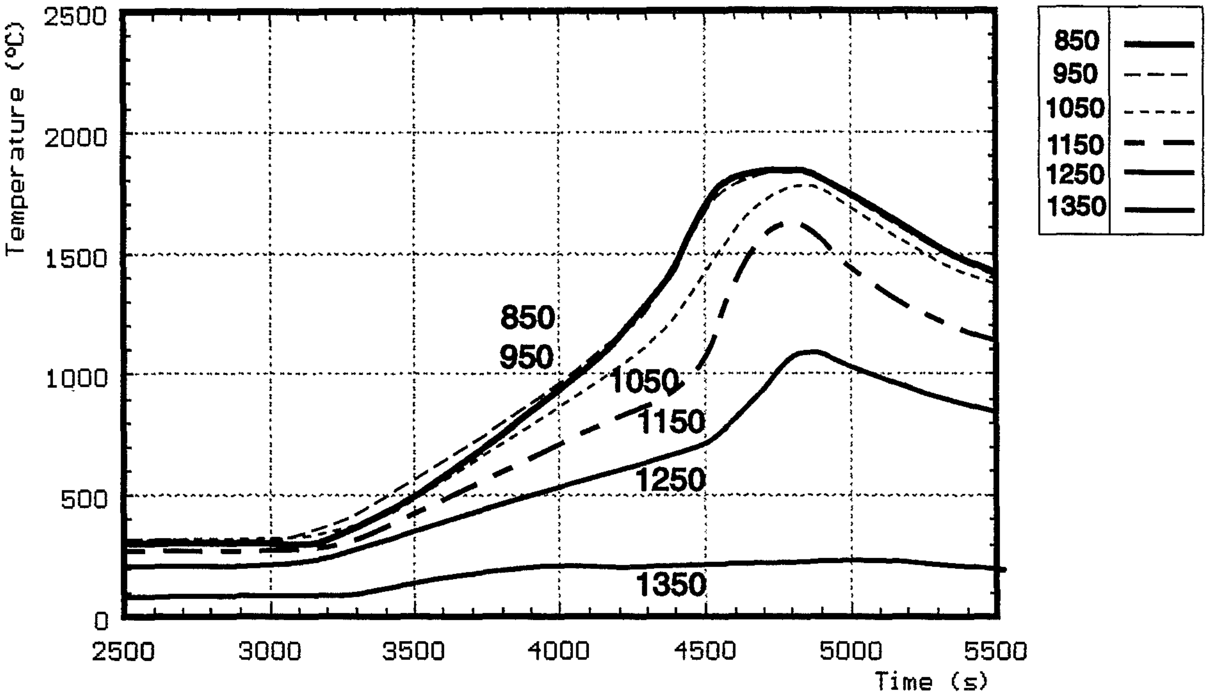

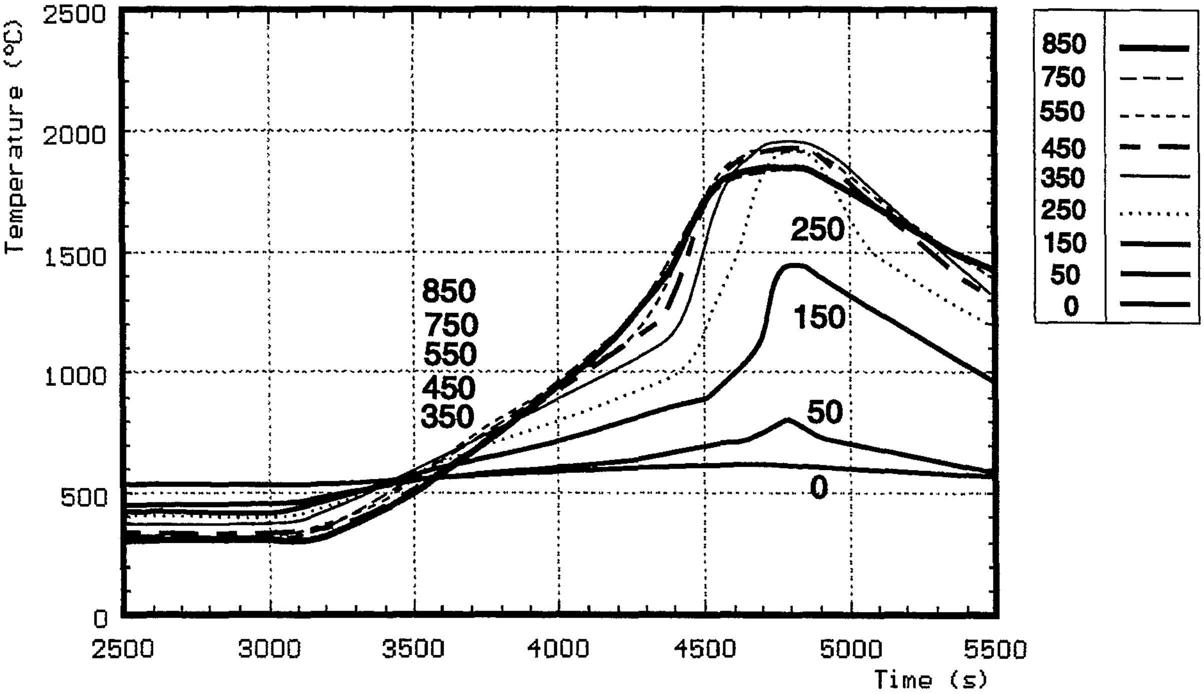

Fig. 48: CORA-28; Best-estimate bundle temperatures at different elevations

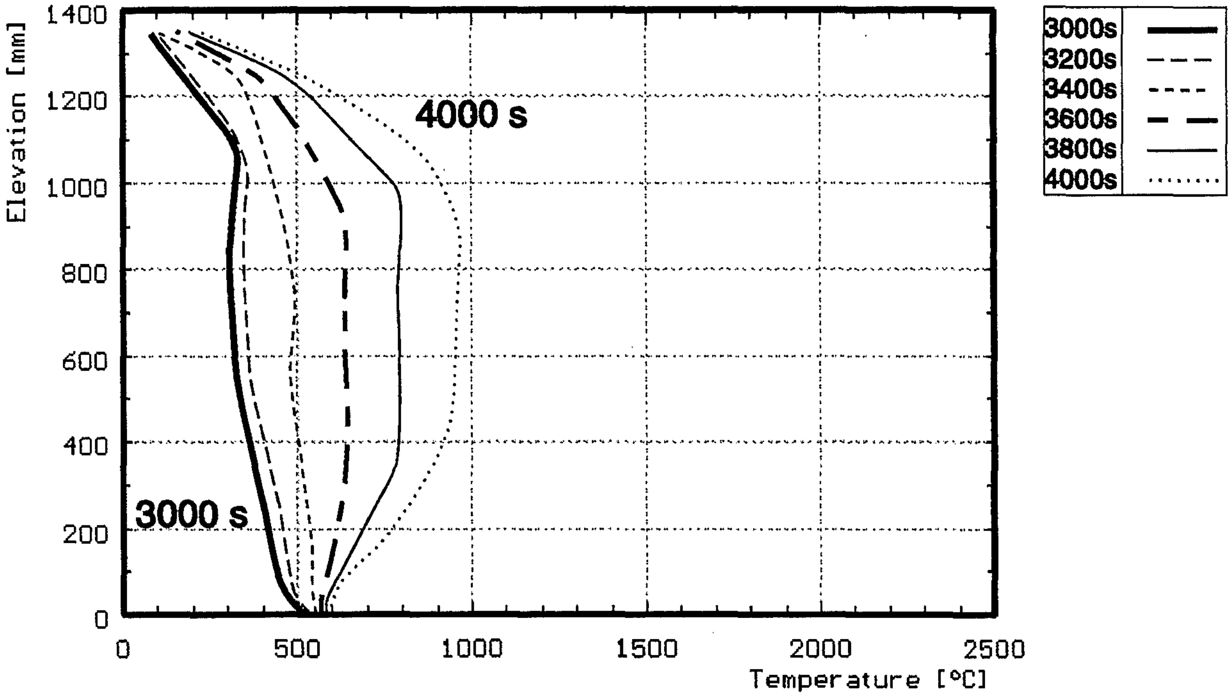

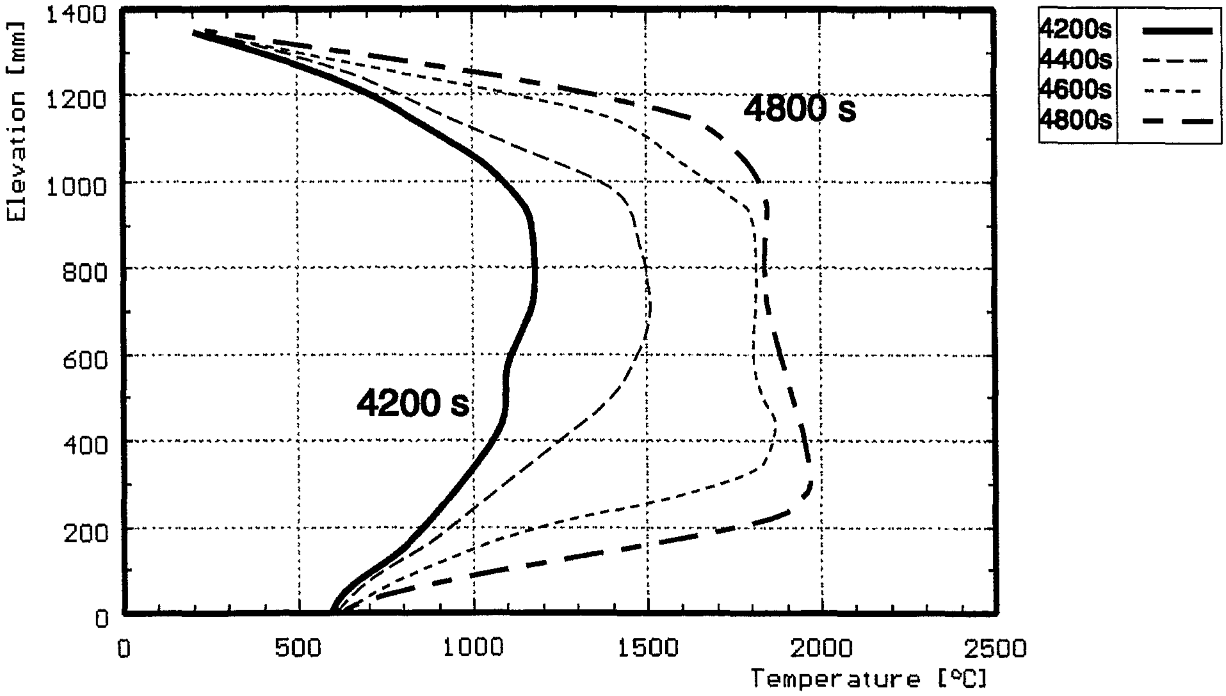

Fig. 49: Axial temperature distribution during the transient of test CORA-28

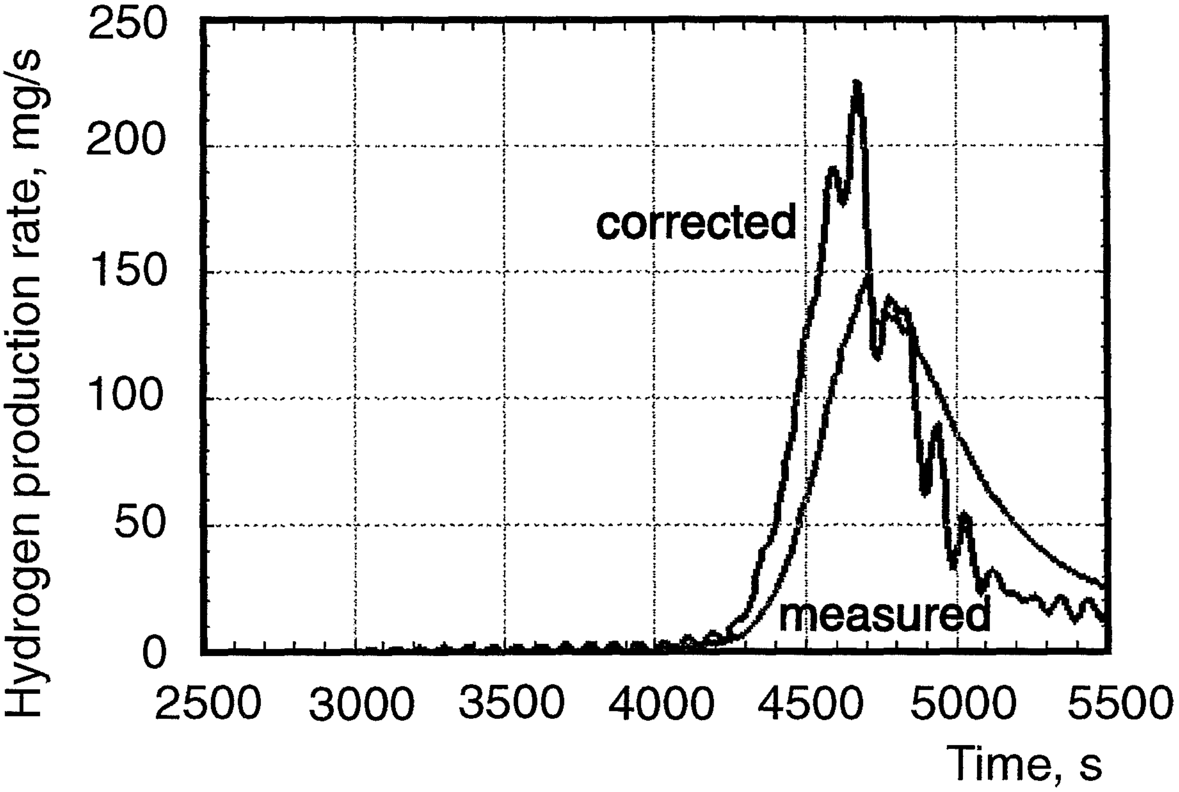

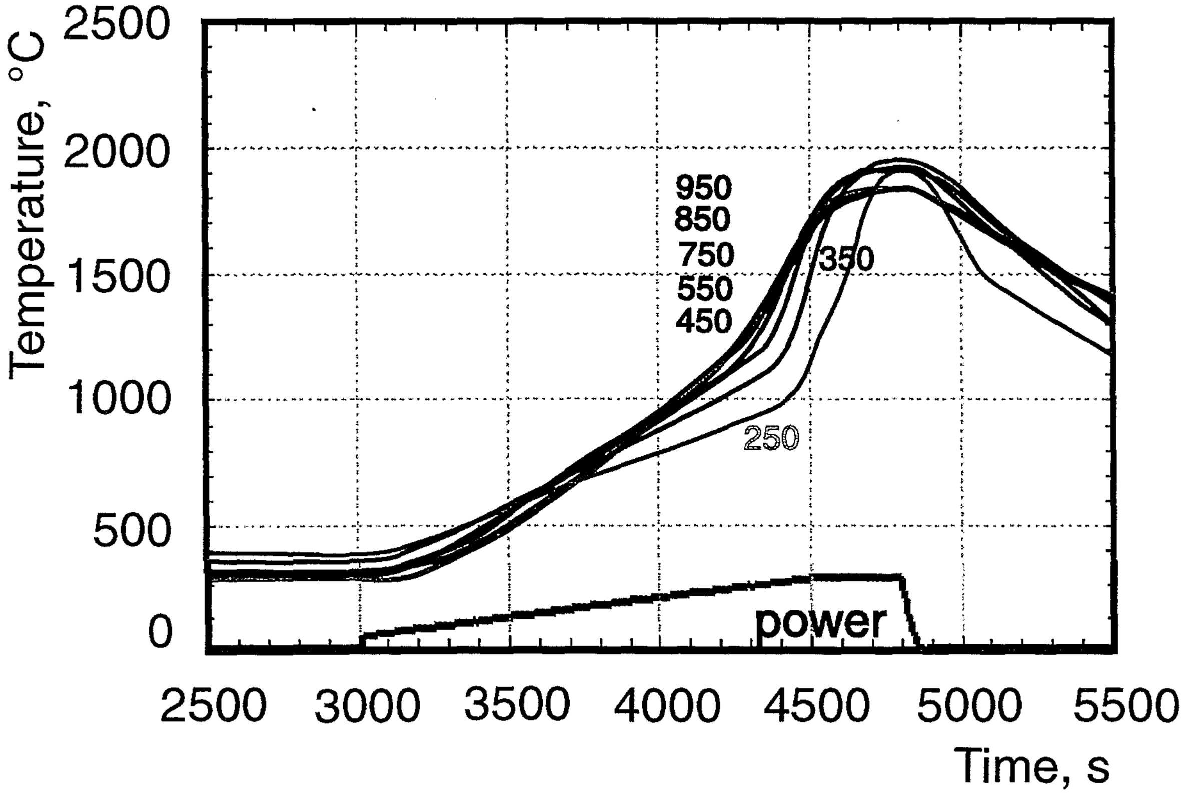

Fig. 50a: CORA-28; Comparison of hydrogen production rate and best estimate temperatures

c28_050a.cdr

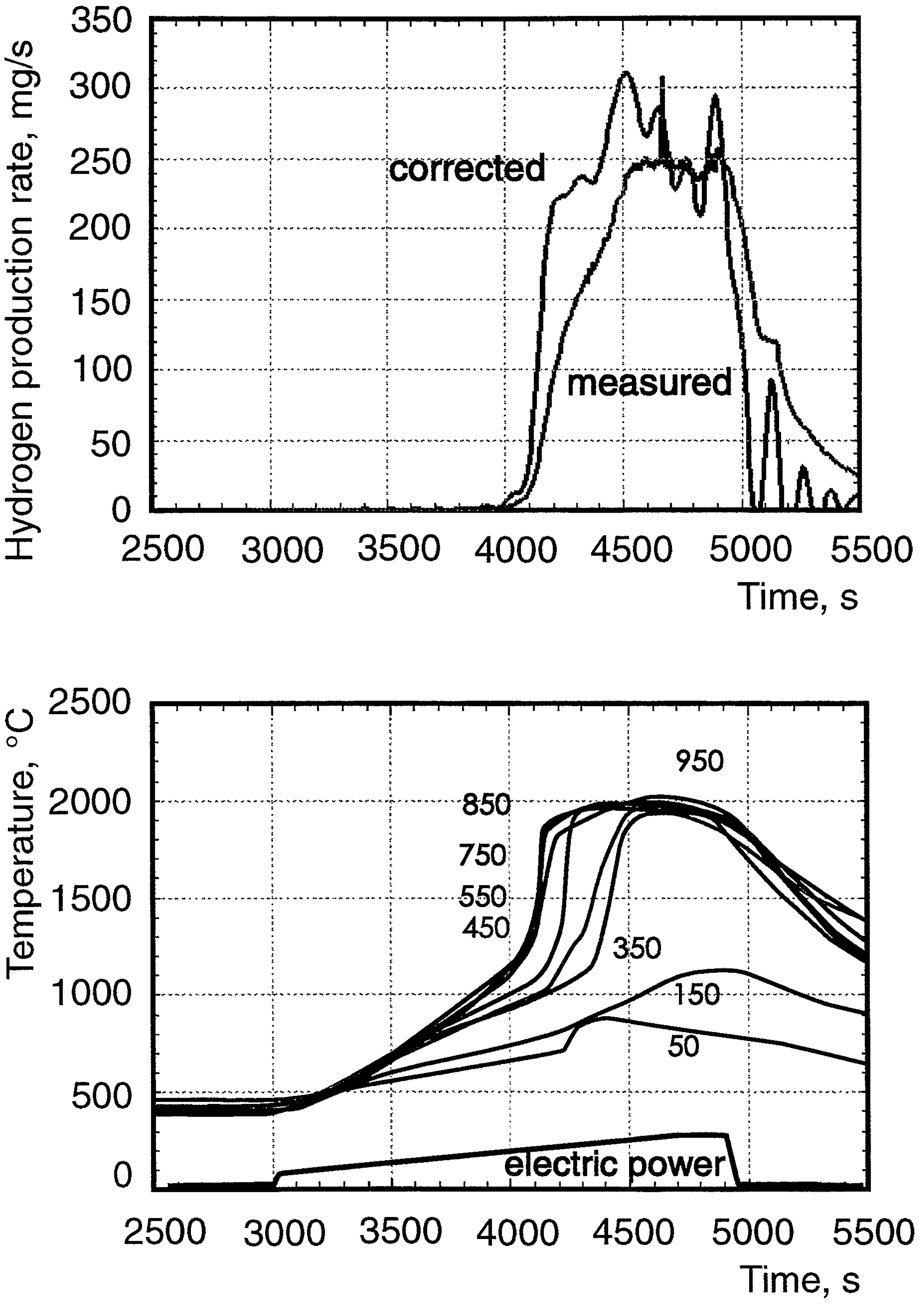

Fig. 50b: CORA-29: Comparison of hydrogen production rate and best estimate temperatures

c28_050b.cdr

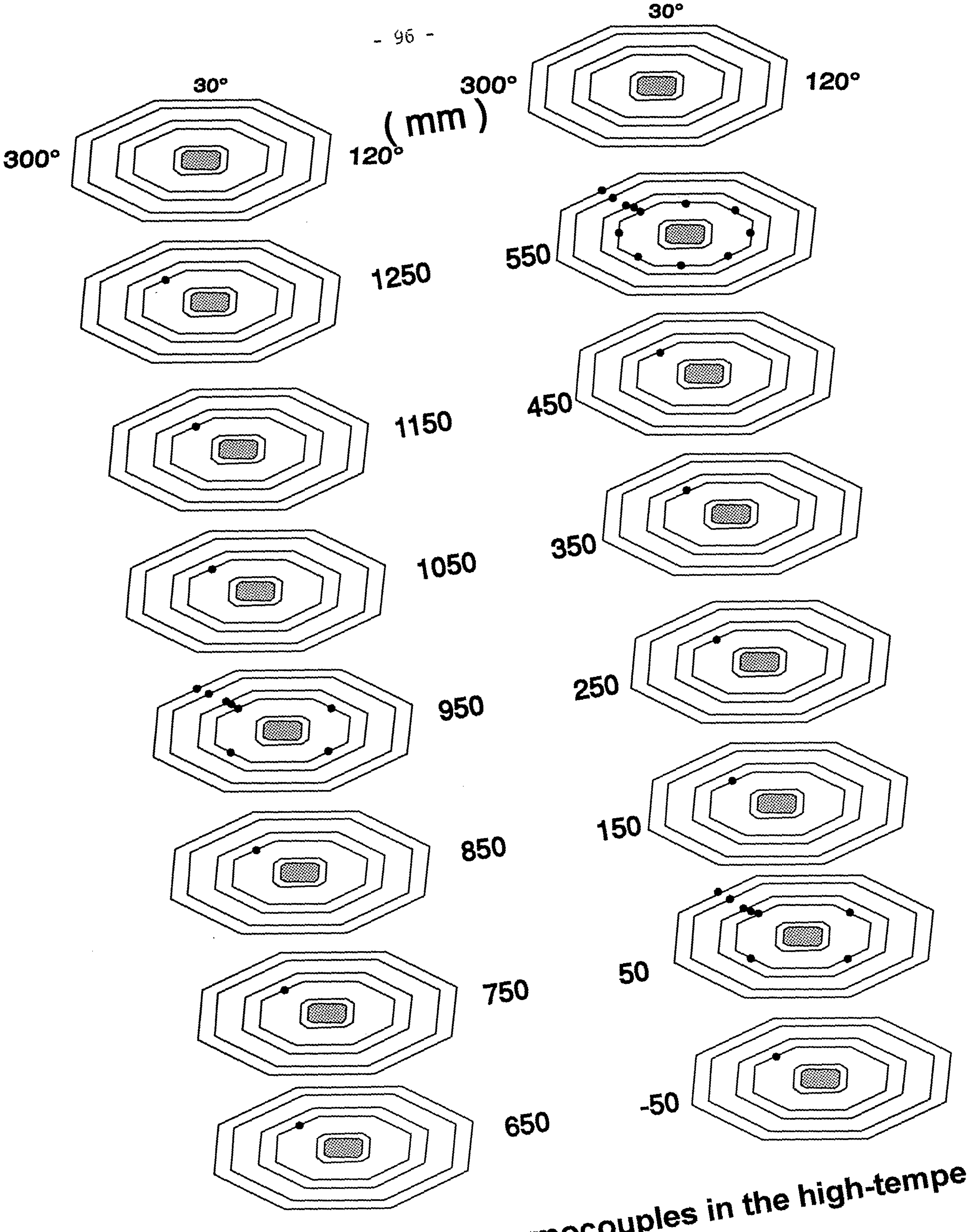

Fig. 51a: Locations of thermocouples in the high-temperature shield (CORA-28)

ANGLE		30°	75°	100°	120°		165°	210°	255°	300°	345°				
RADIUS (mm)		153	153	380	153	380	153	153	153	153	153	172	192	255	293
ELEVATION in BUNDLE [mm]	1270			208 283Ni											
	1250										174 33Ni				
	1150										175 32Ni				
	1050										176 31Ni				
	990					209 284Ni									
	950		162 28Ni				166 27Ni		170 26Ni		177 25Ni	188 29Ni	191 30Ni	194 38Ni	197 39Ni
	850										178 24Ni				
	750										179 23Ni				
	650										180 22Ni				
	550	161 19Ni	163 18Ni		165 17Ni		167 16Ni	169 15Ni	171 14Ni	173 13Ni	181 12Ni	189 20Ni	192 21Ni	195 36Ni	198 37Ni
	450										182 11Ni				
	350										183 10Ni				
	250										184 9Ni				
	150										185 8Ni				
	50		164 5Ni				168 4Ni		172 3Ni		186 2Ni	190 6Ni	193 7Ni	196 34Ni	199 35Ni
	0					210 286Ni									
	-50										187 1Ni				

Fig. 51b: Positions of thermocouples in the high-temperature shield for test CORA-28

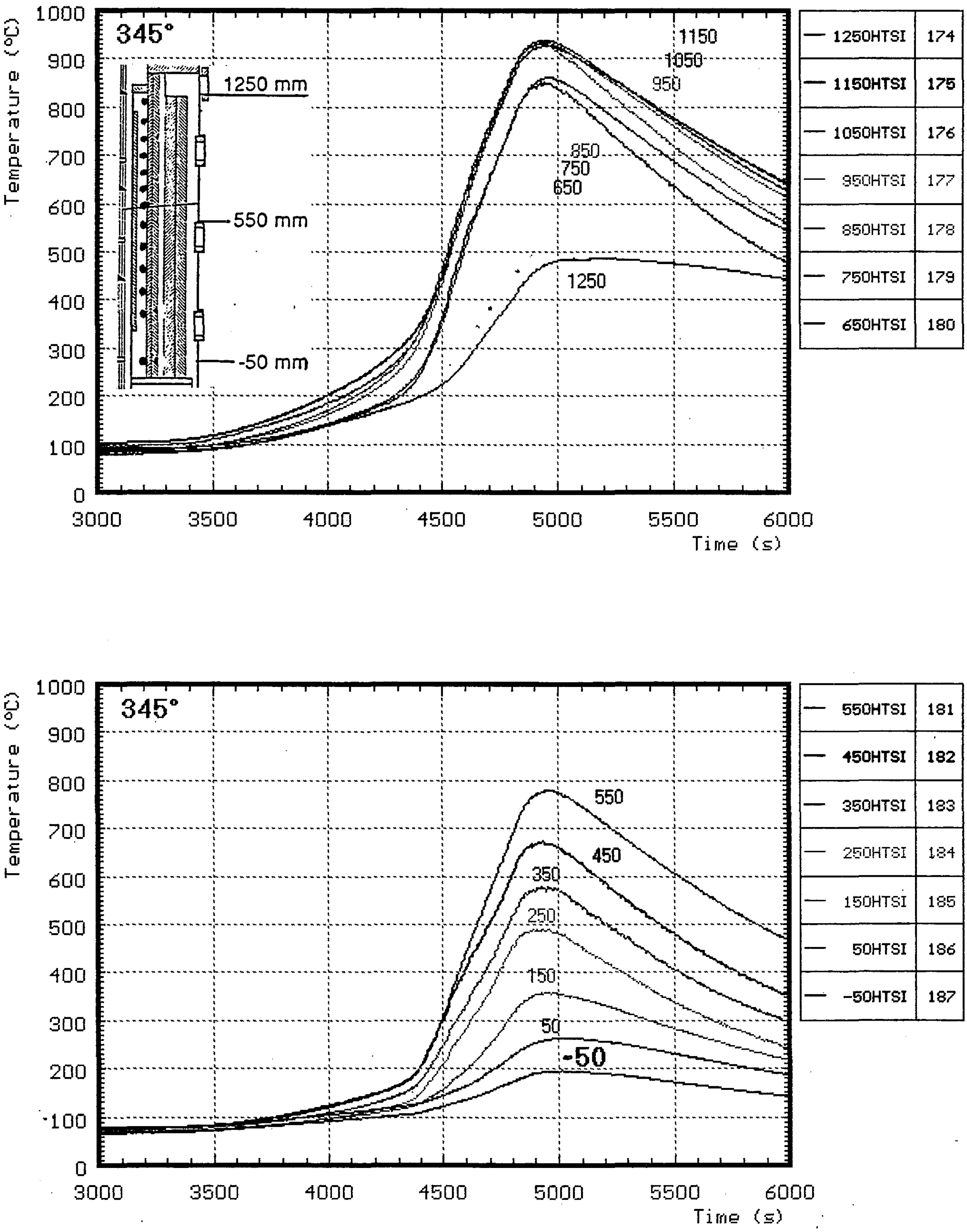

Fig. 52: CORA-28; Temperatures of HTS, Inner surface at 153 mm radius, 345°

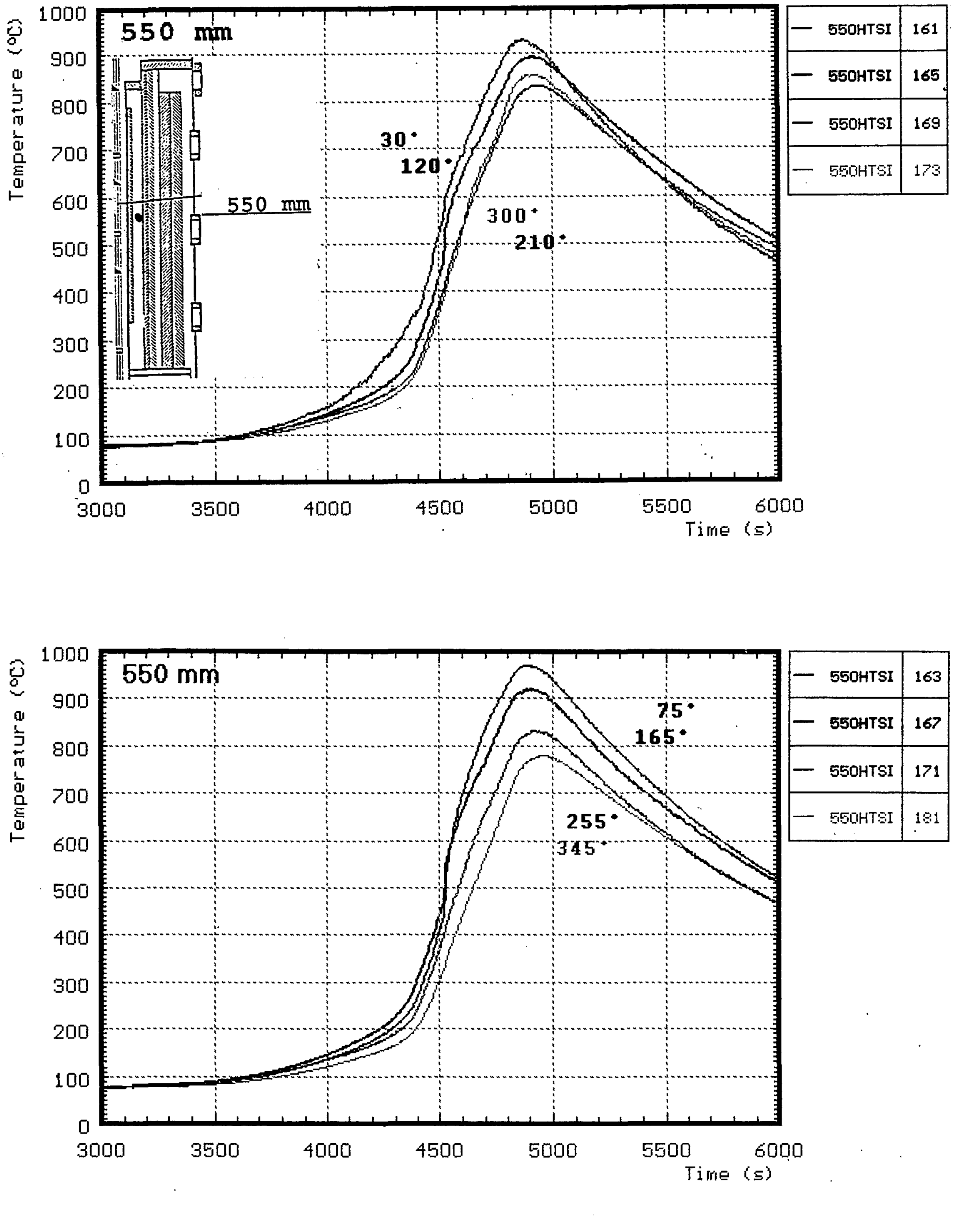

Fig. 53: CORA-28; Temperatures of HTS, Comparison: inner surface at 153 mm radius and 550 mm elevation

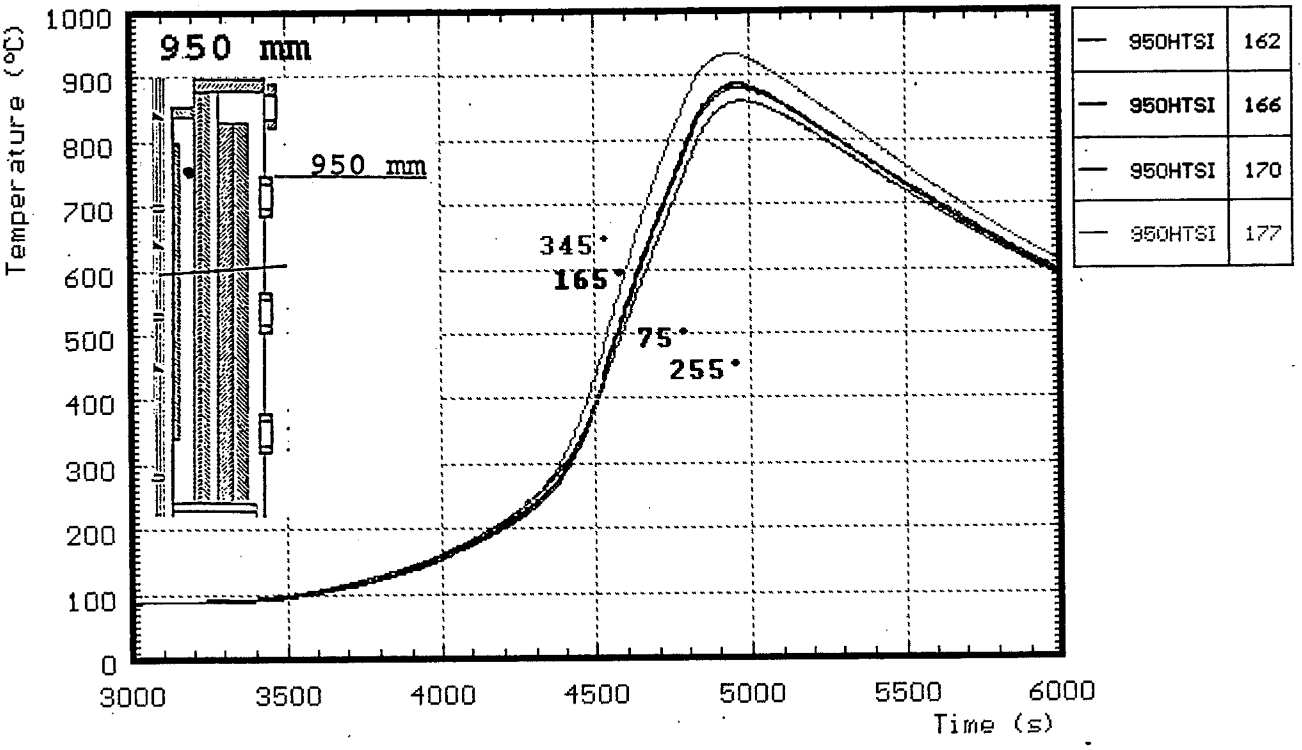

Fig. 54: CORA-28; Temperatures of HTS, Comparison: inner surface at 153 mm radius and 950 mm elevation

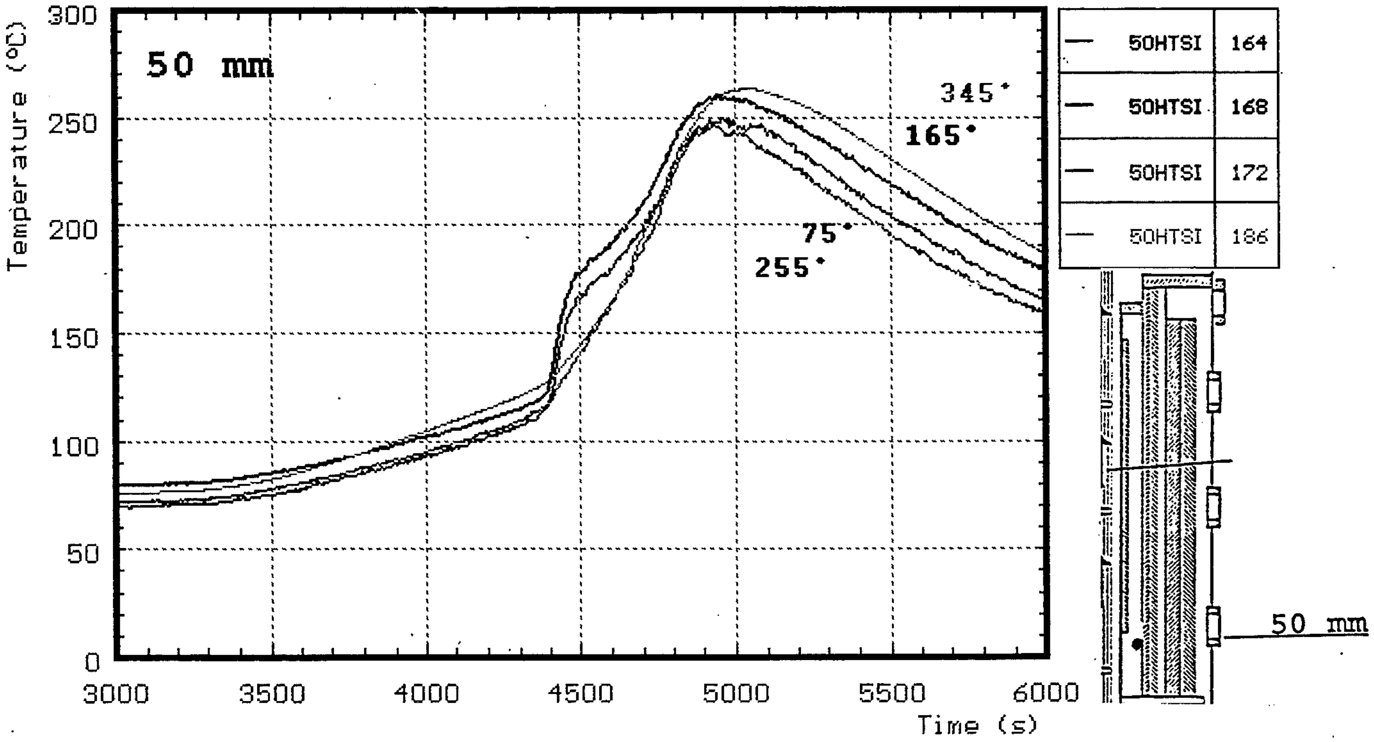

Fig. 55: CORA-28; Temperatures of HTS, Comparison: inner surface at 153 mm radius and 50 mm elevation

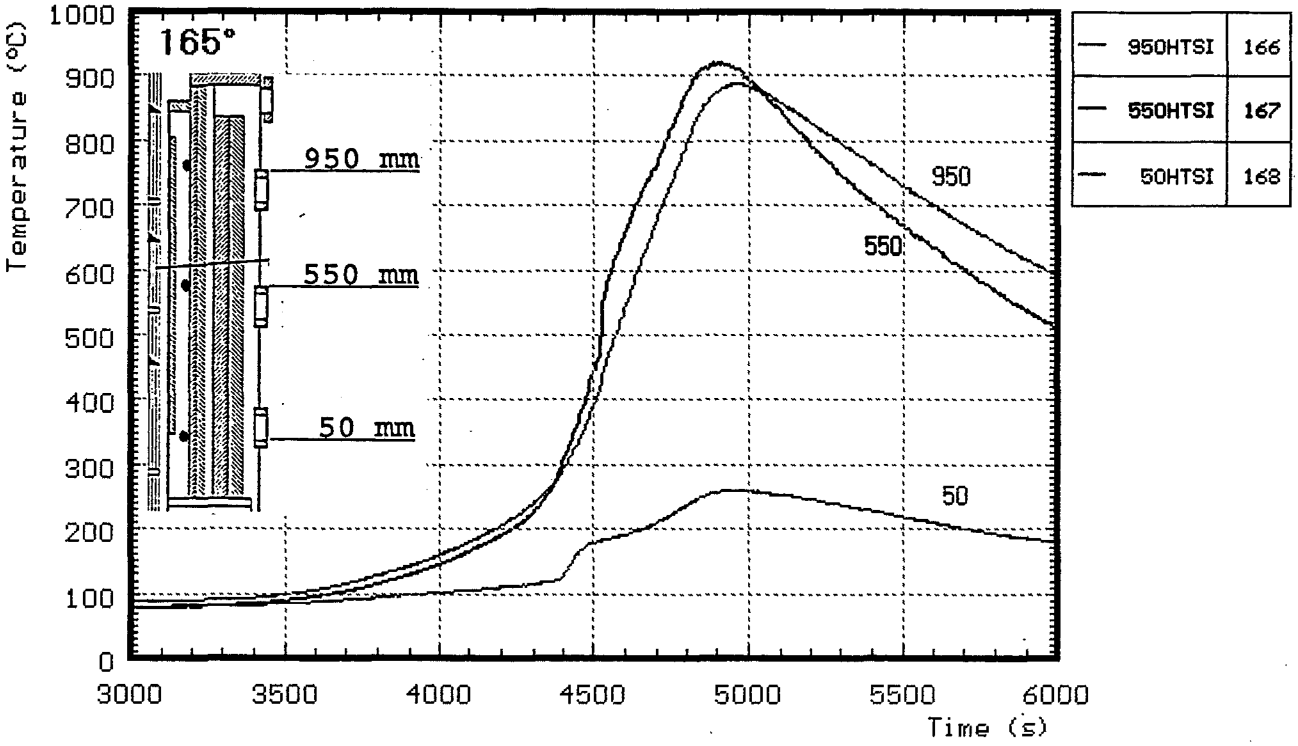

Fig. 56: CORA-28; Temperatures of HTS, inner surface at 153 mm radius, 165°

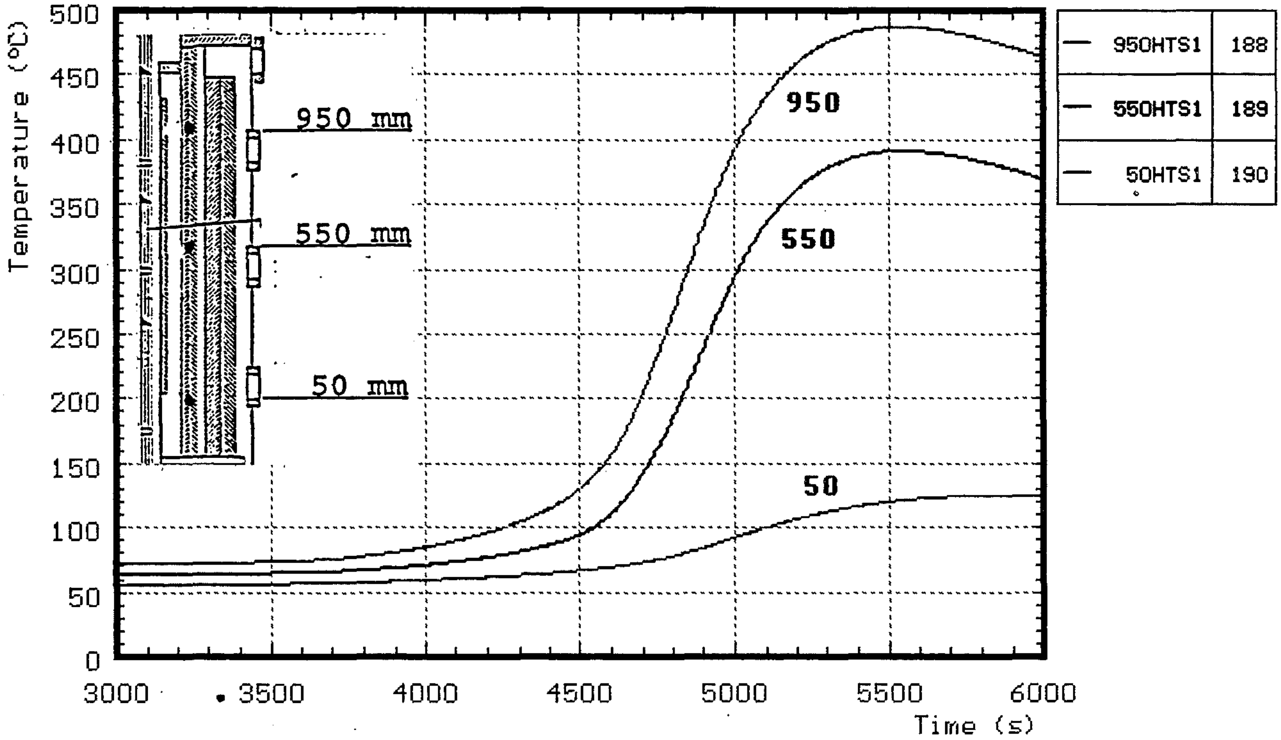

Fig. 57: CORA-28; Temperatures of HTS, Temperatures in HT shield at 172 mm radius

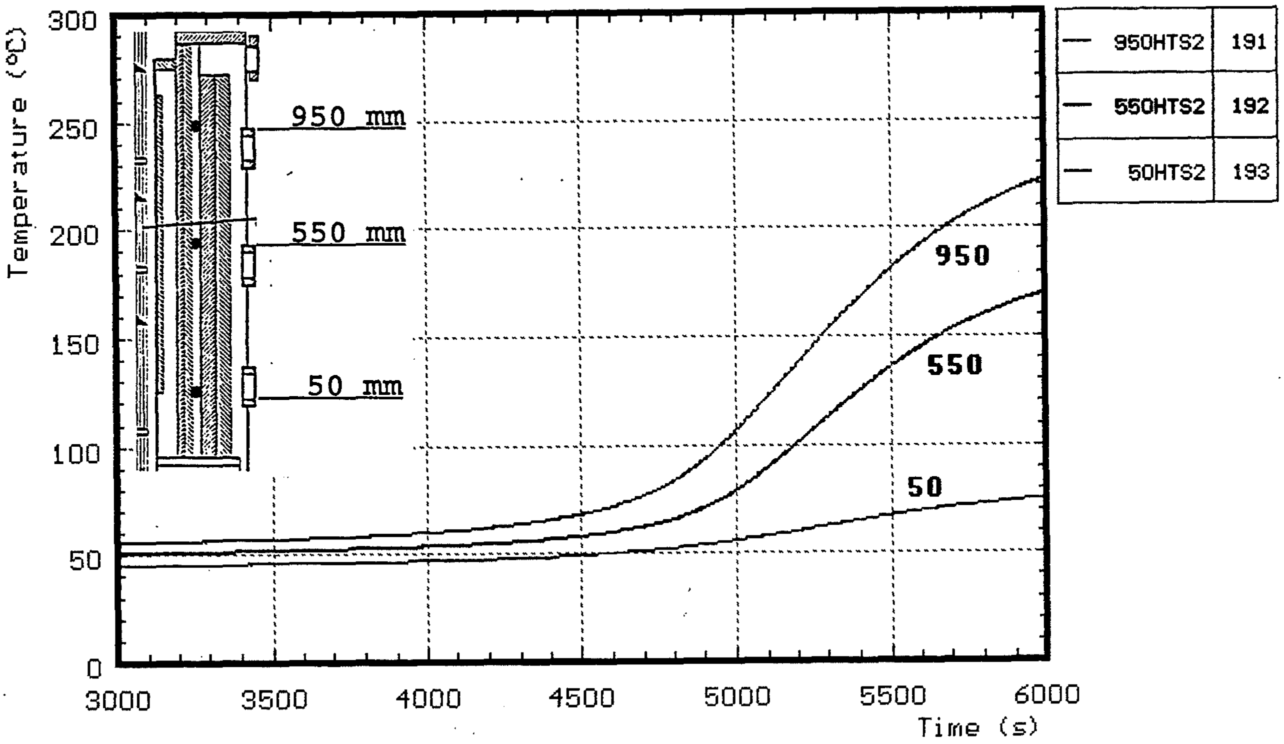

Fig. 58: CORA-28; Temperatures of HTS, Temperatures in HT shield at 192 mm radius

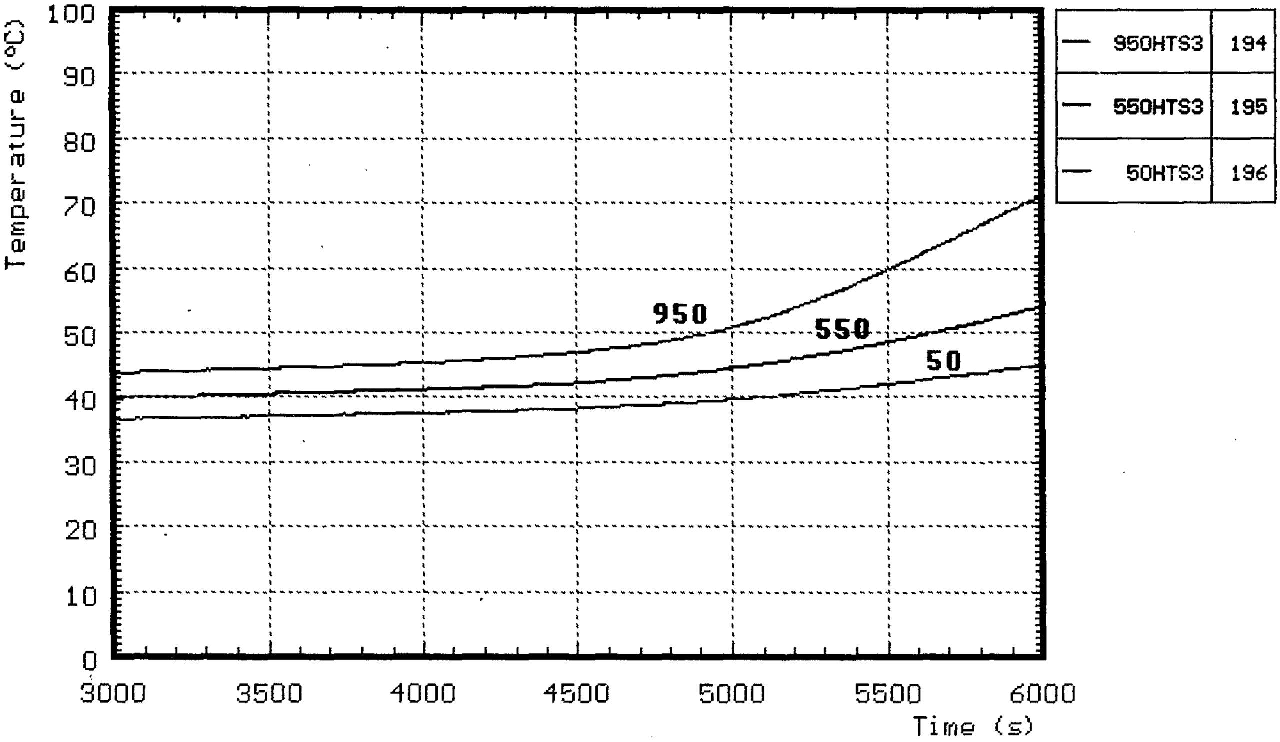

Fig. 59: CORA-28; Temperatures of HTS, Temperatures in HT shield at 255 mm radius

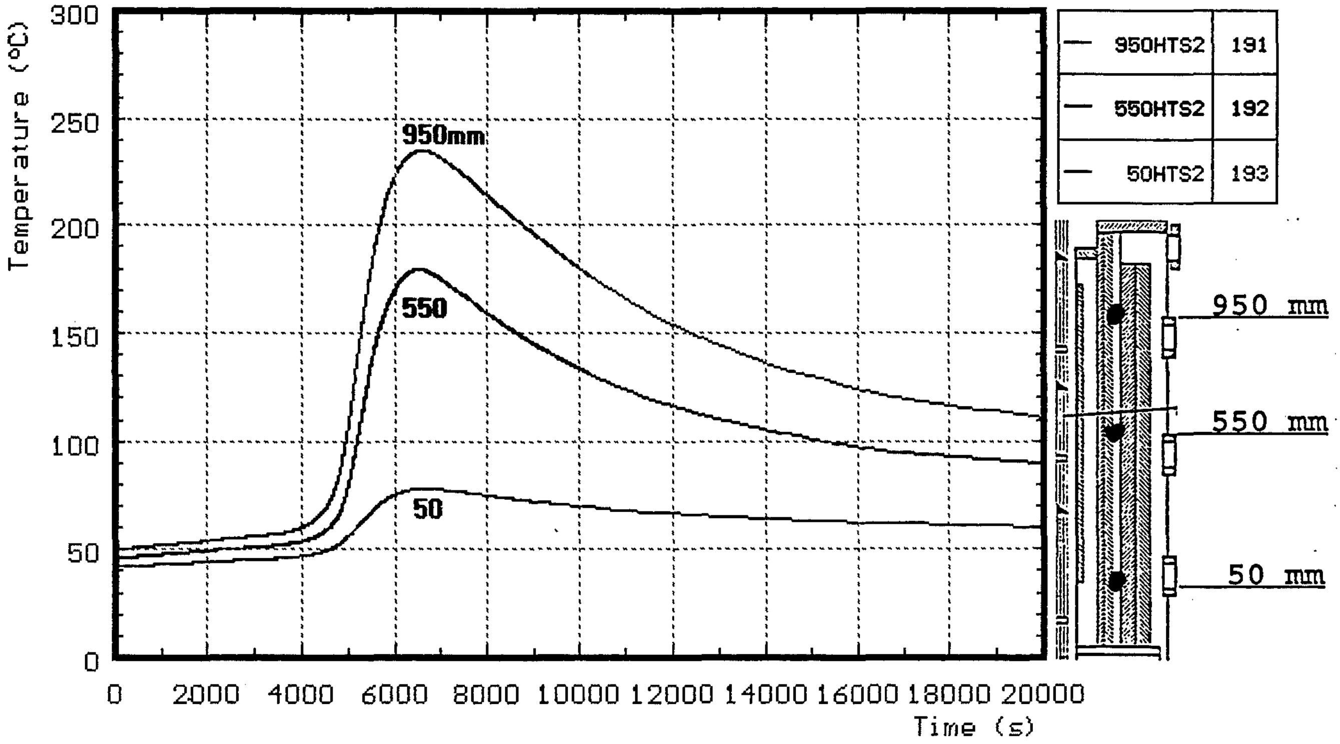

Fig. 60: CORA-28; Temperatures of HTS, Temperatures in HT shield at 192 mm radius (0-20000 s)

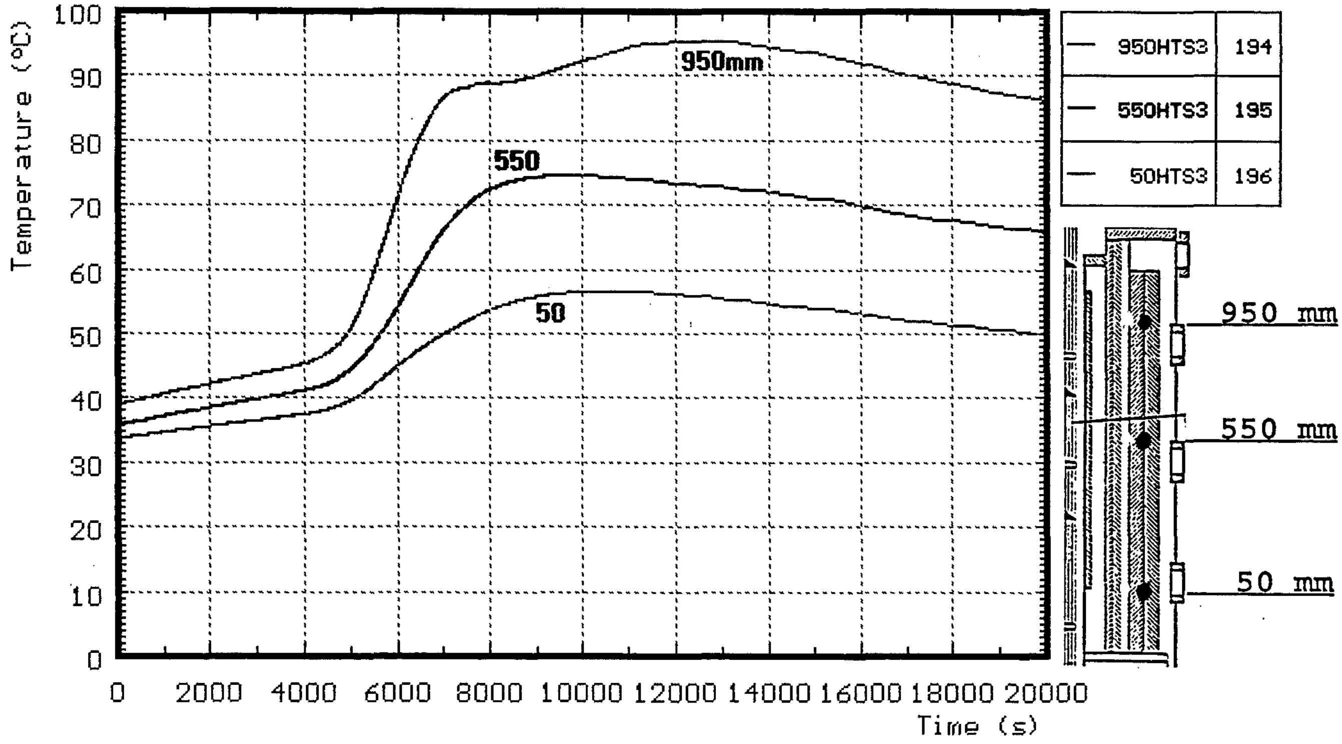

Fig. 61: CORA-28; Temperatures of HTS, Temperatures in HT shield at 255 mm radius (0-20000 s)

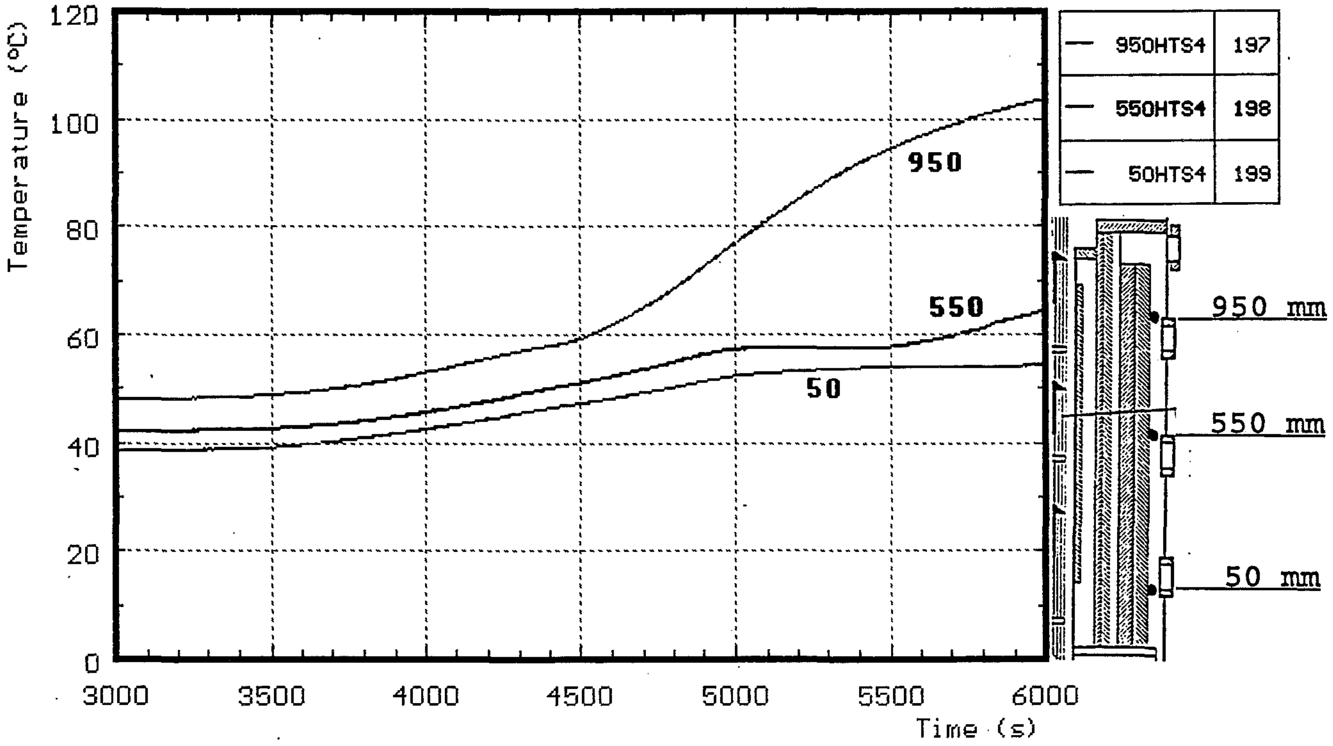

Fig. 62: CORA-28; Temperatures of HTS, Temperatures in HT shield at 293 mm radius

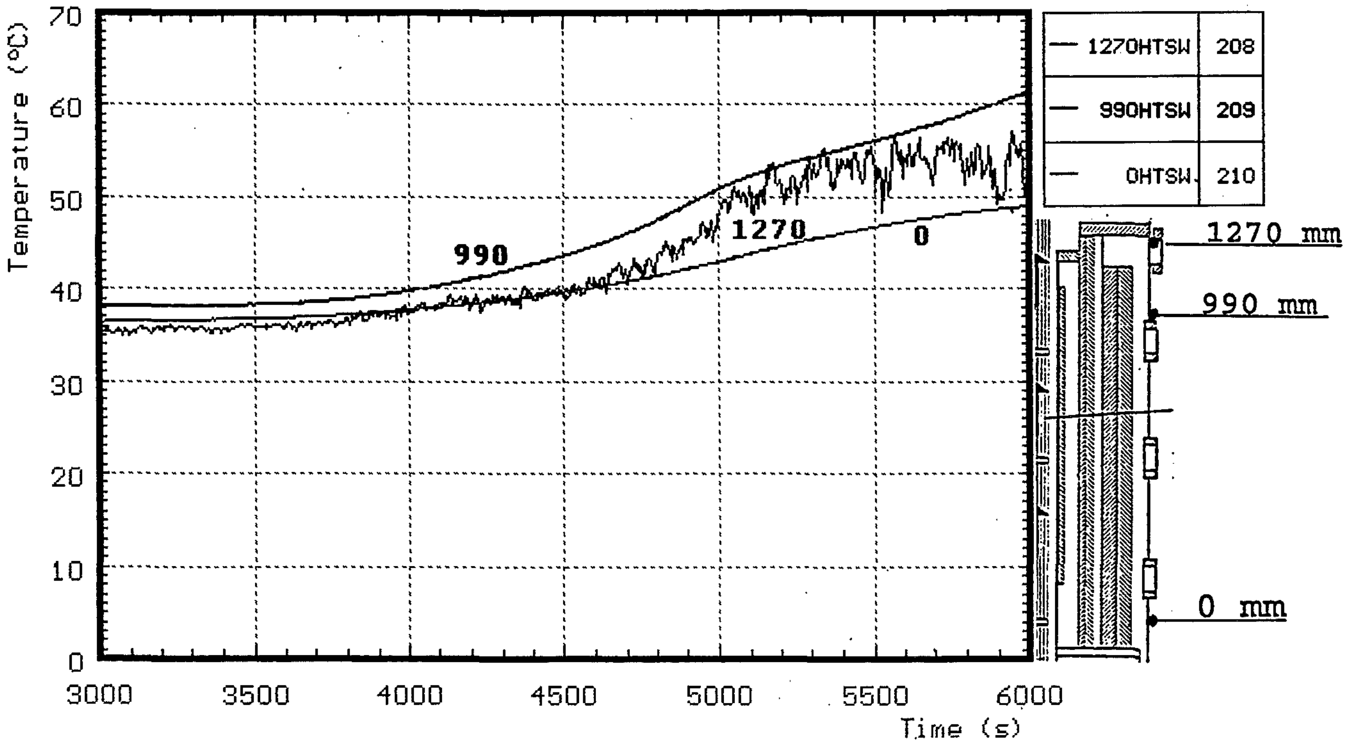

Fig. 63: CORA-28; Temperatures of HTS, Temperatures at outer surface of pressure vessel, 380 mm radius

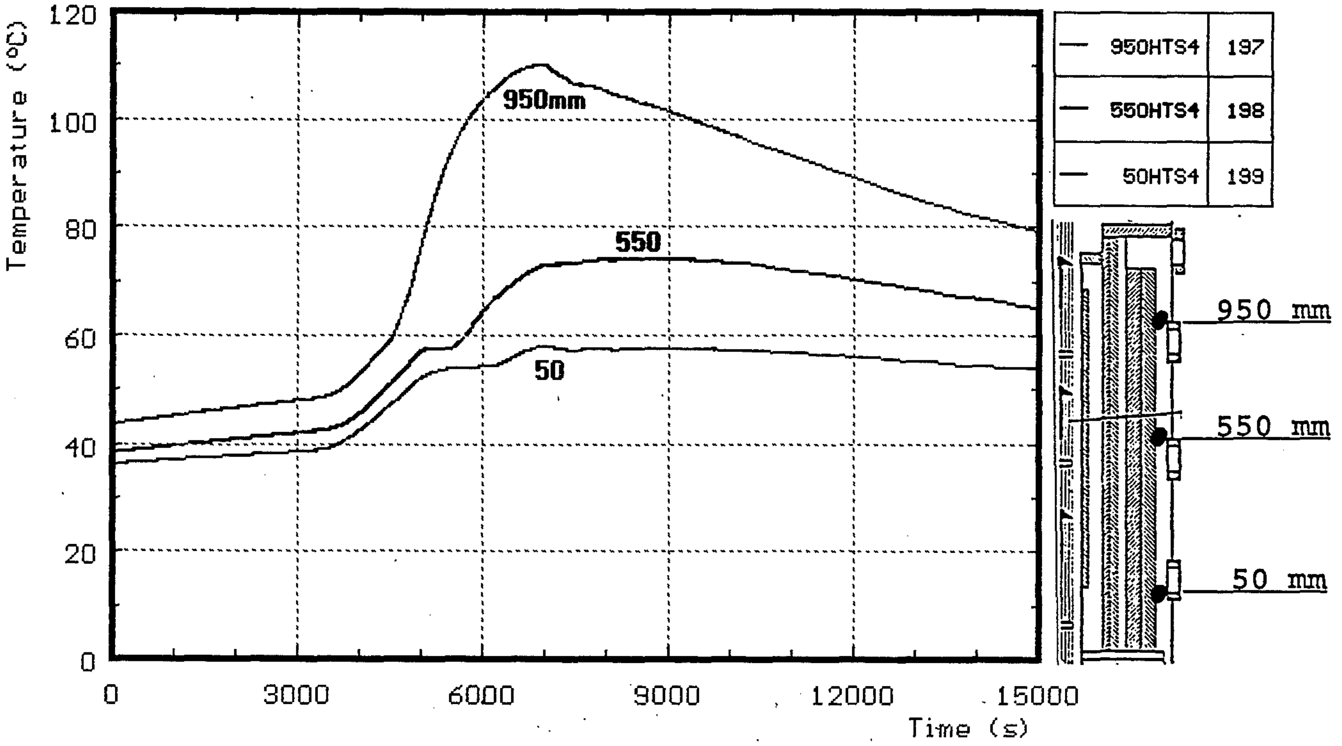

Fig. 64: CORA-28; Temperatures of HTS, Temperatures of HT shield at 293 mm radius (0-15000 s)

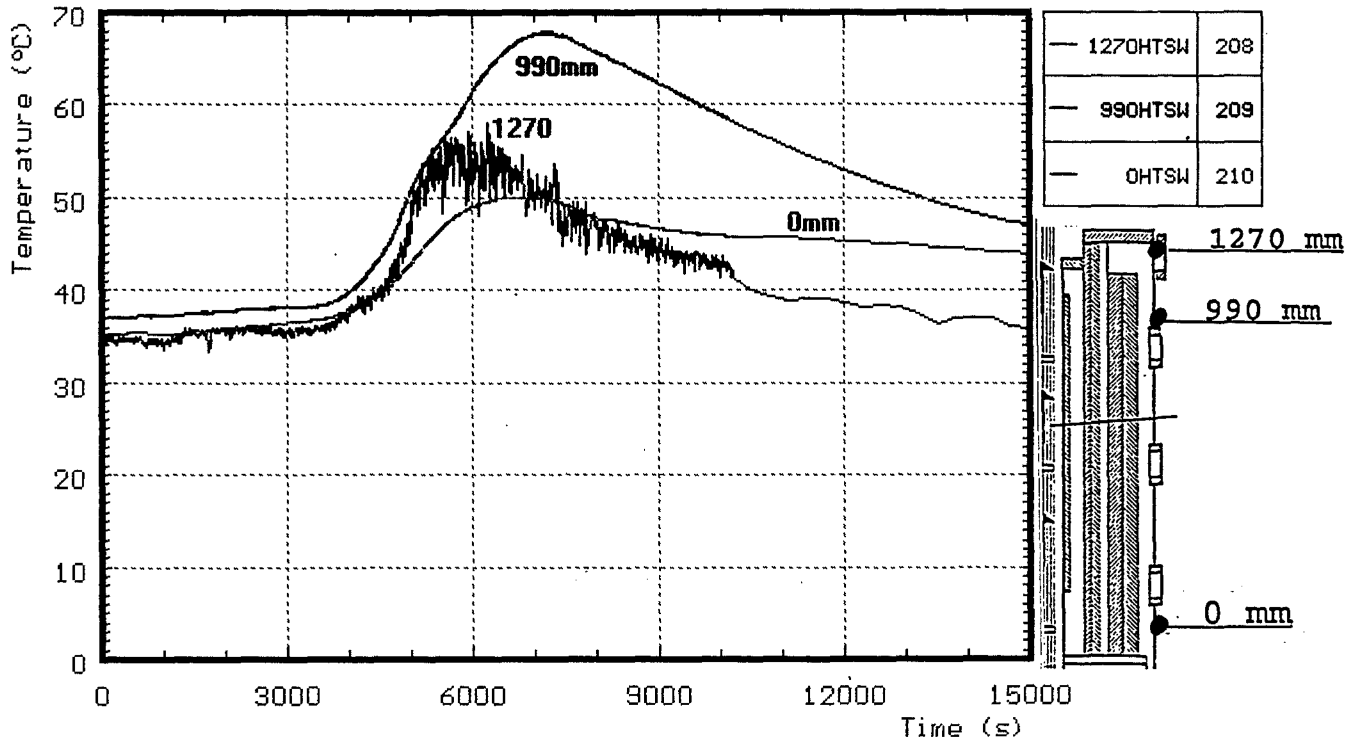

Fig. 65: CORA-28; Temperatures of HTS, Temperatures at outer surface of pressure vessel, 380 mm radius (0-15000 s)

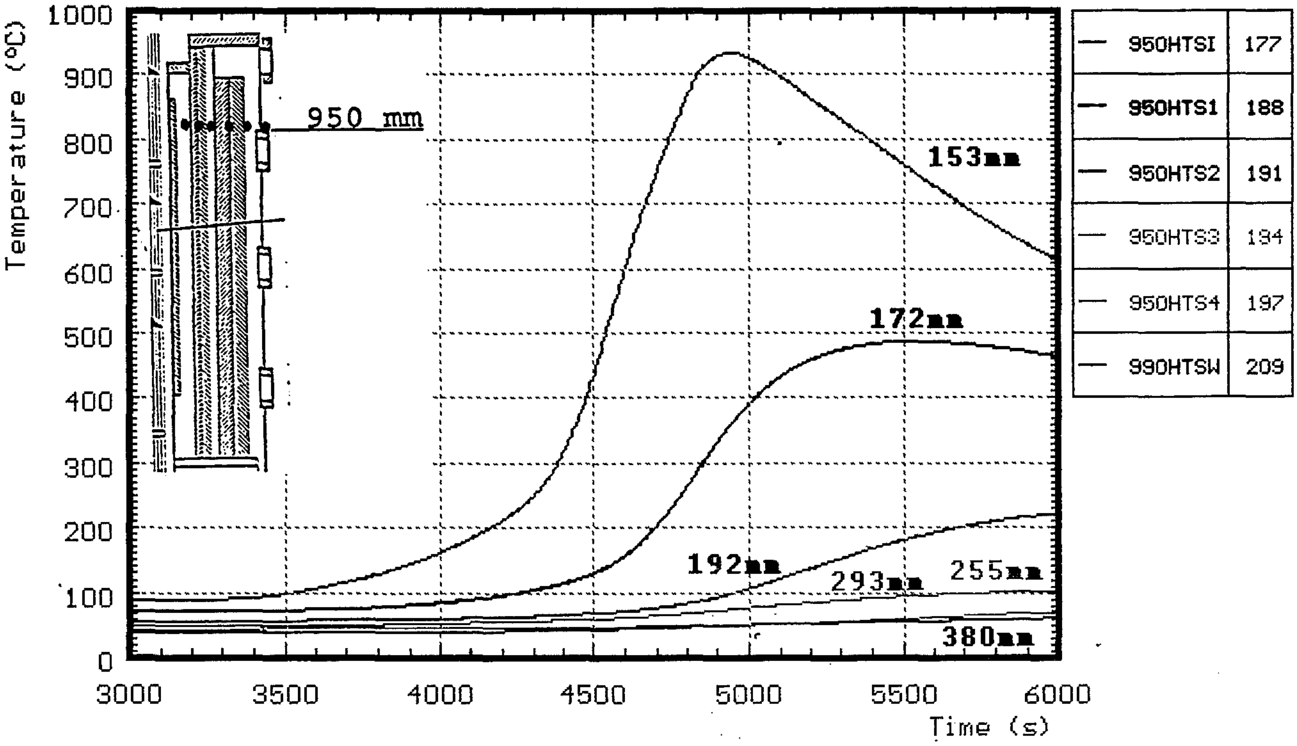

Fig. 66: CORA-28; Temperatures of HTS, Radial dependence at 950 mm elevation

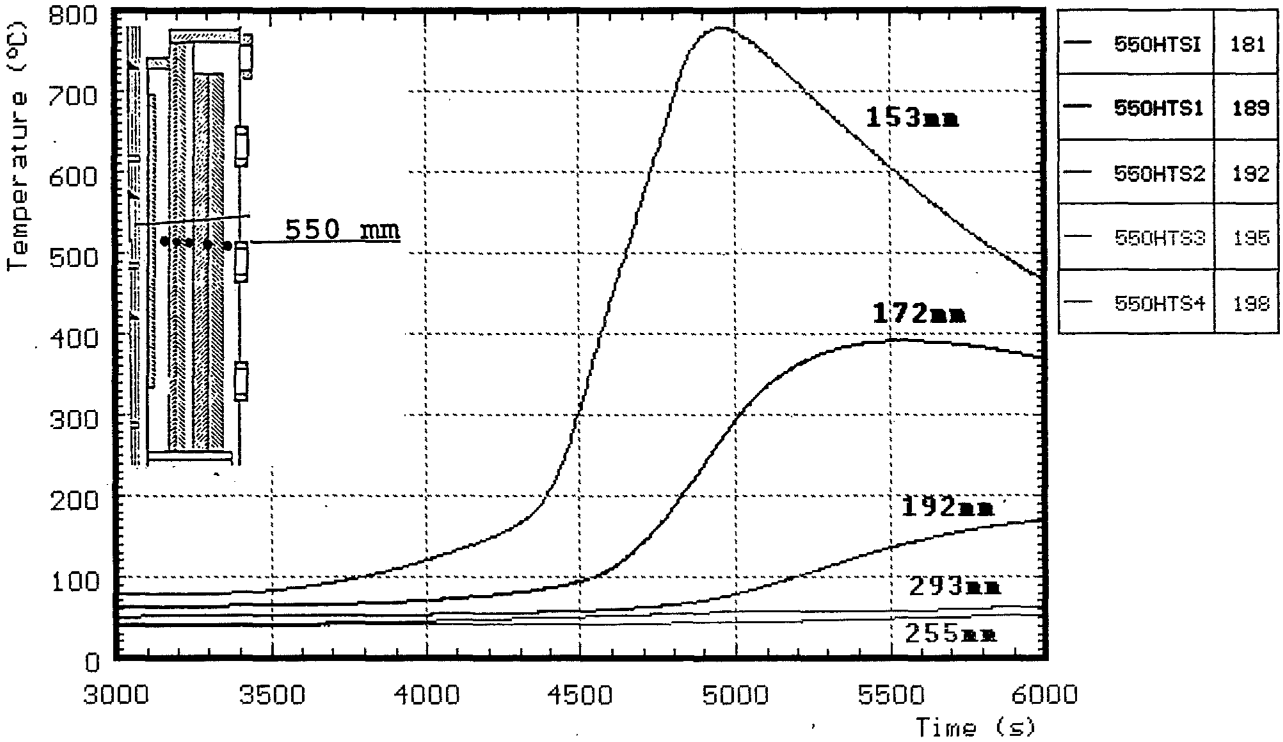

Fig. 67: CORA-28; Temperatures of HTS, Radial dependence at 550 mm elevation

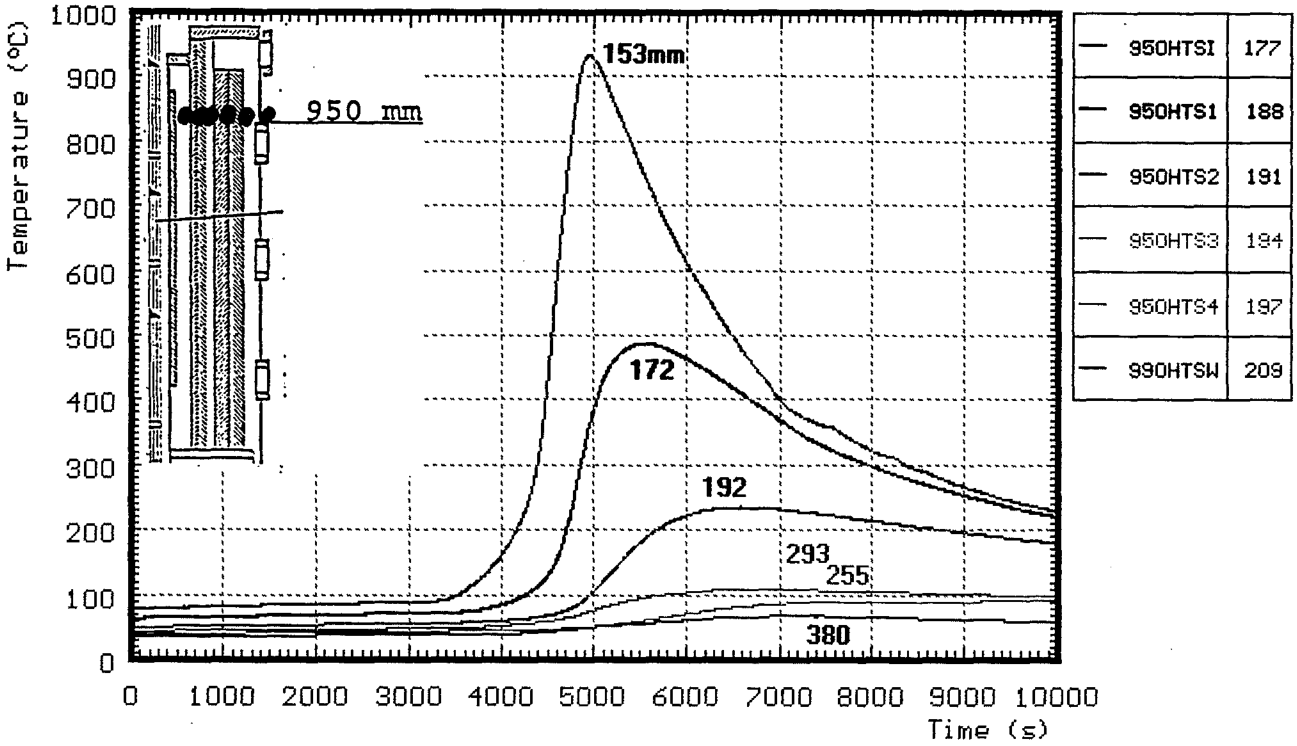

Fig. 68: CORA-28; Temperatures of HTS, Radial dependence at 950 mm elevation (0-10000 s)

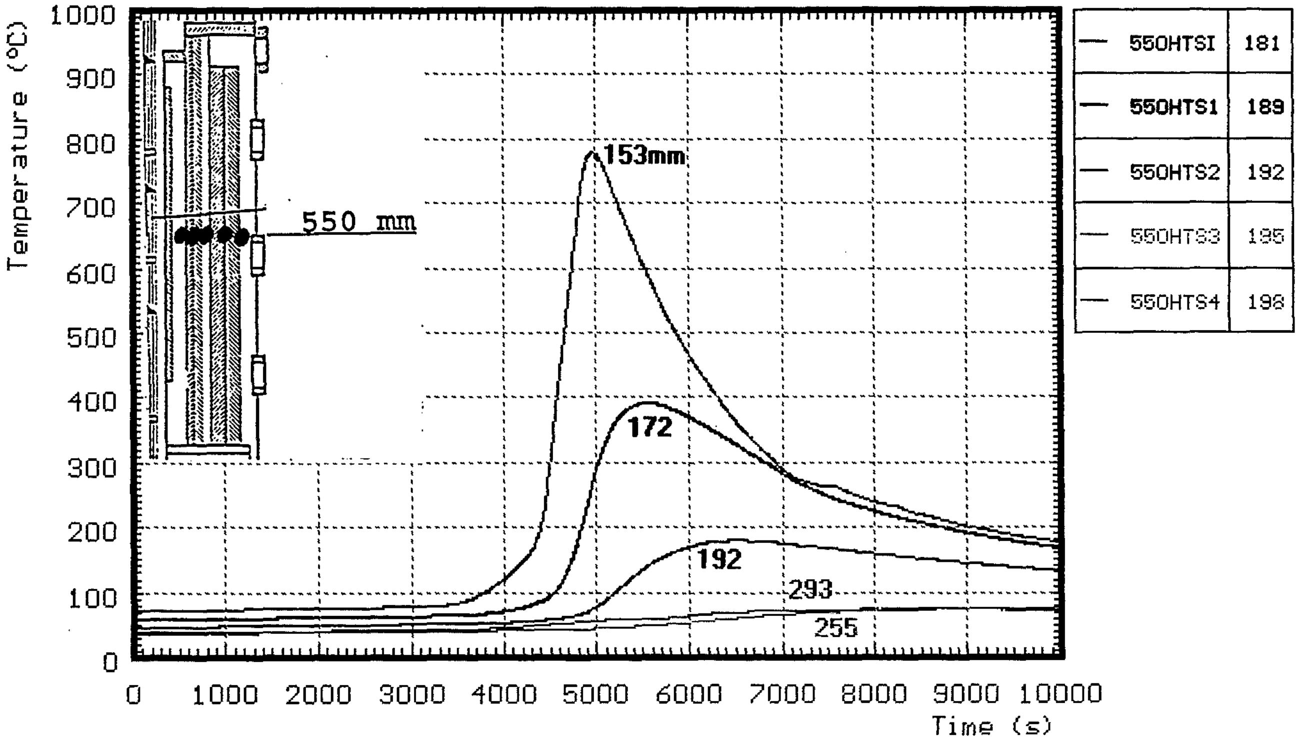

Fig. 69: CORA-28; Temperatures of HTS, Radial dependence at 550 mm elevation (0-10000 s)

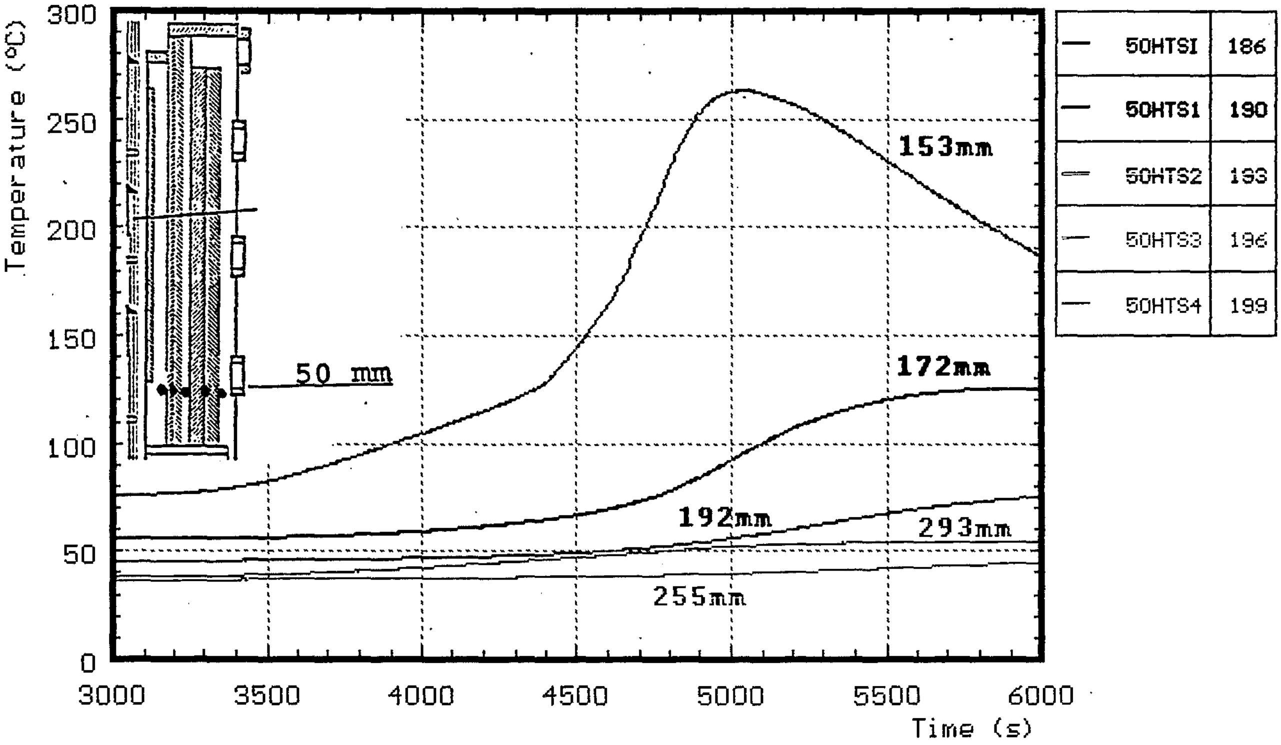

Fig. 70: CORA-28; Temperatures of HTS, Radial dependence at 50 mm elevation (3000-6000 s)

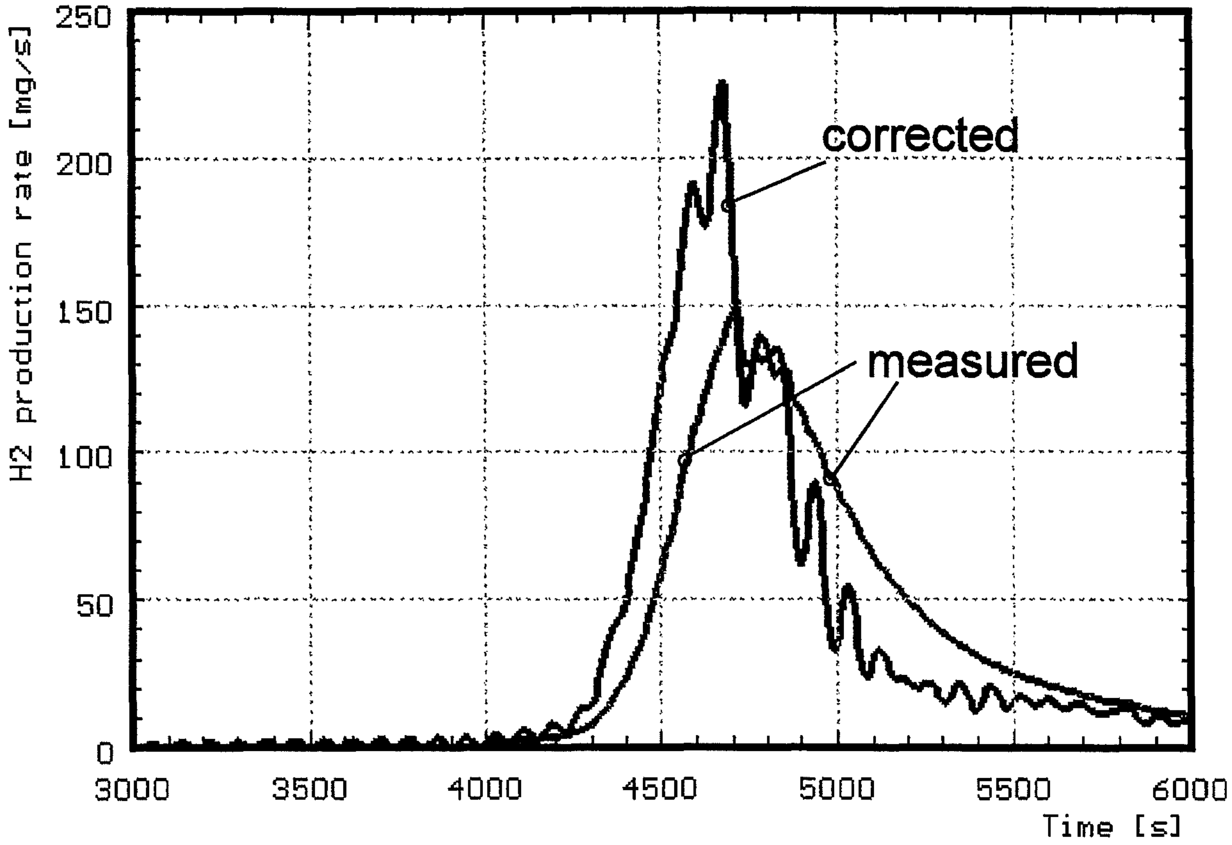

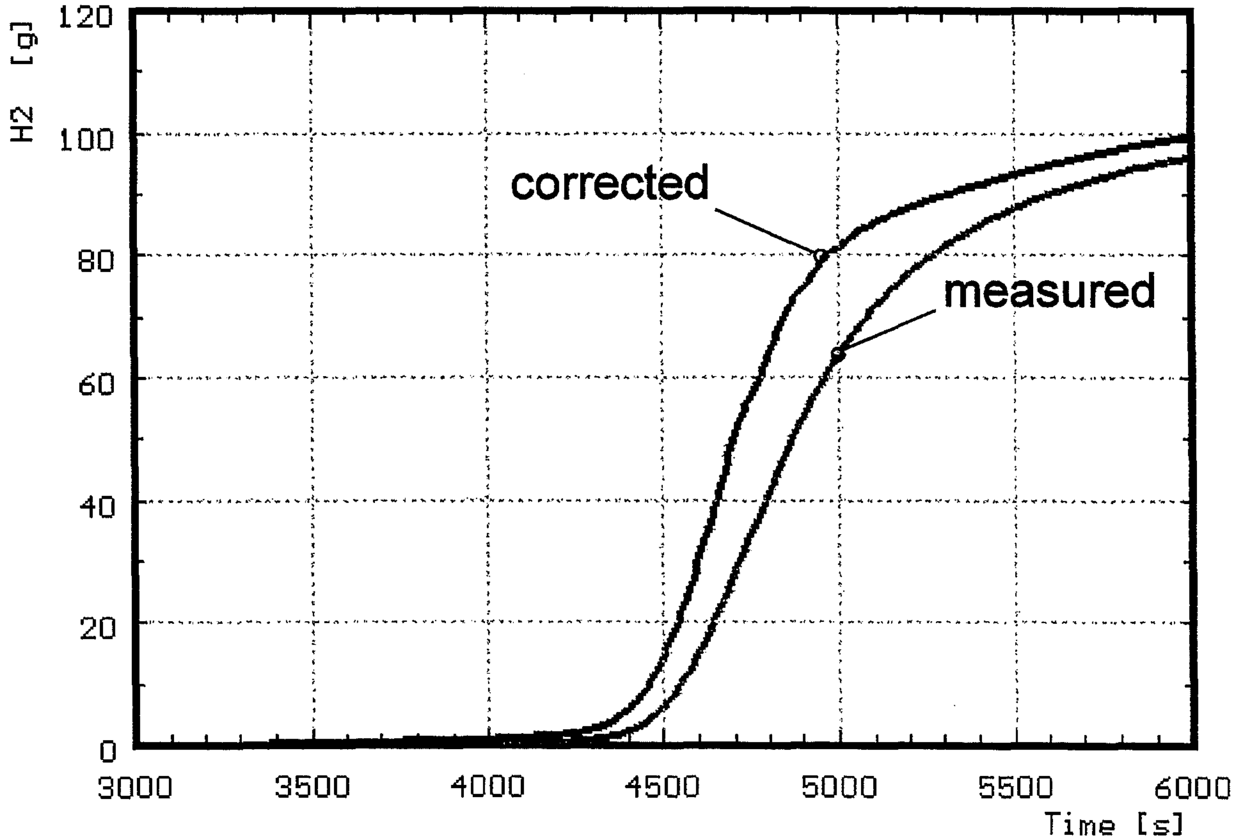

Fig. 71: Hydrogen production in test CORA-28; production rate (top) and integral values (bottom)

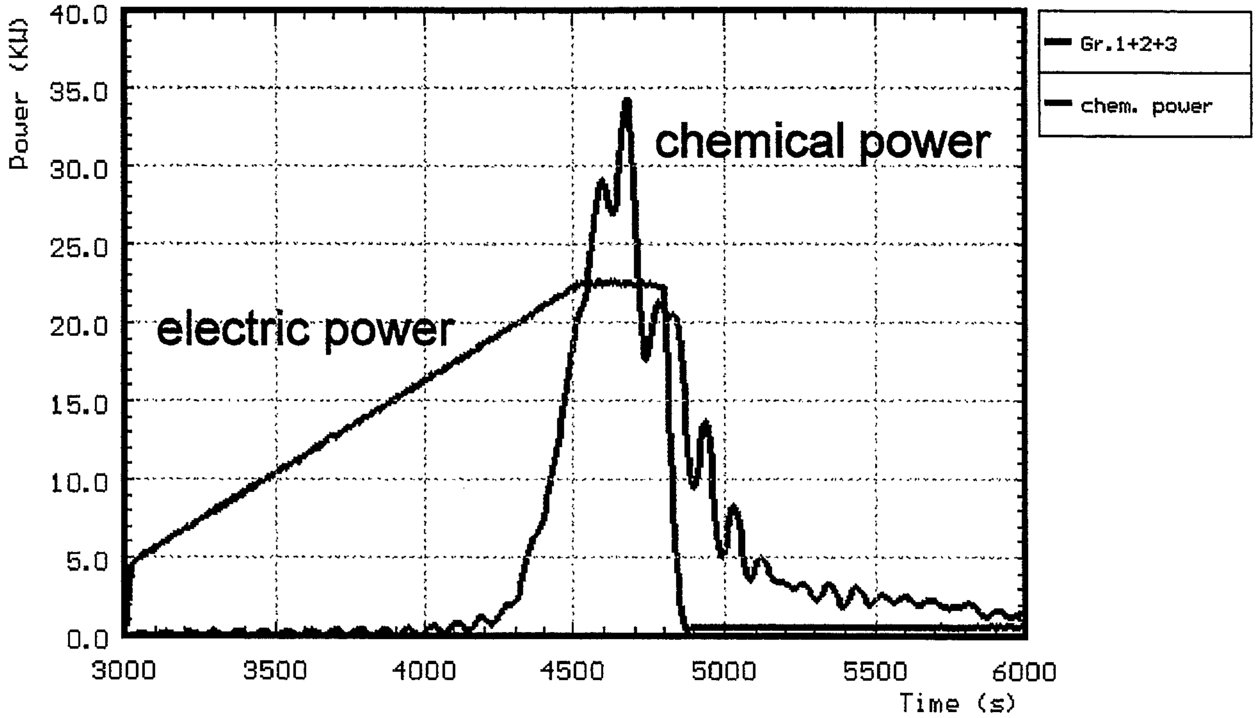

Fig. 72: CORA-28; Comparison of chemical and electric power

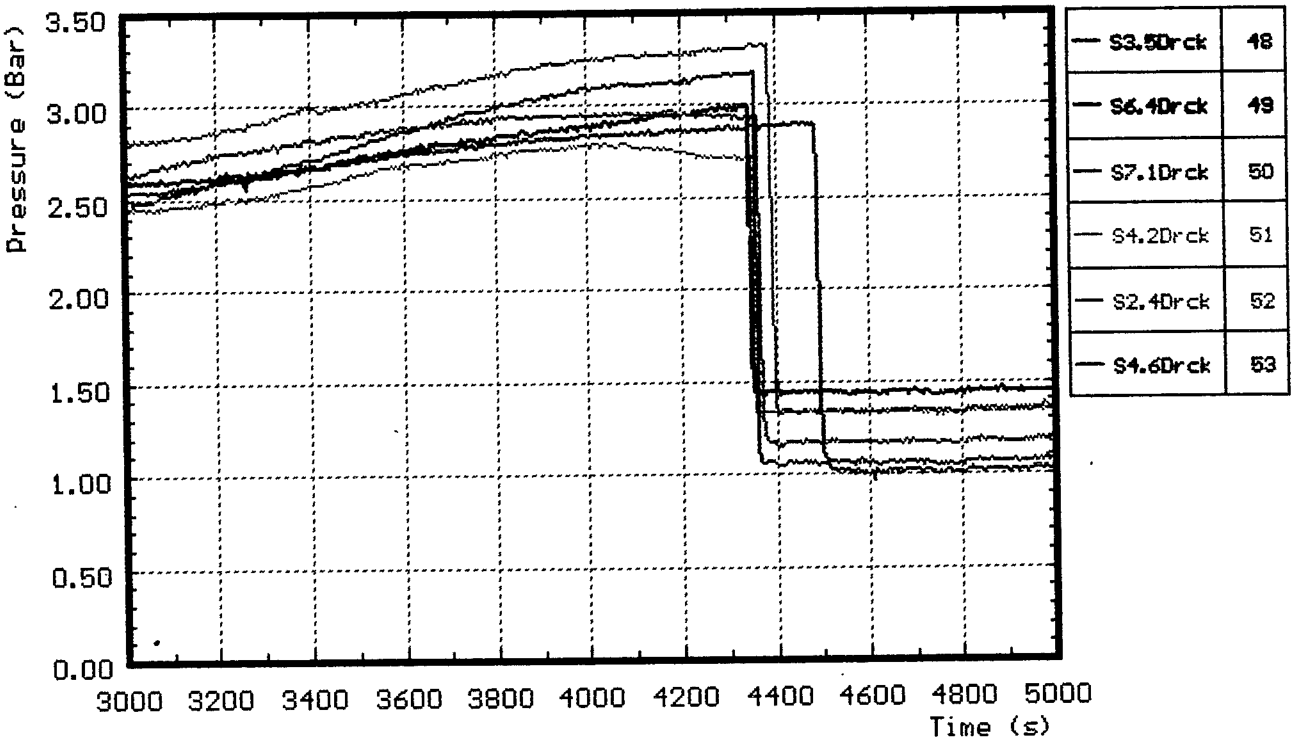

Fig. 73: CORA-28; Internal pressure of fuel rod simulators

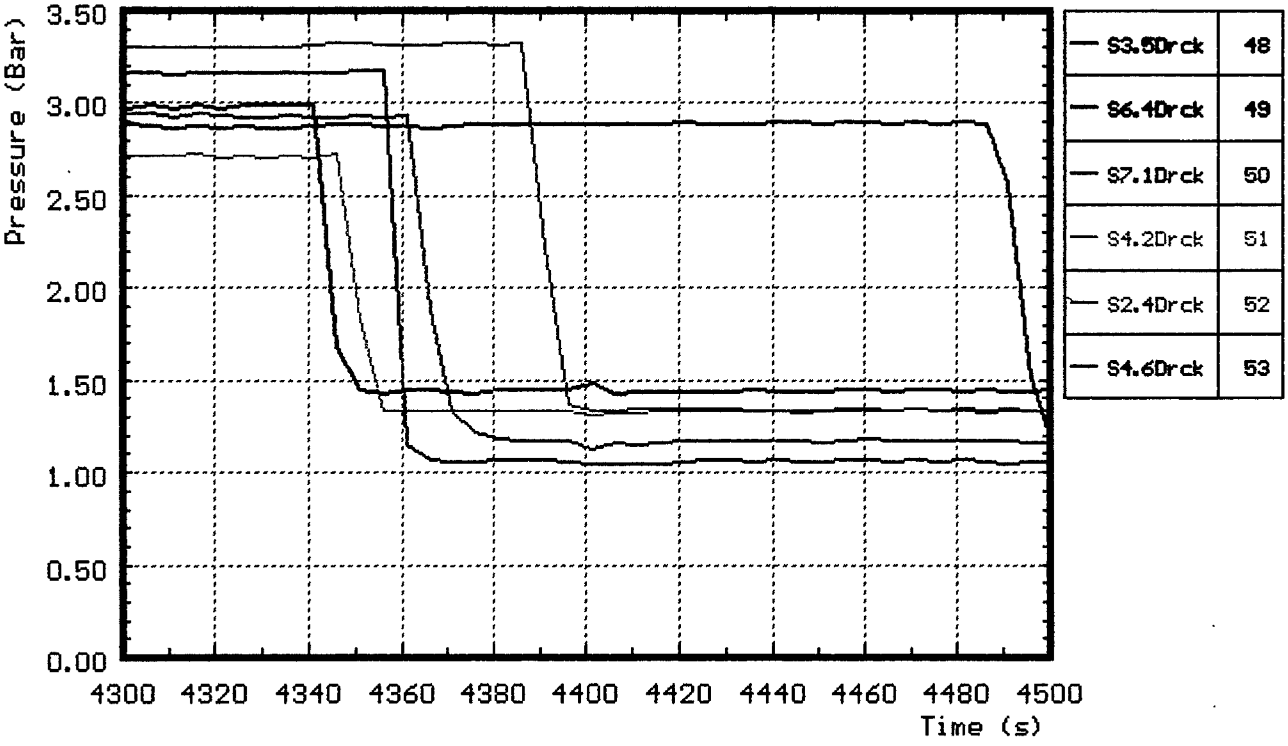

Failure time:

rod 6.4:	**4340 s**
rod 4.2:	**4345 s**
rod 4.6:	**4355 s**
rod 7.1:	**4360 s**
rod 2.4:	**4385 s**
rod 3.5:	**4485 s**

Fig. 74: CORA-28; Determination of failure time by pressure loss measurement

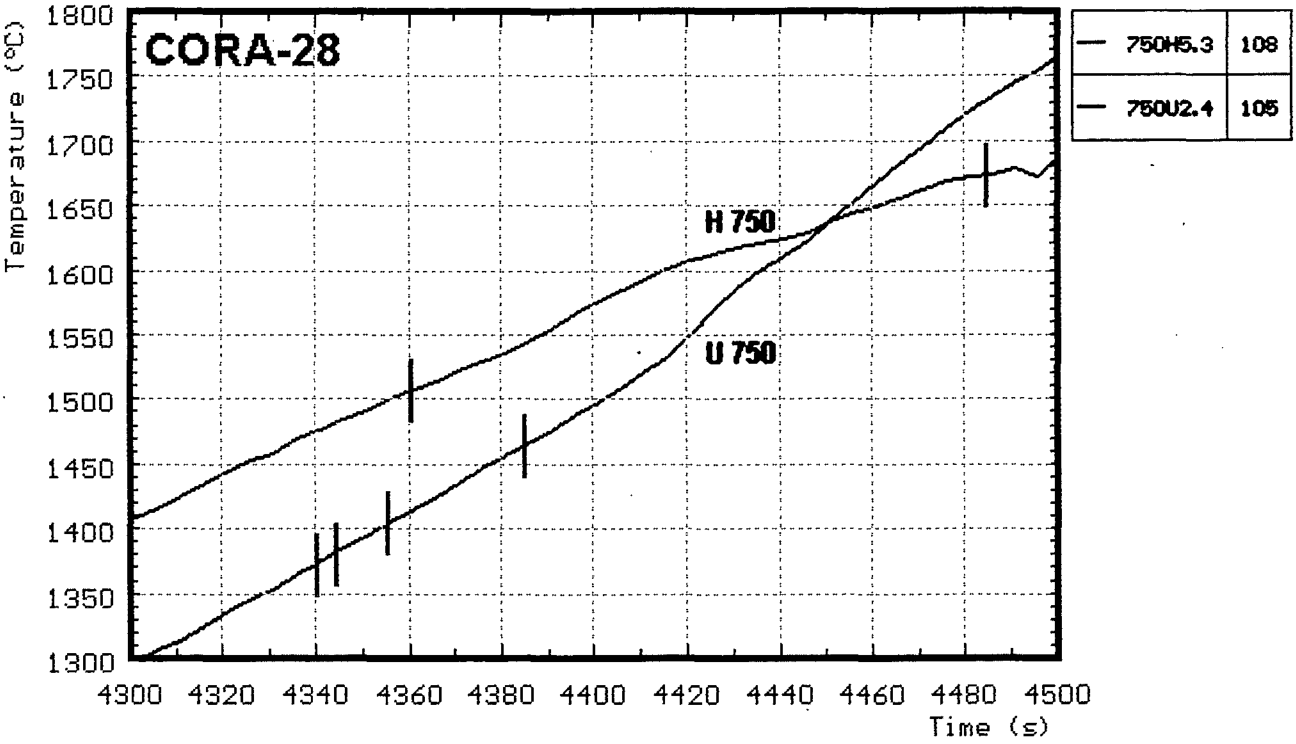

Failure temperatures:

rod 6.4:	1370 °C
rod 4.2:	1380 °C
rod 4.6:	1400 °C
rod 7.1:	1500 °C
rod 2.4:	1470 °C
rod 3.5:	1670 °C

Fig. 75: CORA-28; Temperatures at time of pressure loss

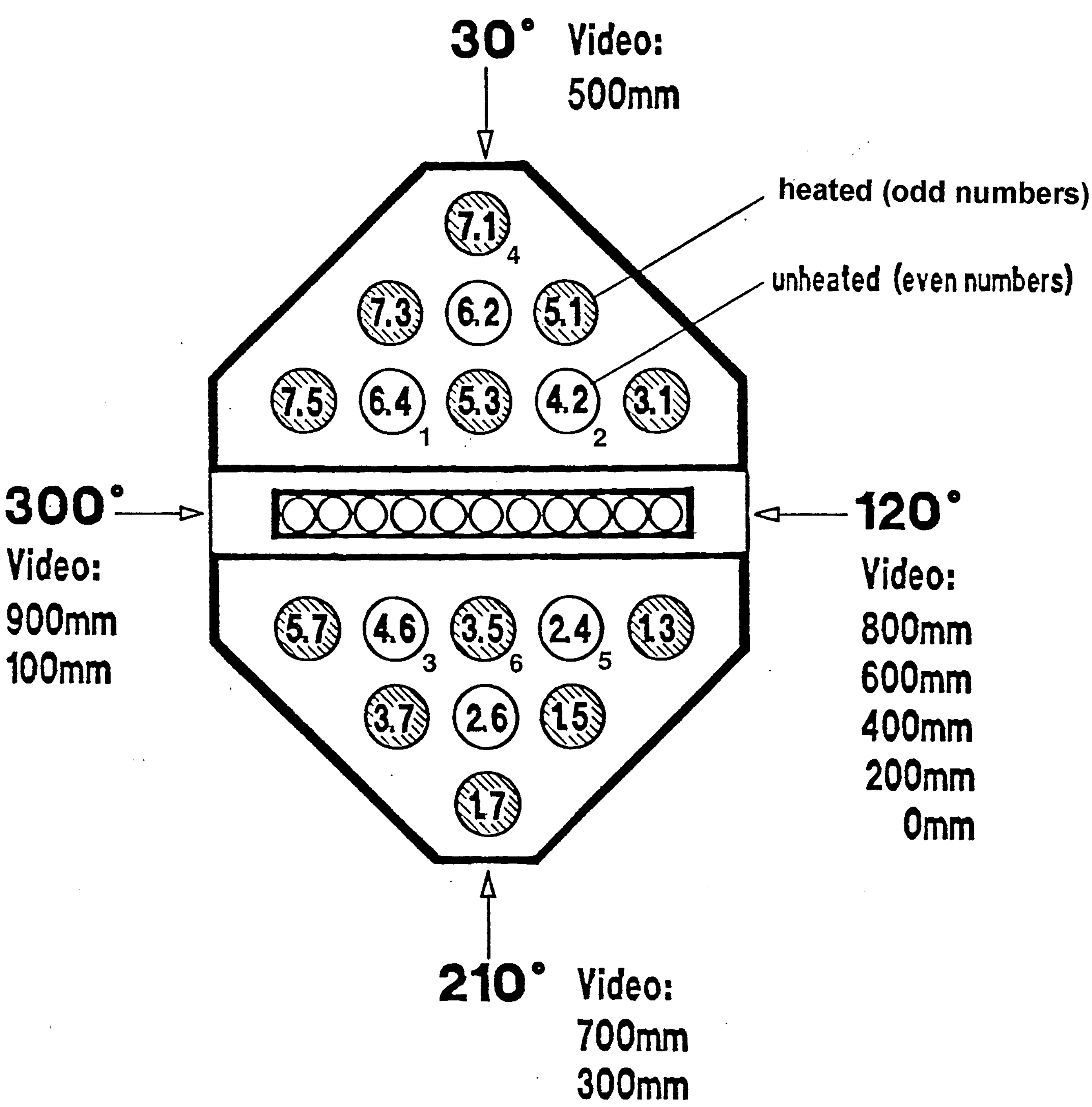

Heating group 1: 1.3, 1.5, 3.1, 5.1
" " 2: 3.7, 5.7, 7.3, 7.5
" " 3: 3.5, 5.3, 1.7, 7.1

Fig. 76: CORA-28; Position and sequence of failed fuel rod simulators

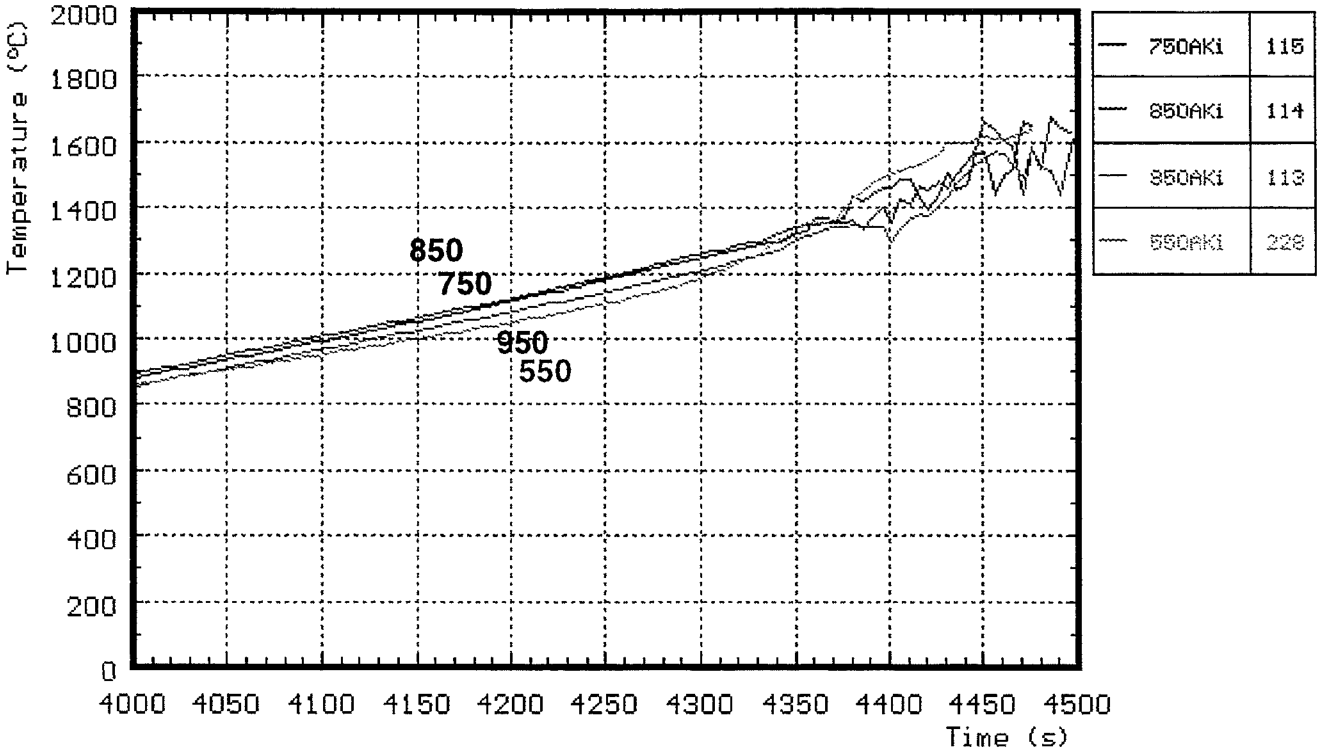

Fig. 77: **CORA-28; Irregularities in the temperatures of absorber blade used for estimation of absorber failure time**

c28_077.cdr

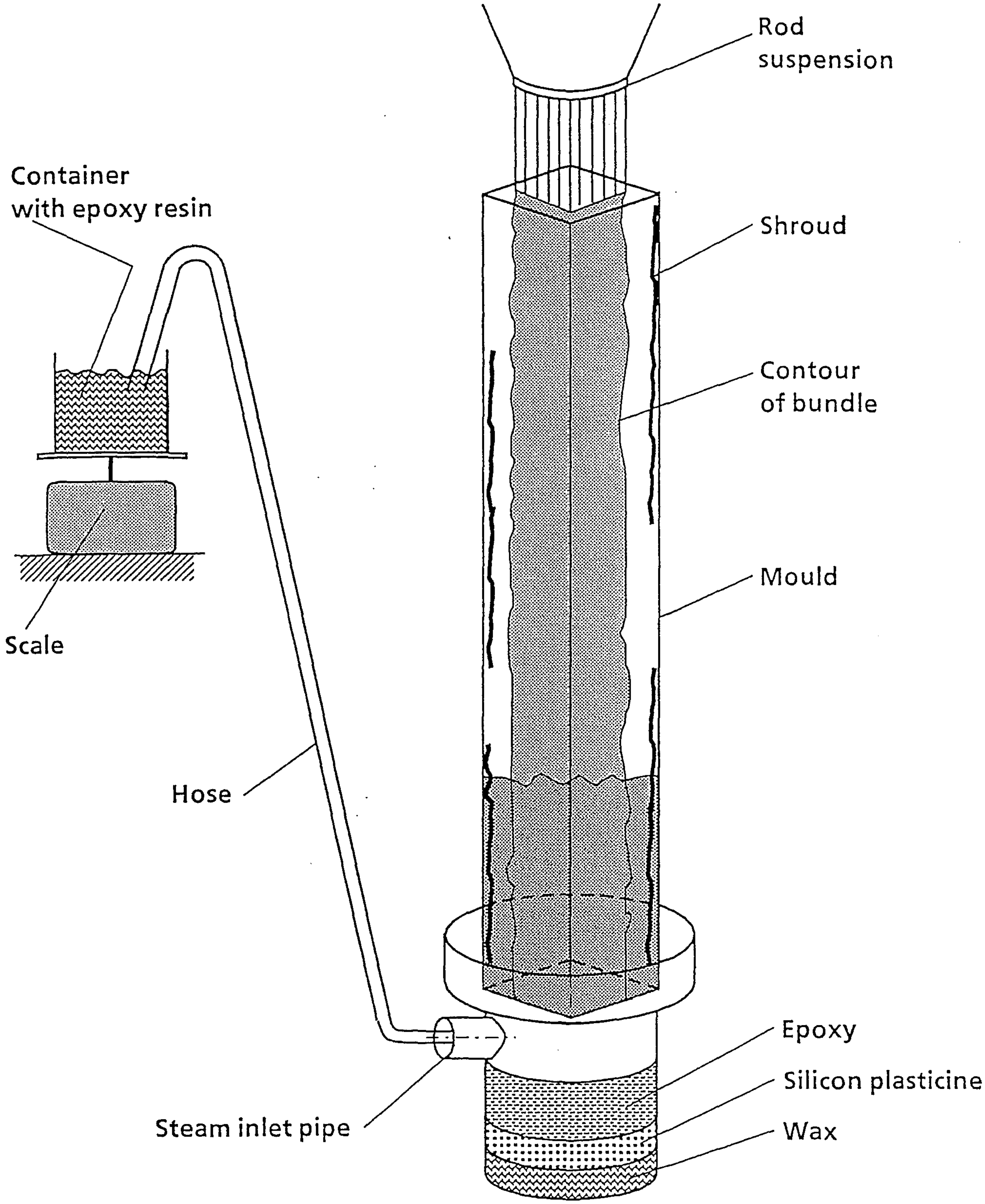

Fig. 80: CORA-28 Epoxying process of the tested bundle

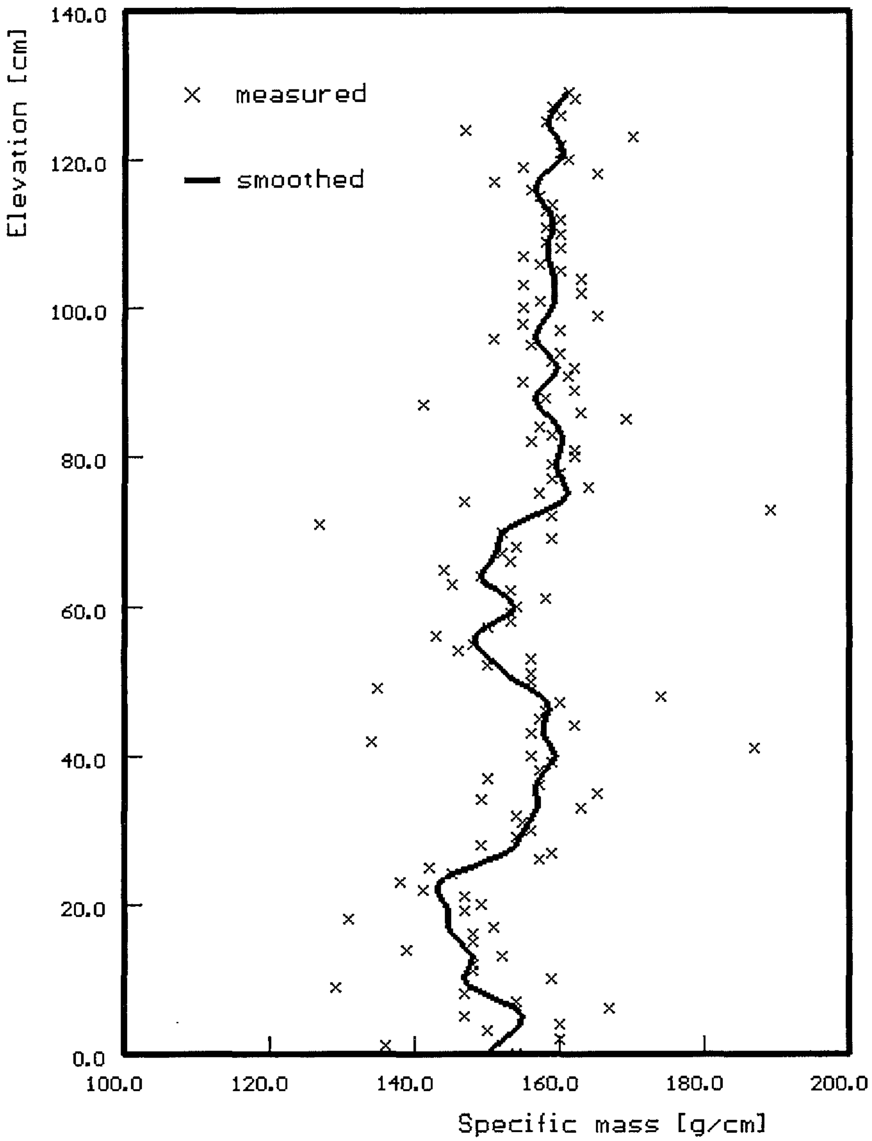

Fig. 81: CORA-28; Axial distribution of the bundle fill-up with epoxy resin

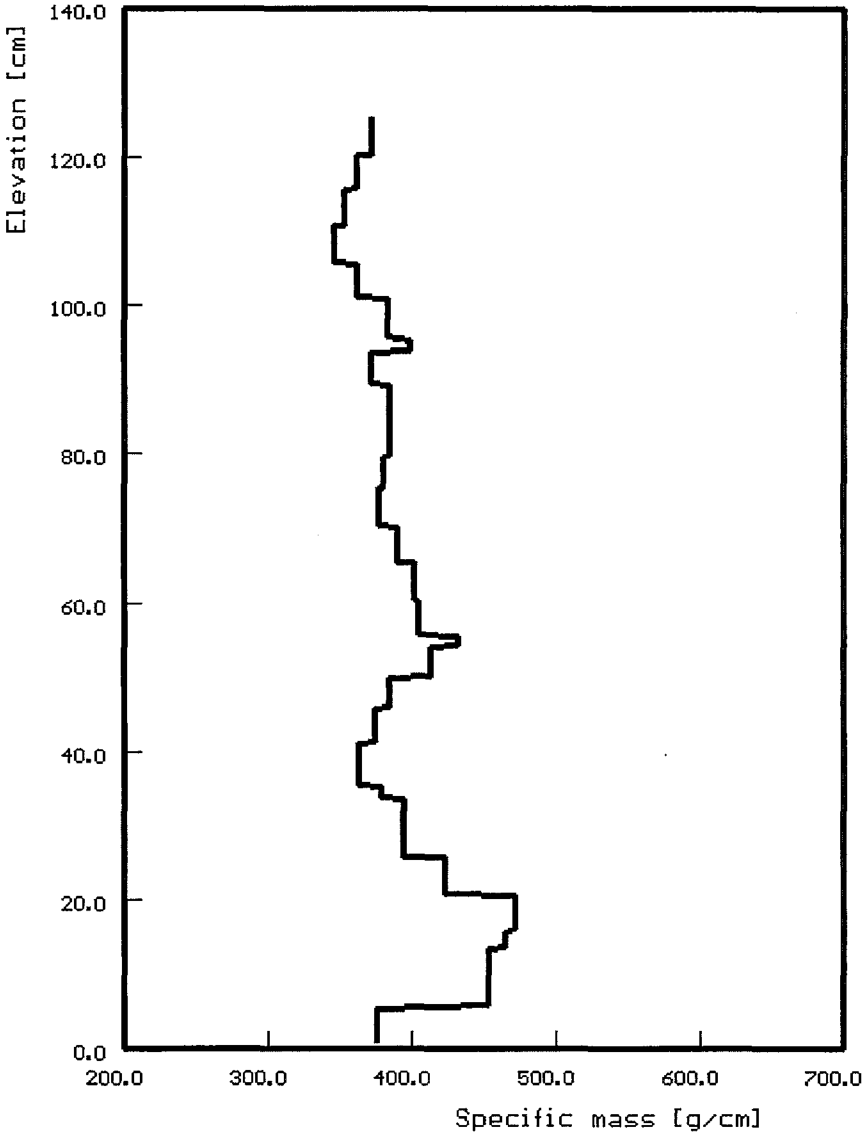

Fig. 82: CORA-28; Axial mass distribution of bundle segments filled with epoxy resin

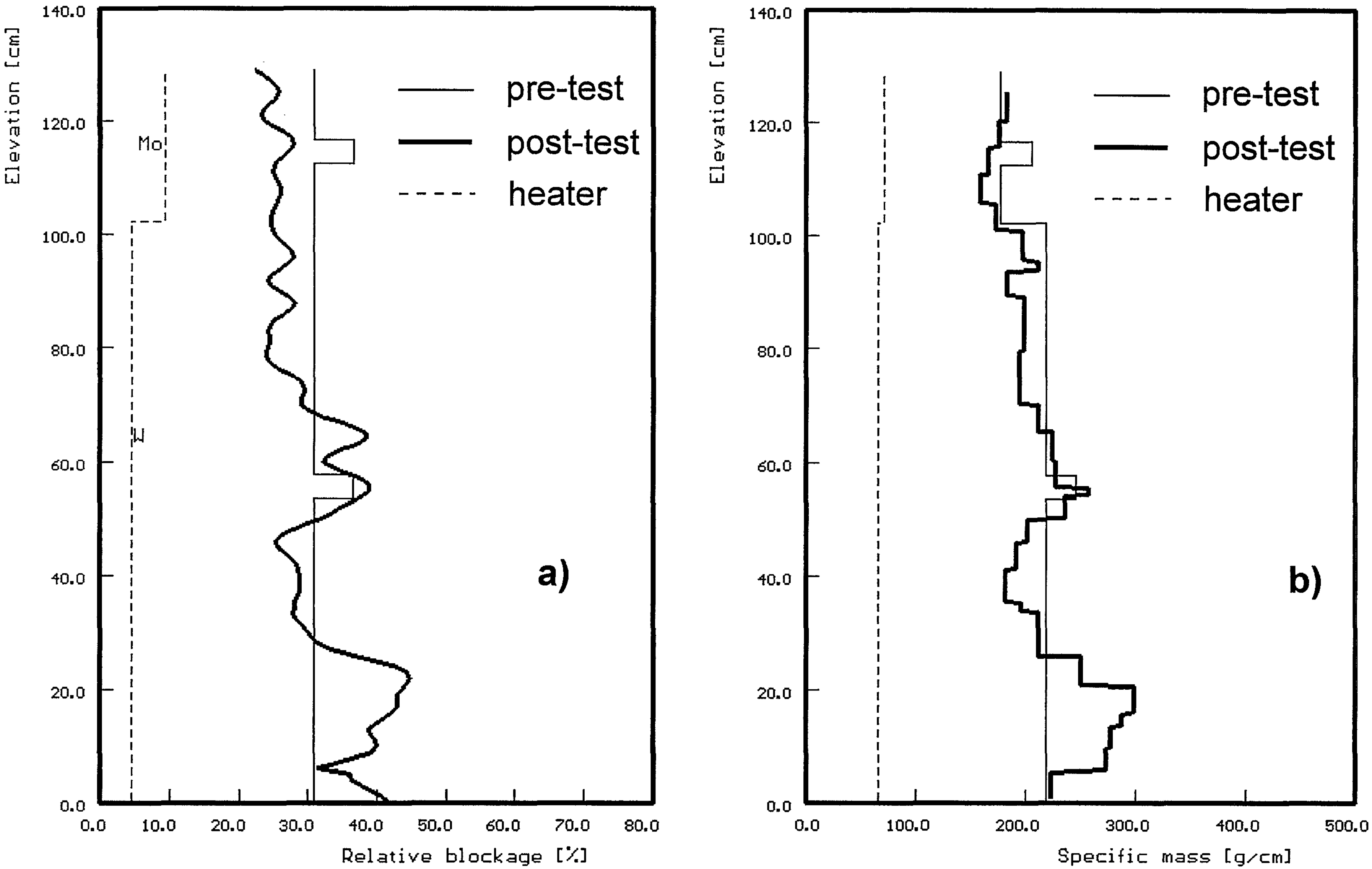

Fig. 83: CORA-28; Comparison of axial mass distribution (b) and axial volume distribution (a) after the test

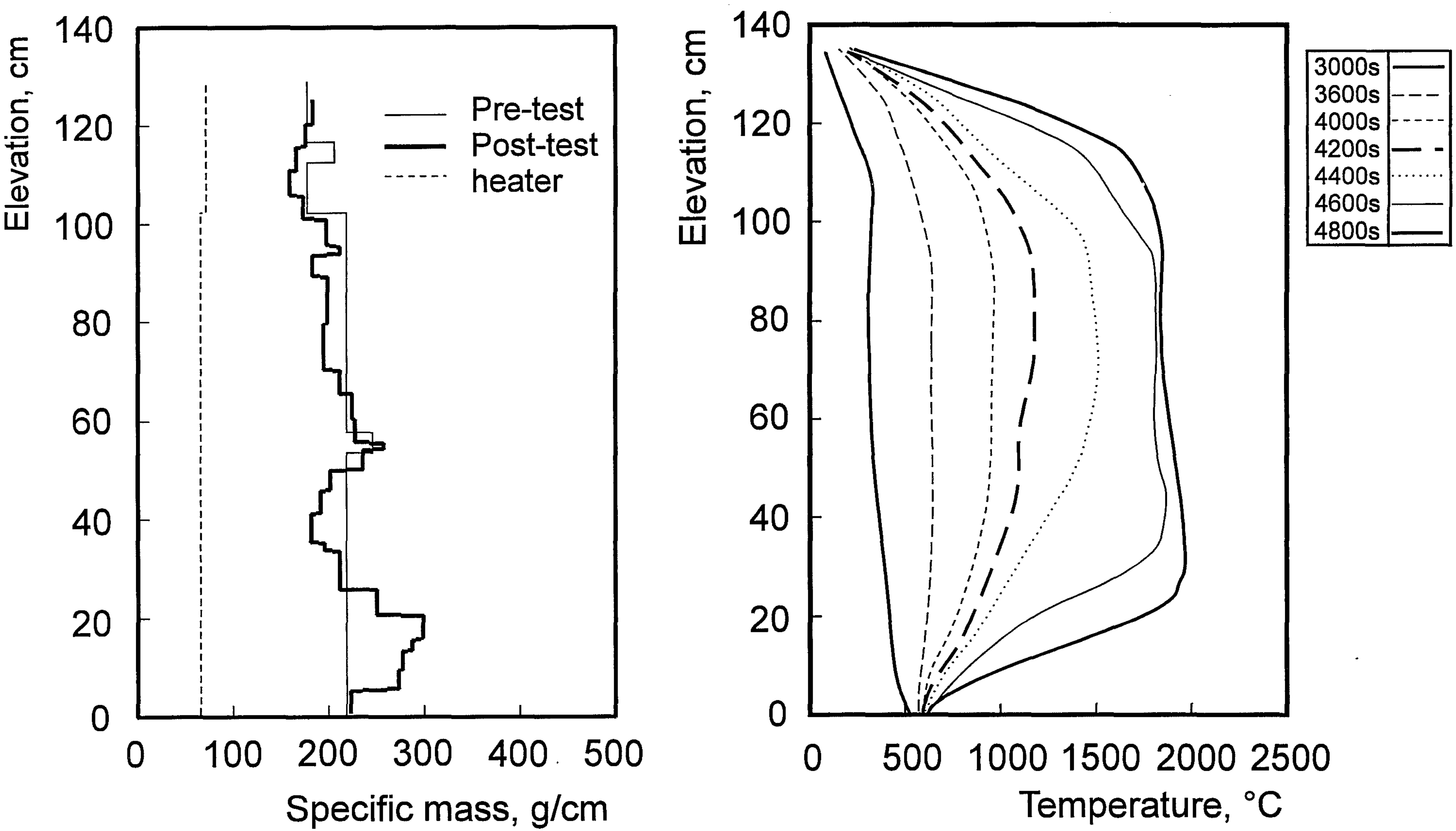

Fig. 84: CORA-28; Axial mass distribution after the test and axial temperature distribution during the test

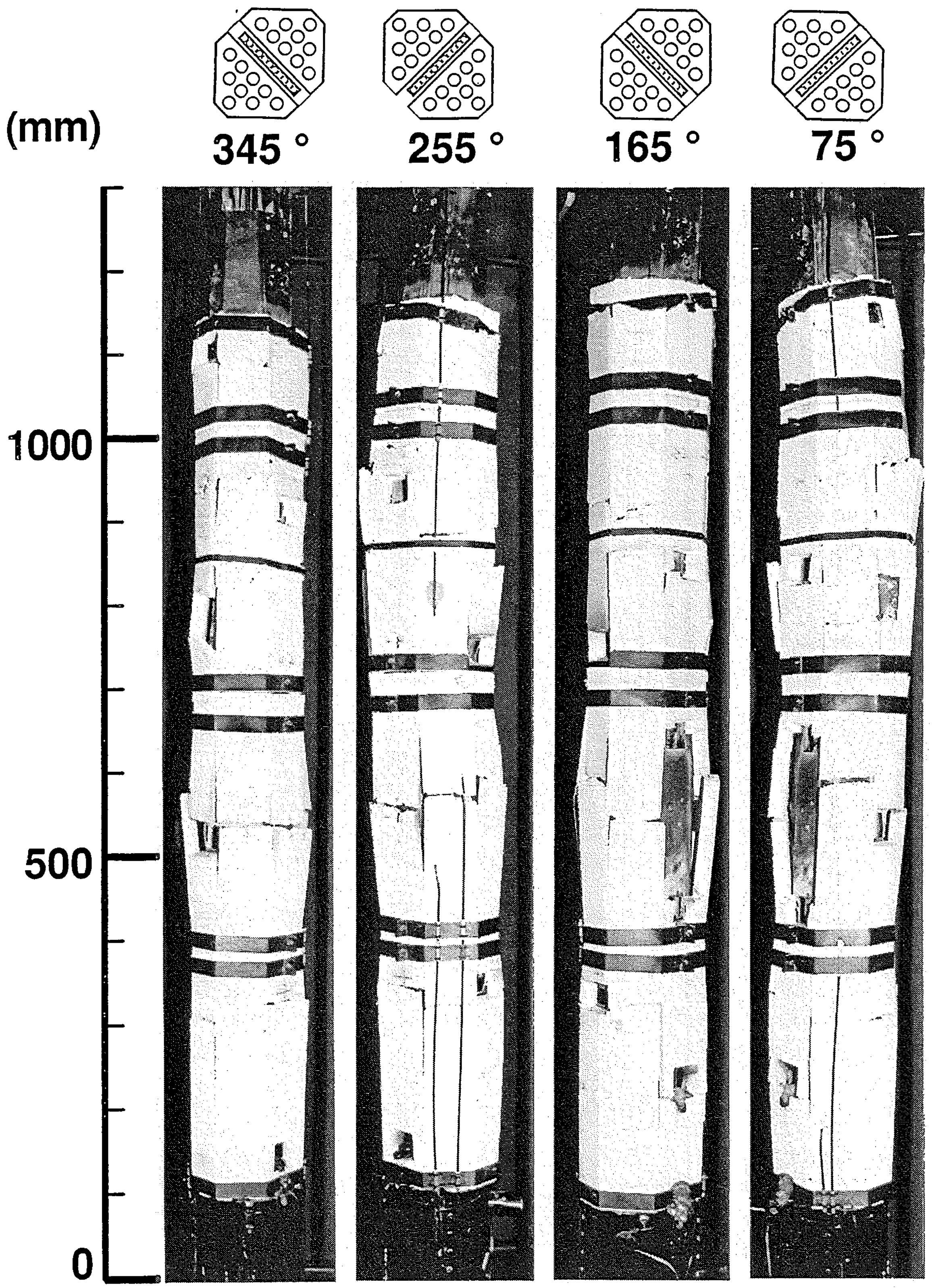

Fig. 85: CORA-28; Posttest appearance of the entire bundle length (with shroud insulation), 345°, 255°, 165°, 75° orientation

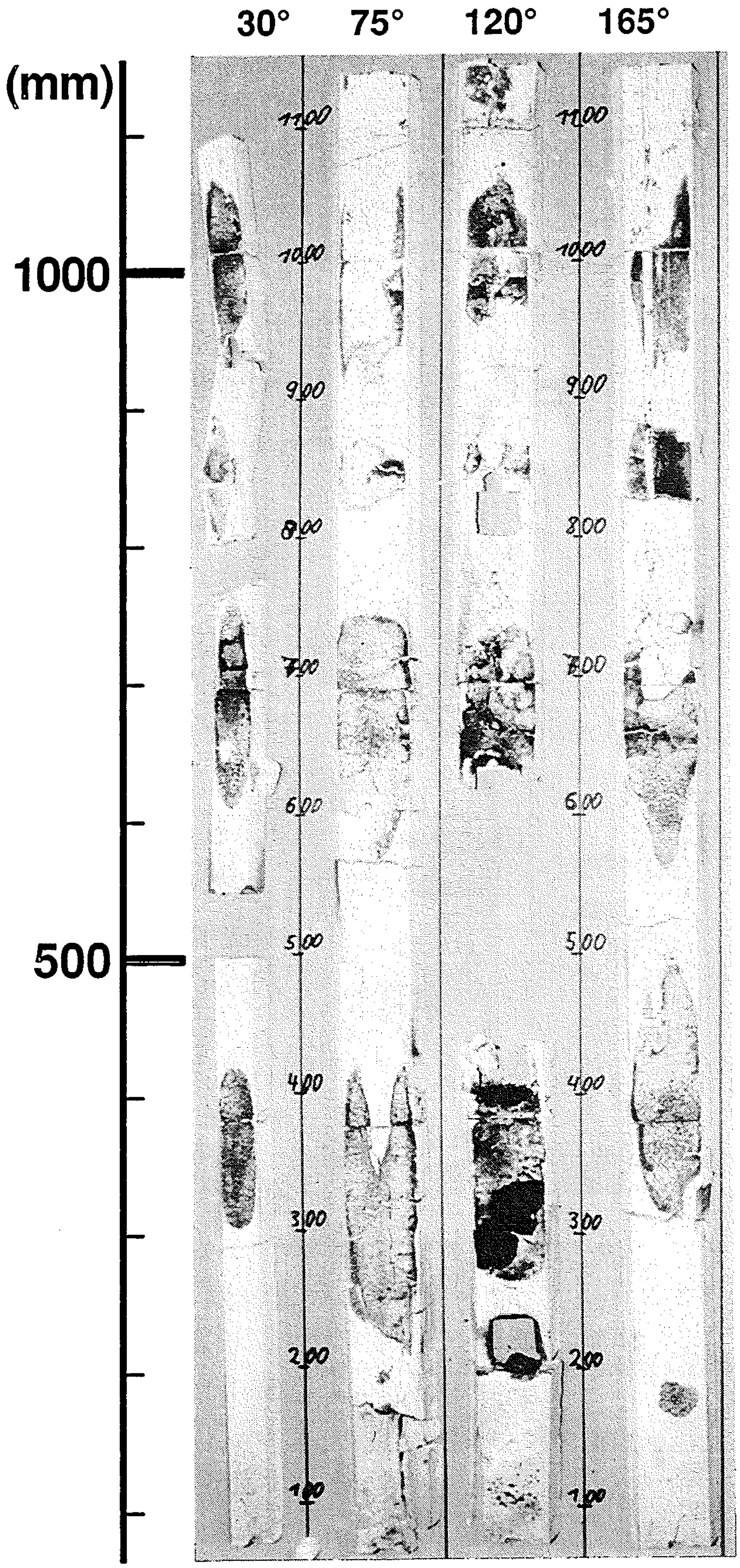

Fig. 86: CORA-28; Posttest view of the inner side of the shroud insulation; 30°, 75°, 120° and 165° orientation

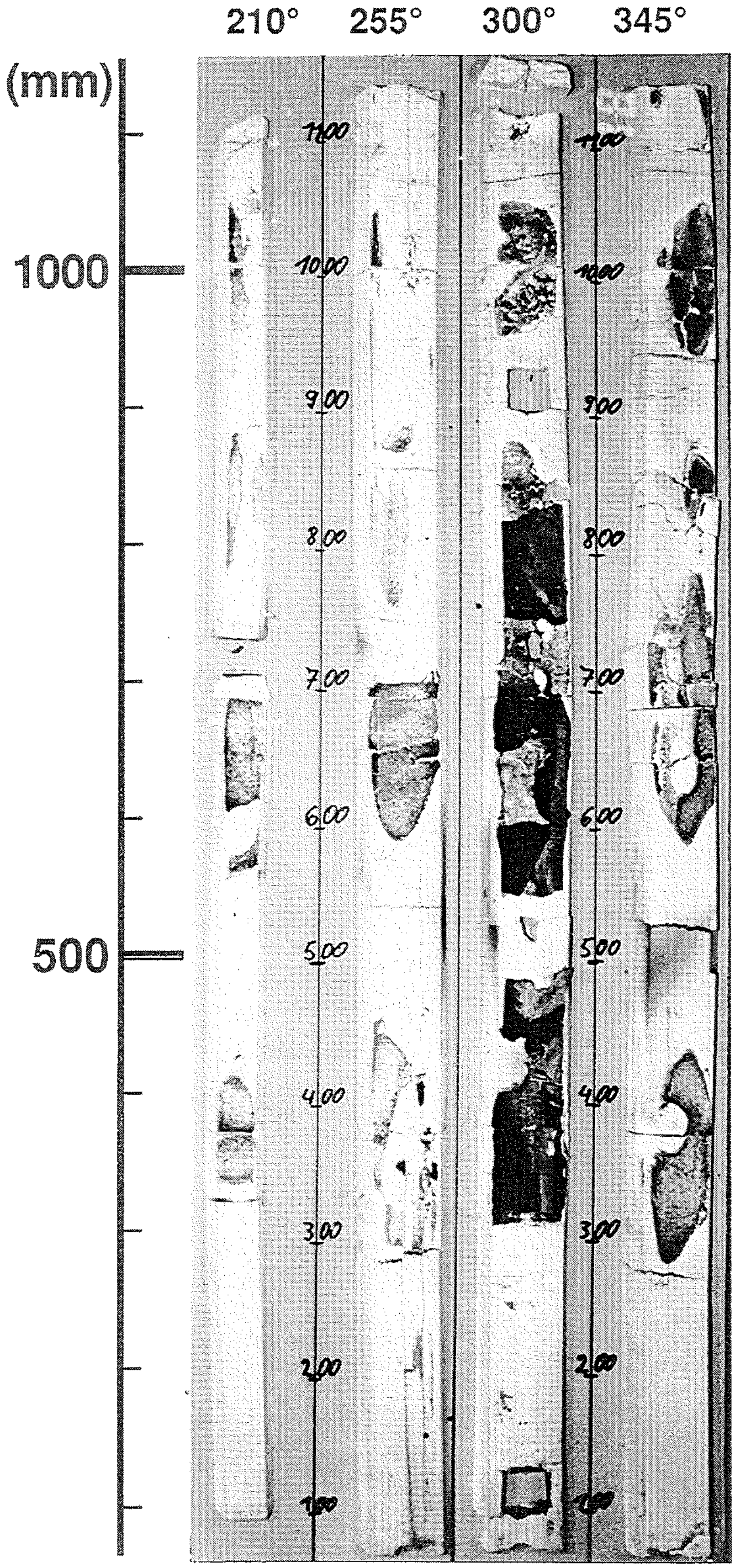

Fig. 87: CORA-28; Posttest view of the inner side of the shroud insulation; 210°, 255°, 300° and 345° orientation

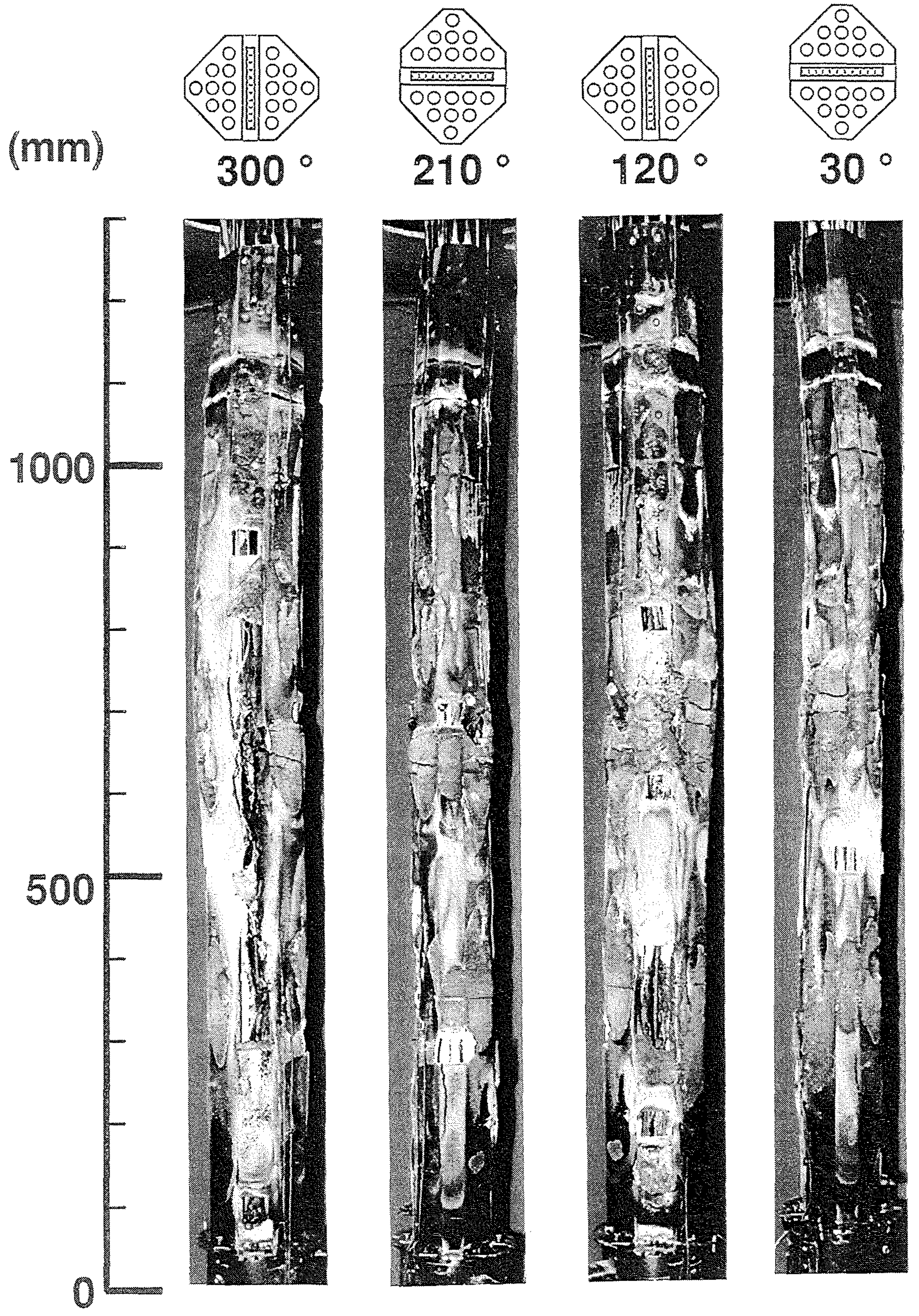

Fig. 88: CORA-28; Posttest appearance of the entire bundle length after removal of the shroud insulation; 300°, 210°, 120°, 30° orientation

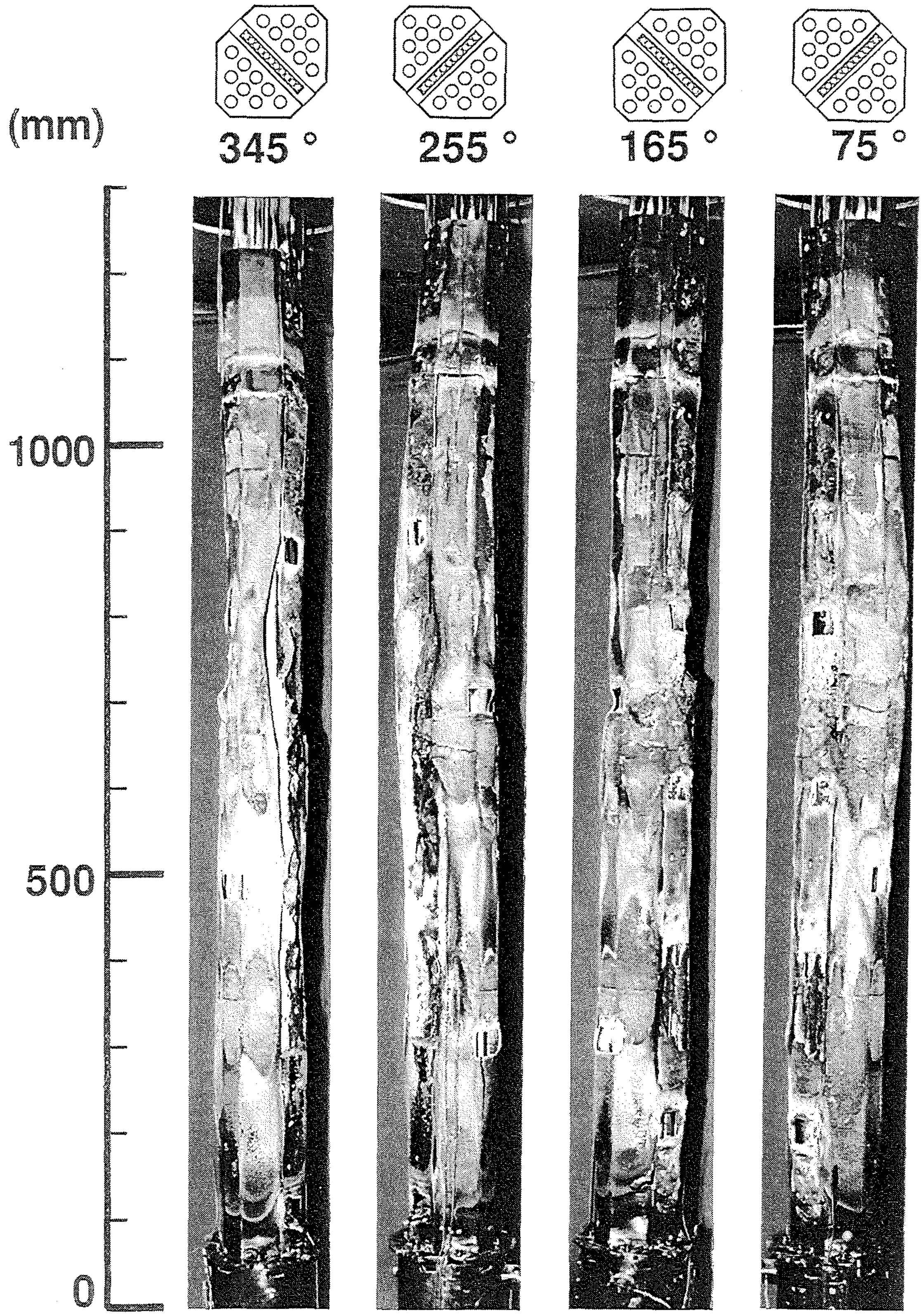

Fig. 89: CORA-28; Posttest appearance of the entire bundle length after removal of the shroud insulation; 345°, 255°, 165°, 75° orientation

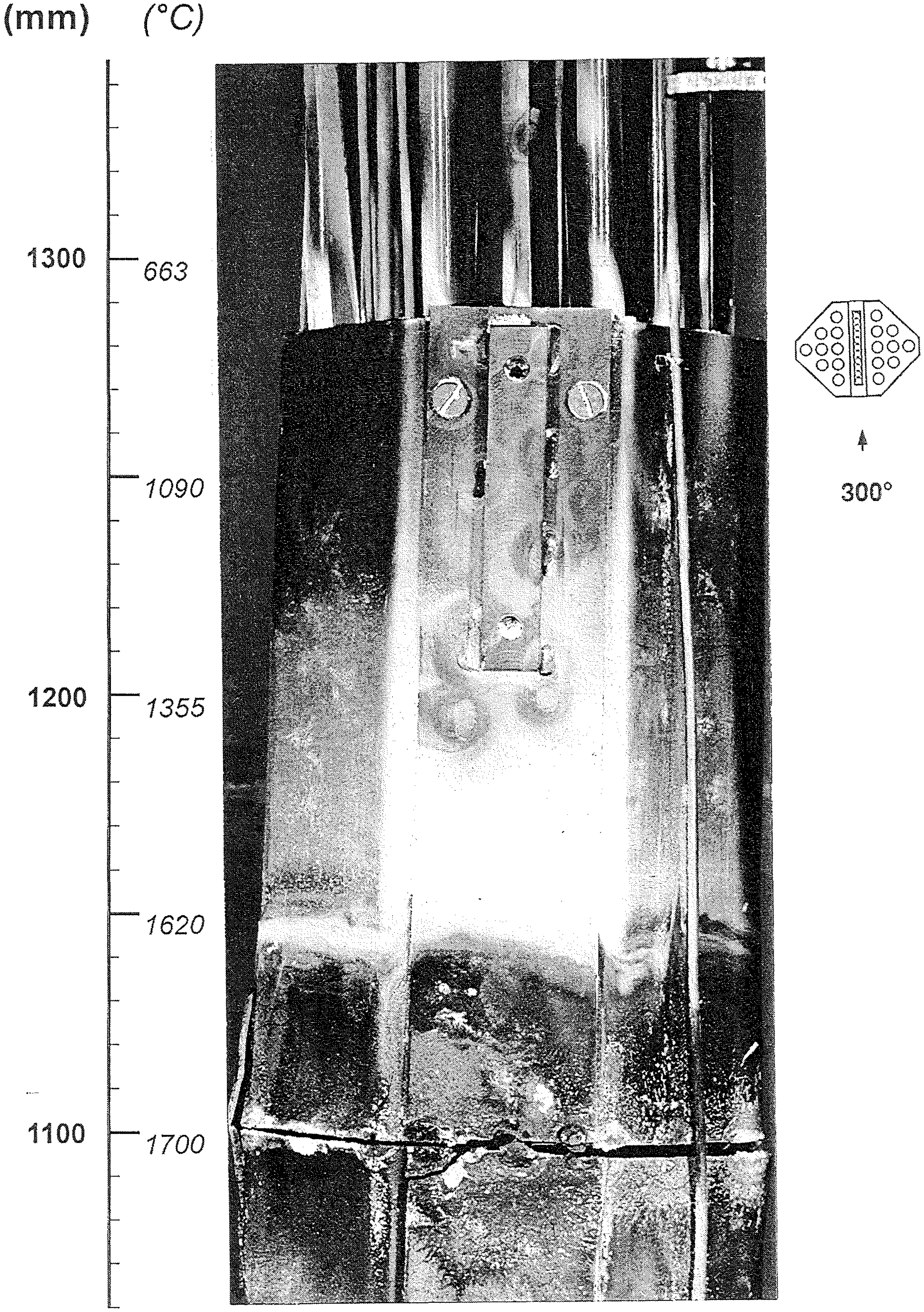

Fig. 90: CORA-28; Posttest view; 300° orientation; 1000 - 1400 mm

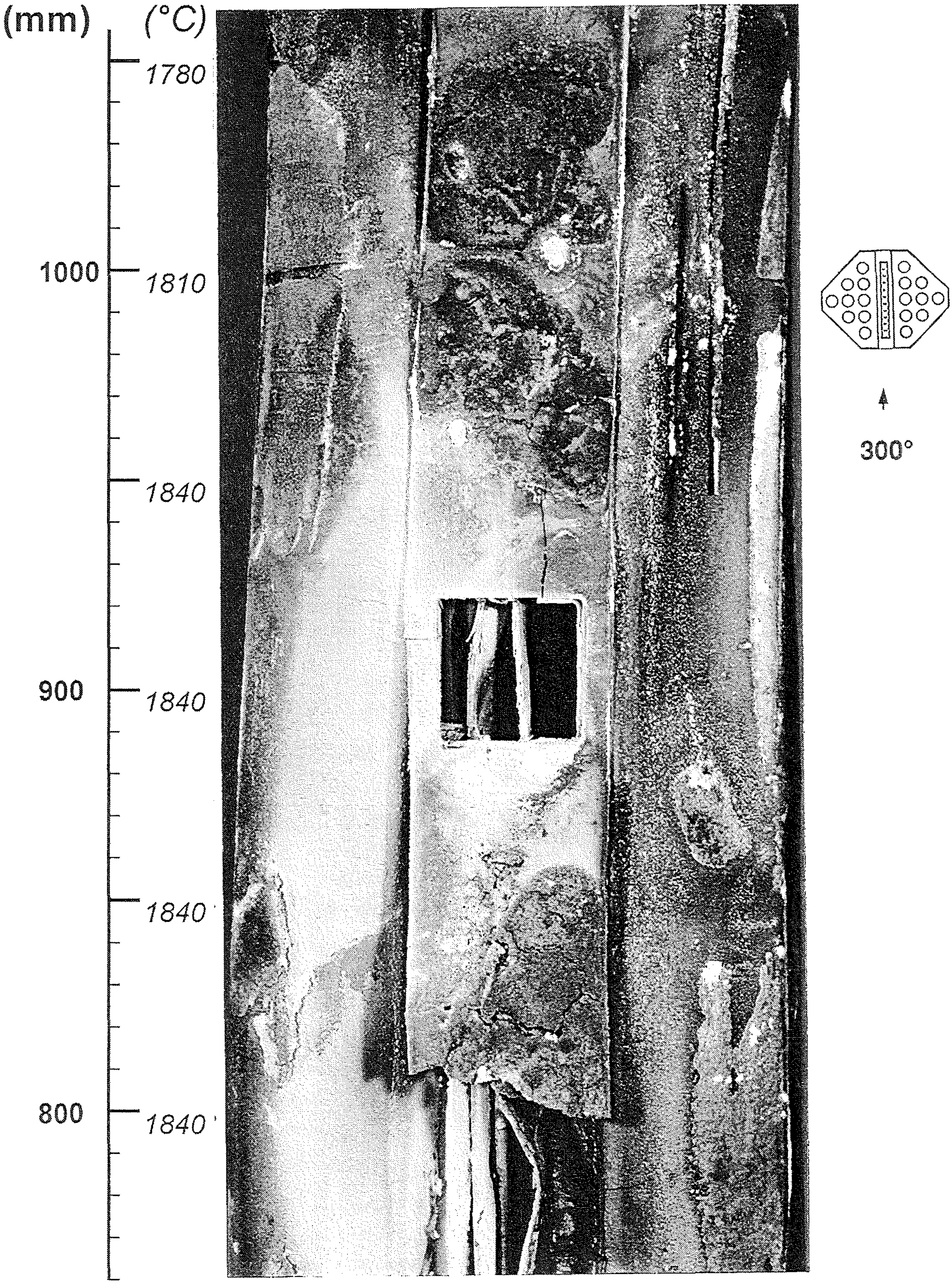

Fig. 91: CORA-28; Posttest view; 300° orientation; 700 - 1100 mm

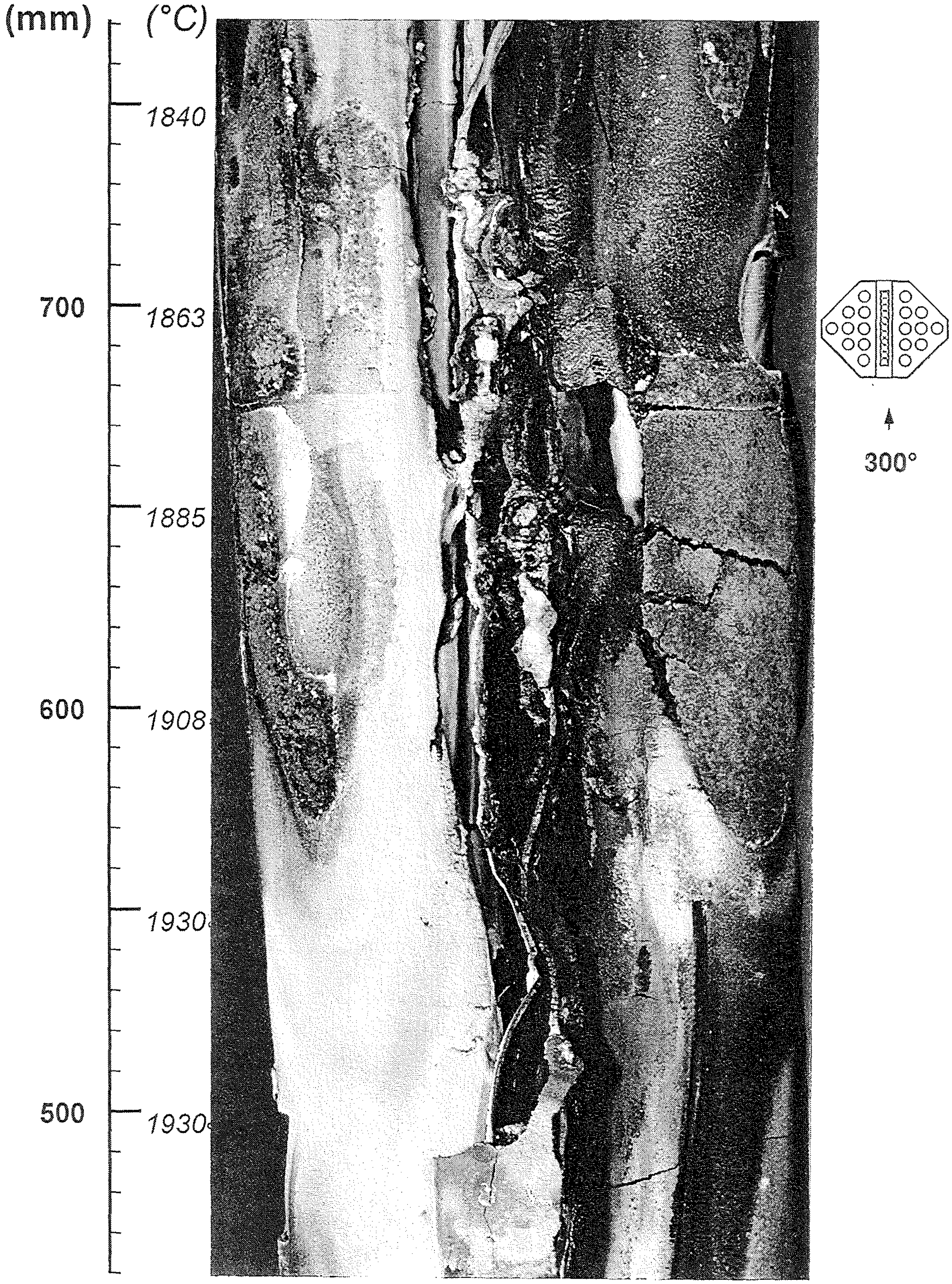

Fig. 92: CORA-28; Posttest view; 300° orientation; 400 - 800 mm

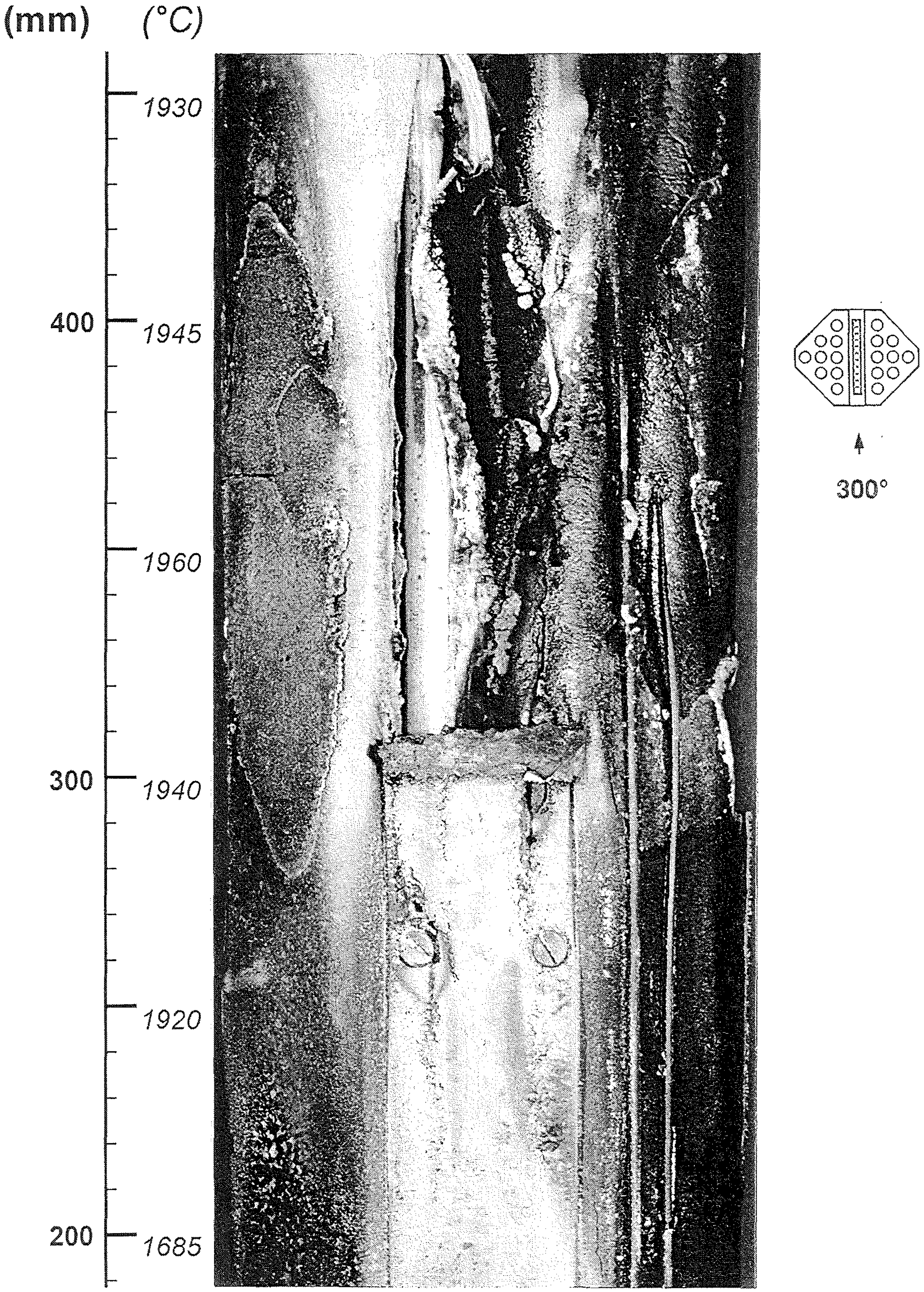

Fig. 93: CORA-28; Posttest view; 300° orientation; 200 - 500 mm

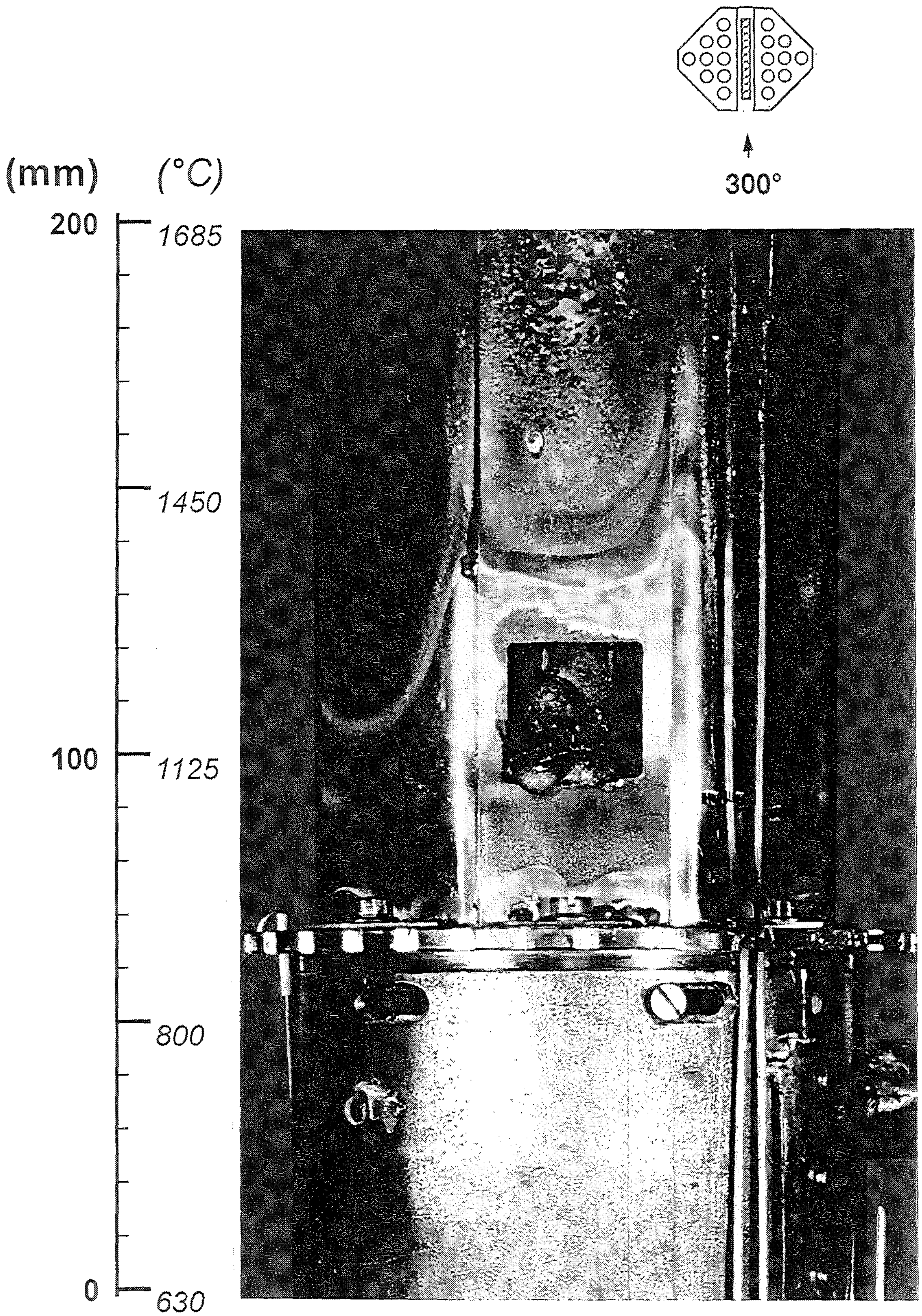

Fig. 94: CORA-28; Posttest view; 300° orientation; 0 - 200 mm

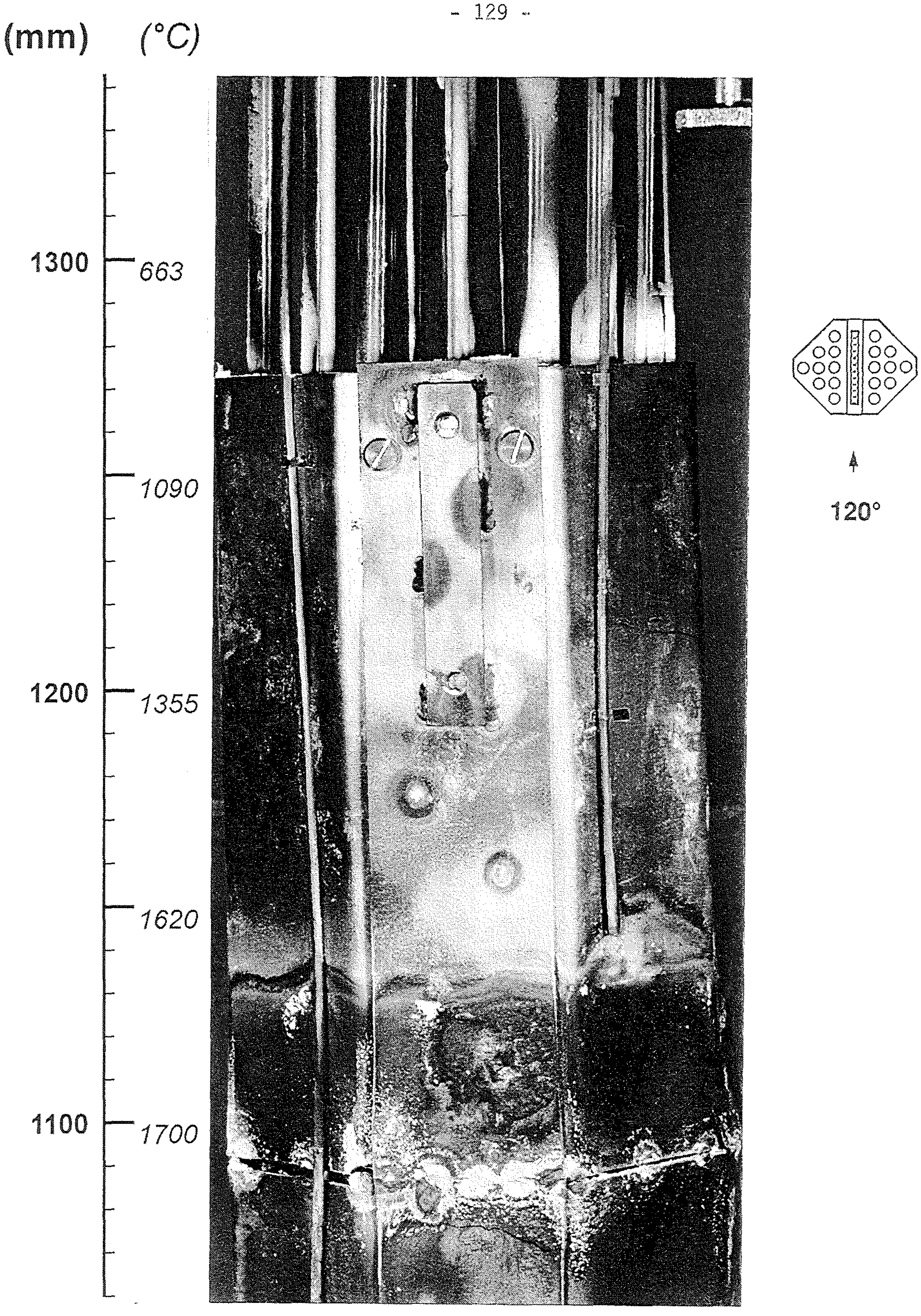

Fig. 95: CORA-28; Posttest view; 120° orientation; 1000 - 1400 mm

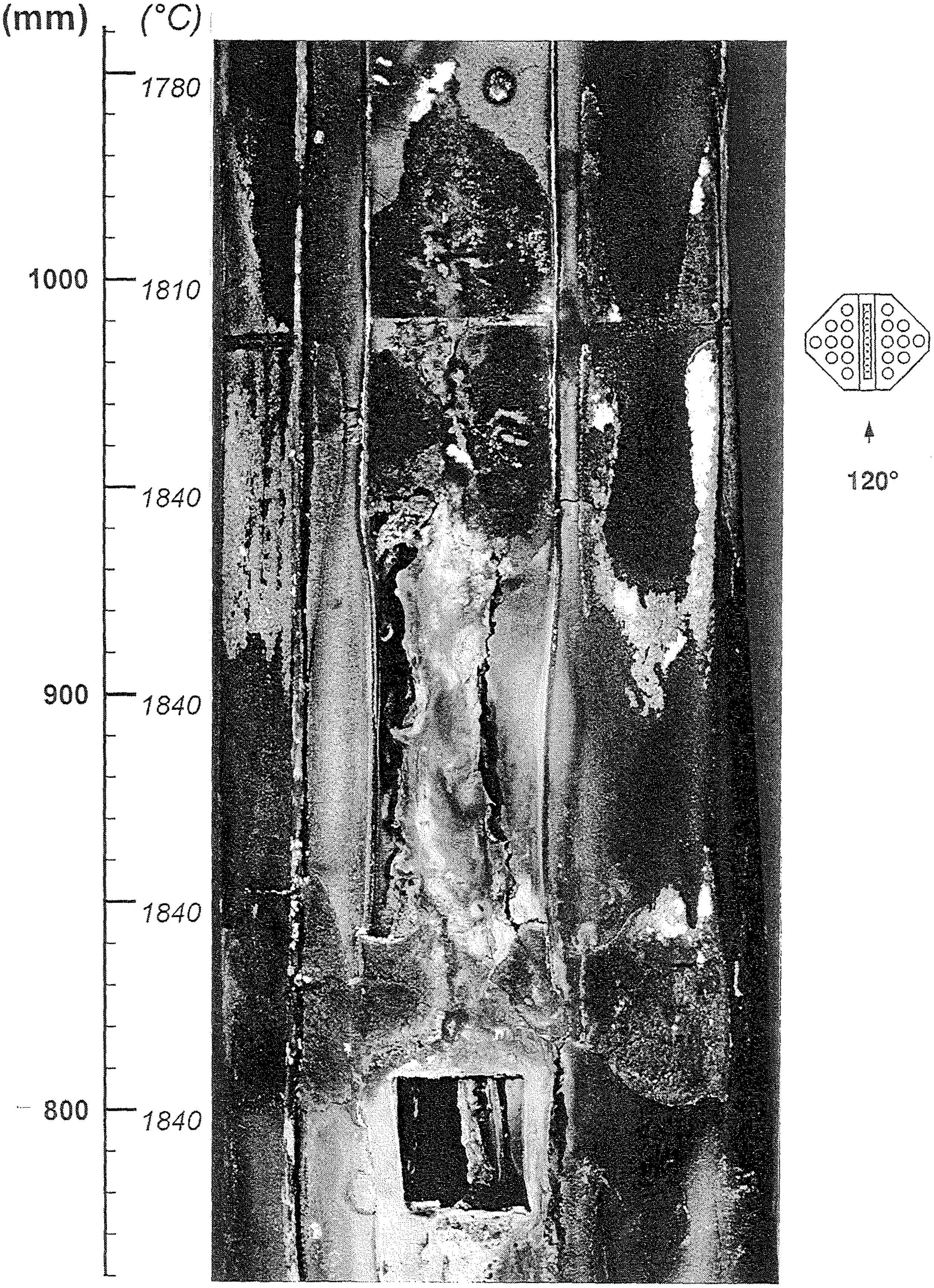

Fig. 96: CORA-28; Posttest view; 120° orientation; 700 - 1100 mm

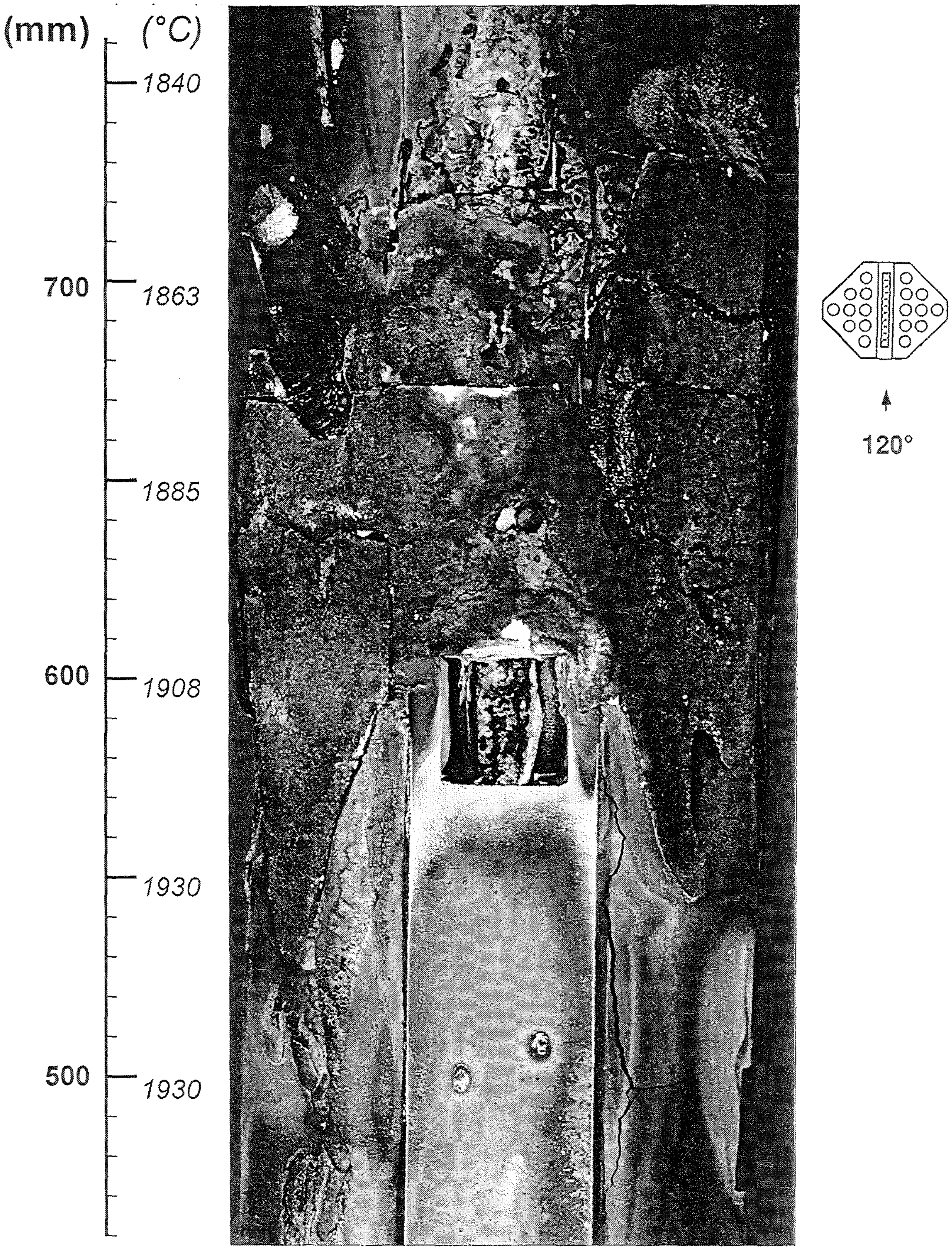

Fig. 97: CORA-28; Posttest view; 120° orientation; 400 - 800 mm

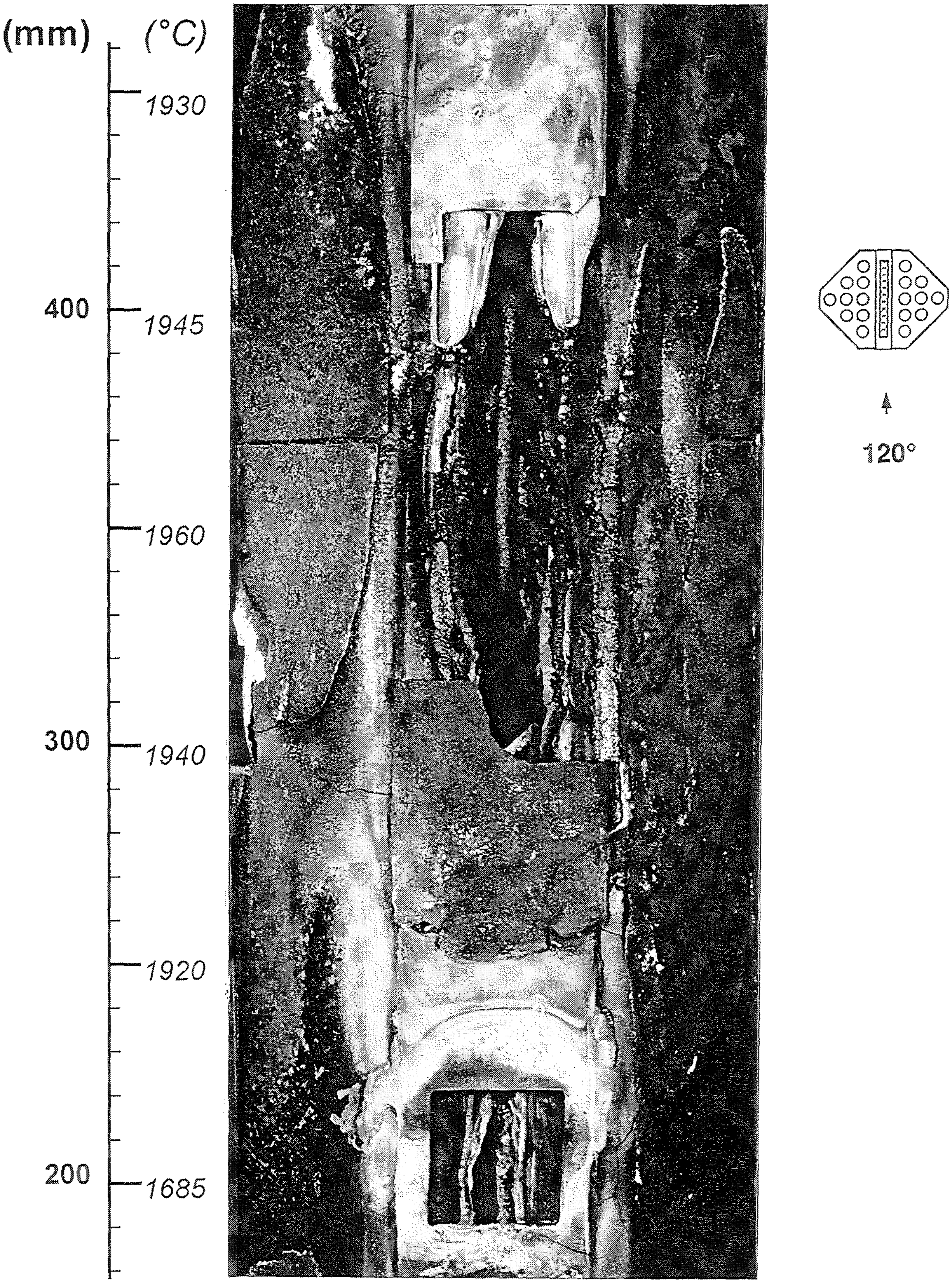

Fig. 98: CORA-28; Posttest view; 120° orientation; 200 - 500 mm

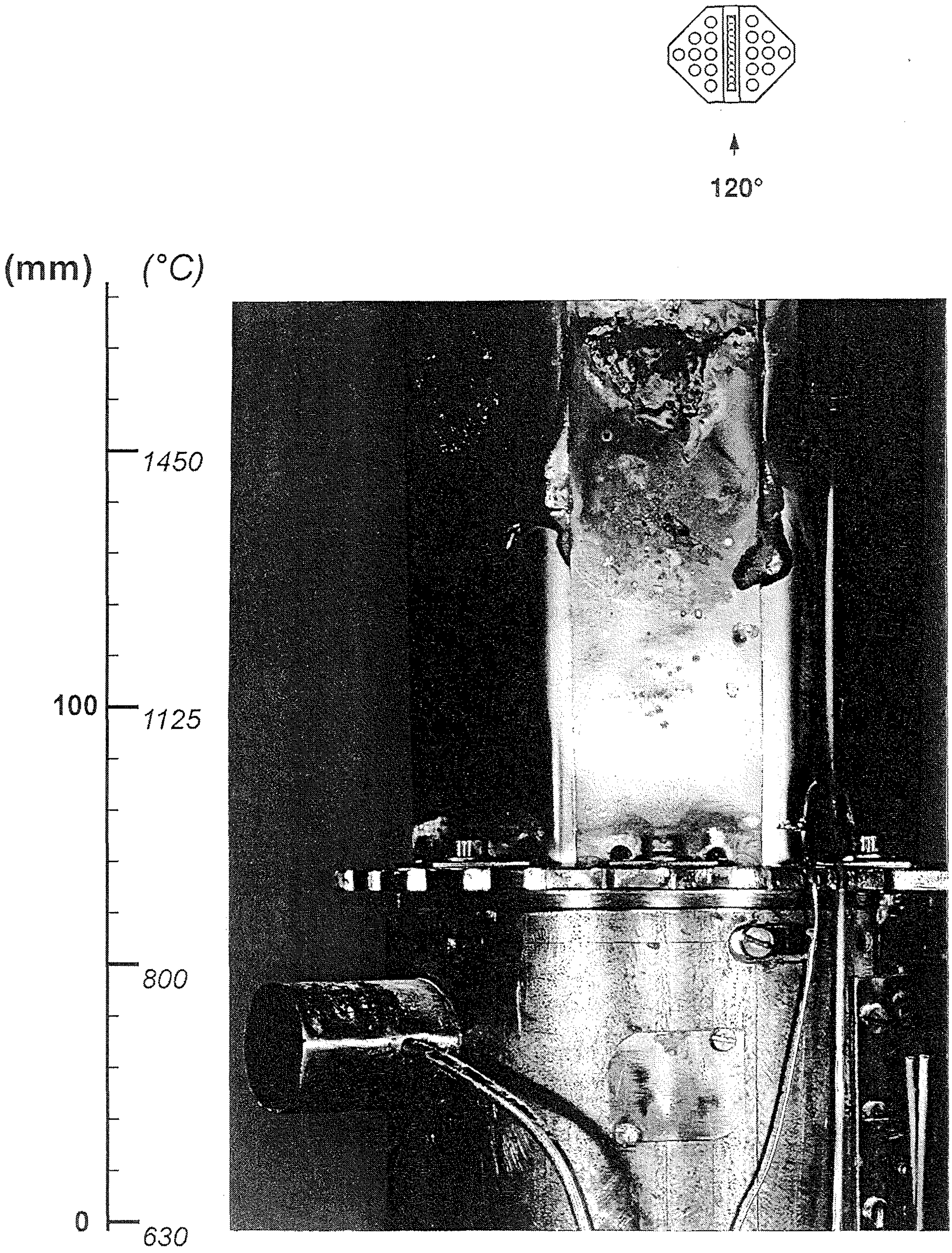

Fig. 99: CORA-28; Posttest view; 120° orientation; 0 - 200 mm

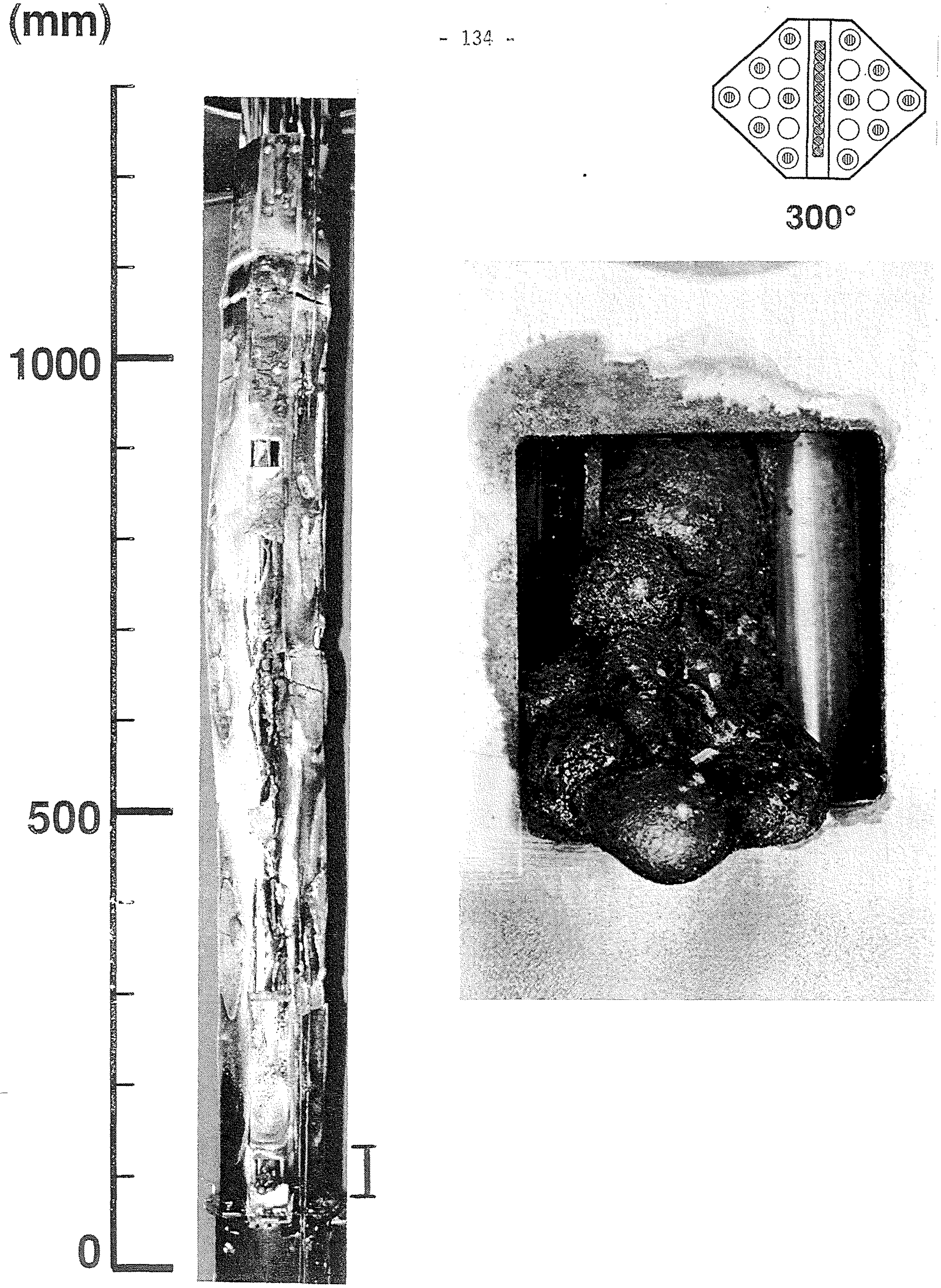

Fig. 100: CORA-28; Posttest view; 300° orientation; window at 100 mm elevation

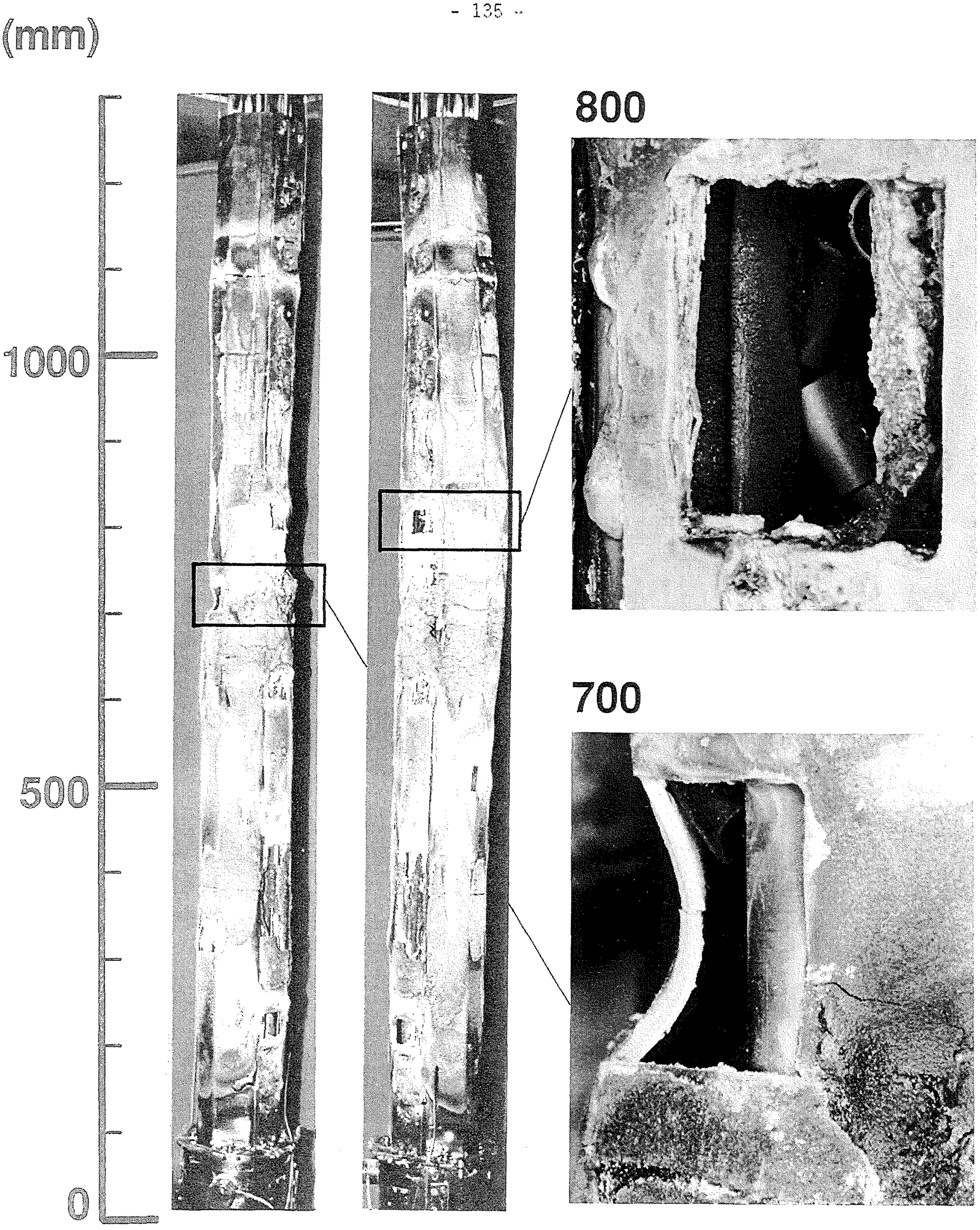

Fig. 101: CORA-28; Posttest view; windows at 700 mm and 800 mm elevation

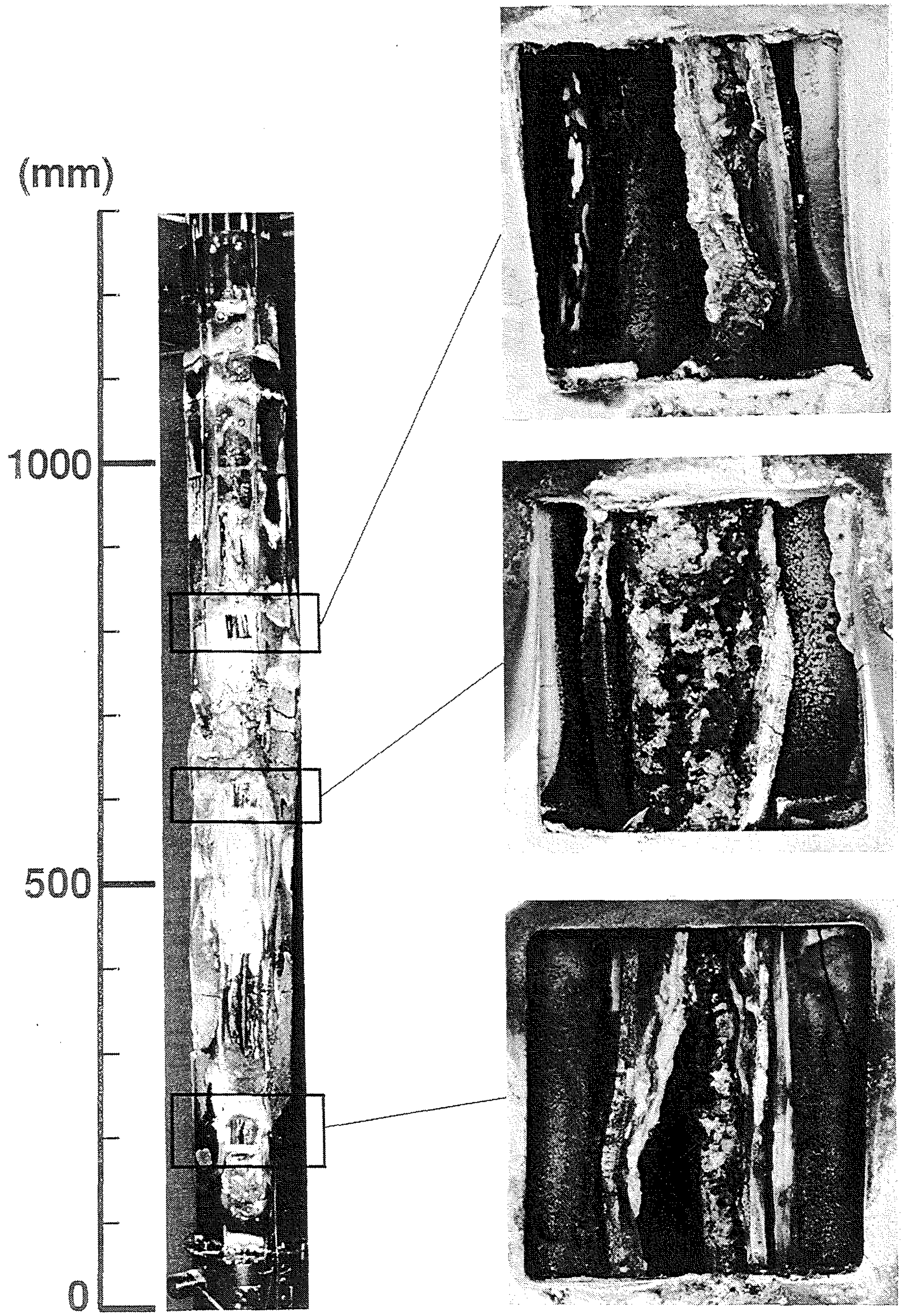

Fig. 102: CORA-28; Posttest view; 120° orientation; windows at 200 mm, 600 mm and 800 mm elevation

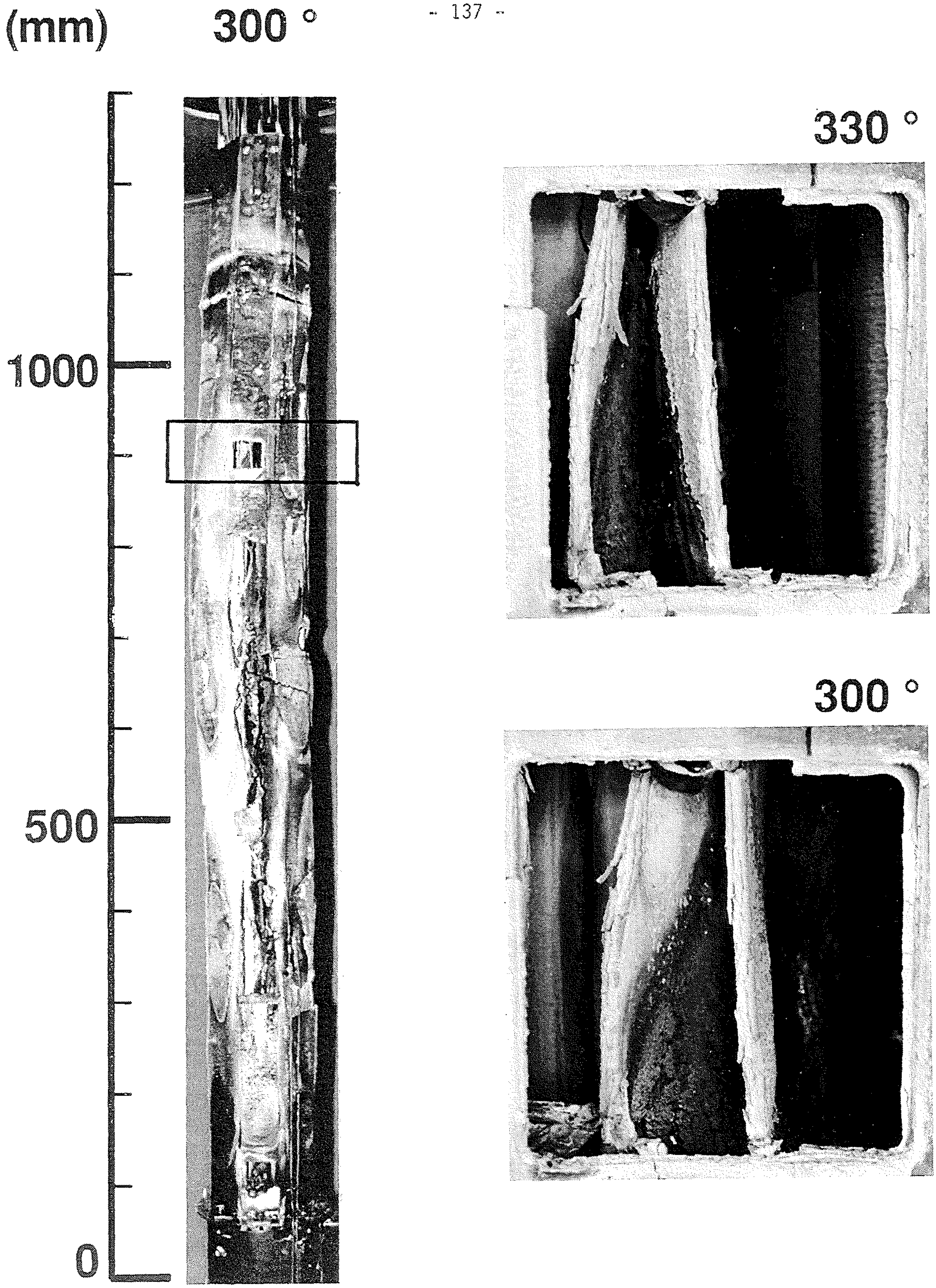

Fig. 103: CORA-28; Posttest view; 300° orientation; window at 900 mm elevation

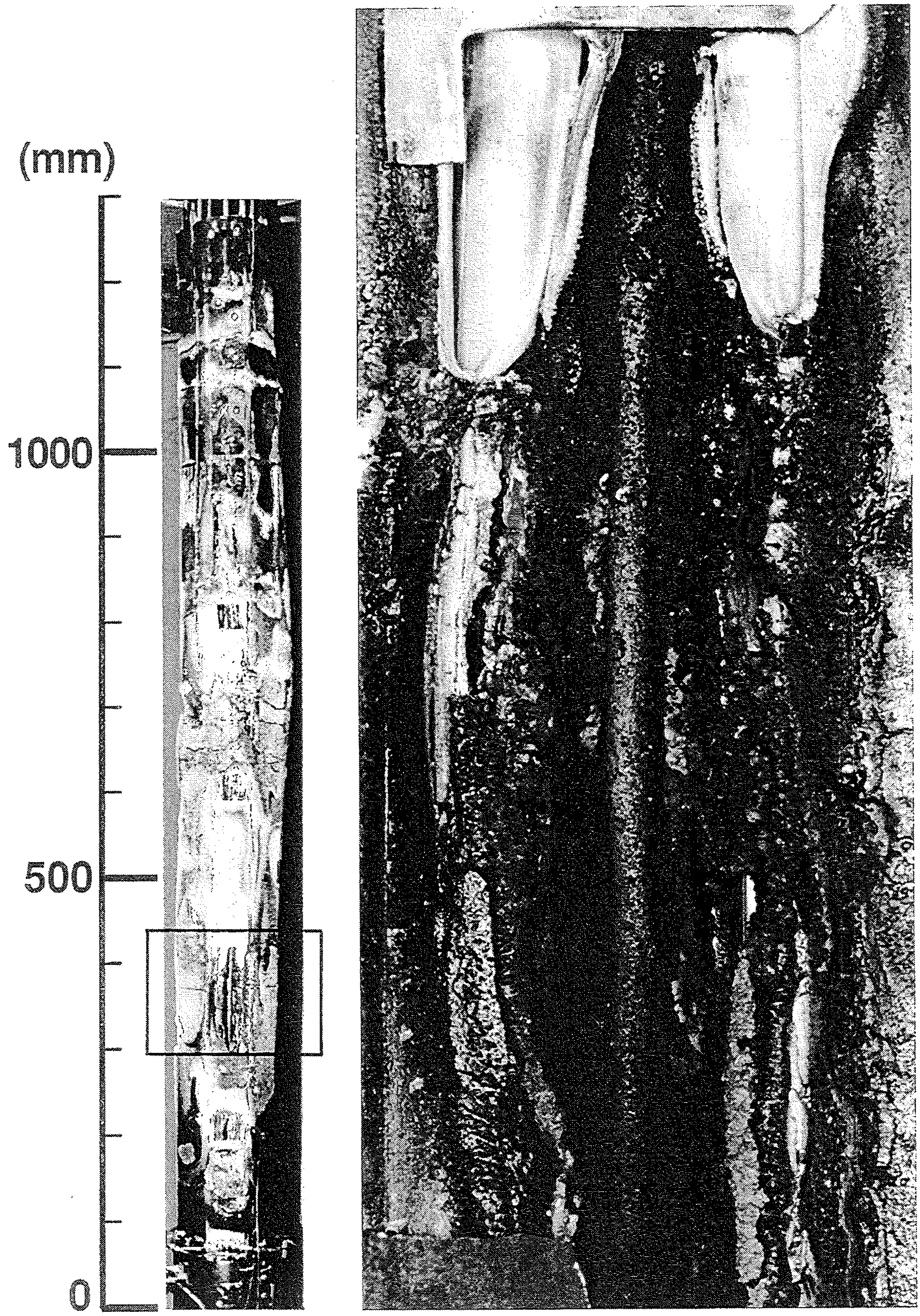

Fig. 104: CORA-28; Posttest view; 120° orientation; 300 - 450 mm

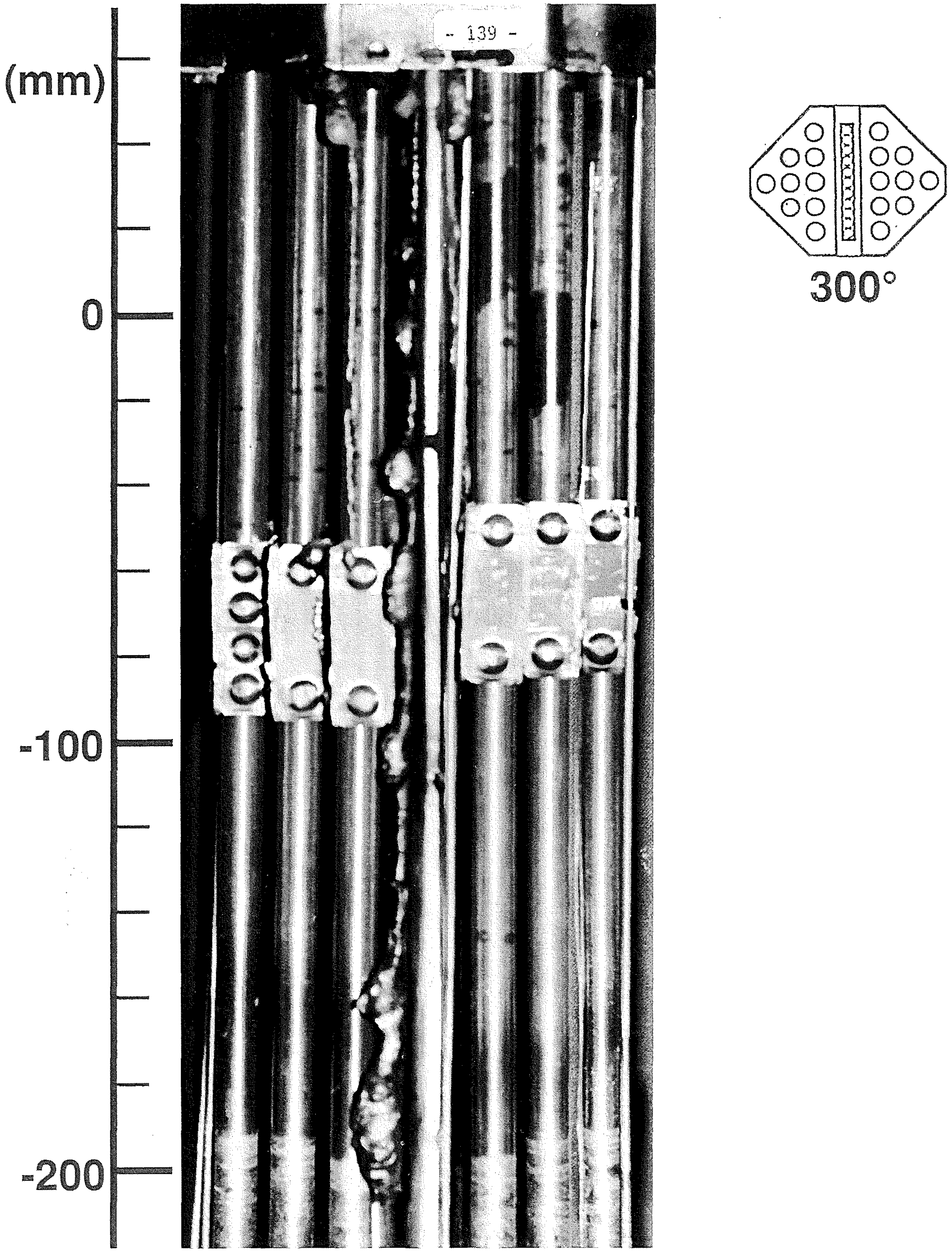

Fig. 105: CORA-28; Posttest view; 300° orientation; -200 - 50 mm

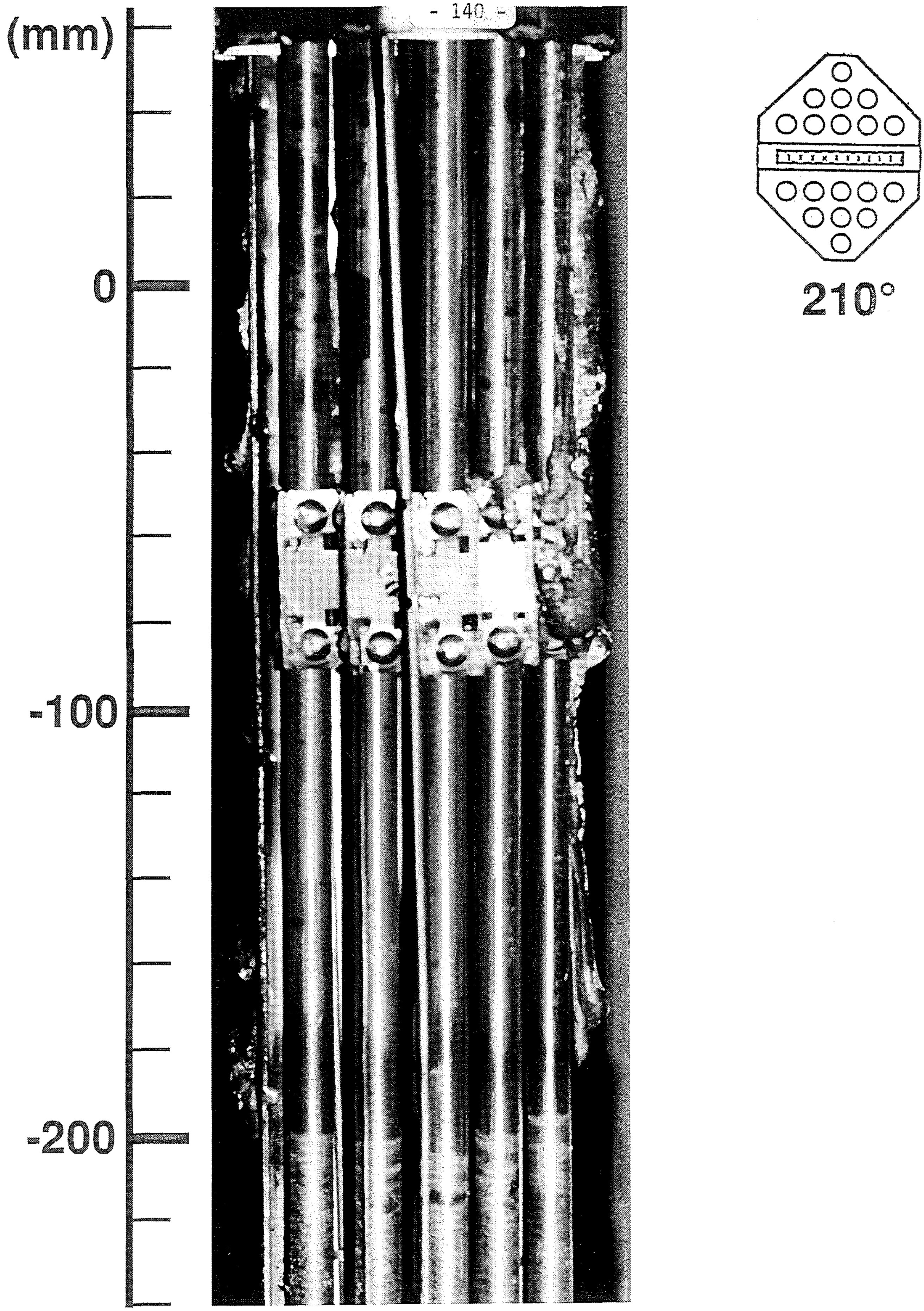

Fig. 106: CORA-28; Posttest view; 210° orientation; -200 - 50 mm

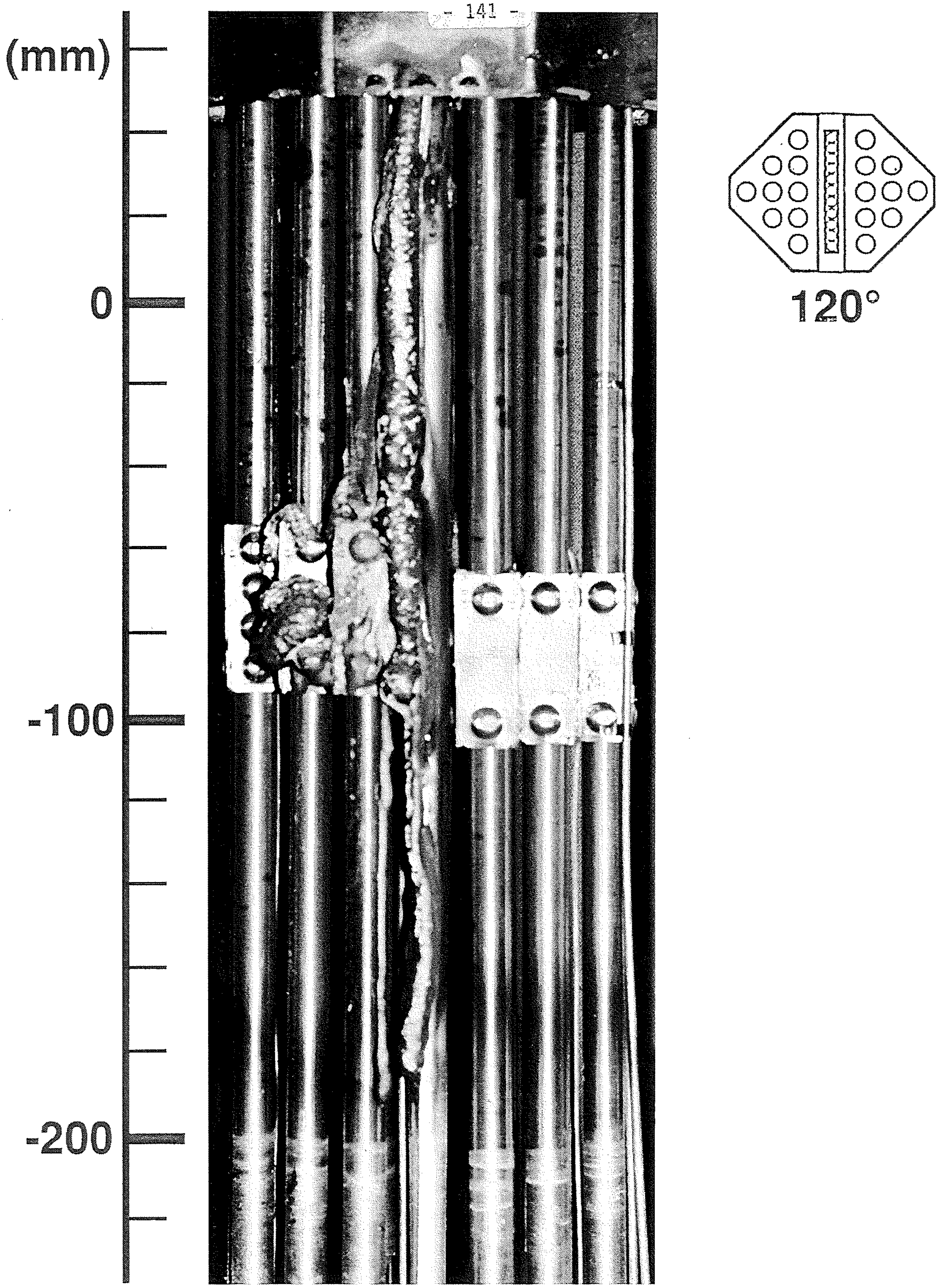

Fig. 107: CORA-28; Posttest view; 120° orientation; -200 - 50 mm

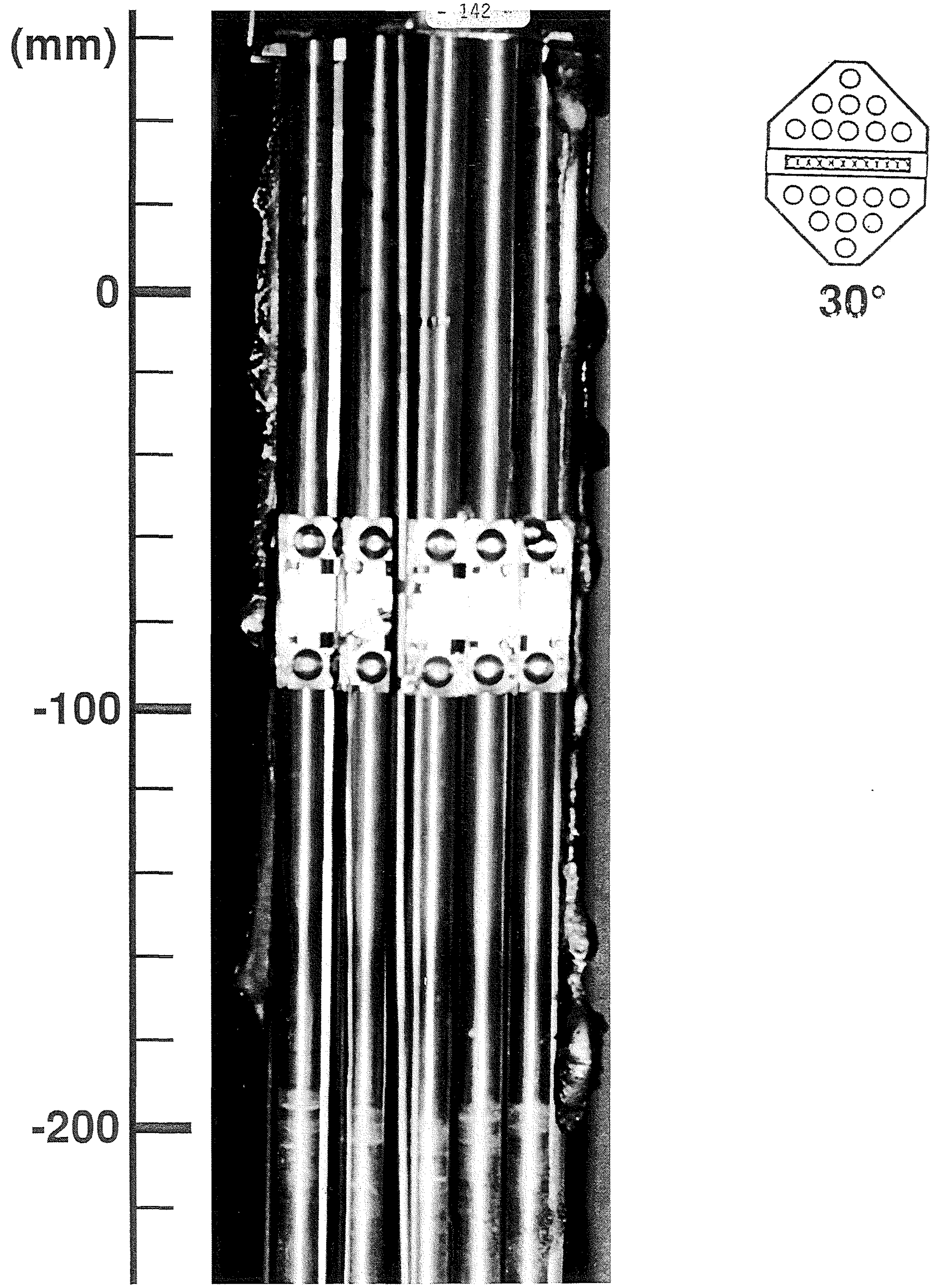

Fig. 108: CORA-28; Posttest view; 30° orientation; -200 - 50 mm

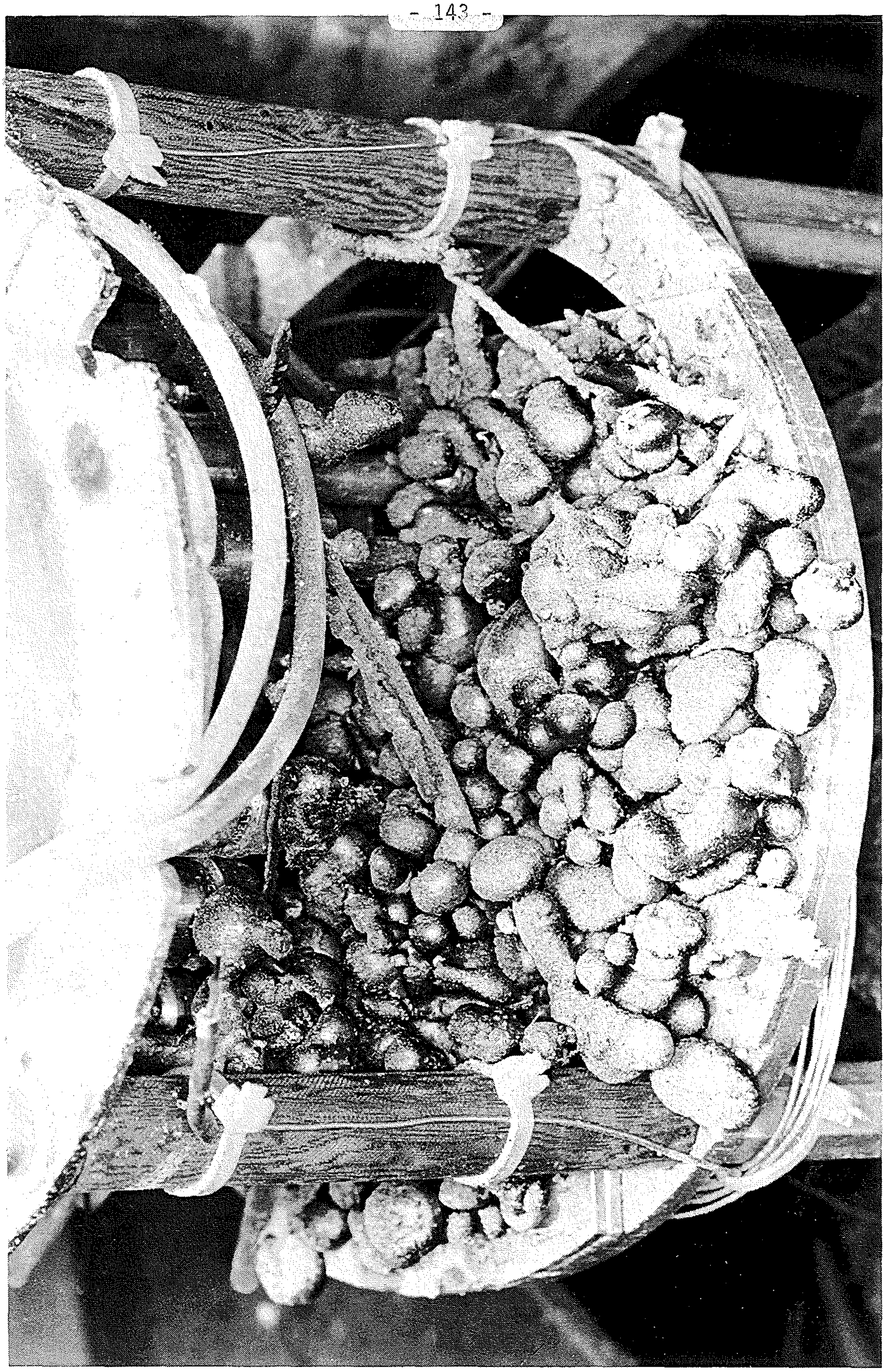

Fig. 109: CORA-28; Melt refrozen on the comb plate in the water of the quench cylinder

Fig. 110: CORA-28; Solidified melt taken from the quench cyinder

(top view)

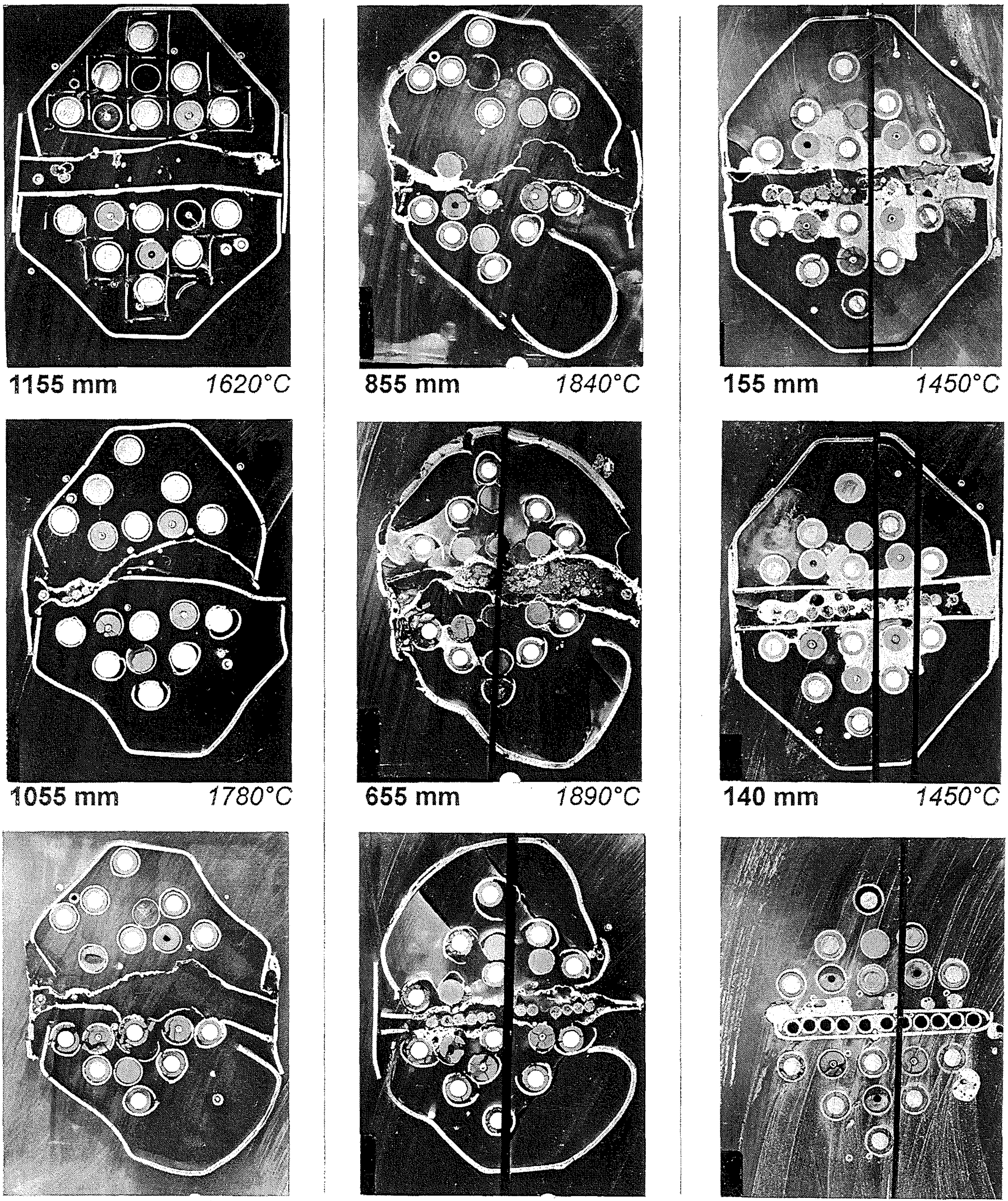

1155 mm *1620°C*

1055 mm *1780°C*

955 mm *1840°C*

855 mm *1840°C*

655 mm *1890°C*

455 mm *1930°C*

155 mm *1450°C*

140 mm *1450°C*

55 mm *800°C*

Fig. 111: Horizontal cross sections of bundle CORA-28, top view (1155-55 mm)

(bottom view)

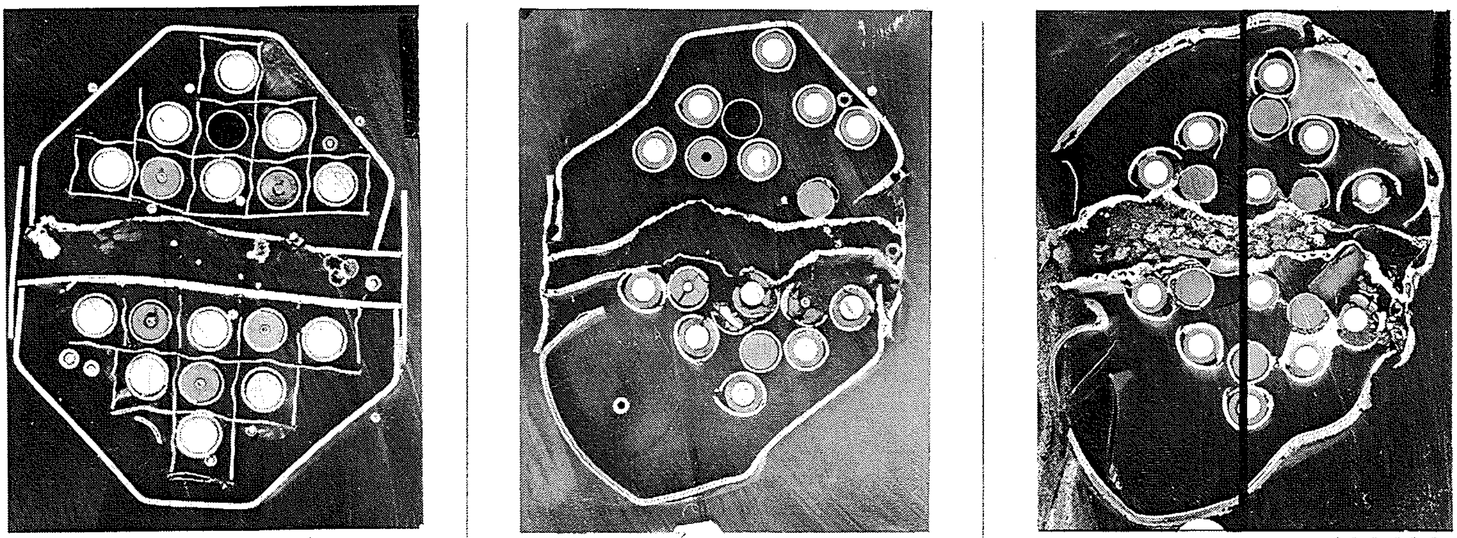

1157 mm *1620°C* **942 mm** *1840°C* **657 mm** *1890°C*

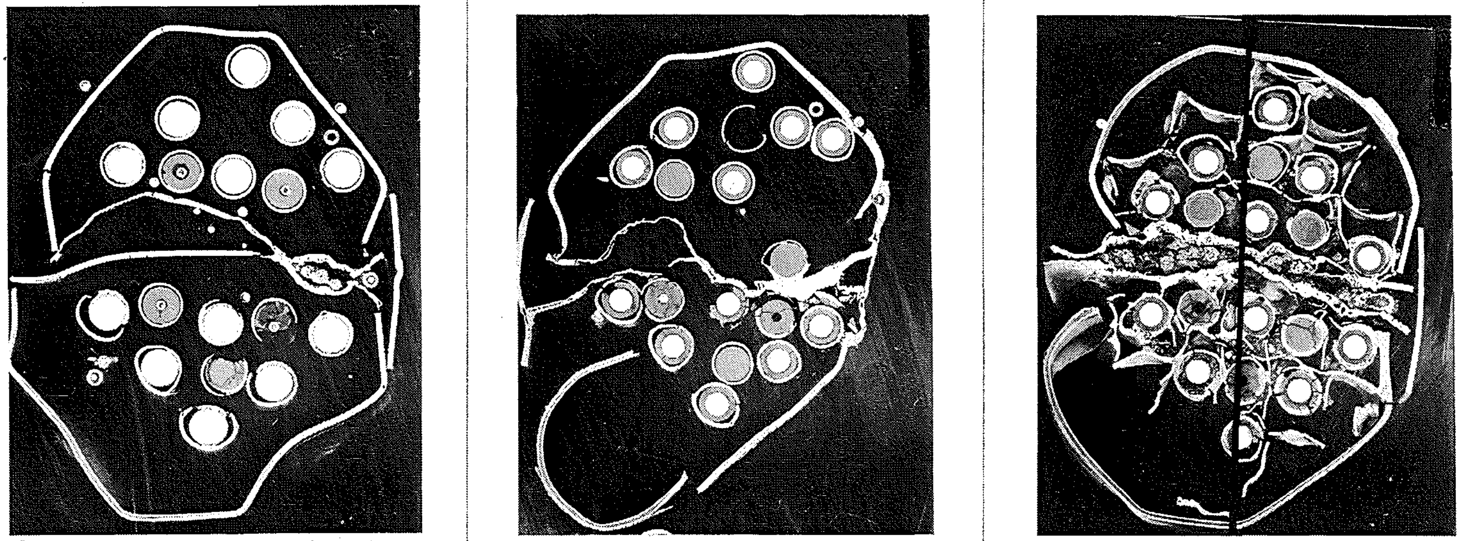

1057 mm *1780°C* **857 mm** *1840°C* **557 mm** *1930°C*

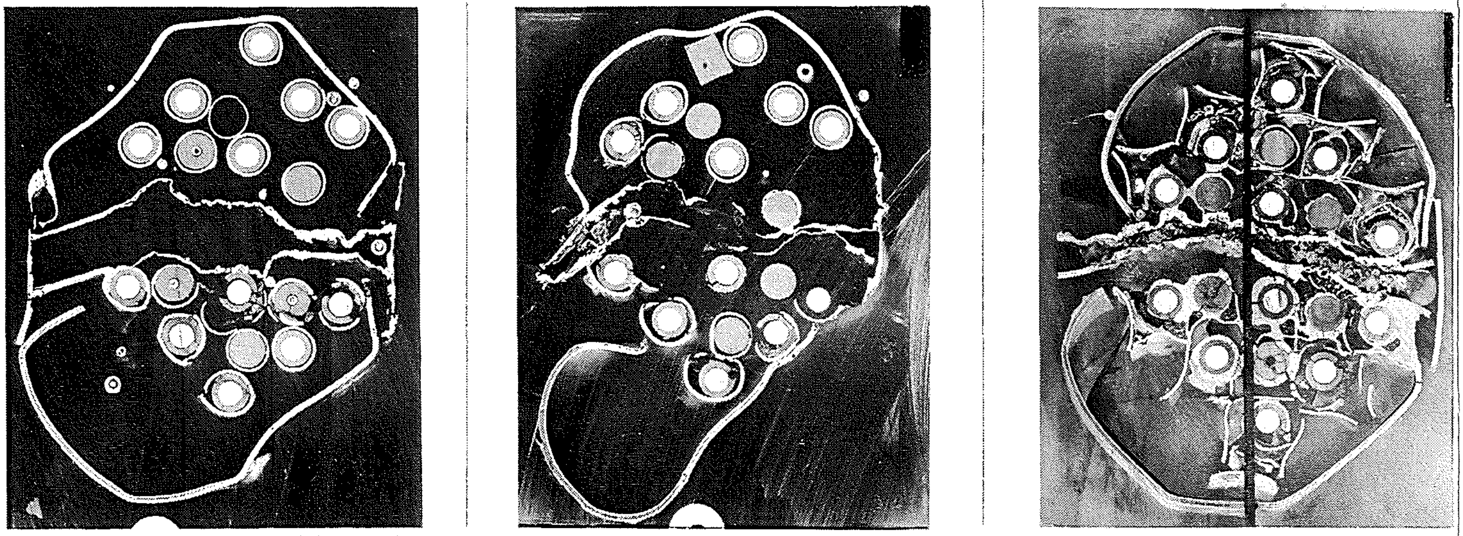

957 mm *1840°C* **757 mm** *1840°C* **542 mm** *1930°C*

Fig. 112: Horizontal cross sections of bundle CORA-28, bottom view (1157-542 mm)

(bottom view)

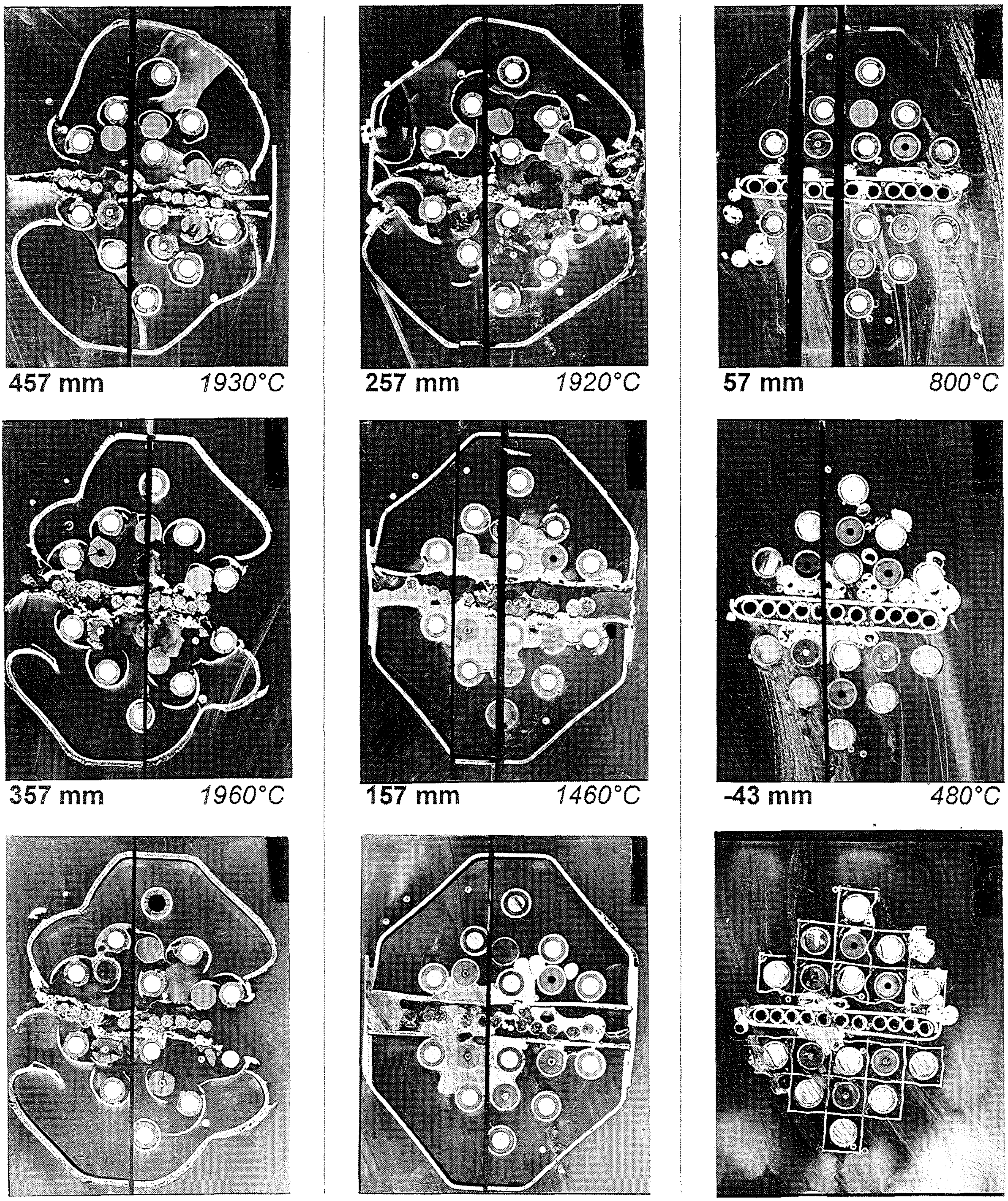

457 mm 1930°C

357 mm 1960°C

342 mm 1960°C

257 mm 1920°C

157 mm 1460°C

142 mm 1440°C

57 mm 800°C

-43 mm 480°C

-58 mm 460°C

Fig. 113: Horizontal cross sections of bundle CORA-28, bottom view (457-58 mm)

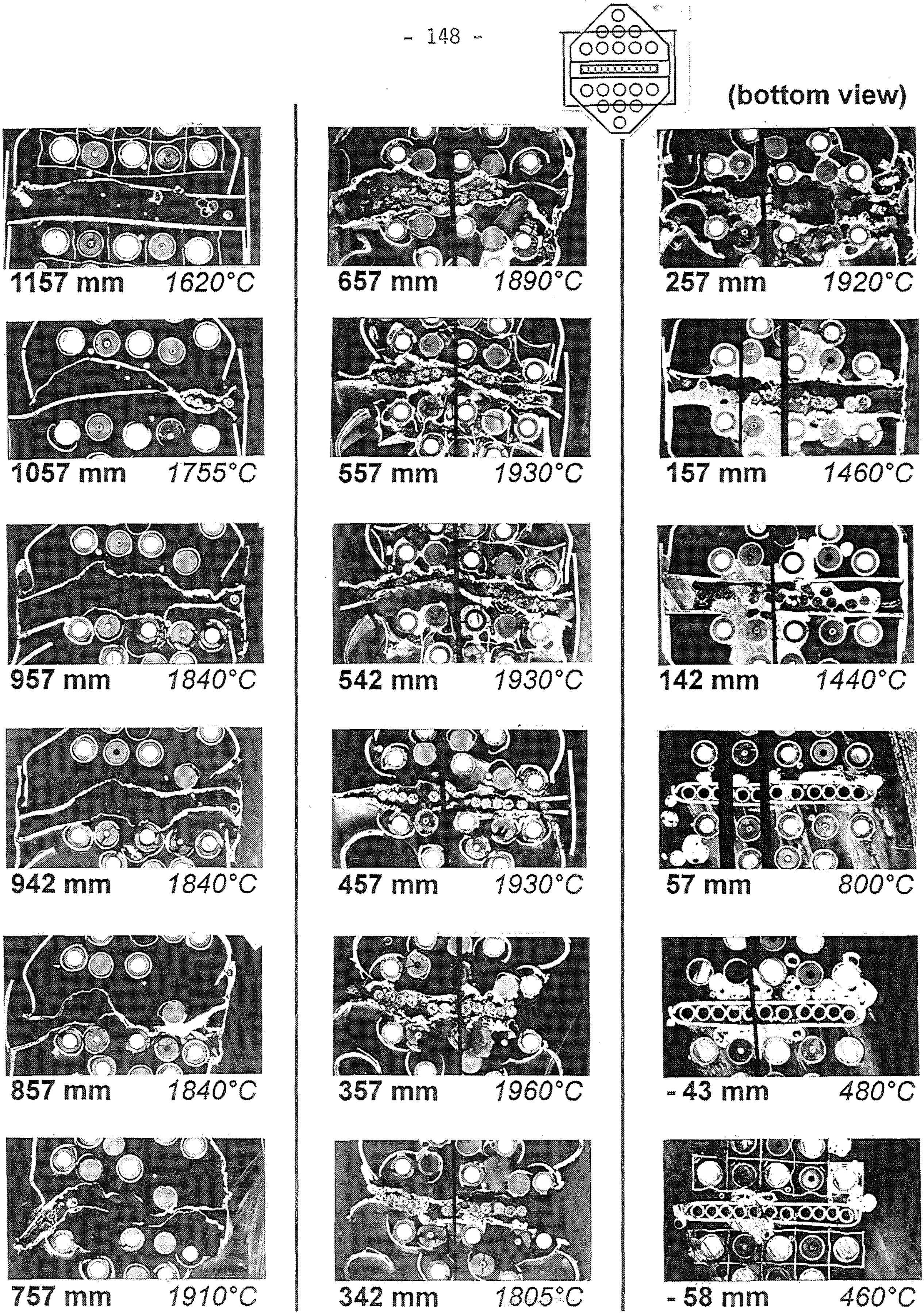

1157 mm *1620°C*

1057 mm *1755°C*

957 mm *1840°C*

942 mm *1840°C*

857 mm *1840°C*

757 mm *1910°C*

657 mm *1890°C*

557 mm *1930°C*

542 mm *1930°C*

457 mm *1930°C*

357 mm *1960°C*

342 mm *1805°C*

257 mm *1920°C*

157 mm *1460°C*

142 mm *1440°C*

57 mm *800°C*

- 43 mm *480°C*

- 58 mm *460°C*

Fig. 114: Horizontal cross sections of the absorber region of bundle CORA-28 (bottom view) (1157- -58 mm)

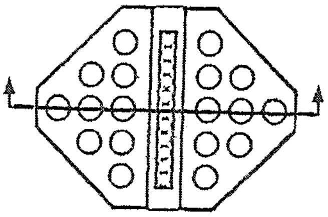

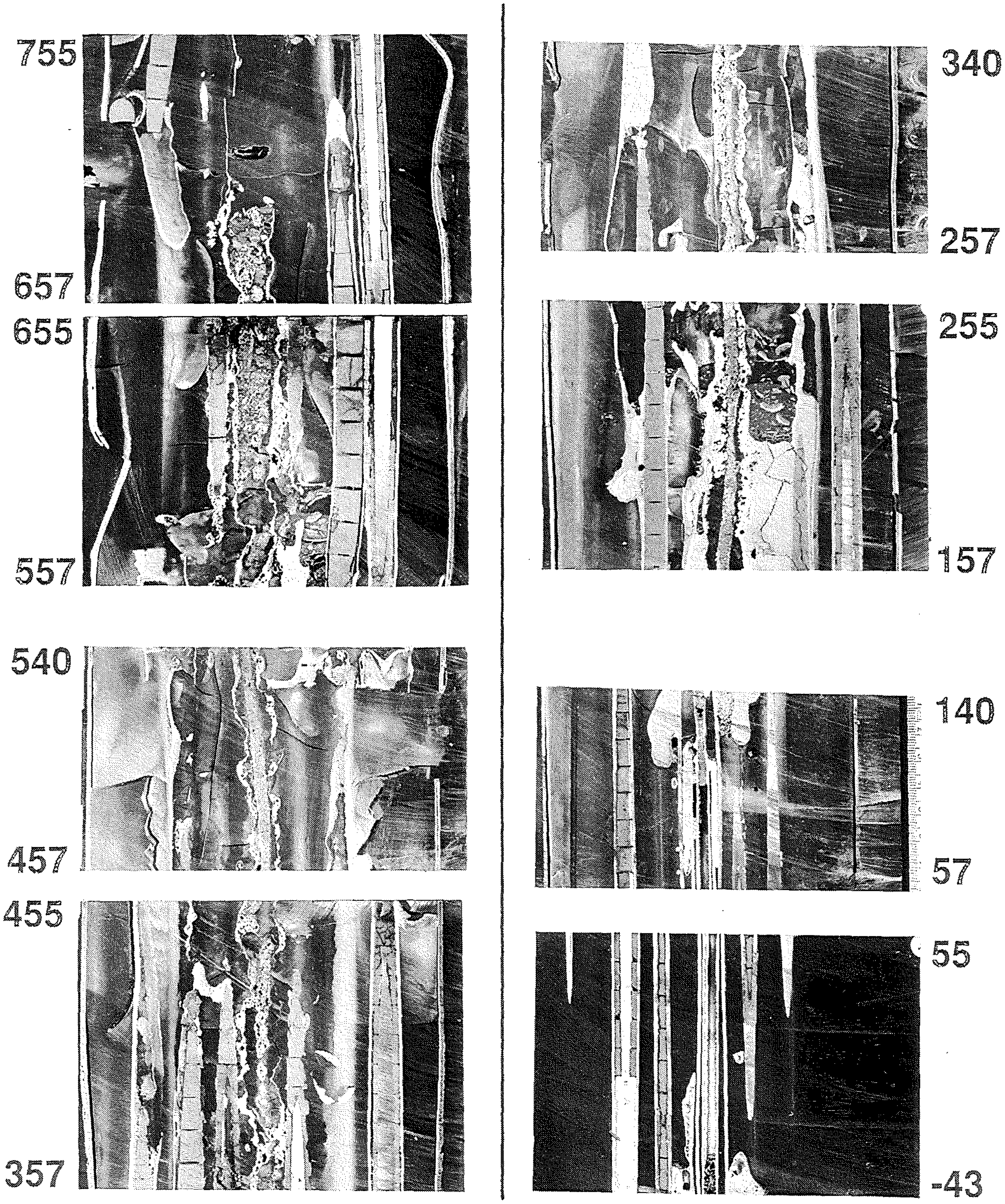

Fig. 115: Vertical cross sections of bundle CORA-28, total view

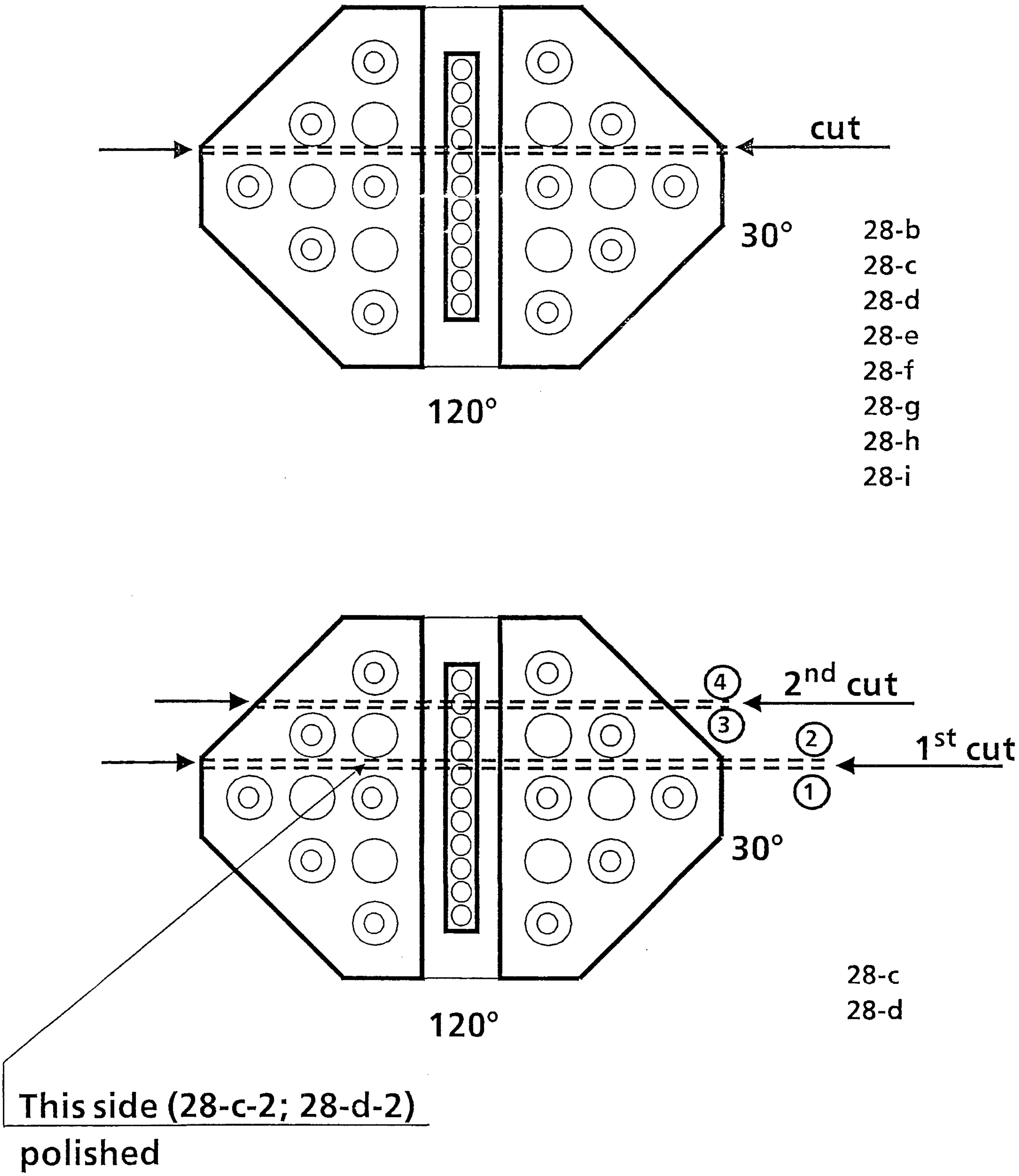

Fig. 115a: Locations of vertical cuts through sections 28-b, 28-c, 28-d, 28-e, 28-f, 28-g, 28-h, 28-i (top- viewed)

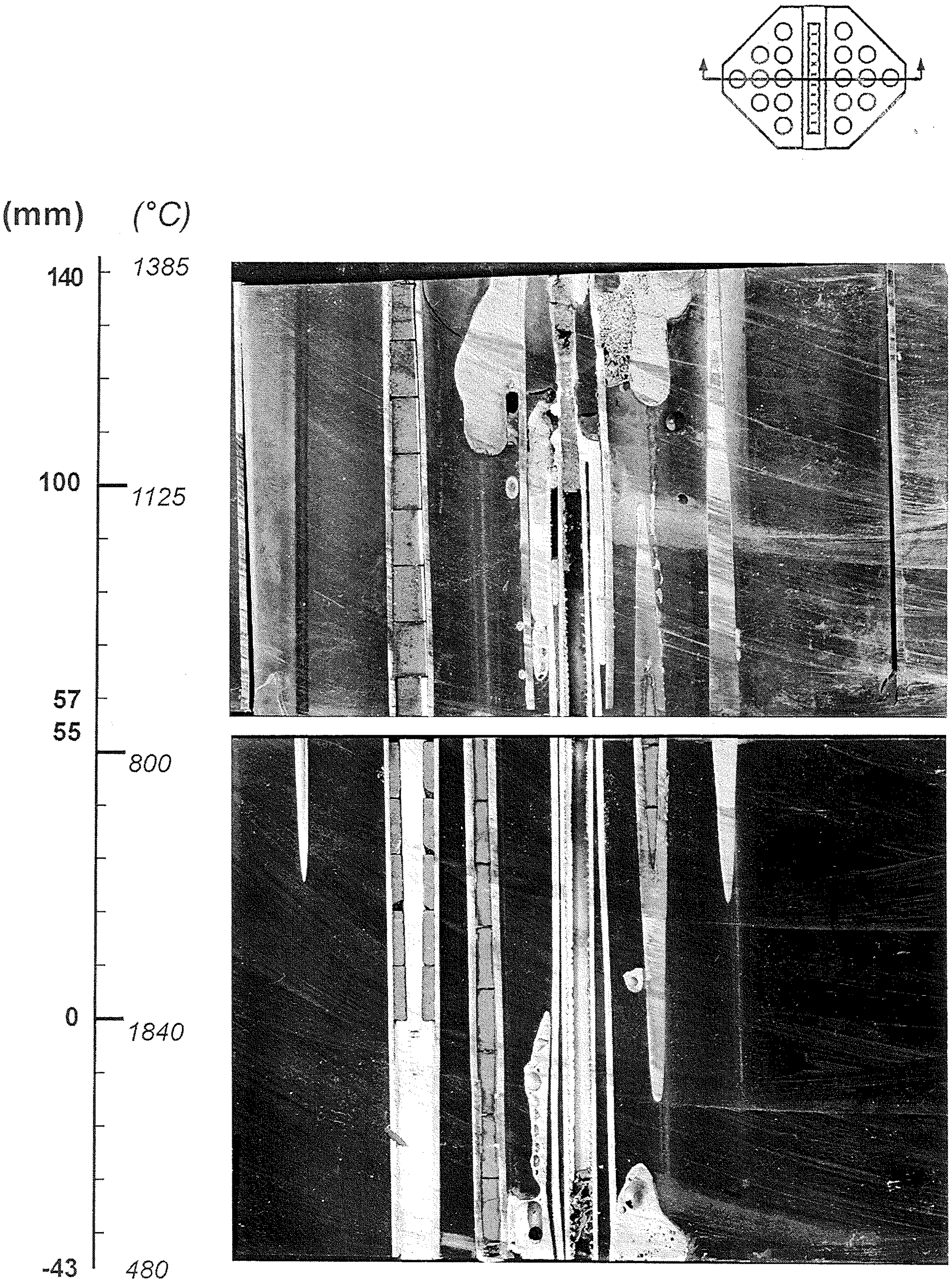

Fig. 116: Vertical cross sections of bundle CORA-28, -43 - 140 mm

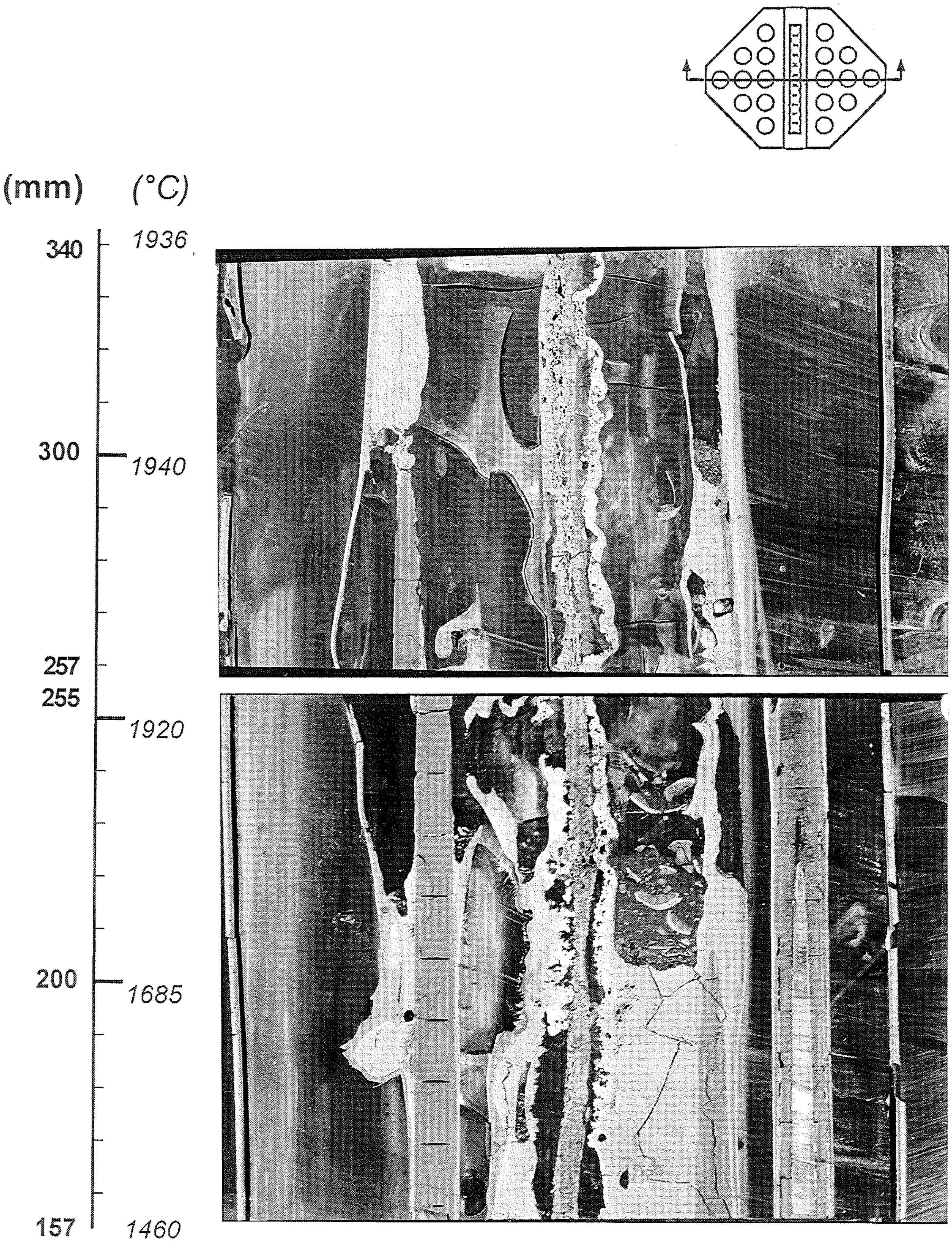

Fig. 117: Vertical cross sections of bundle CORA-28, 157 - 340 mm

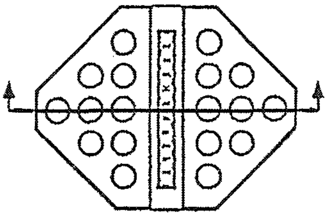

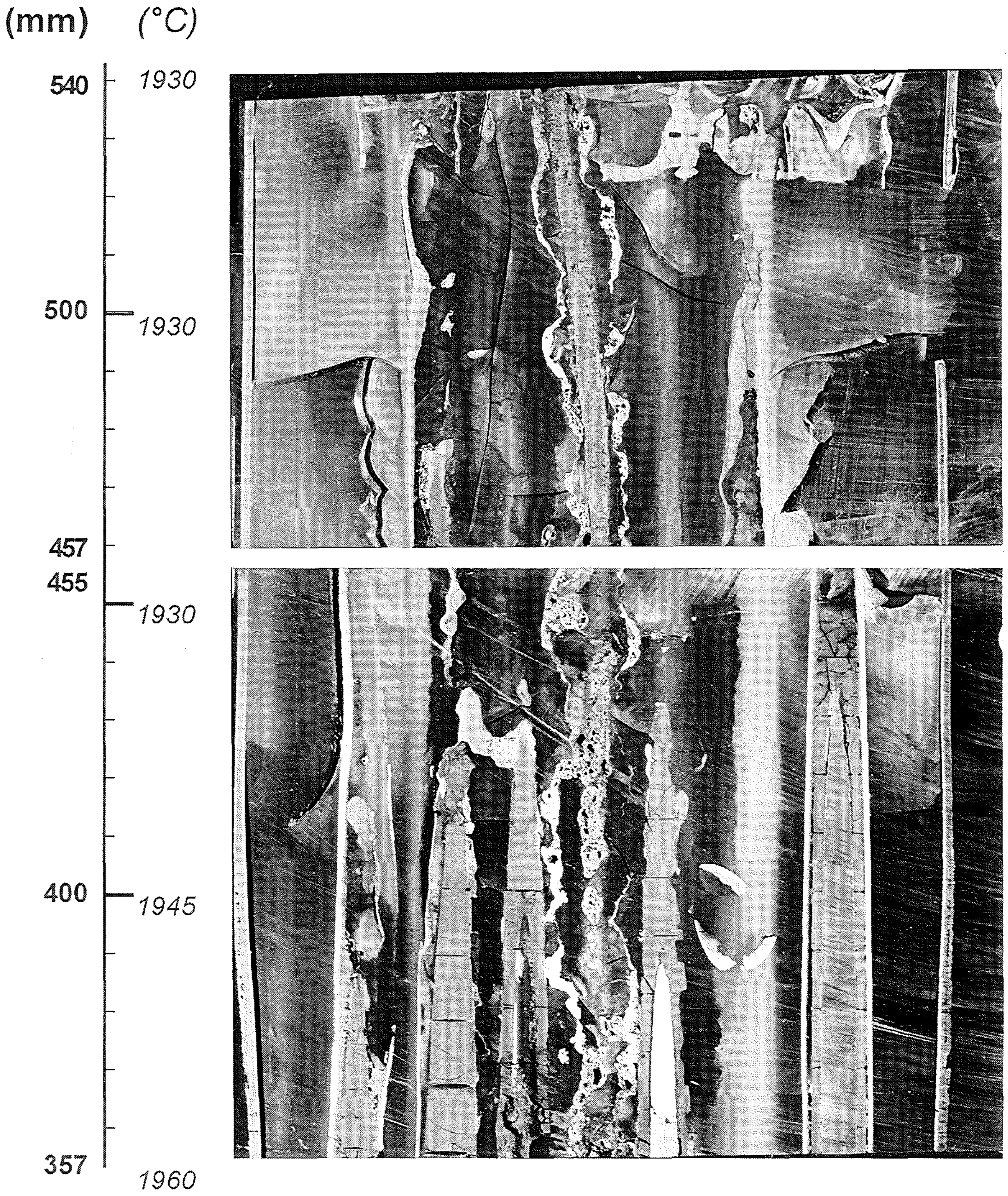

Fig. 118: Vertical cross sections of bundle CORA-28, 357 - 540 mm

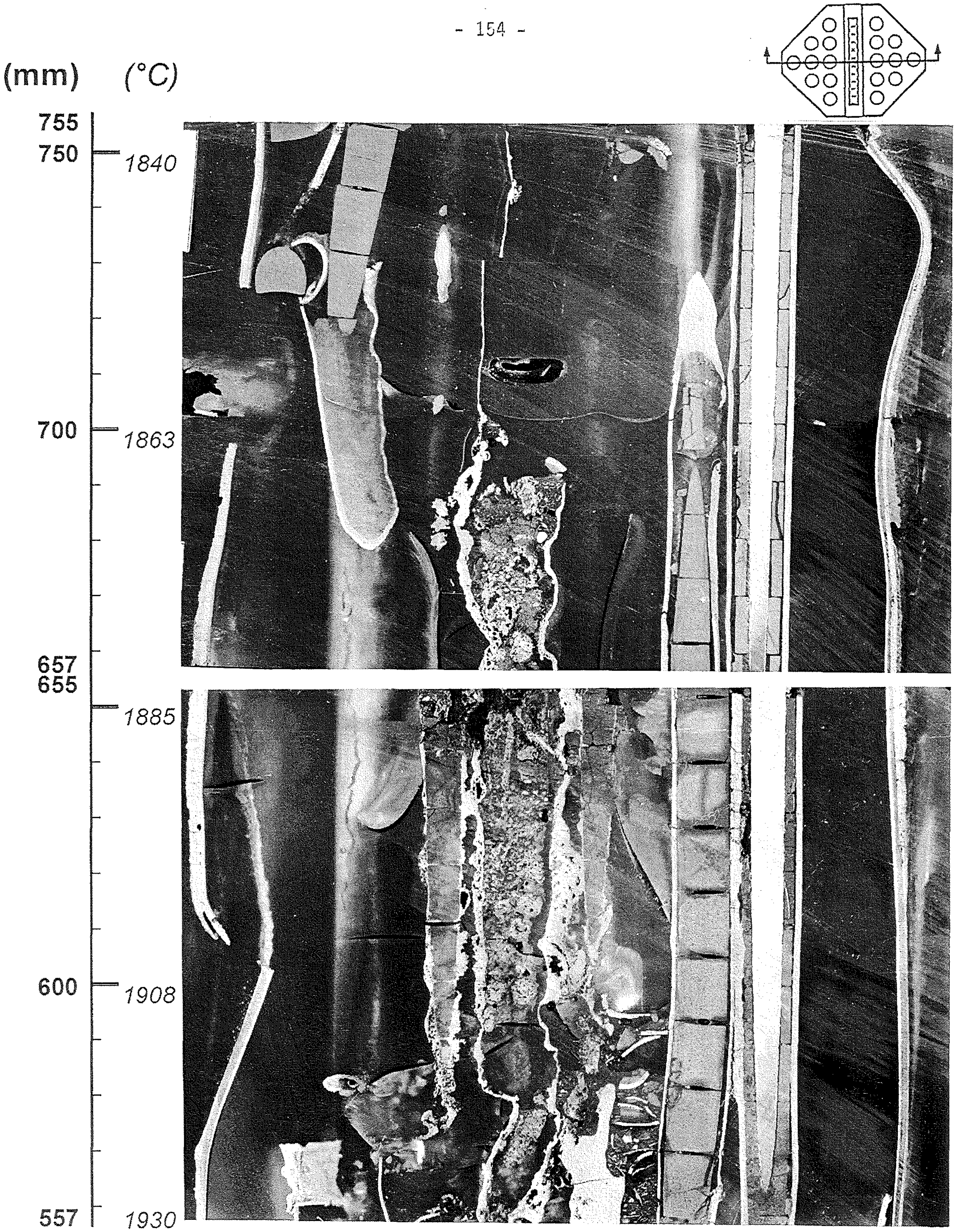

Fig. 119: Vertical cross sections of bundle CORA-28, 557 - 755 mm

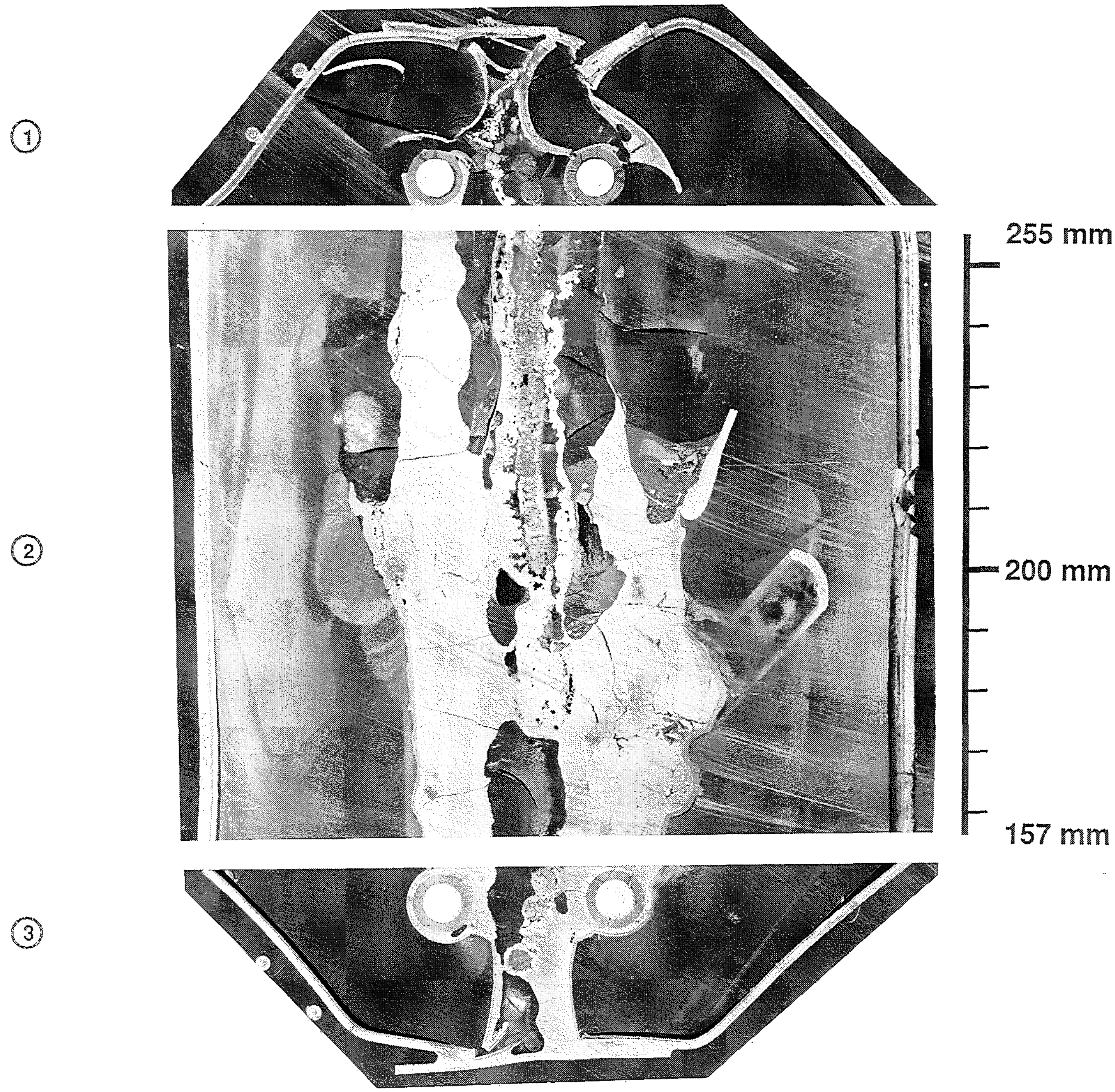

Fig. 120: CORA-28; Combination of horizontal and vertical cross sections, 157 - 255mm

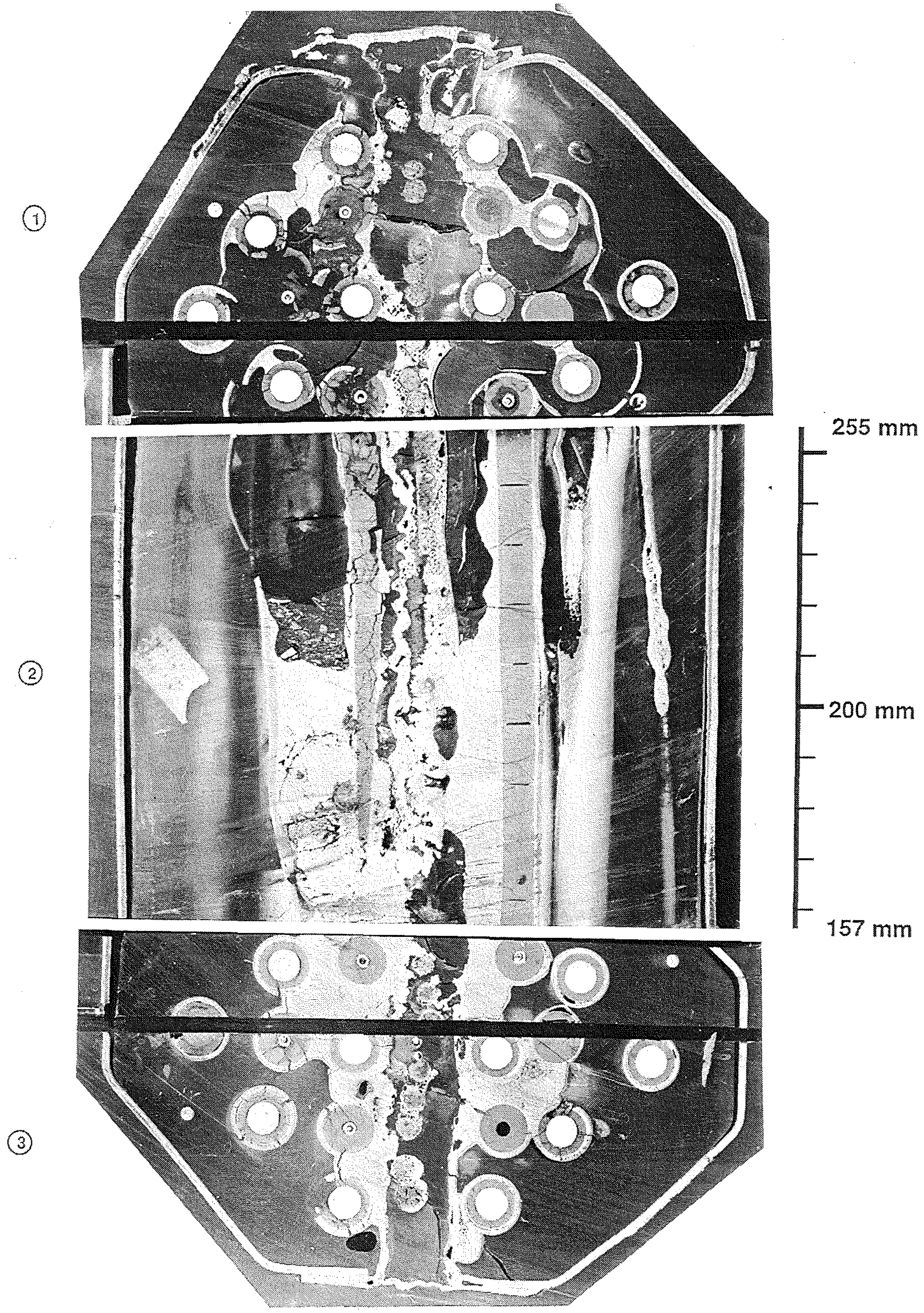

Fig. 121: CORA-28; Combination of horizontal and vertical cross sections, 157 - 255mm

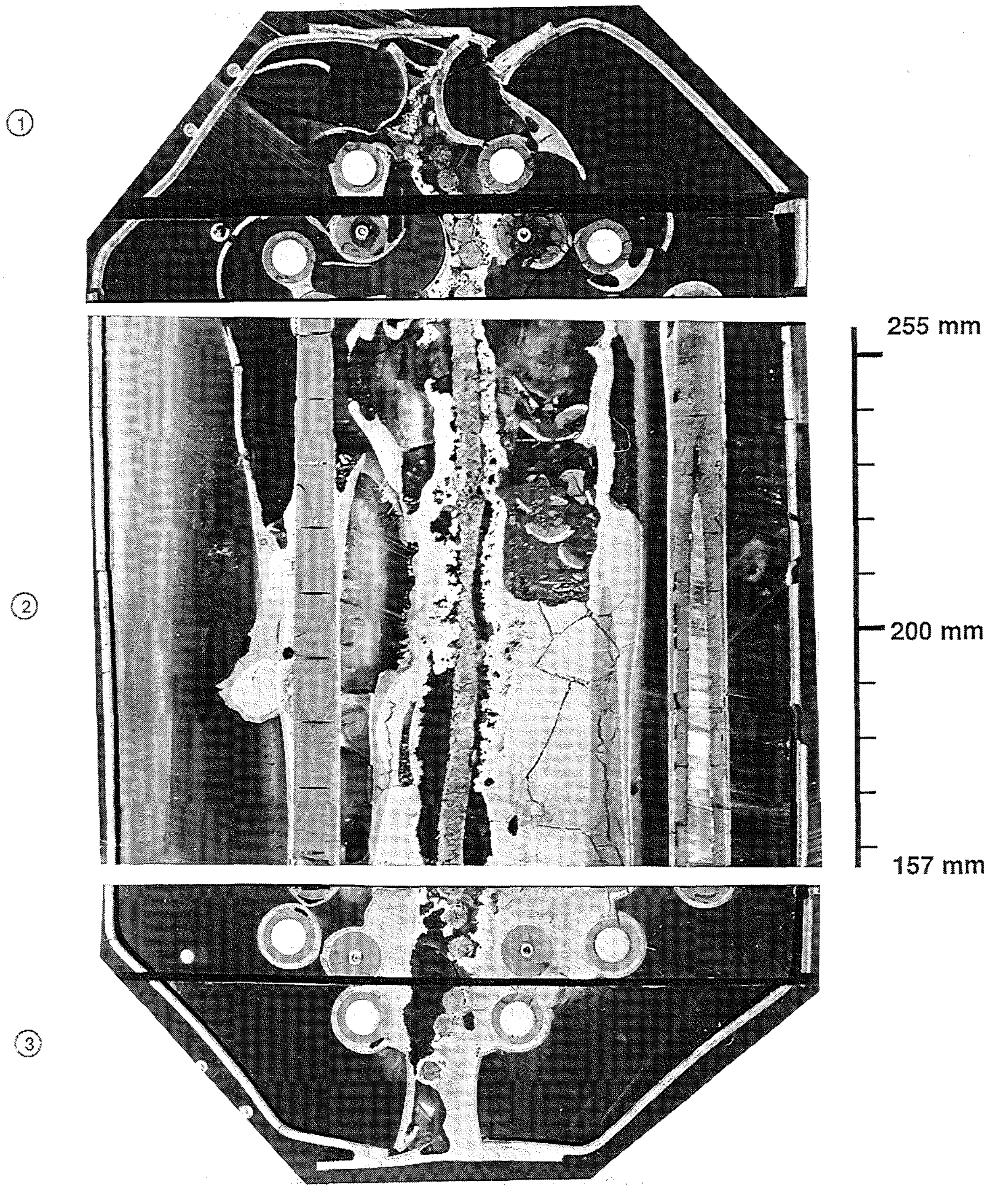

Fig. 122: CORA-28; Combination of horizontal and vertical cross sections, 157 - 255mm

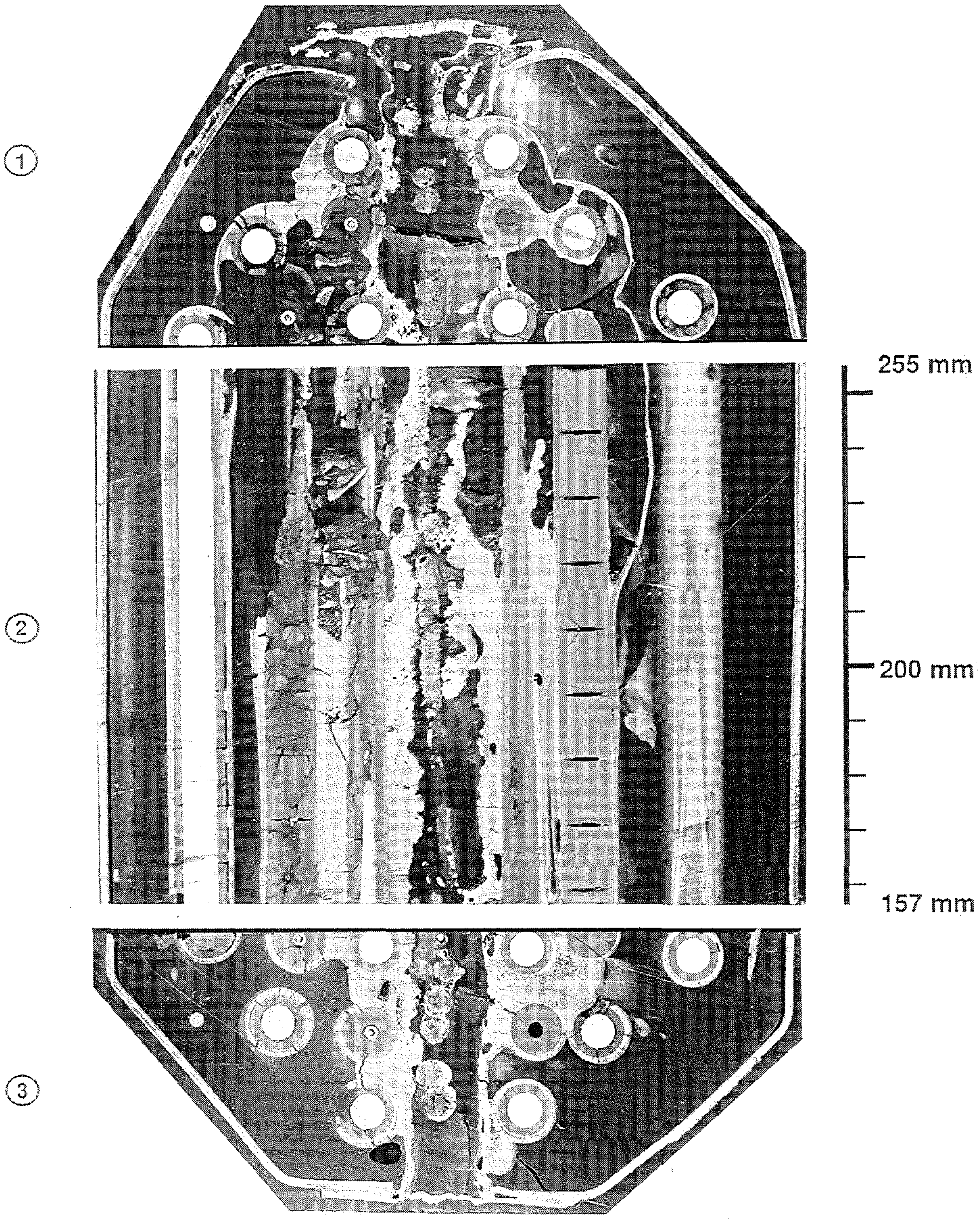

Fig. 123: CORA-28; Combination of horizontal and vertical cross sections, 157 - 255mm

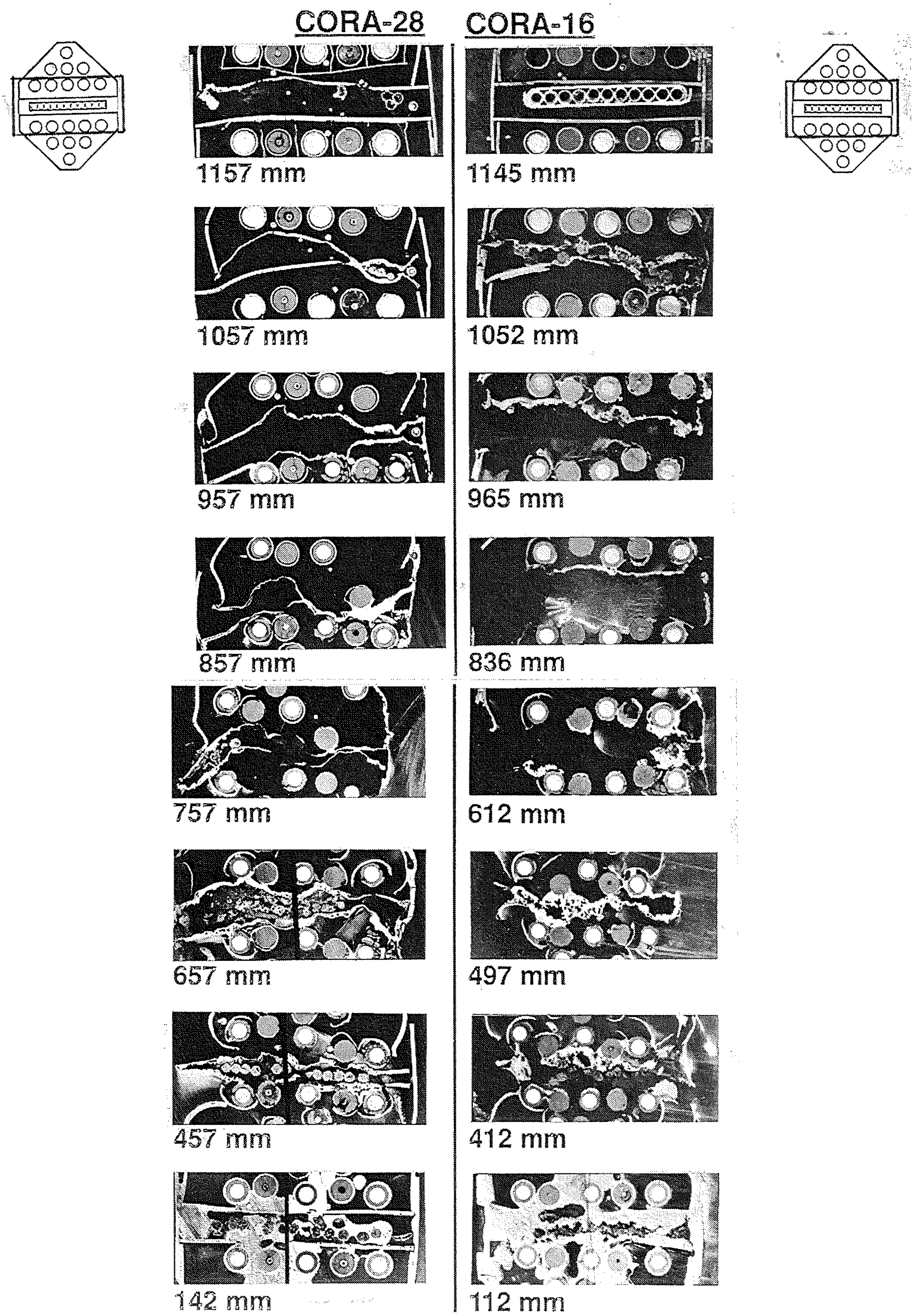

Fig. 124: Comparison of absorber region of preoxidized and standard test CORA-28/CORA-16 (bottom view)

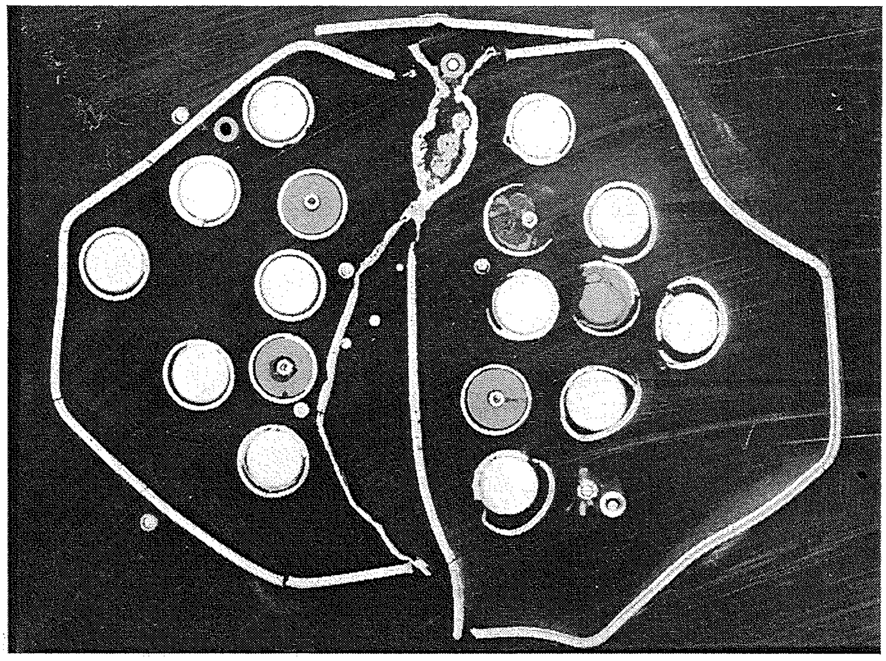

CORA-28

1057mm

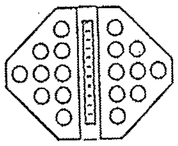

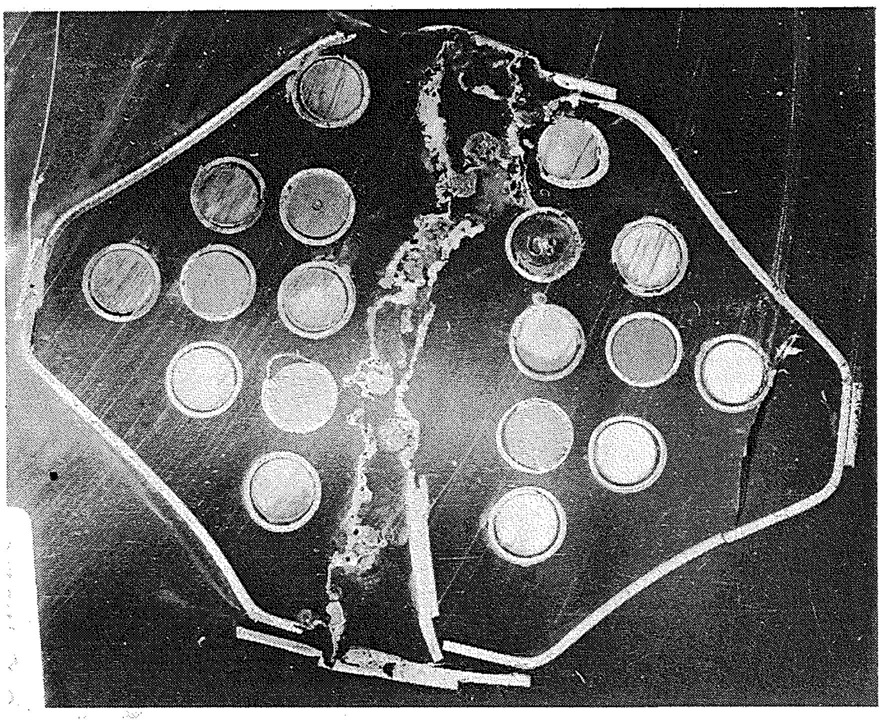

CORA-16

1052mm

Fig. 125: Comparison of cross sections CORA-28/CORA-16, (1057,1052 mm)

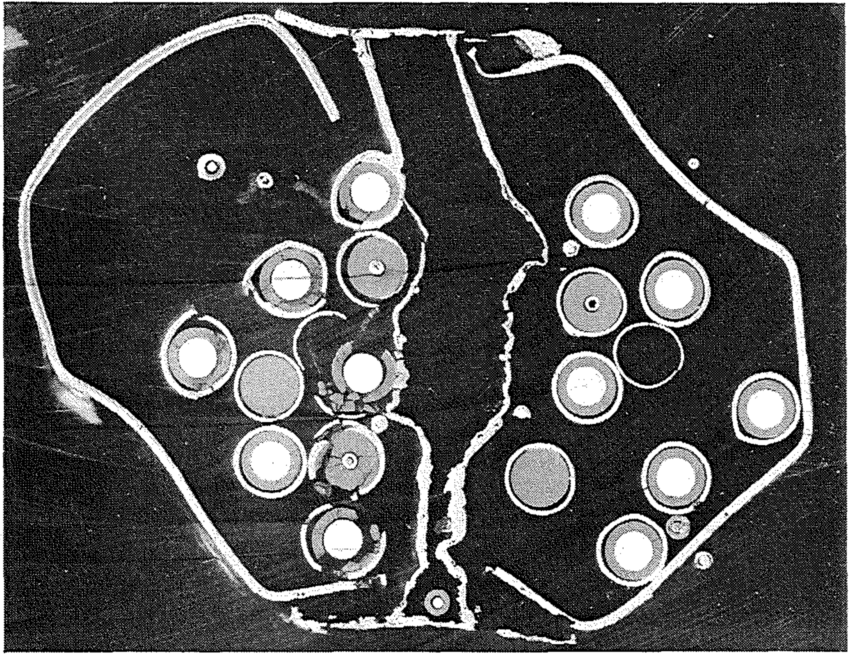

957 mm

CORA-28

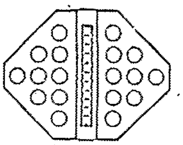

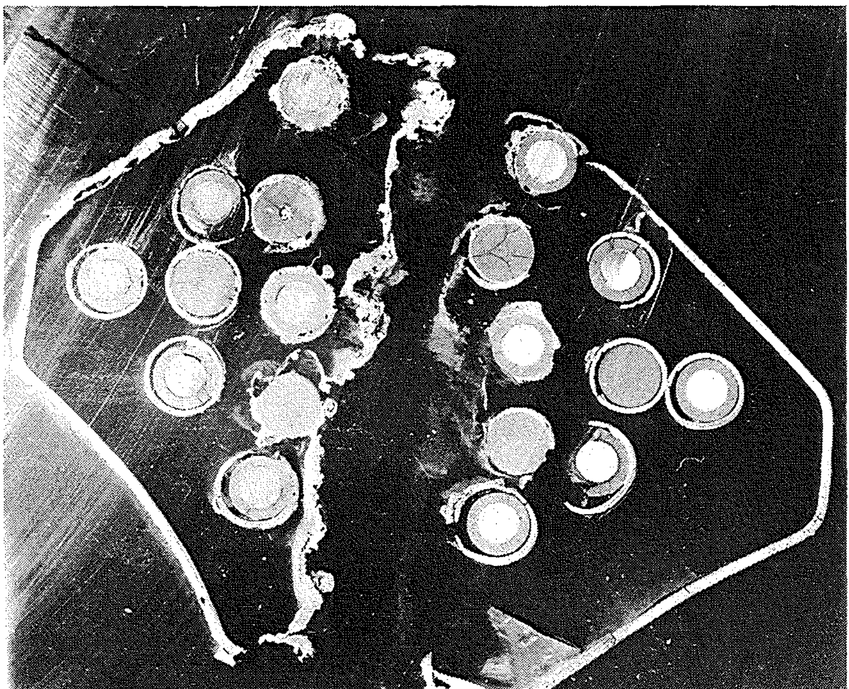

965 mm

CORA-16

Fig. 126: Comparison of cross sections CORA-28/CORA-16, (957, 965 mm)

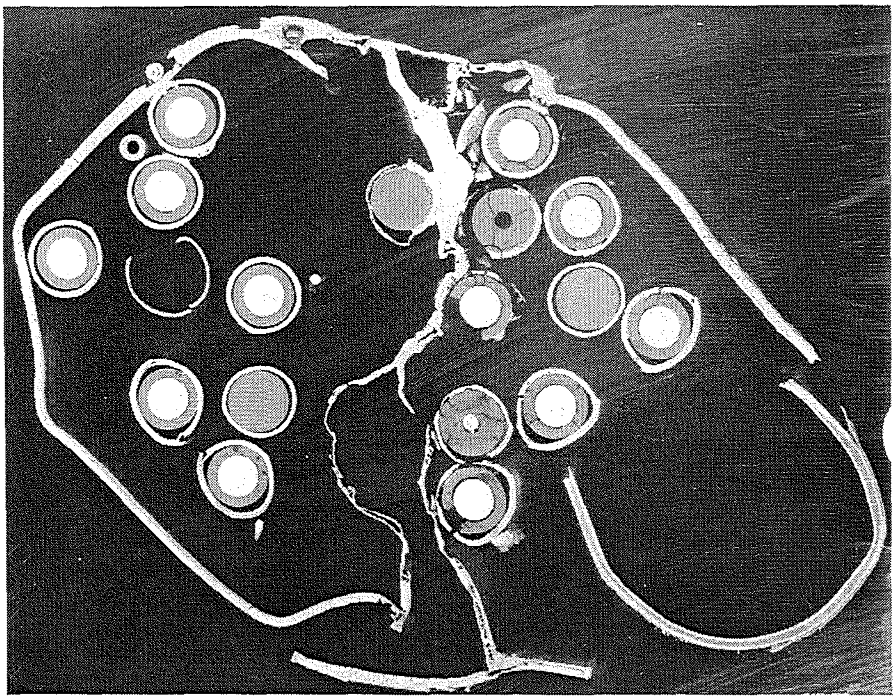

CORA-28

857mm

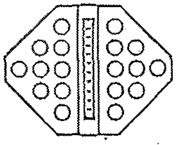

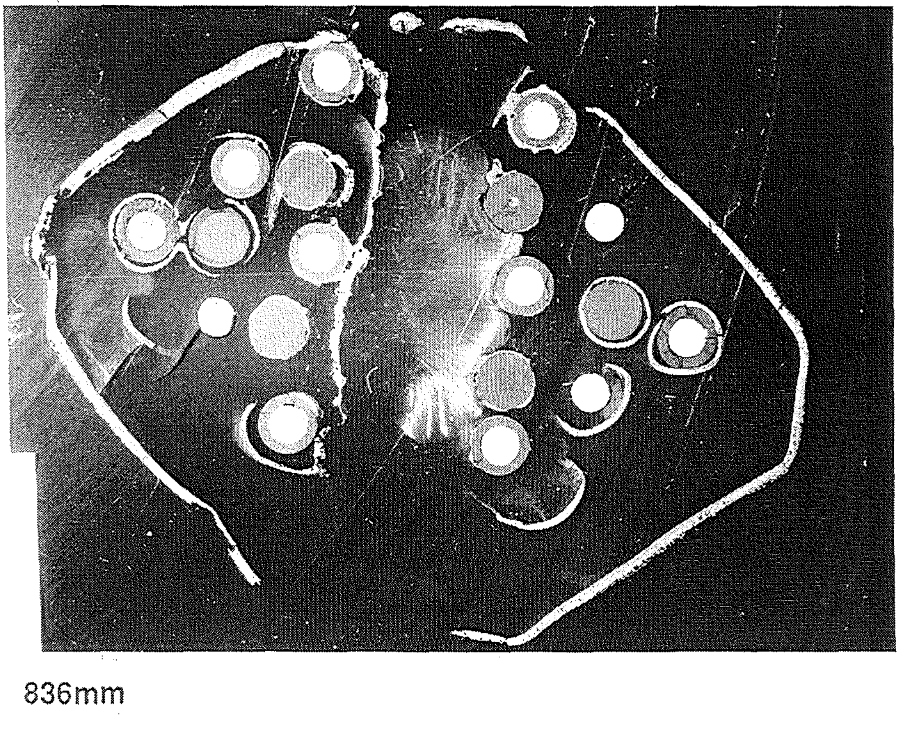

CORA-16

836mm

Fig. 127: Comparison of cross sections CORA-28/CORA-16, (857, 836 mm)

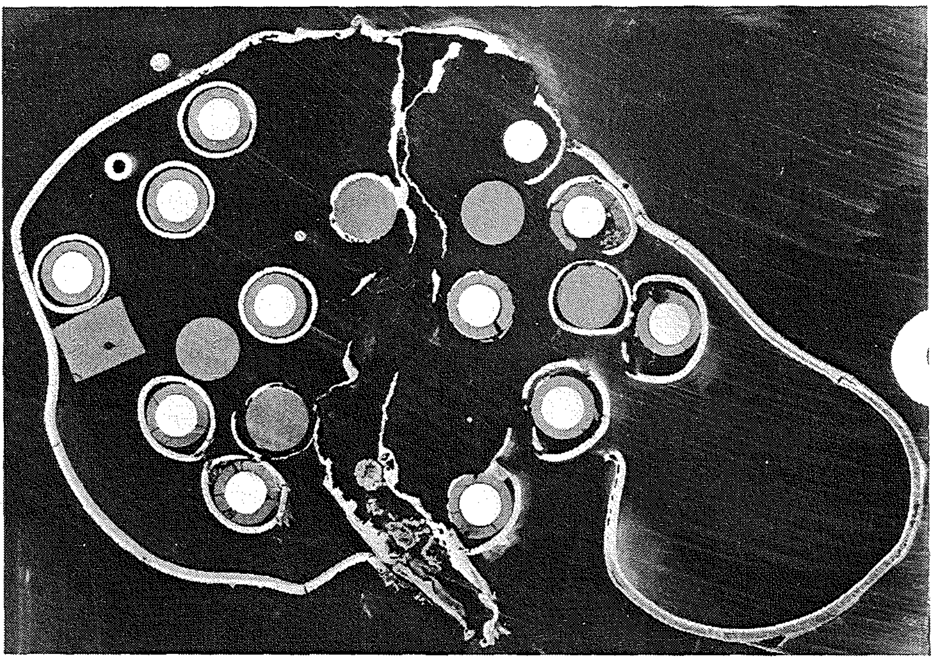

CORA-28

757mm

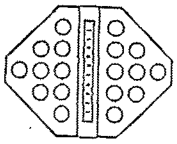

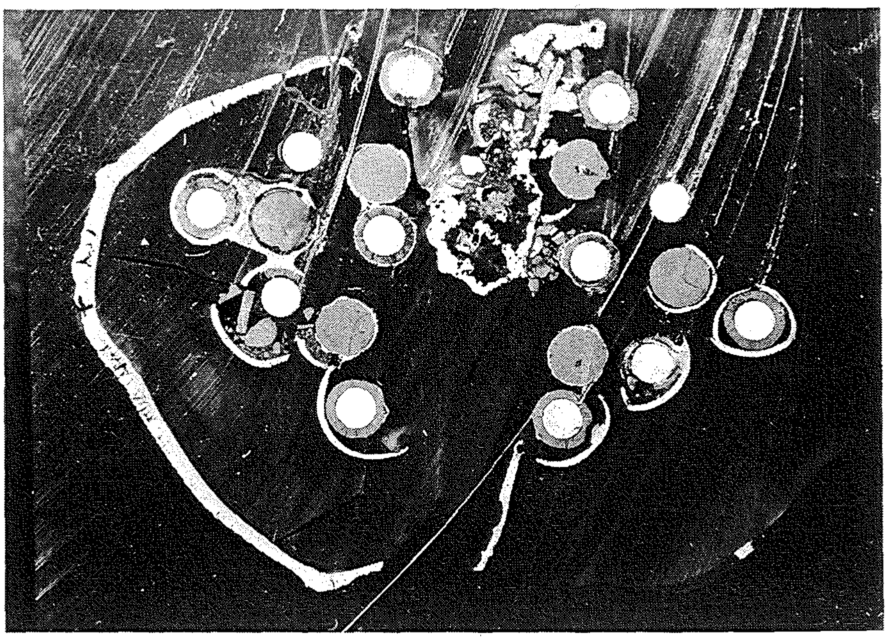

CORA-16

724mm

Fig. 128: Comparison of cross sections CORA-28/CORA-16, (757, 724 mm)

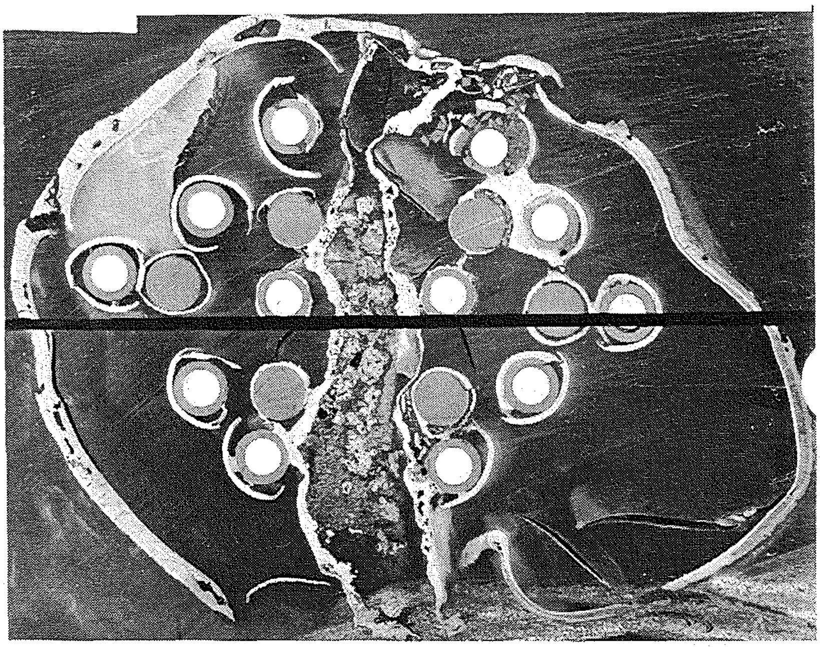

657mm

CORA-28

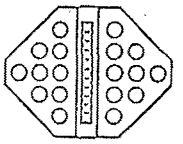

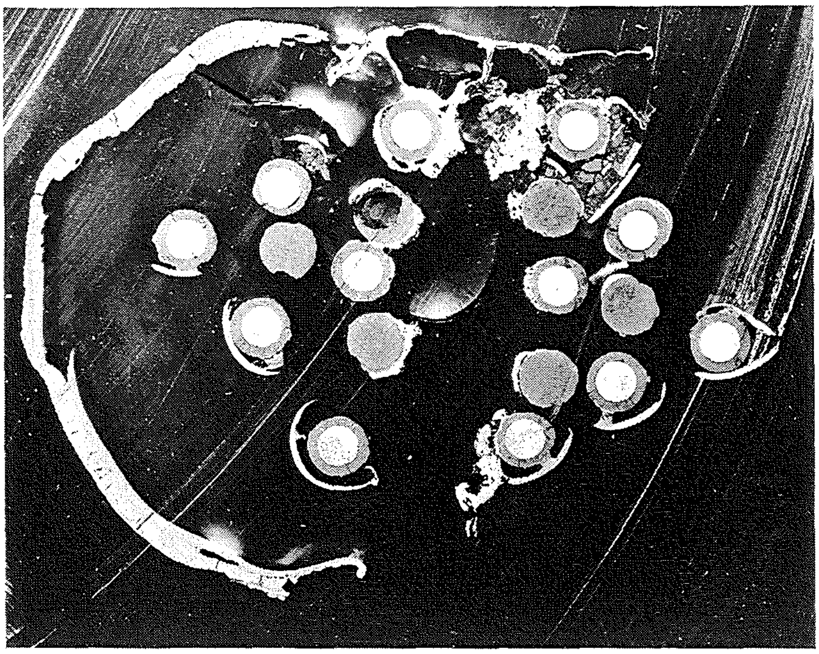

612mm

CORA-16

Fig. 129: Comparison of cross sections CORA-28/CORA-16, (657, 612 mm)

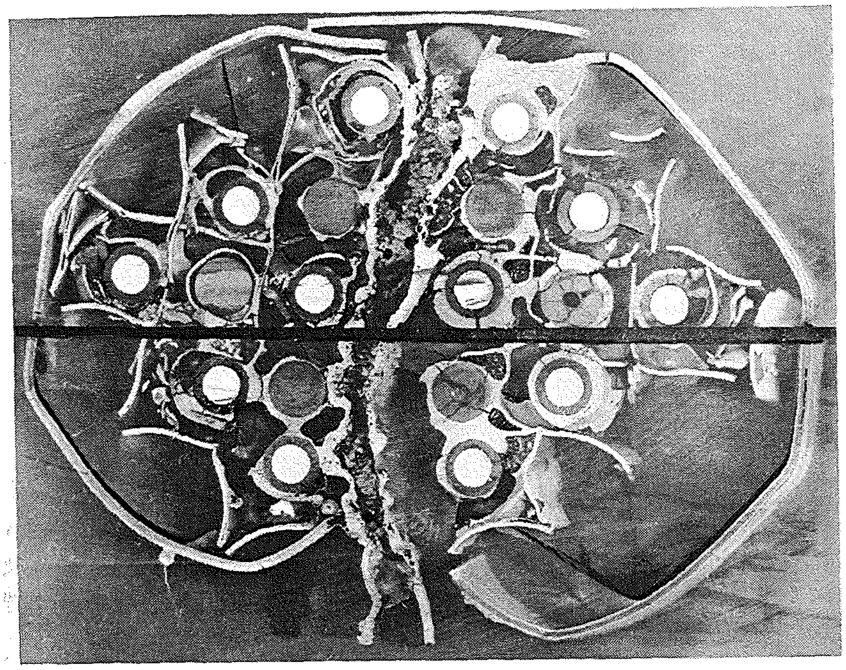

CORA-28

542mm

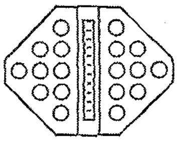

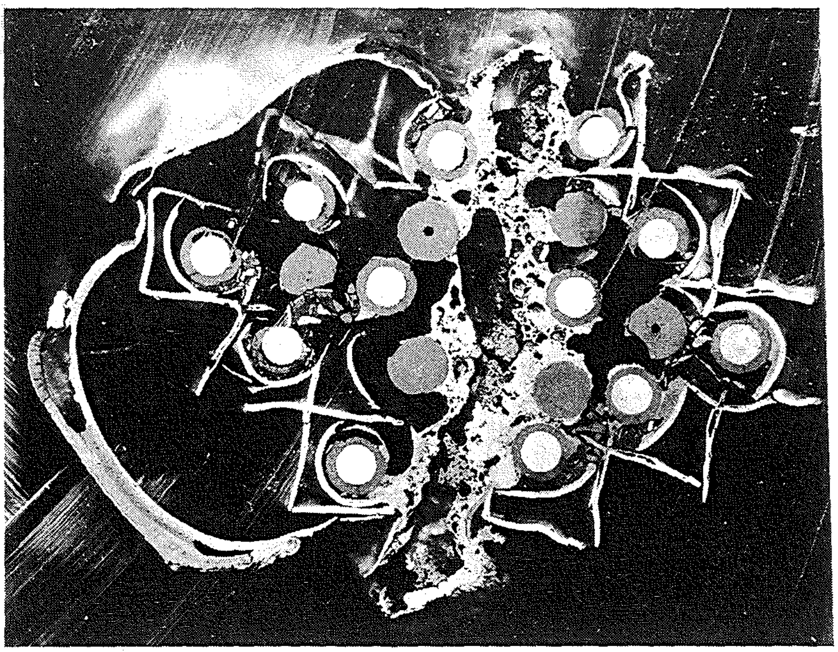

CORA-16

512mm

Fig. 130: Comparison of cross sections CORA-28/CORA-16, (542, 512 mm)

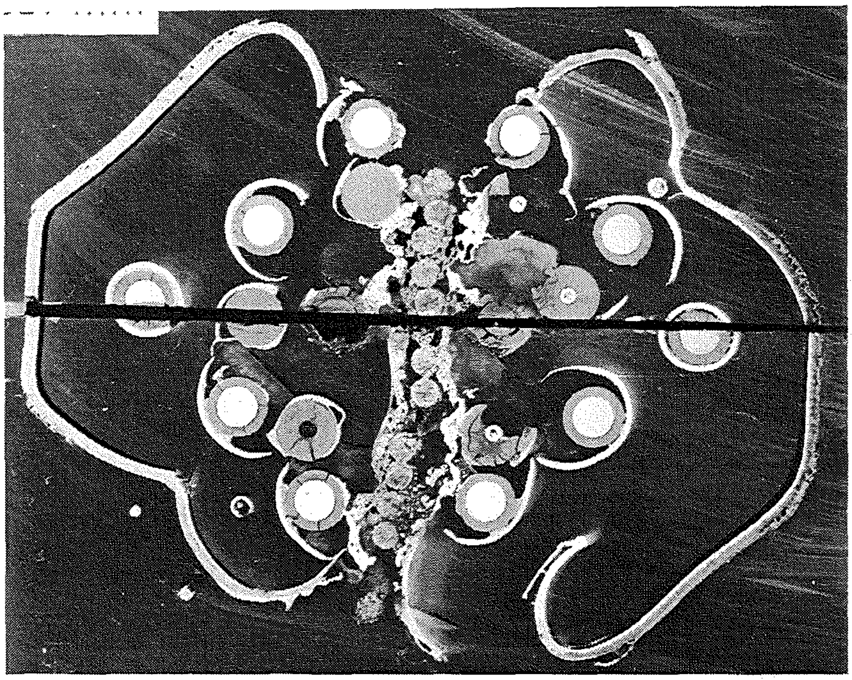

CORA-28

357mm

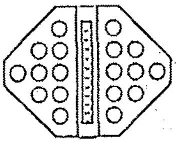

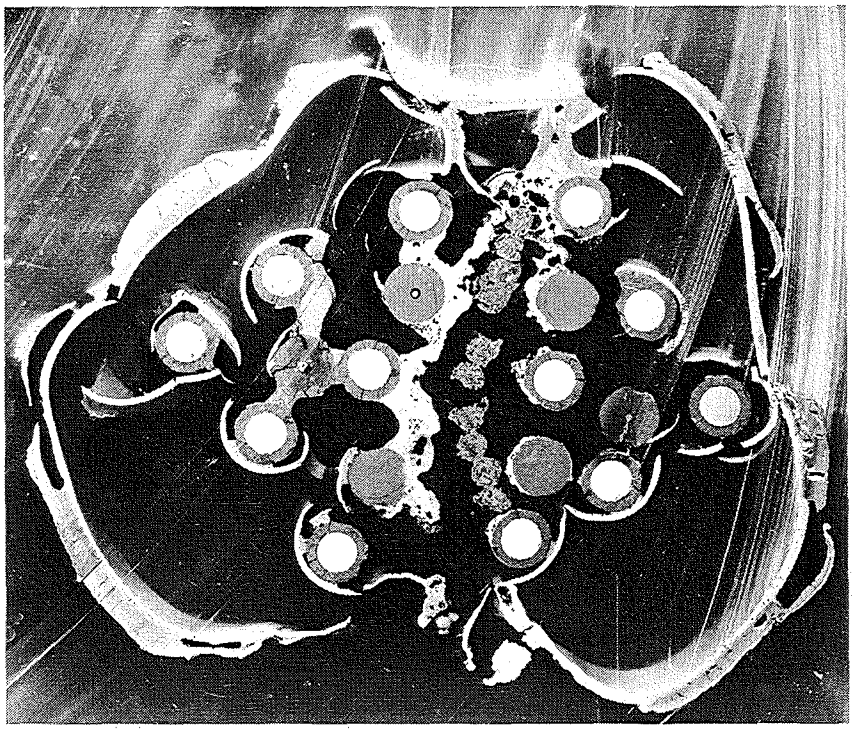

CORA-16

397mm

Fig. 131: Comparison of cross sections CORA-28/CORA-16, (357, 397 mm)

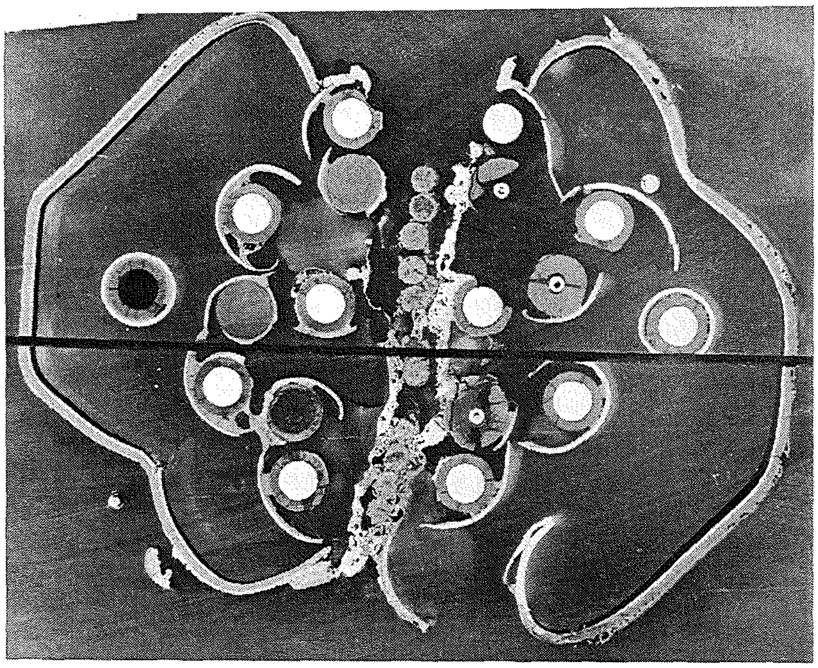

CORA-28

342mm

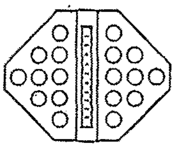

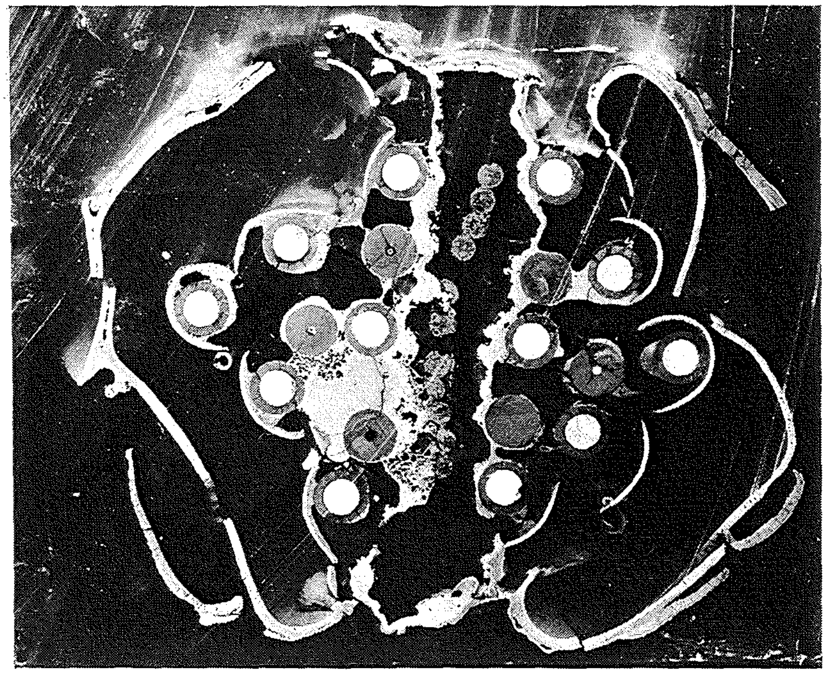

CORA-16

312mm

Fig. 132: Comparison of cross sections CORA-28/CORA-16, (342, 312 mm)

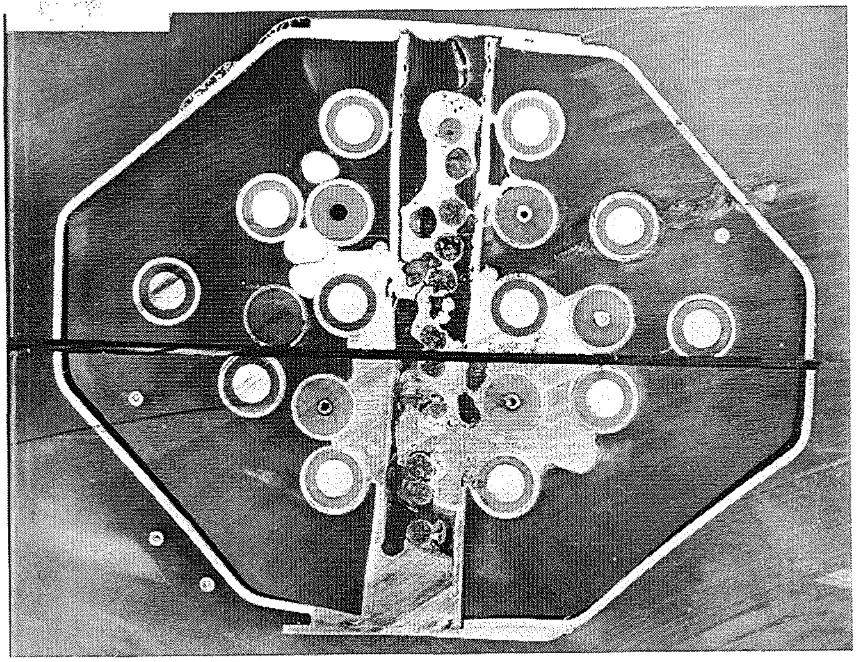

142mm

CORA-28

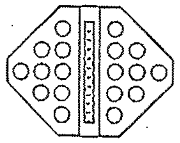

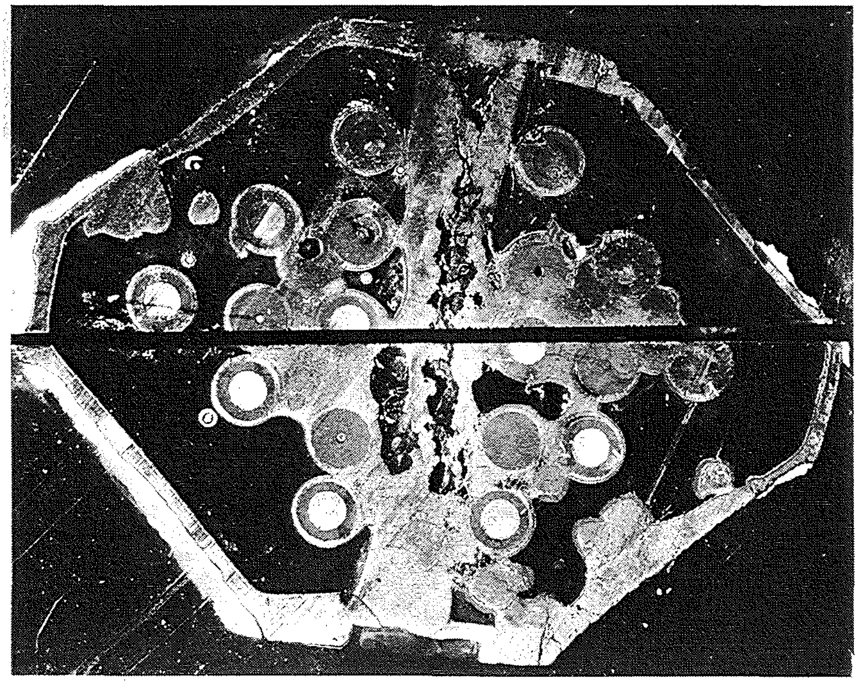

112mm

CORA-16

Fig. 133: Comparison of cross sections CORA-28/CORA-16, (142,112 mm)

APPENDIX A

Test Data of the pre-heating phase

Figures: A1 - A32

Complete set of cross sections

Figures: A33 - A41

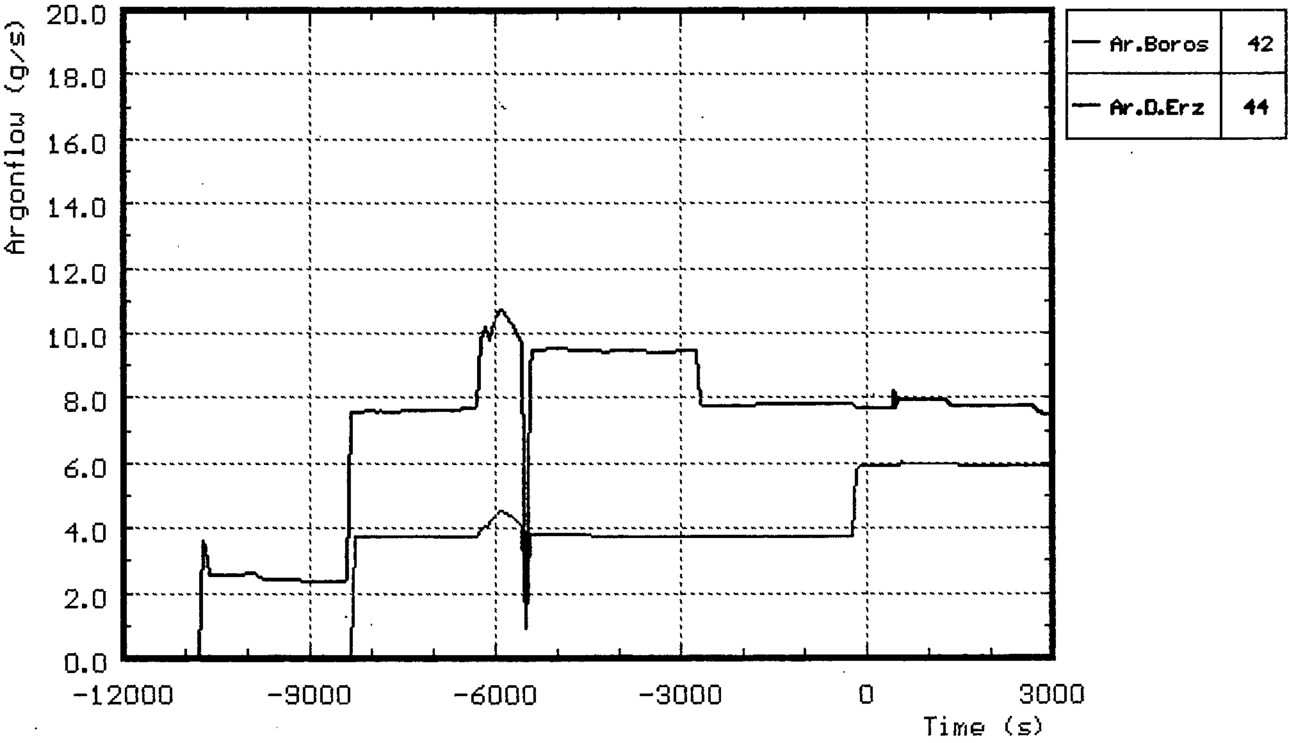

Fig. A1: CORA-28; Argon input prior to test

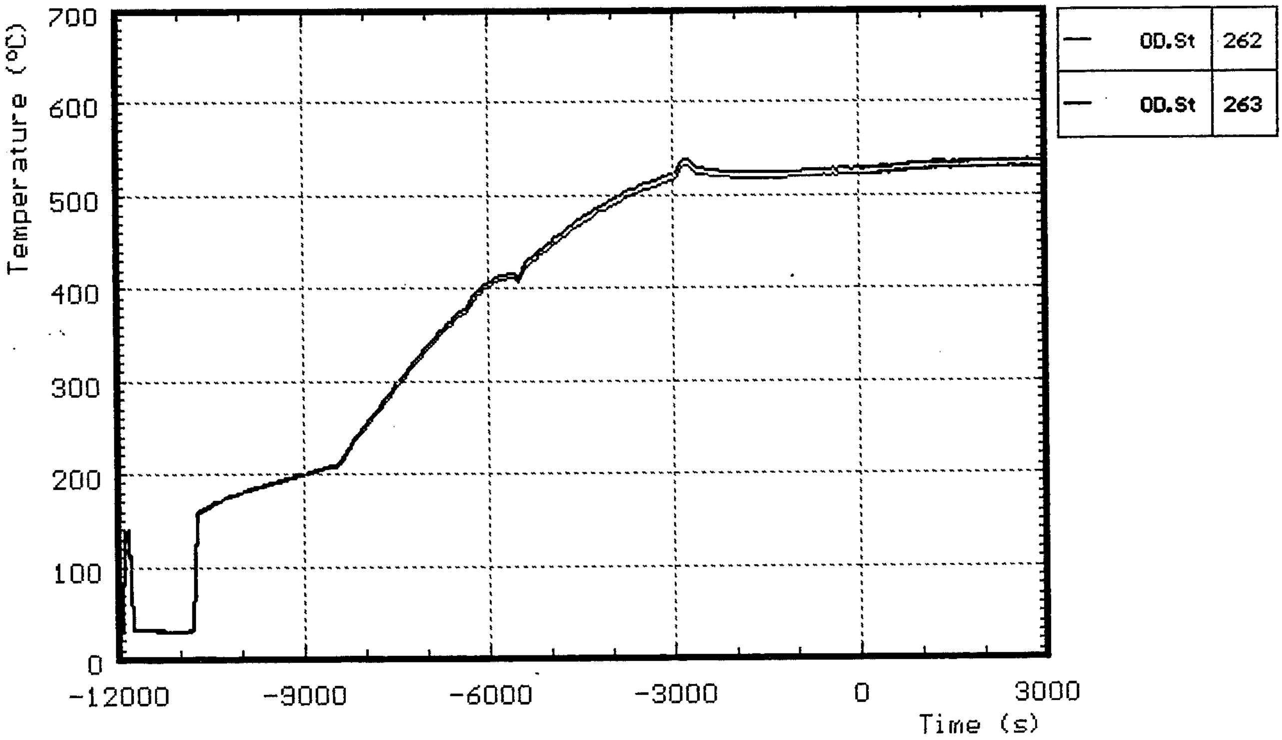

Fig. A2: CORA-28; Temperature at the entrance of the bundle prior to test

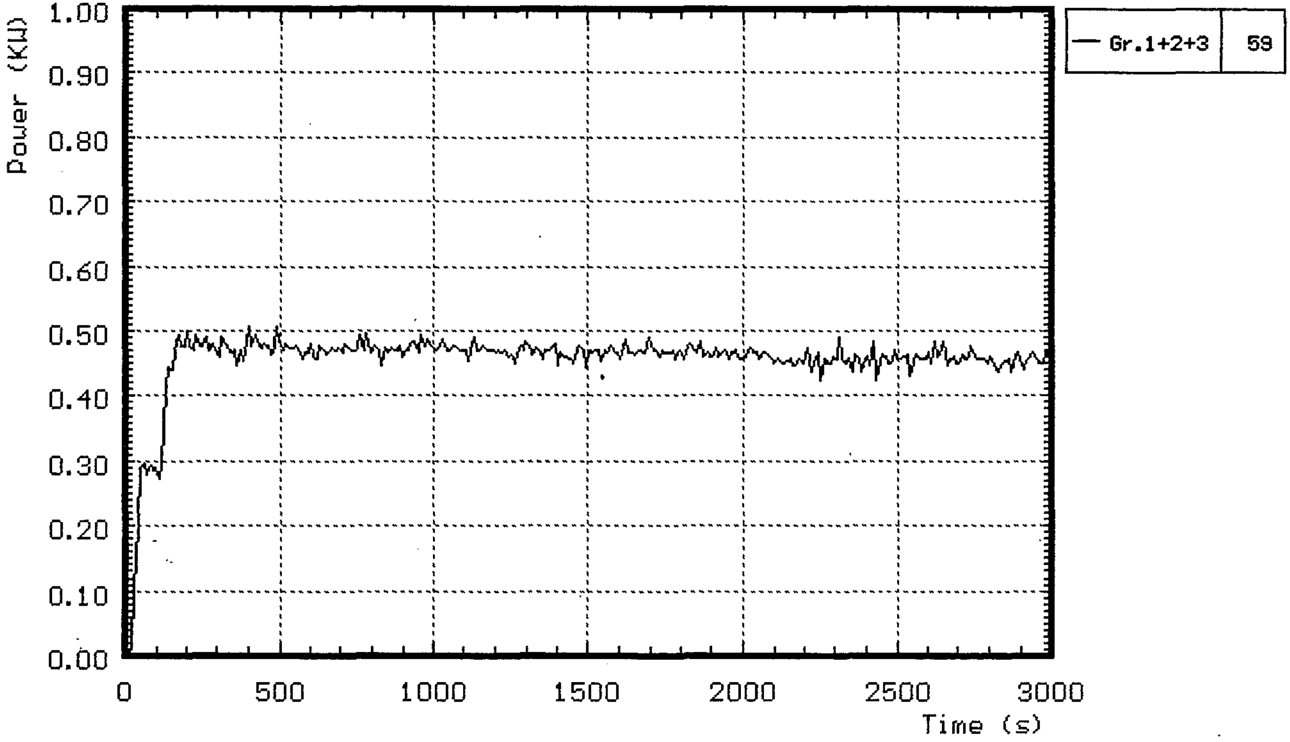

Fig. A3: CORA-28; Power input during pre-heat phase

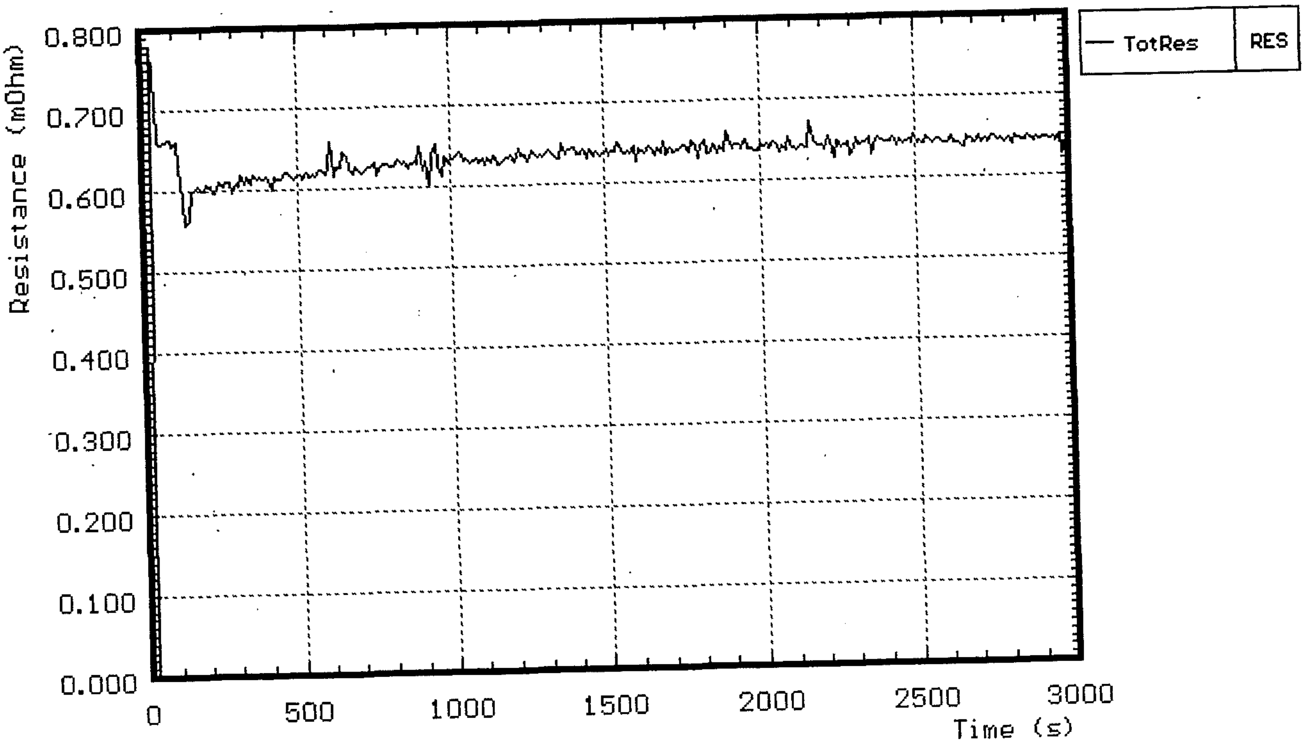

Fig. A5: CORA-28; Resistance of bundle during pre-heat phase

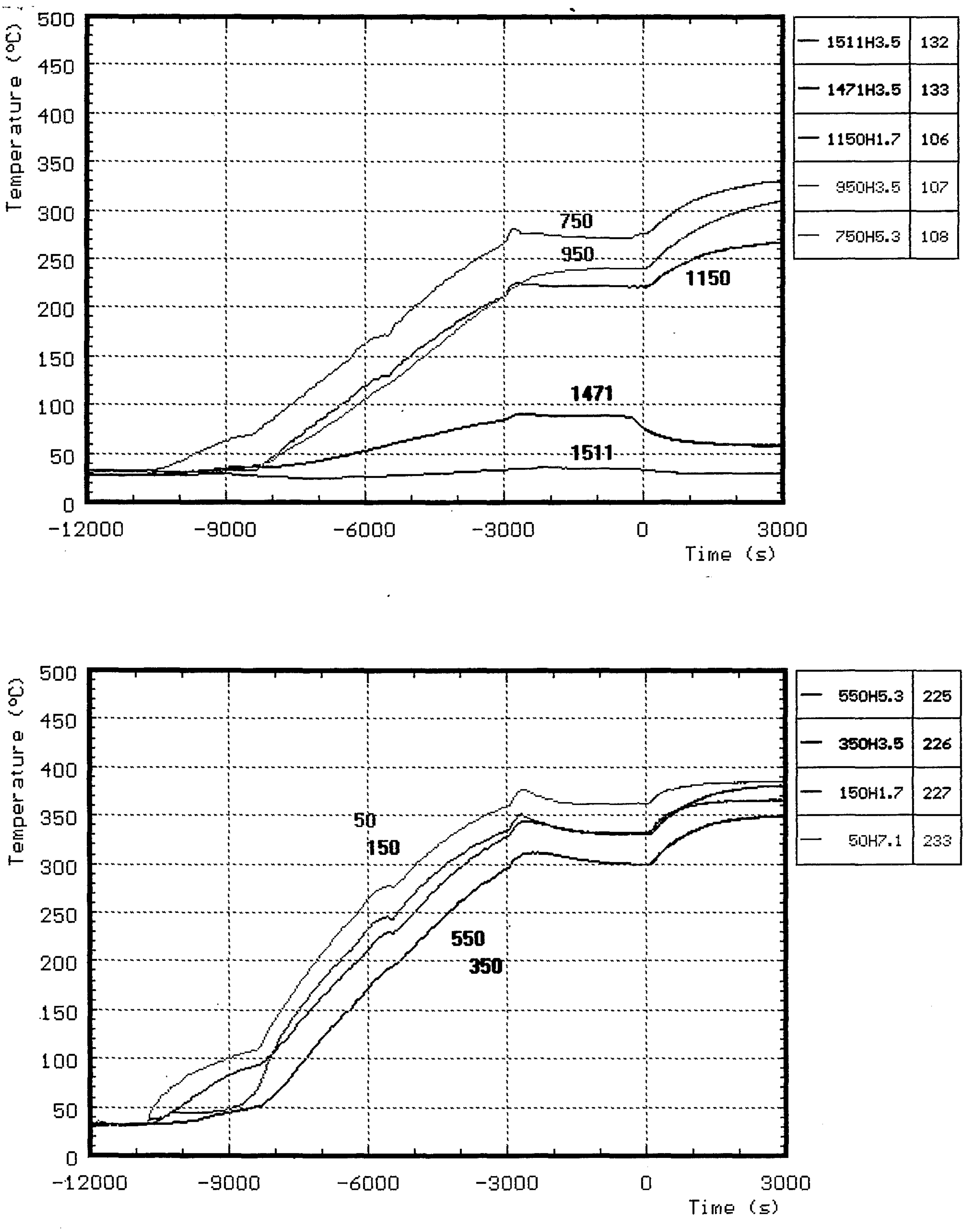

Fig. A6: CORA-28; Temperatures of heated rods, pre-heat phase

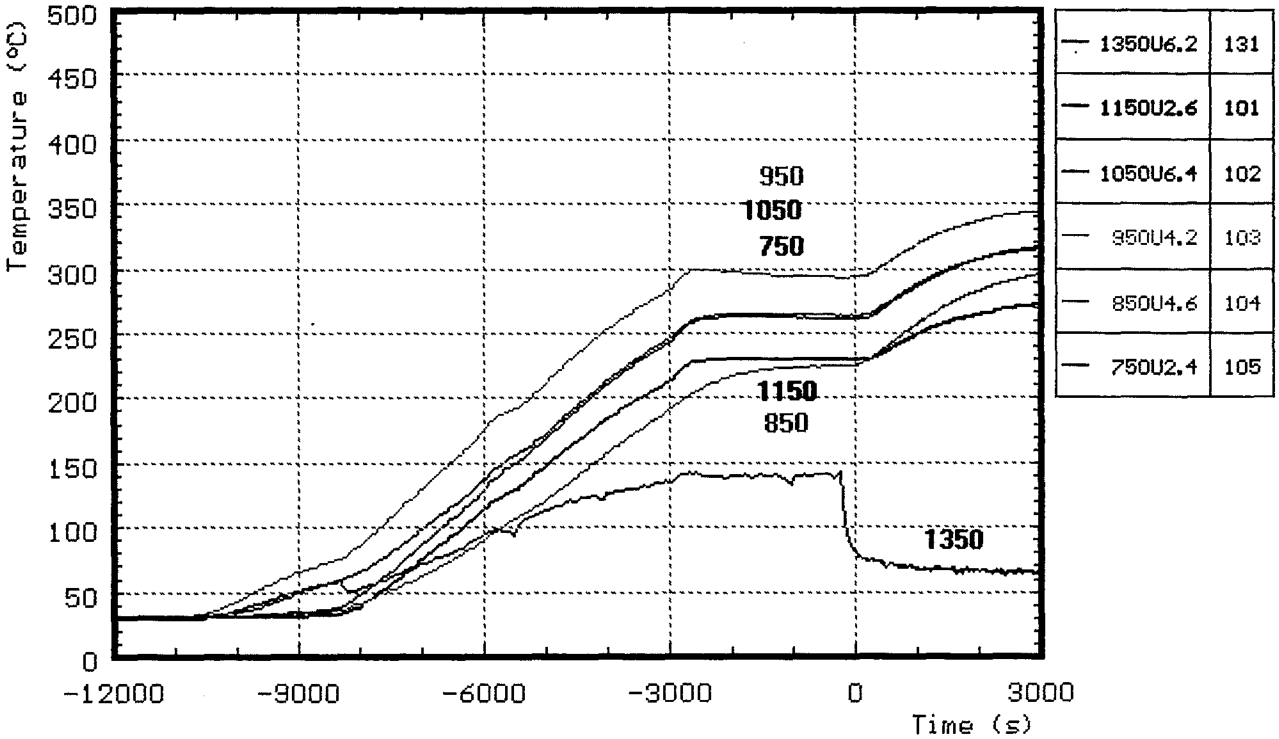

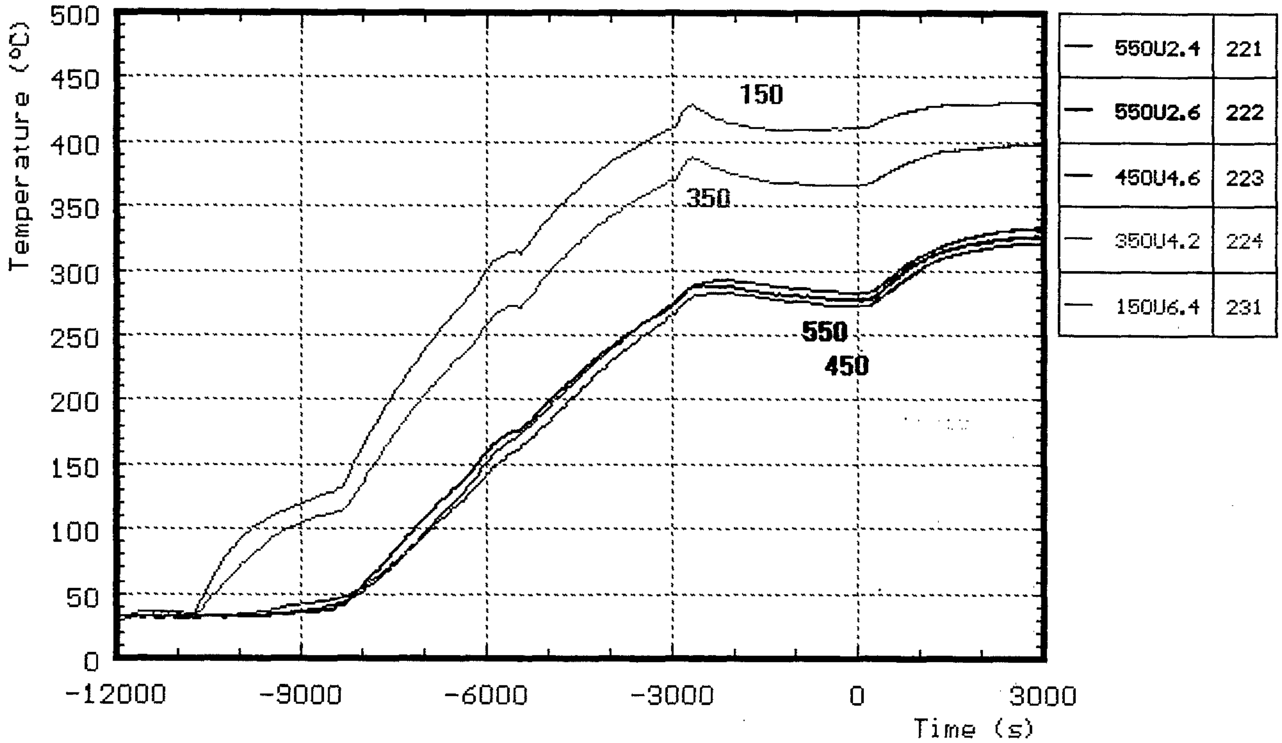

Fig. A7: CORA-28; Temperatures of unheated rods, pre-heat phase

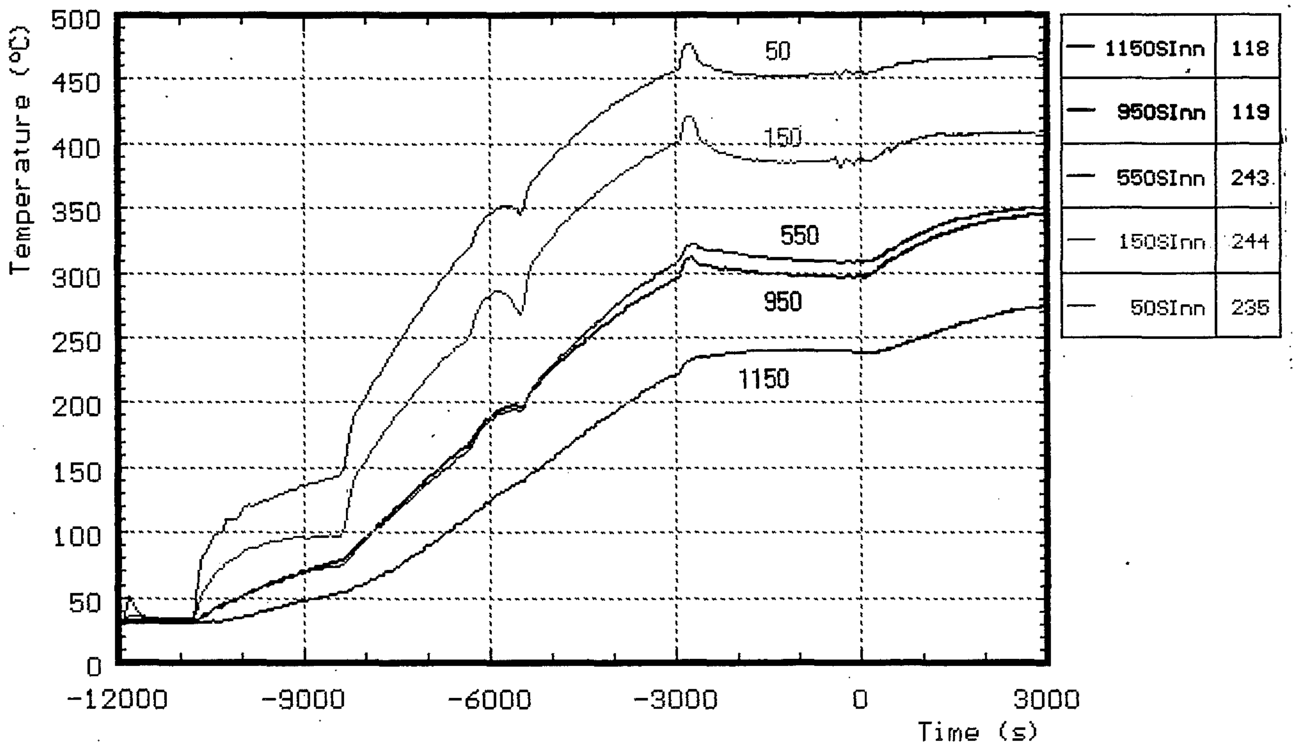

Fig. A8: Temperatures of the channel box wall

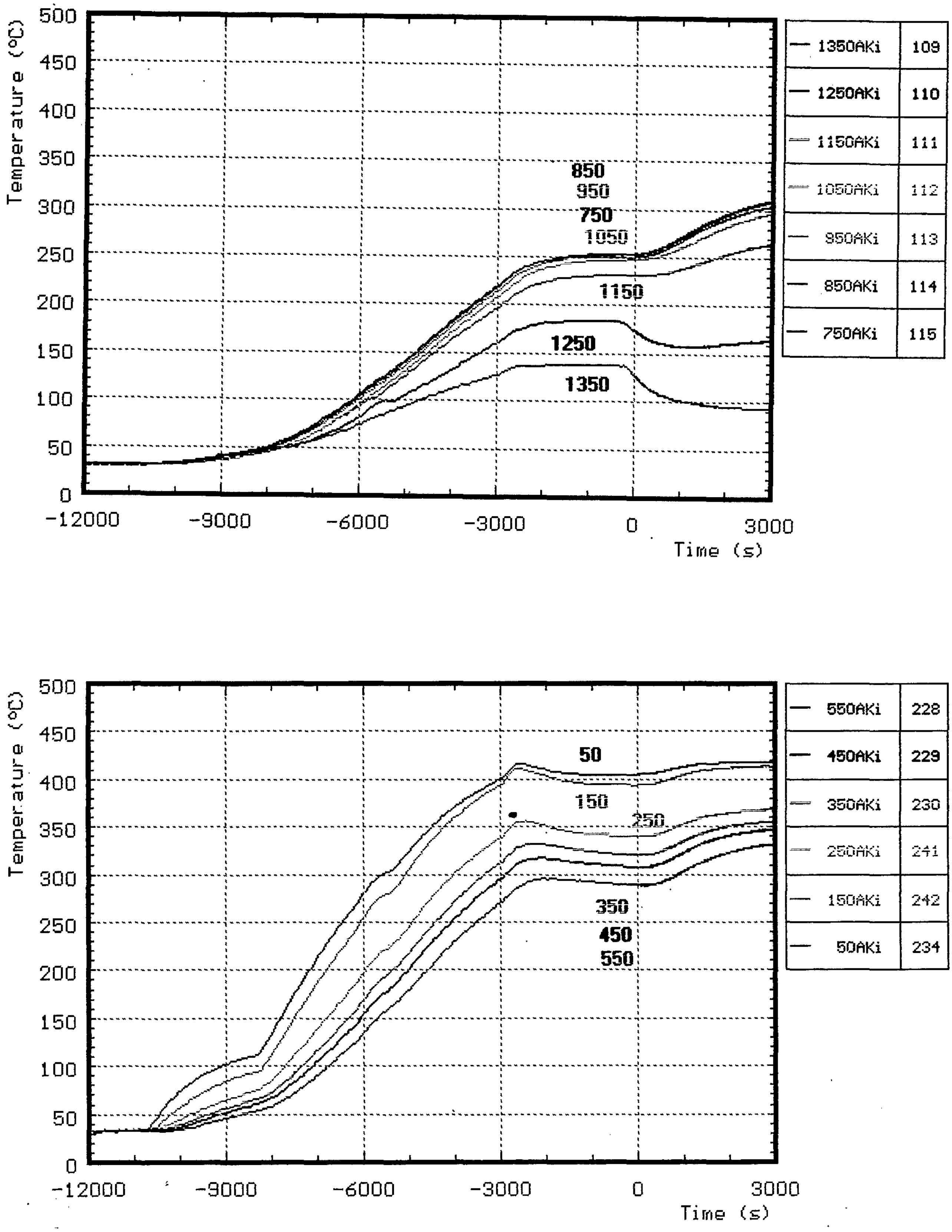

Fig. A9: Temperatures of the absorber blade

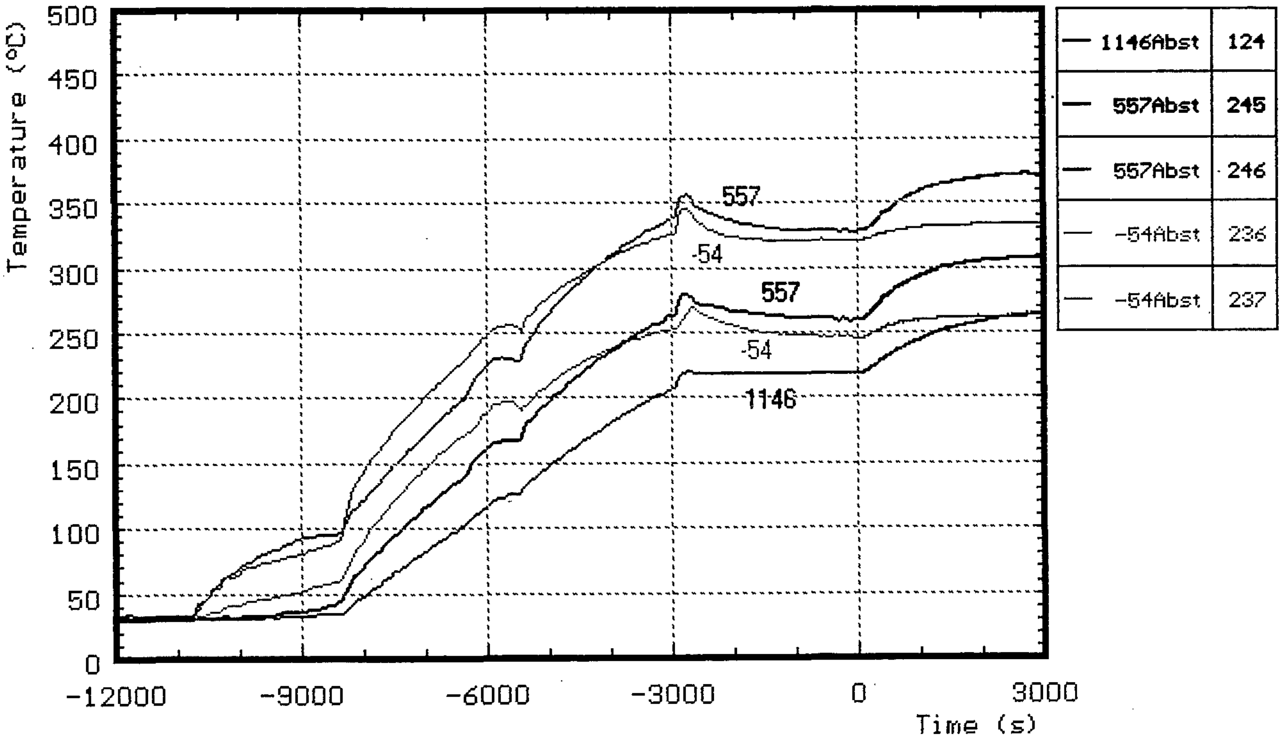

Fig. A10: Temperatures of the spacers used in test CORA-28, pre-heat phase

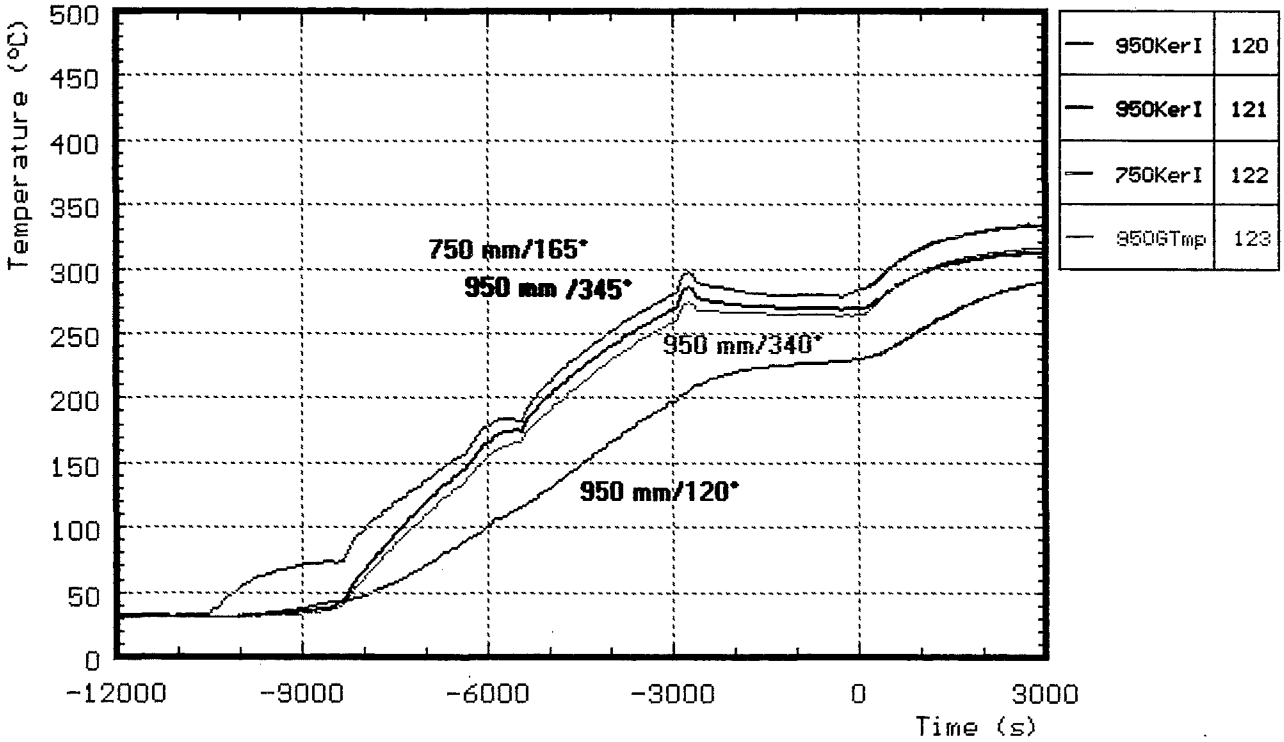

Fig. A11: Temperatures measured with ceramic-protected TCs; pre-heat phase

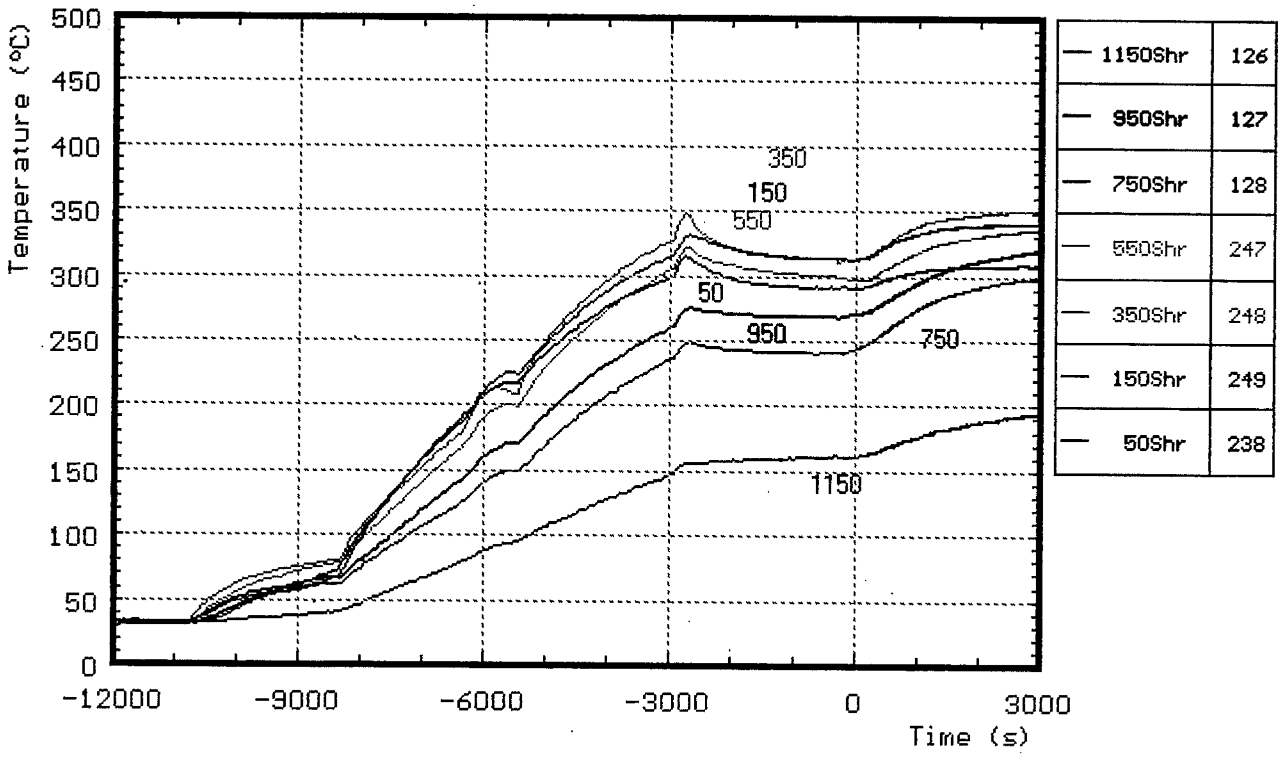

Fig. A12: Temperatures of the outer side of shroud, pre-heat phase

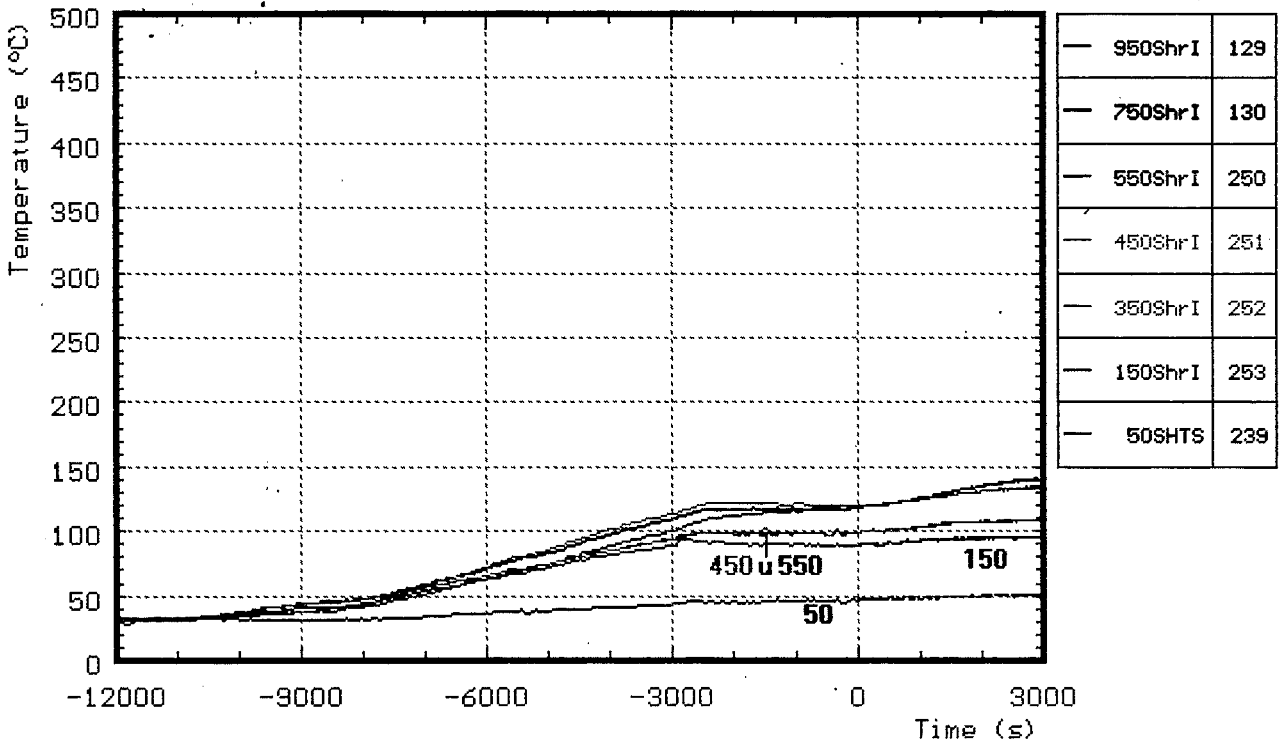

Fig. A13: Temperatures of the shroud insulation, pre-heat phase

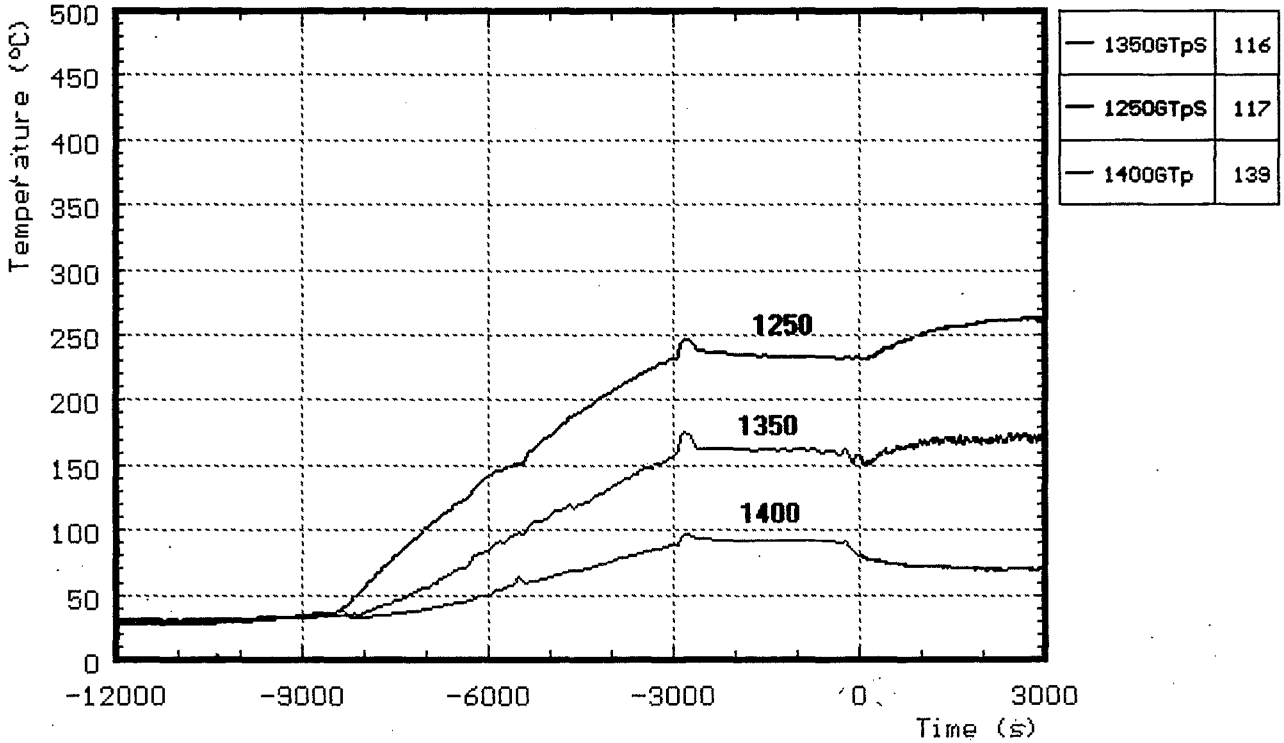

Fig. A14: Gas temperatures measured above the heated zone, pre-heat phase

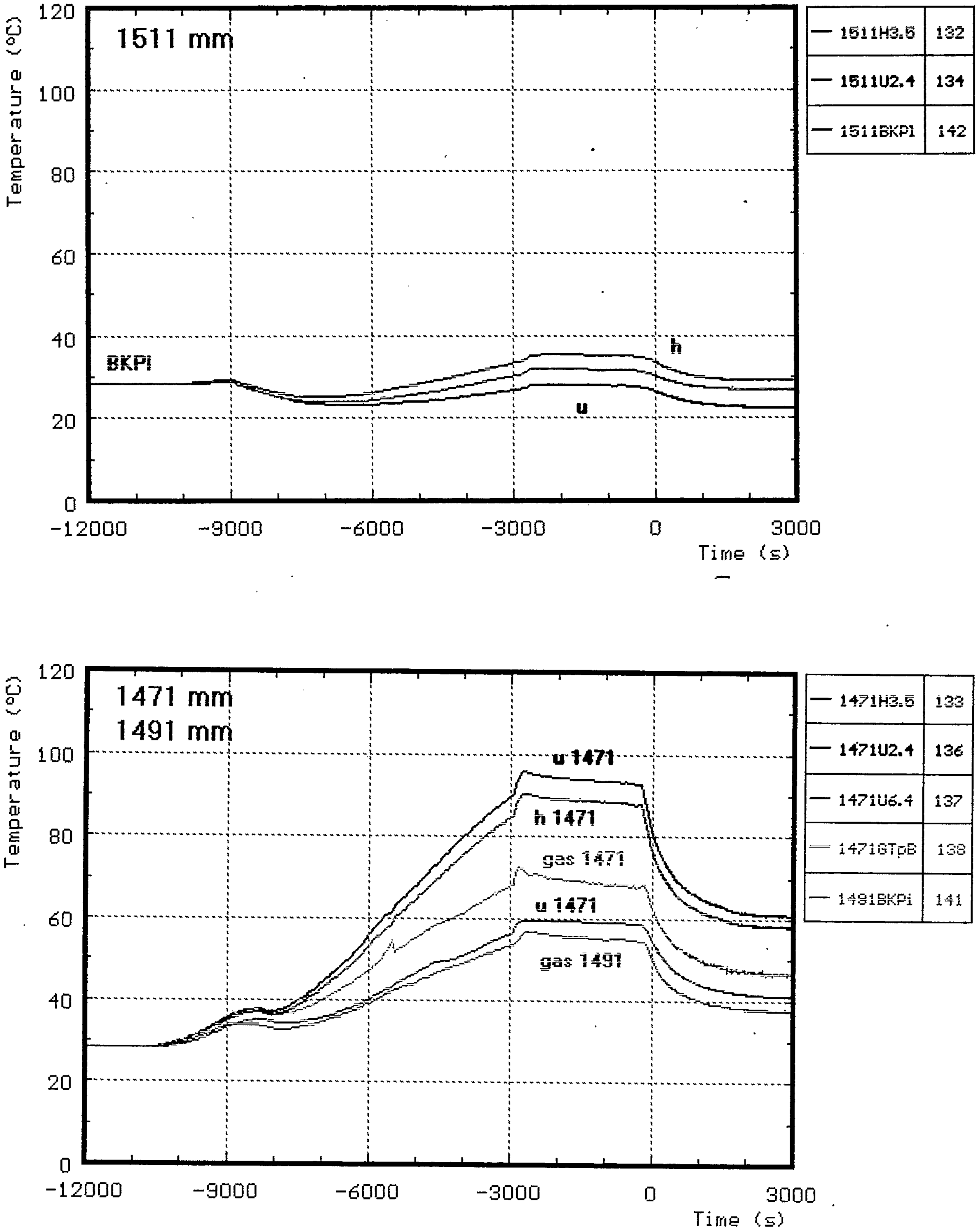

h : heated rods
u : unheated rods

BKPl : bundle heat plate
gas : gas temperature

Fig. A15: CORA-28; Temperatures at elevations given, pre-heat phase (1511, 1471-1491 mm)

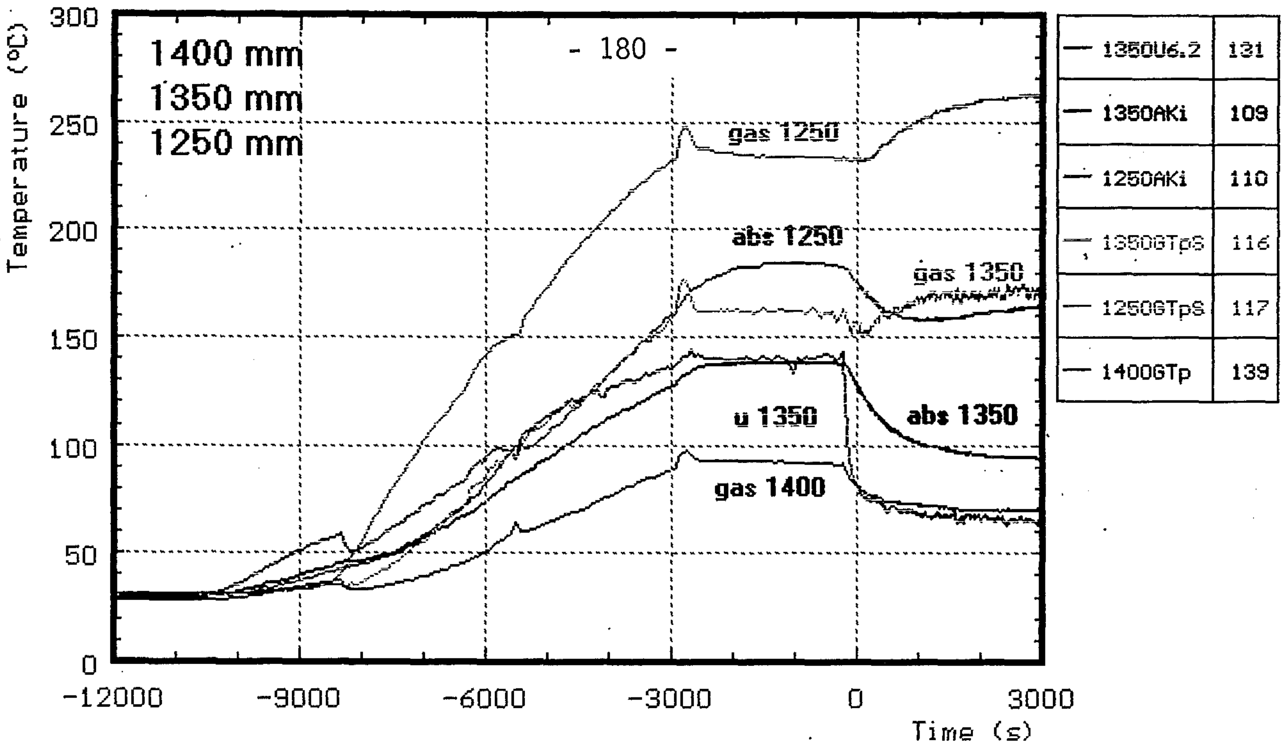

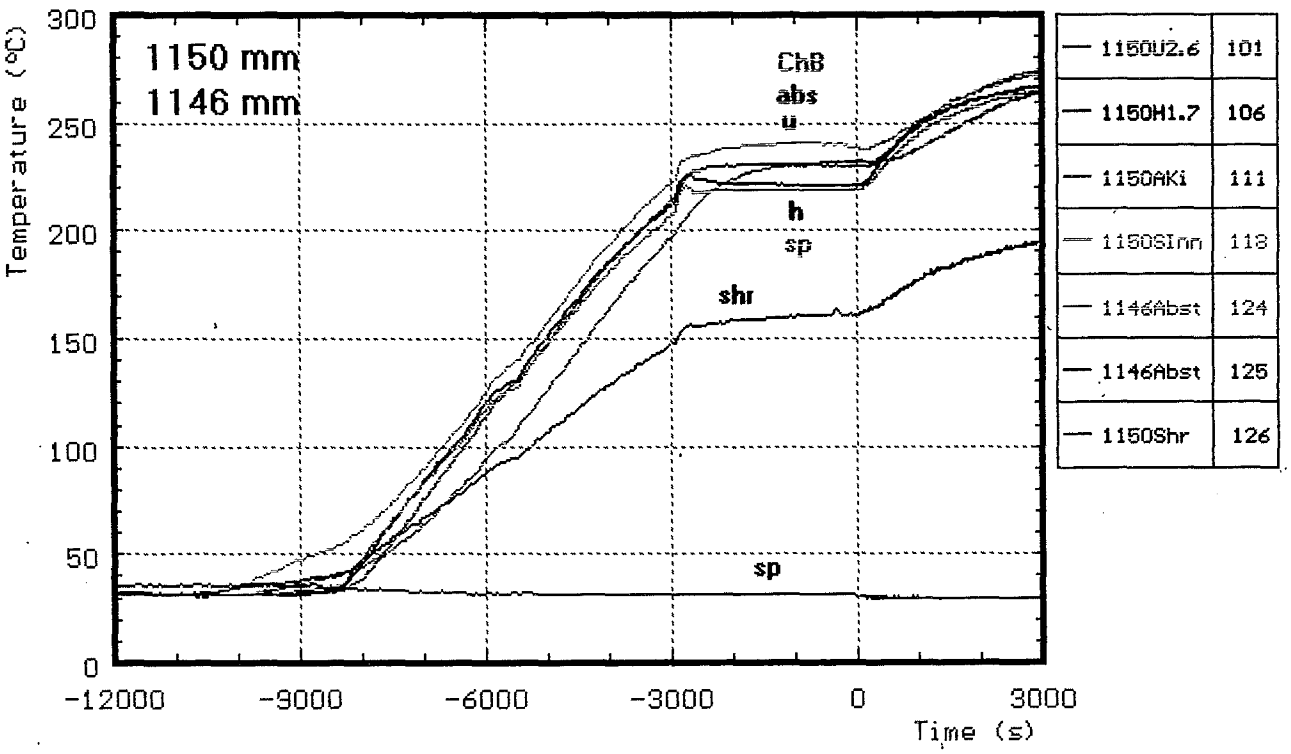

h : heated rods
u : unheated rods
sp : spacer
ChB : channel box wall
abs : in absorberblade
gas : gas temperature
shr : on shroud

Fig. A16: CORA-28; Temperatures at elevations given, pre-heat phase (1400-1250, 1150, 1146 mm)

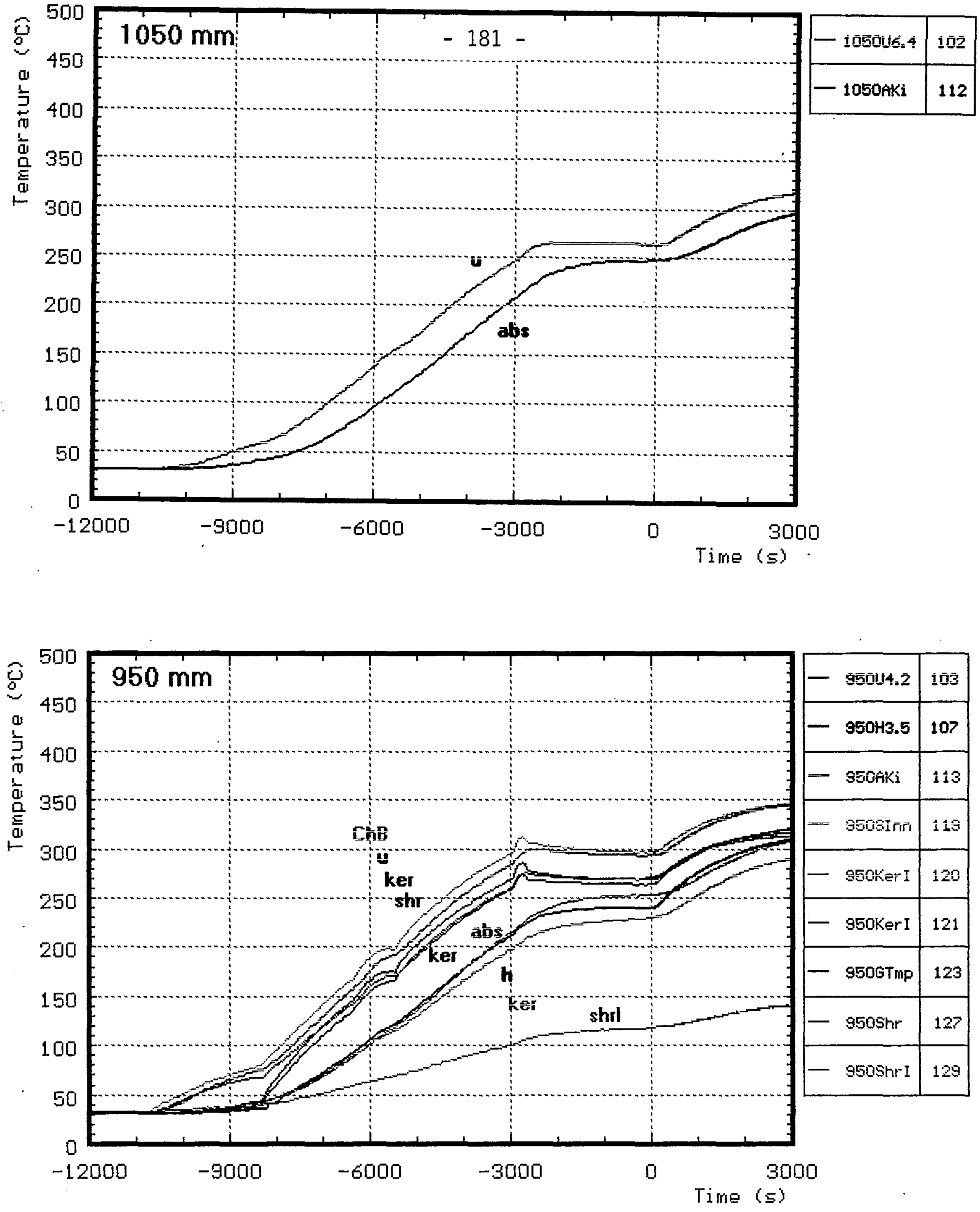

h : heated rods
u : unheated rods
shrl : shroud insolation
ChB : channel box wall

abs : in absorberblade
ker : ceramic protected termocouples
shr : on shroud

Fig. A17: CORA-28; Temperatures at elevations given, pre-heat phase (1050, 950 mm)

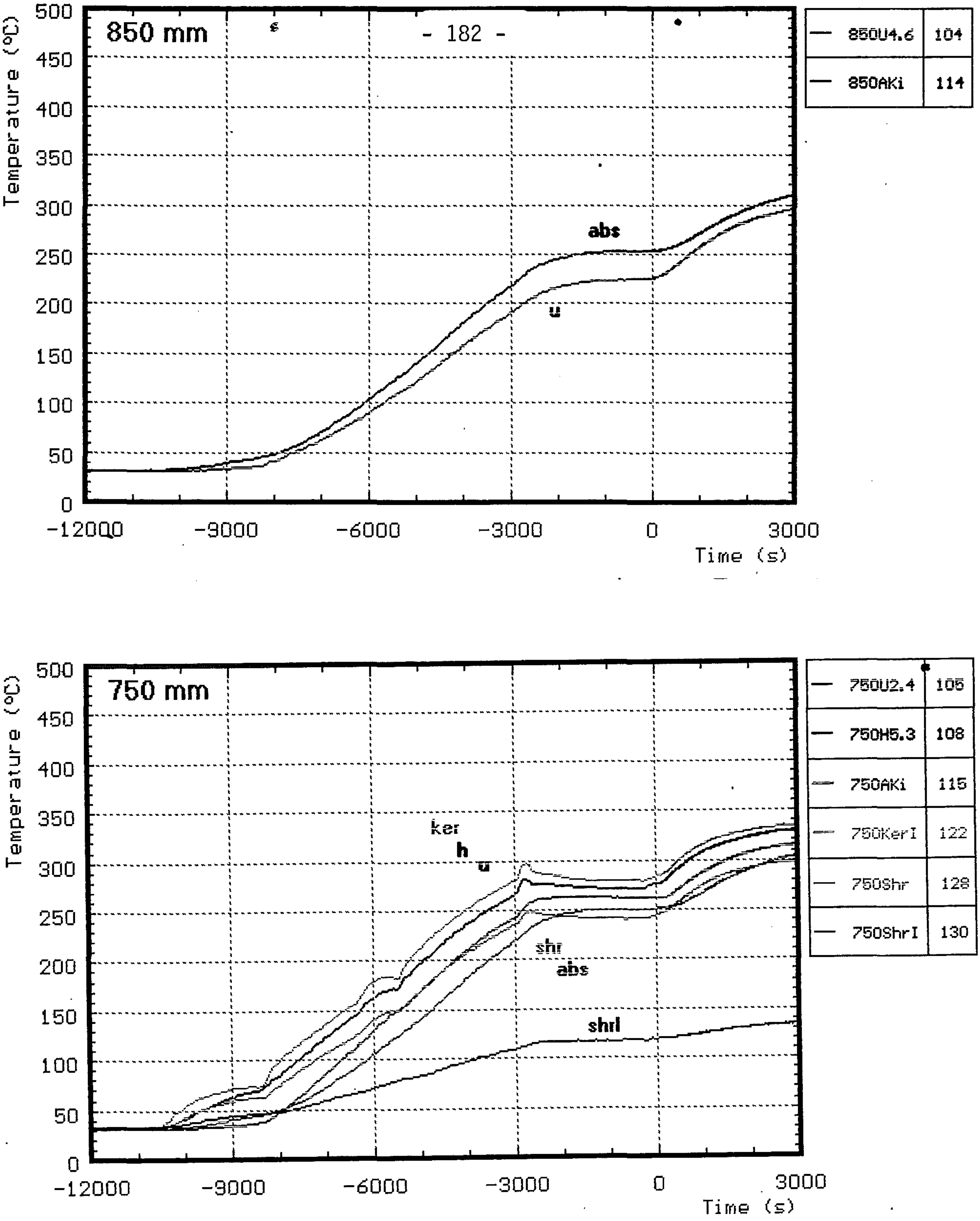

h : heated rods
u : unheated rods
shrl : shroud insolation
abs : in absorberblade
ker : ceramic protected termocouples
shr : on shroud

Fig. A18: CORA-28; Temperatures at elevations given, pre-heat phase (850, 750 mm)

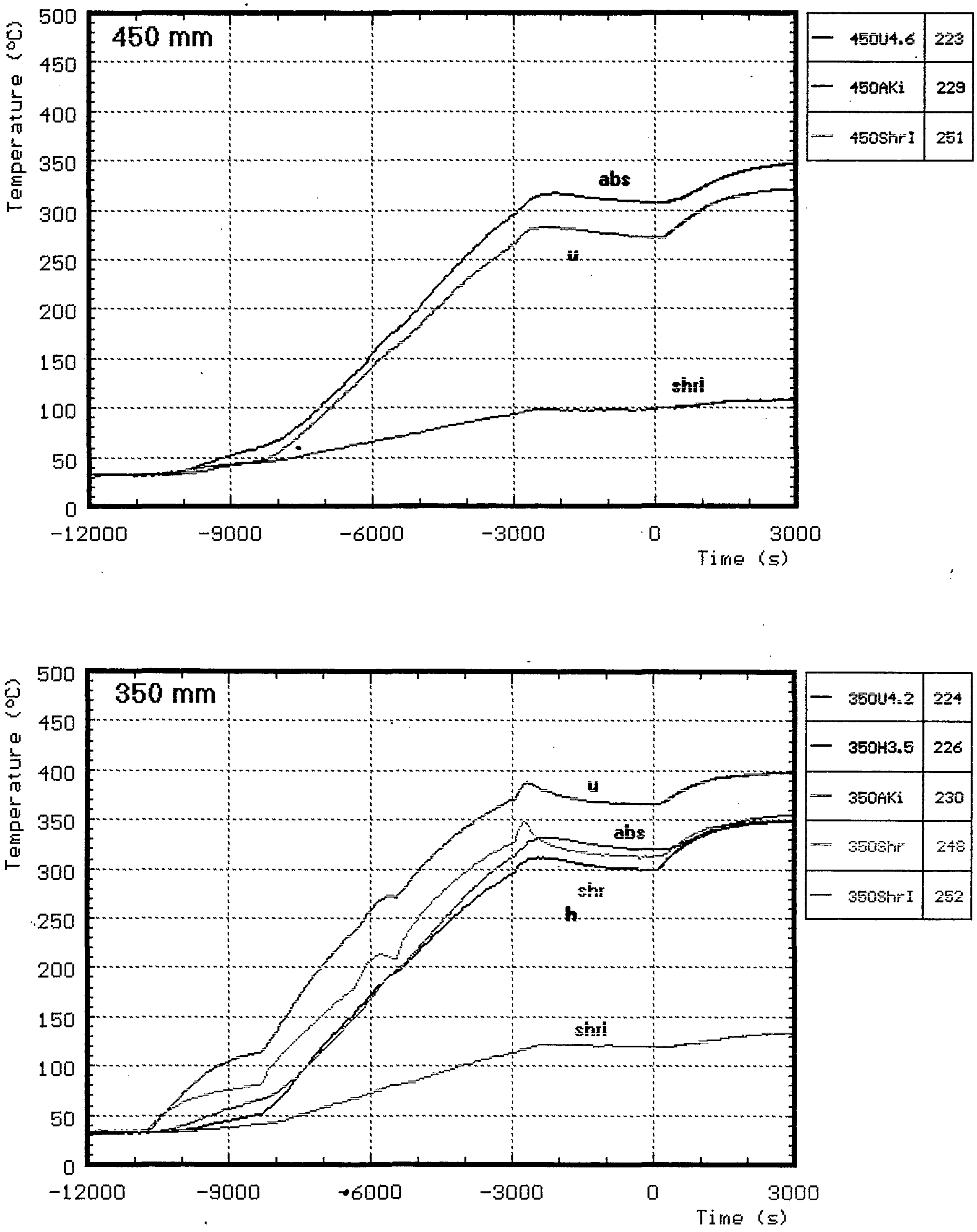

h	: heated rods	abs	: in absorberblade
u	: unheated rods	shr	: on shroud
shrl	: shroud insolation		

Fig. A19: CORA-28; Temperatures at elevations given, pre-heat phase (450, 350 mm)

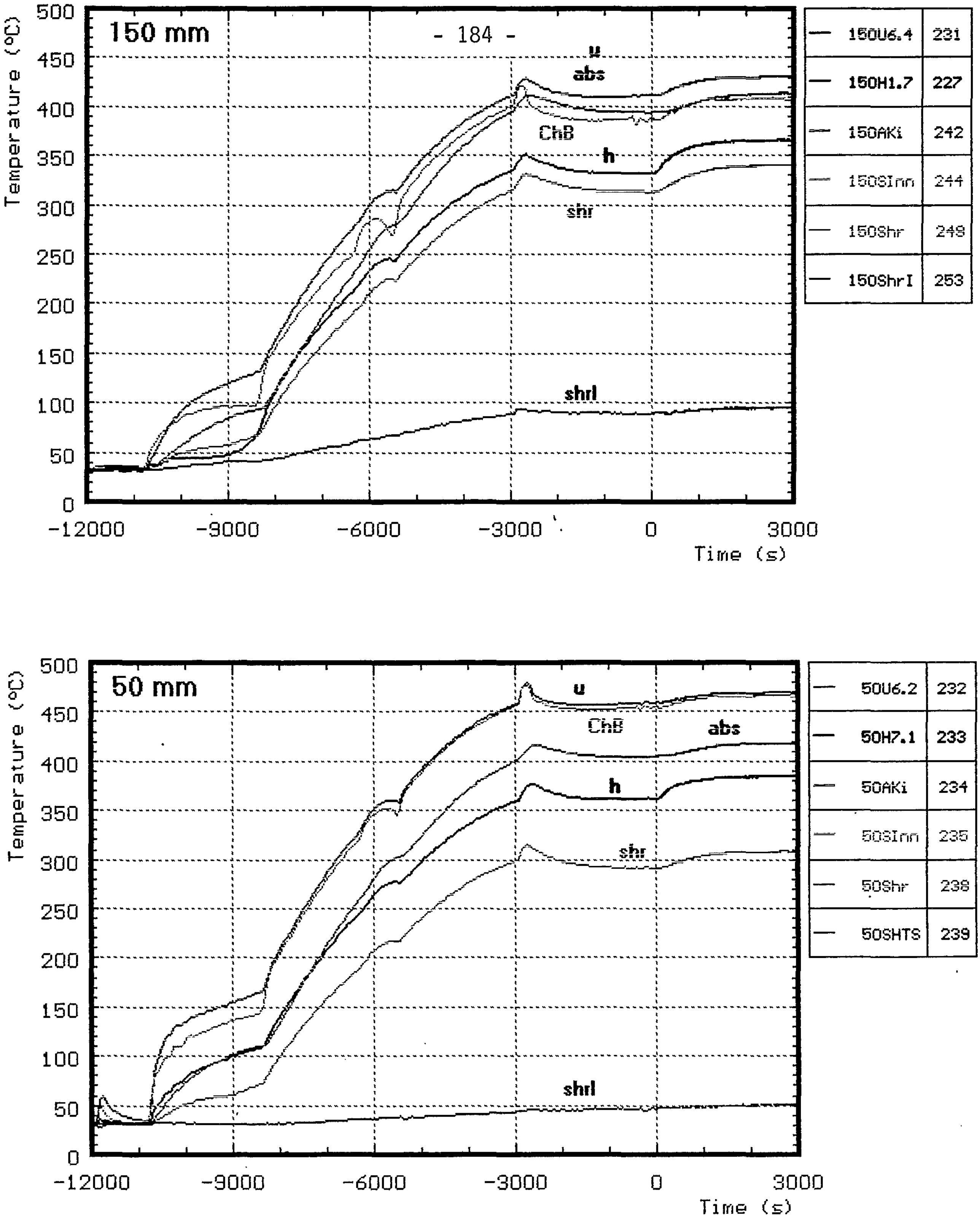

h : heated rods
u : unheated rods
shrl : shroud insolation
abs : in absorberblade
shr : on shroud
ChB : channel box wall

Fig. A20: CORA-28; Temperatures at elevations given, pre-heat phase (150, 50 mm)

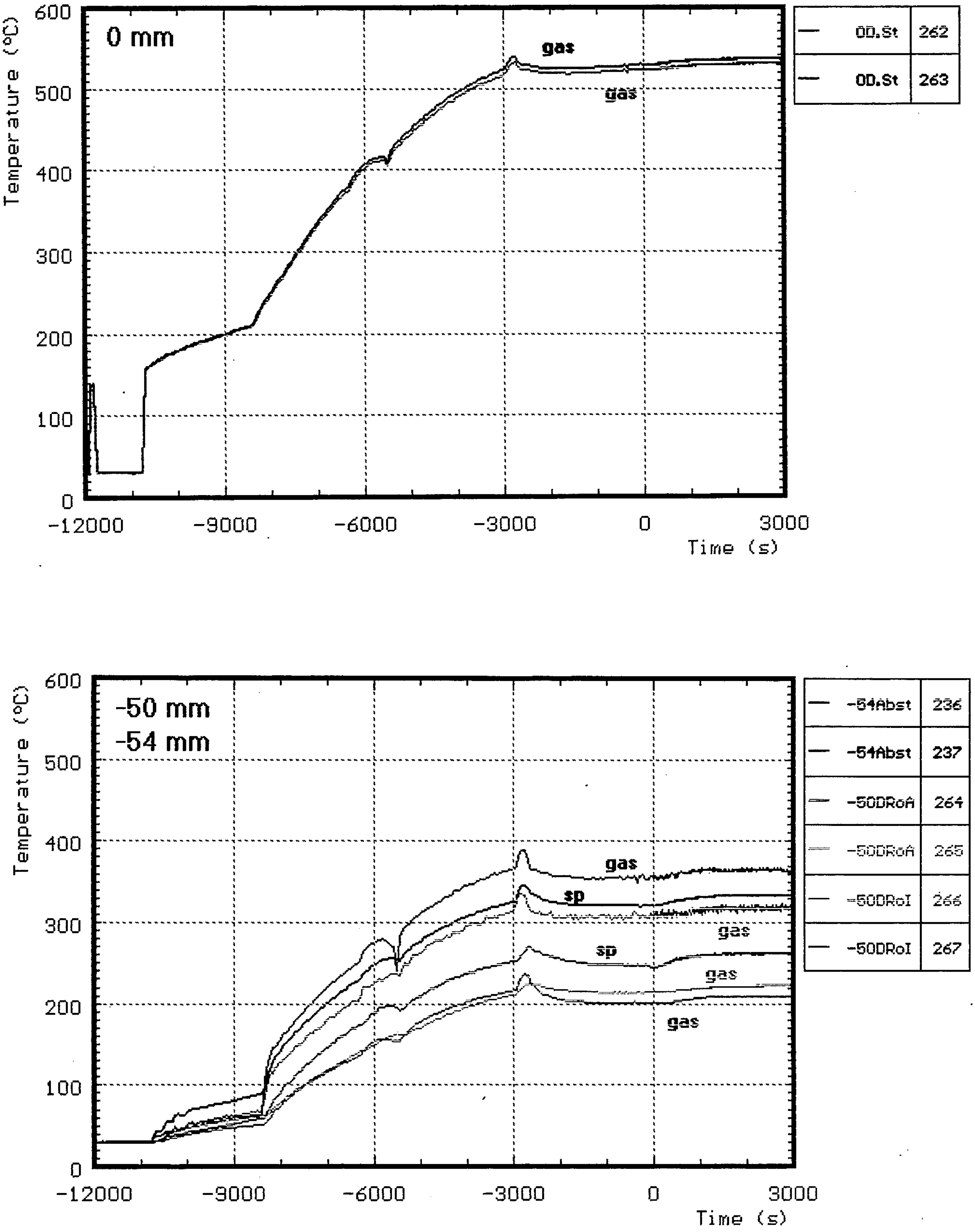

sp : spacer gas : gas temperature

Fig. A21: CORA-28; Temperatures at elevations given, pre-heat phase (0, -50, -54 mm)

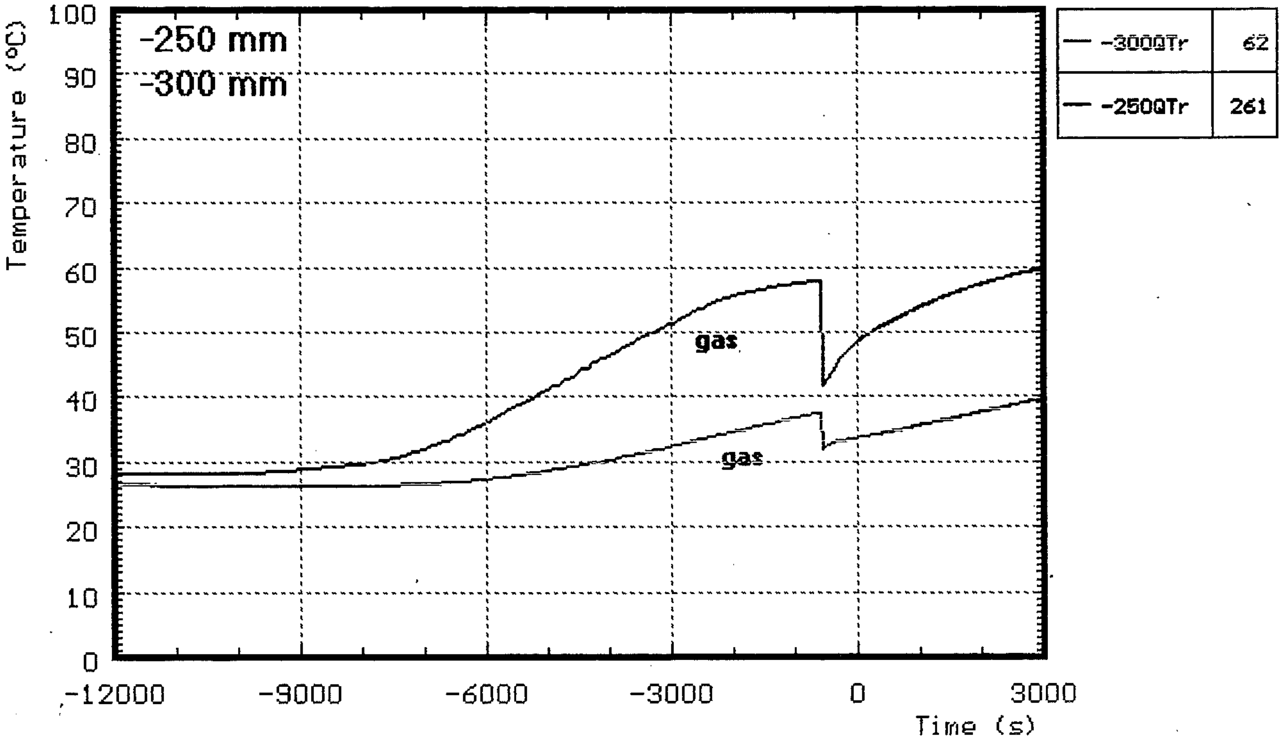

gas: gas temperature

Fig. A22: CORA-28; Temperatures at elevations given, pre-heat phase (-250, -300 mm)

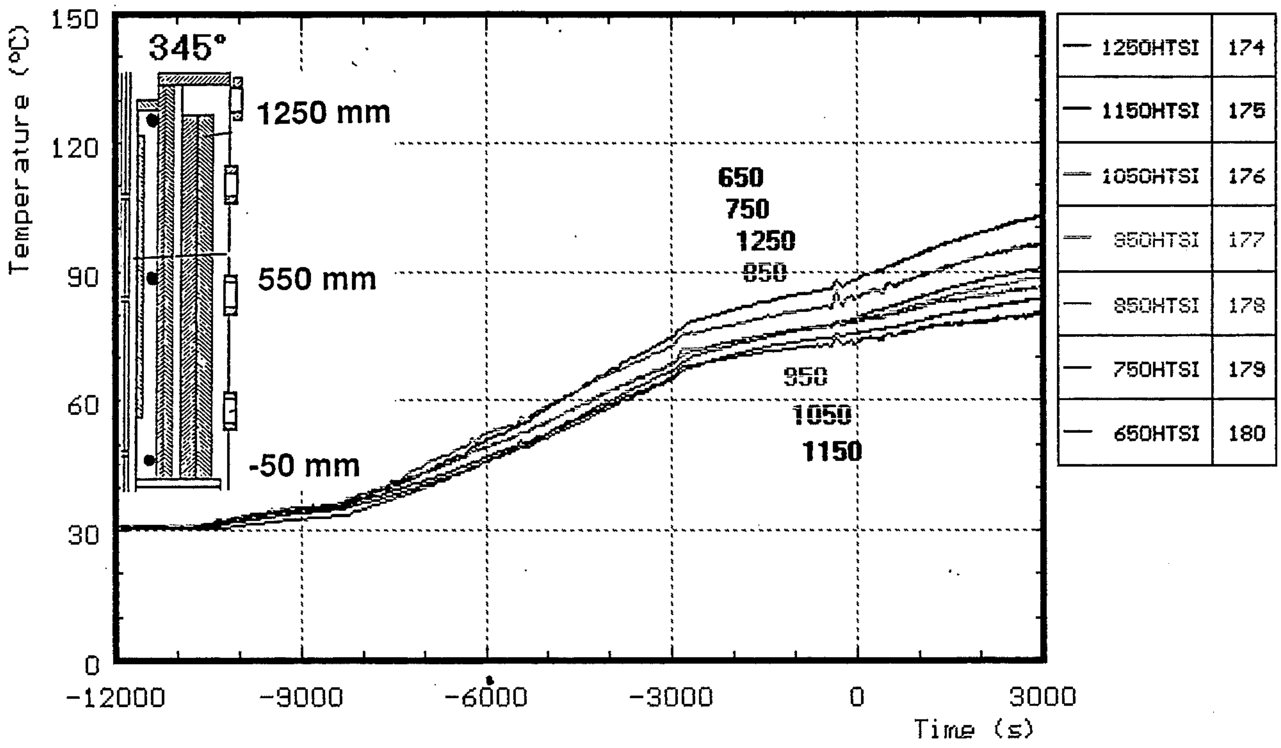

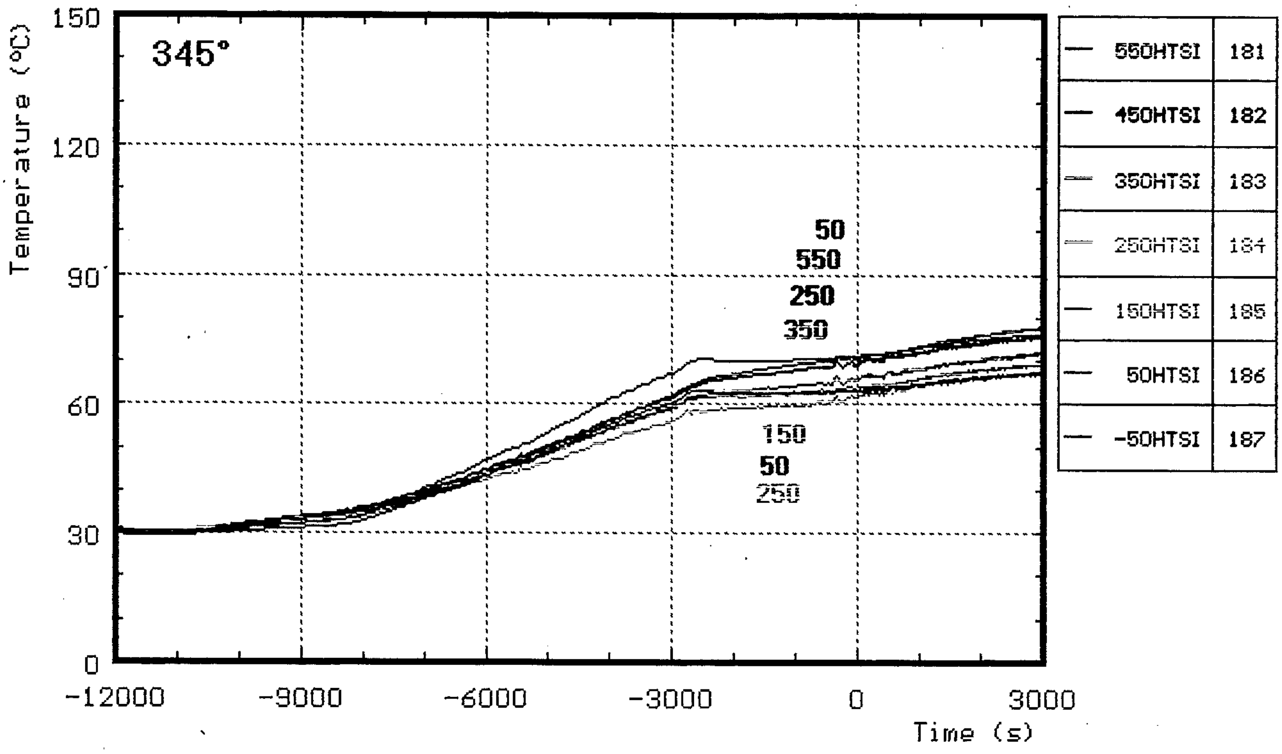

Fig. A23: CORA-28; pre-heating phase temperatures of HTS at 153 mm radius, inner surface, 345°

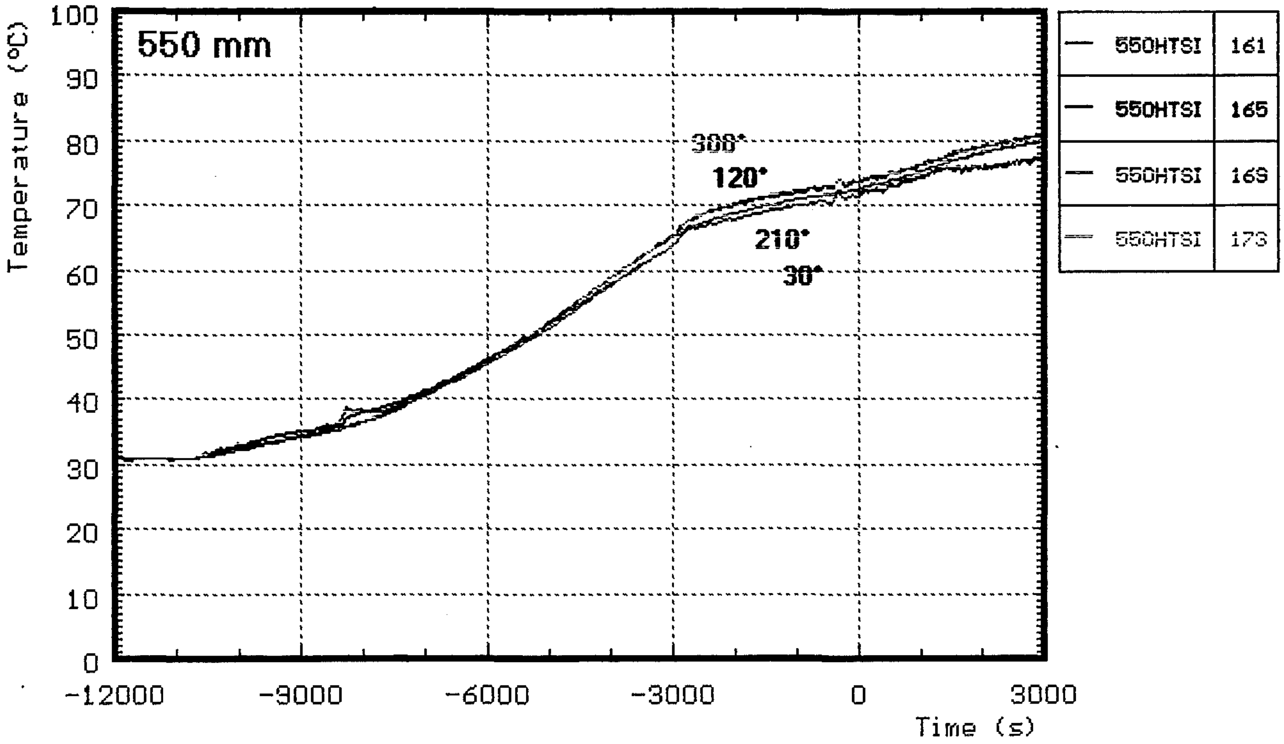

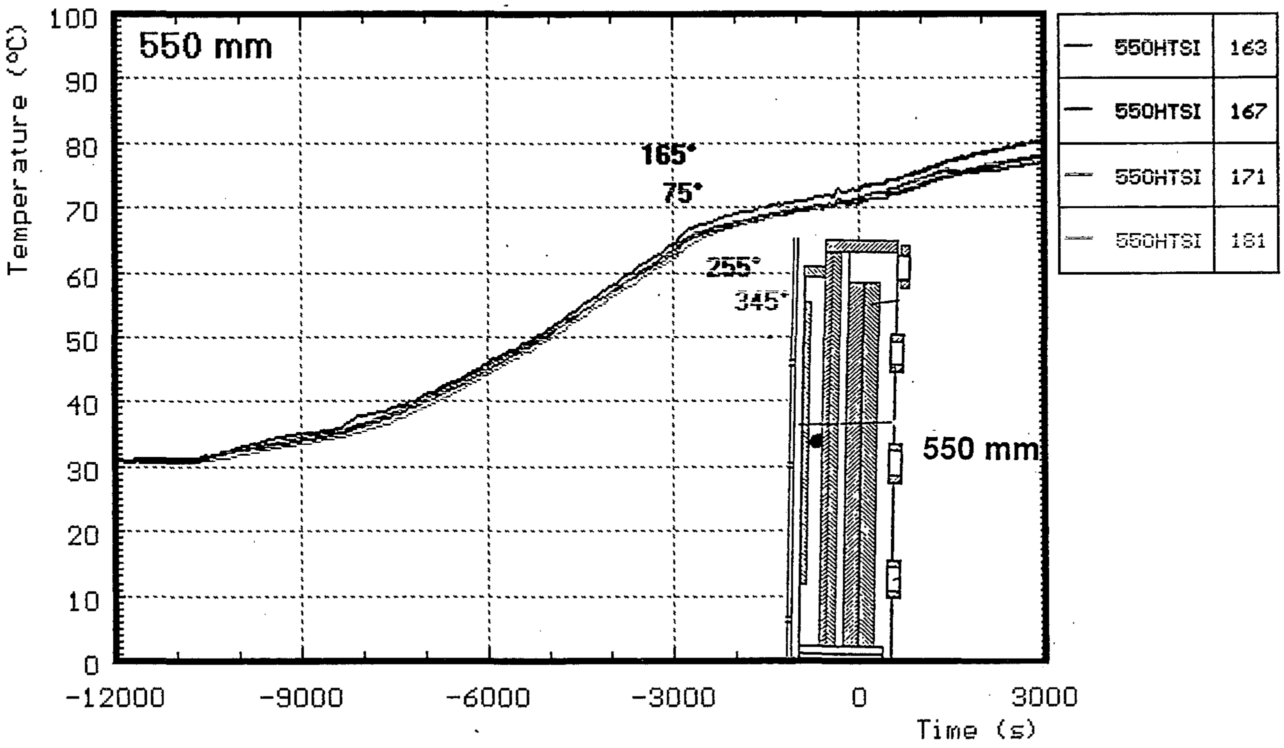

Fig. A24: CORA-28; pre-heating phase temperatures of HTS at 550 mm elevation, inner surface at 153 mm radius

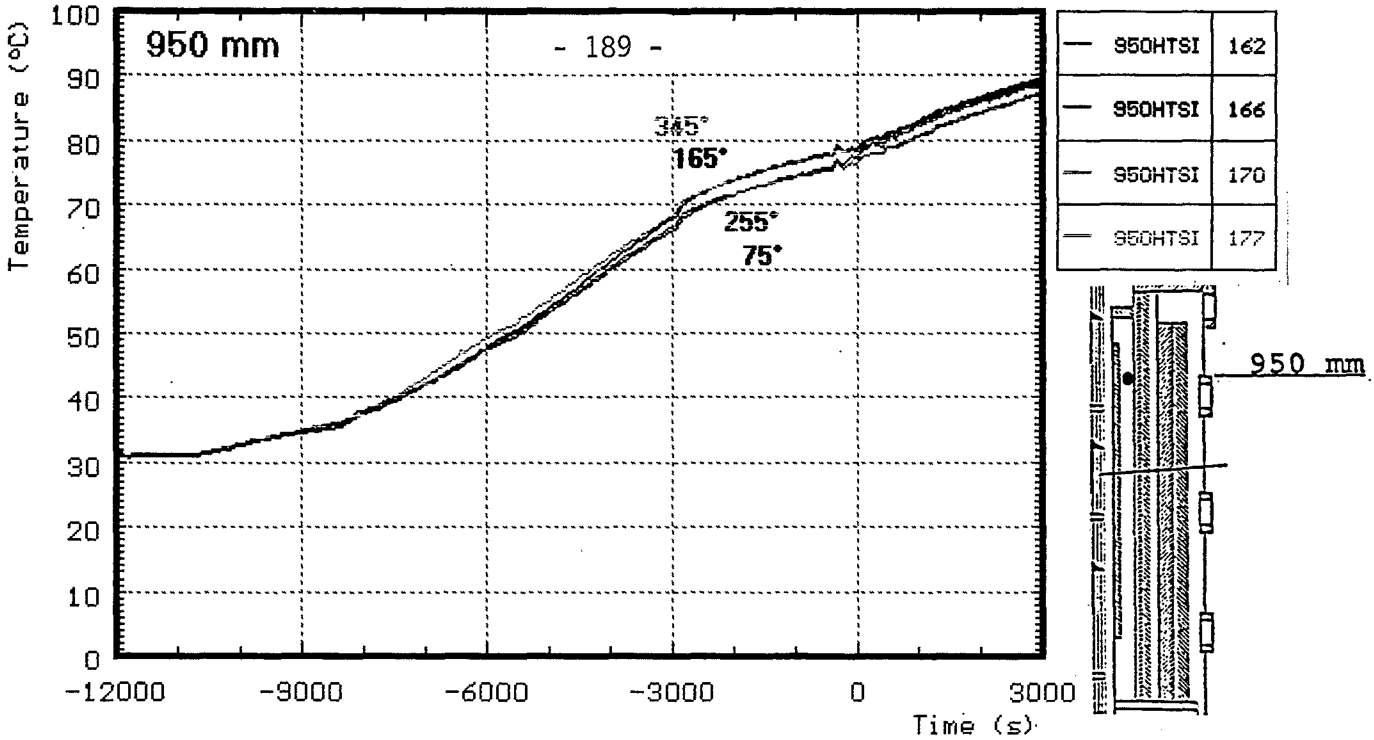

Fig. A25: CORA-28; pre-heating phase temperatures of HTS at 950 mm elevation, inner surface at 153 mm radius

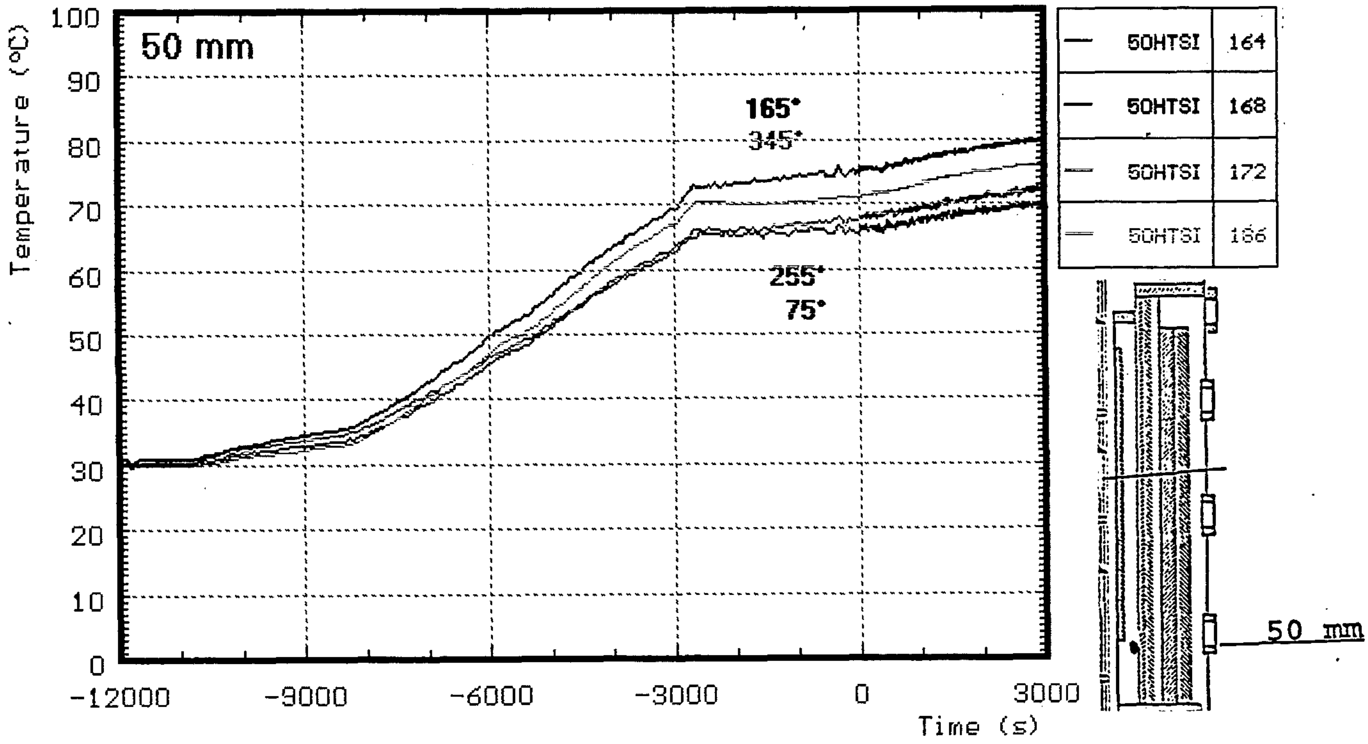

Fig. A26: CORA-28; pre-heating phase temperatures of HTS at 50 mm elevation, inner surface at 153 mm radius

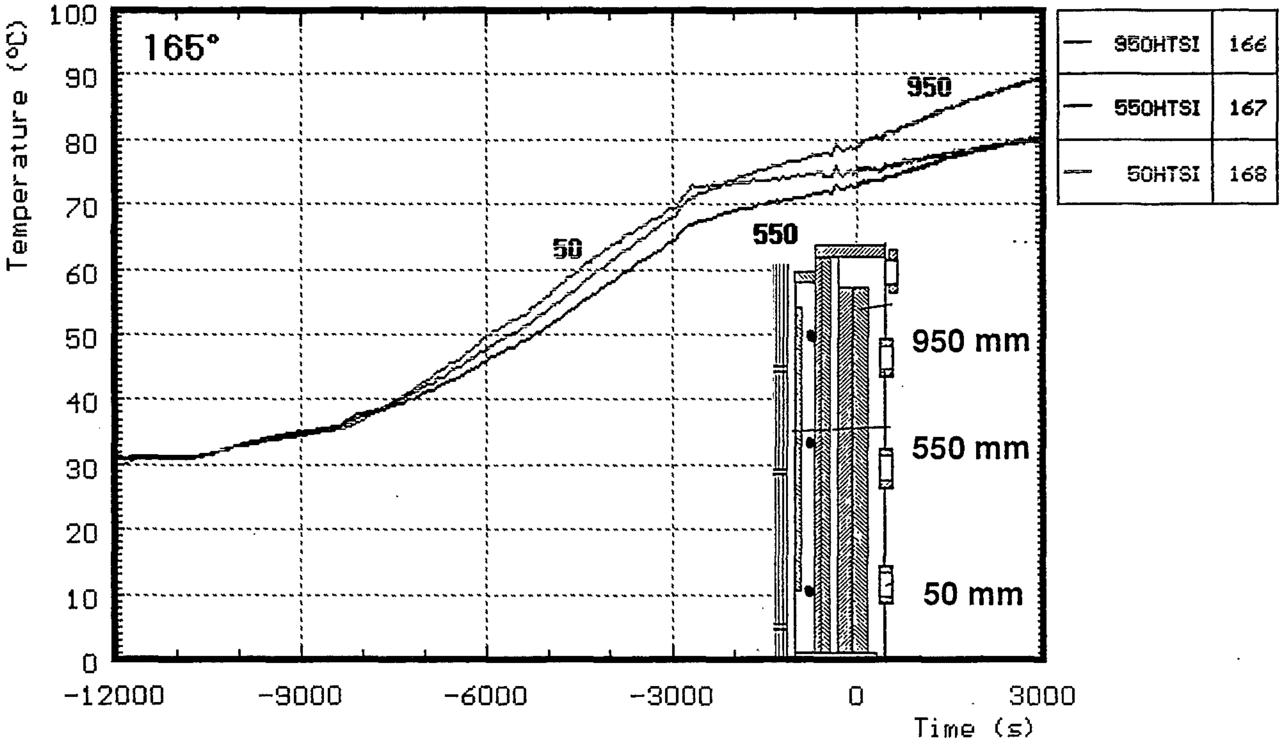

Fig. A27: CORA-28; pre-heating phase temperatures of HTS at 153 mm radius, inner surface, 165°

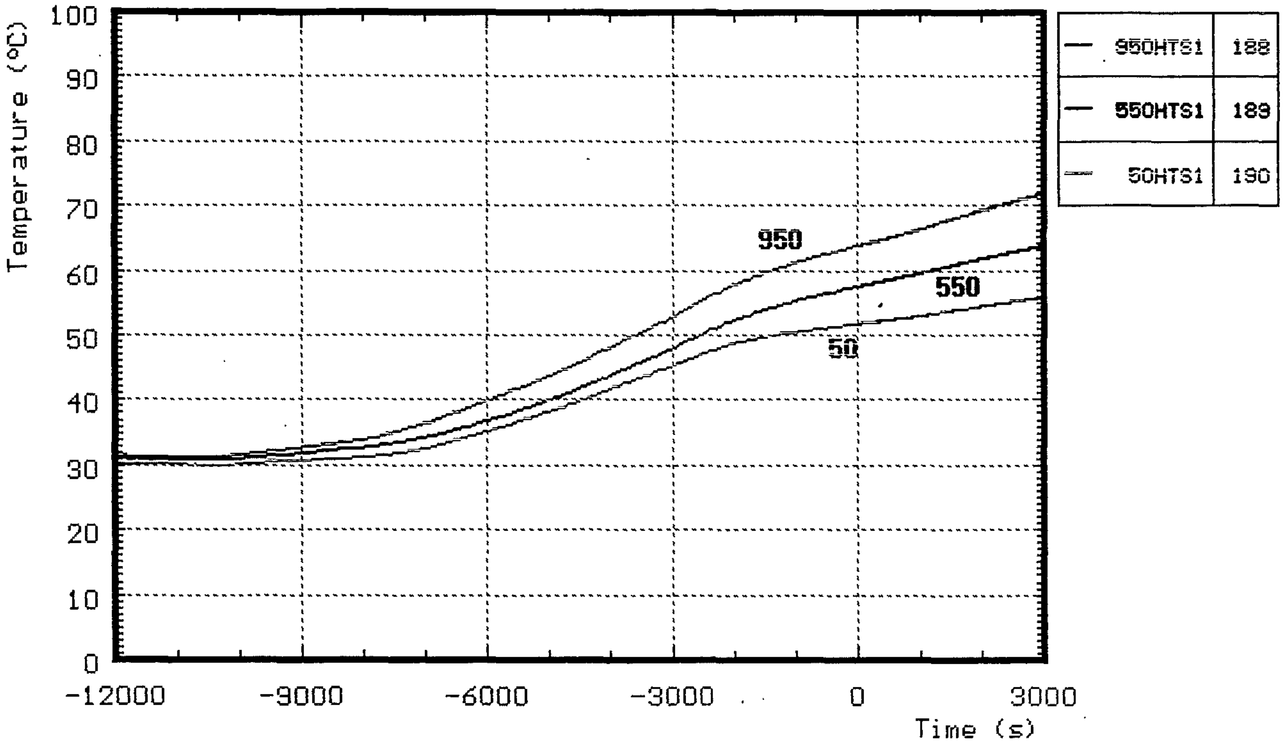

Fig. A28: CORA-28; pre-heating phase temperatures in HT shield at 172 mm radius

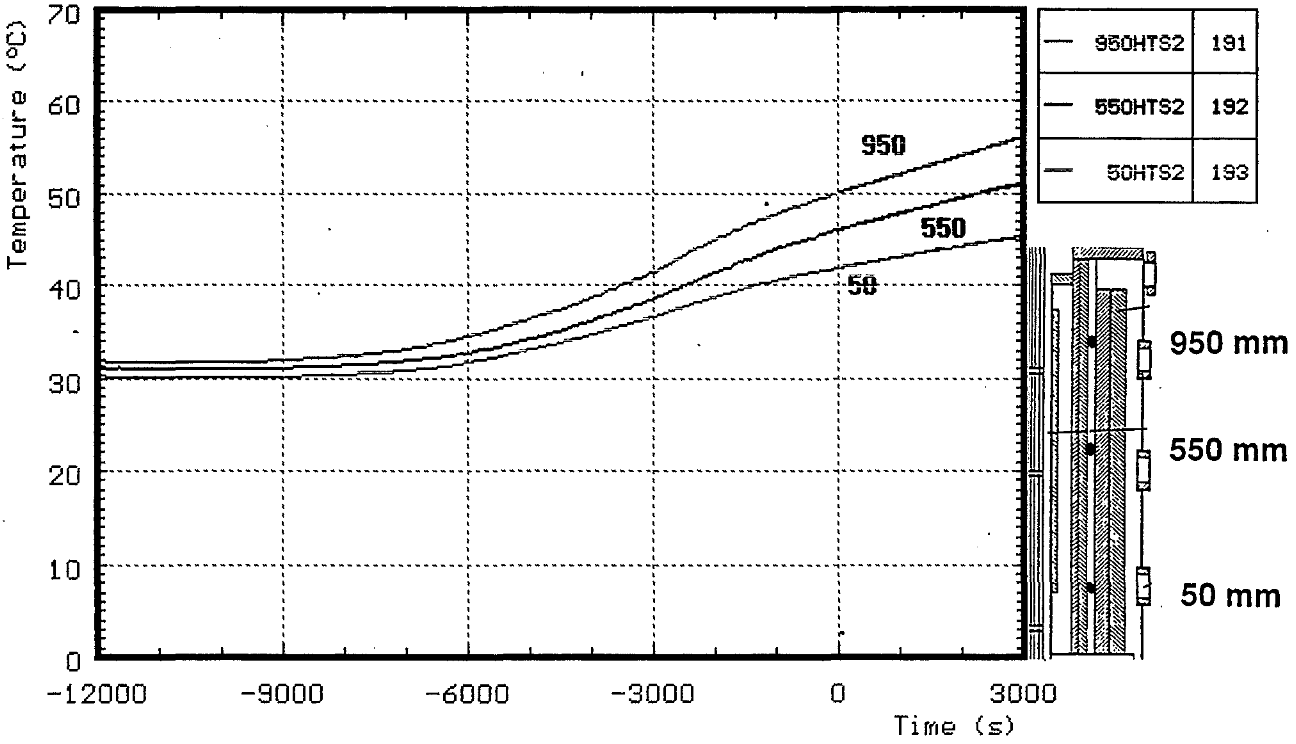

Fig. A29: CORA-28; pre-heating phase temperatures in HT shield at 192 mm radius

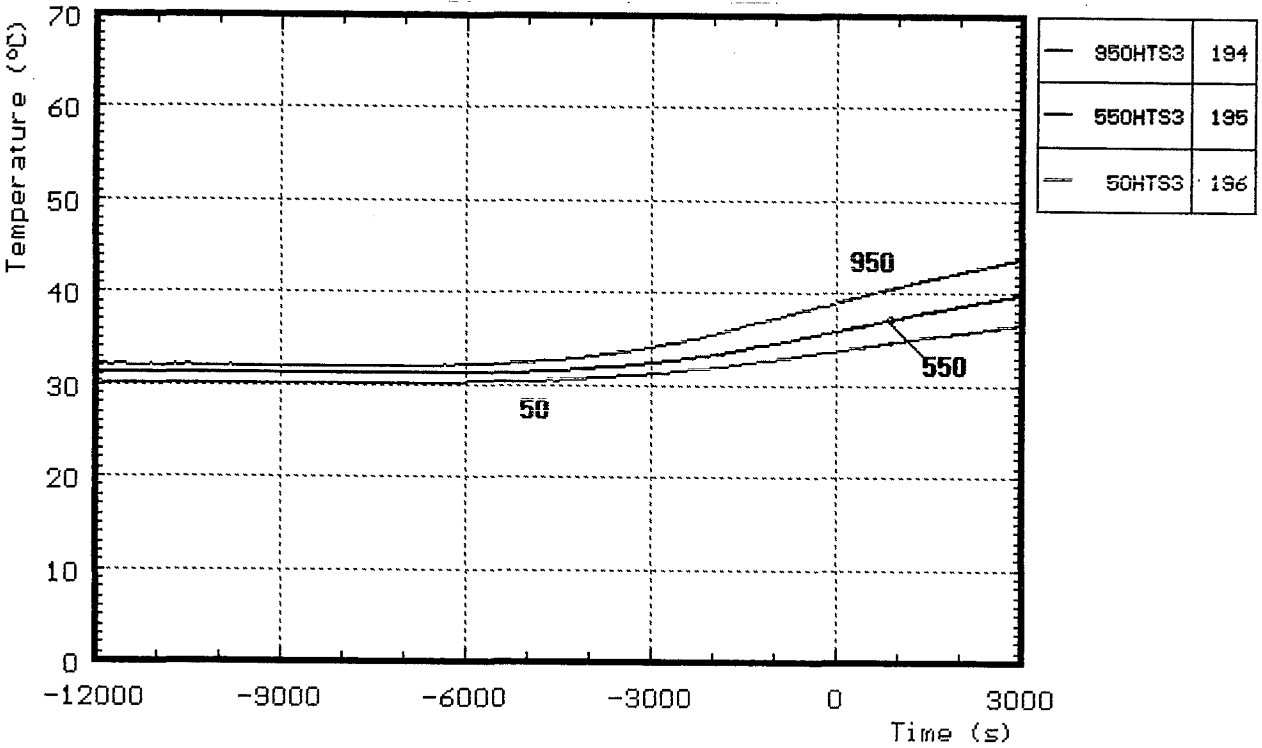

Fig. A30: CORA-28; pre-heating phase temperatures in HT shield at 255 mm radius

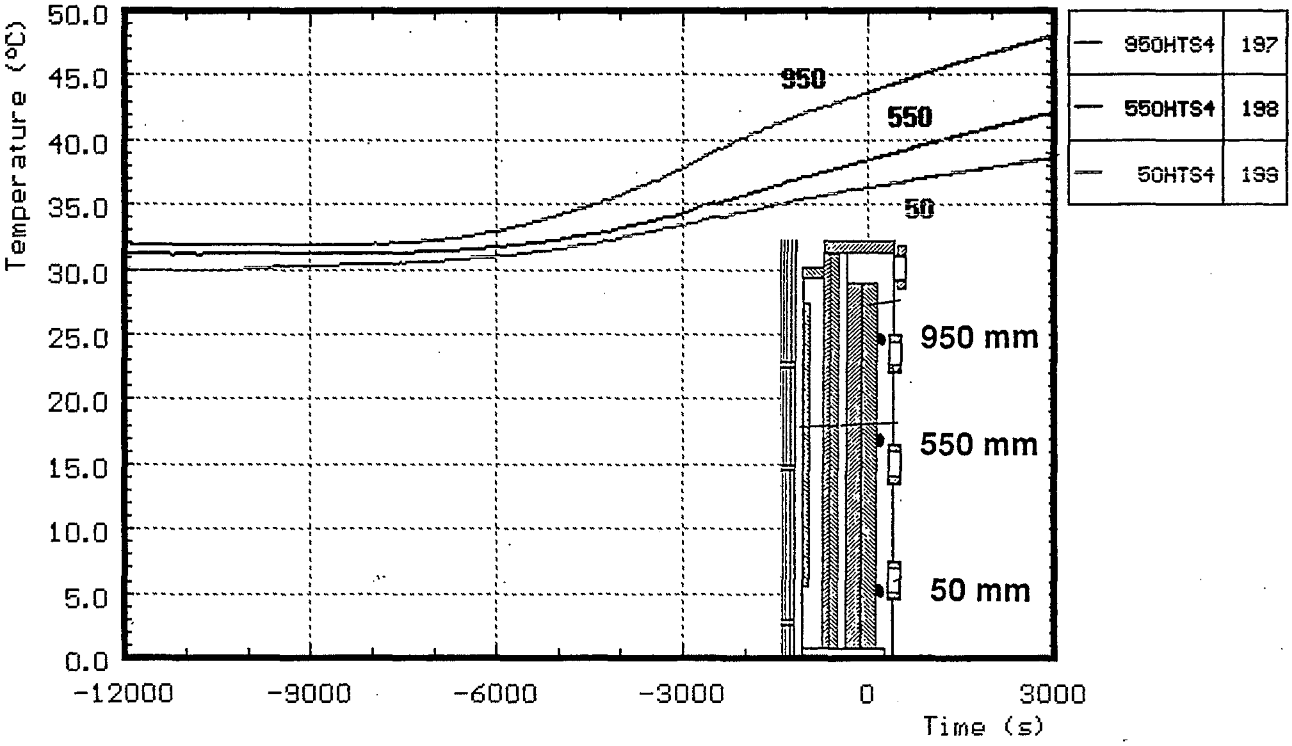

Fig. 31: CORA-28; pre-heating phase temperatures in HT shield at 293 mm radius

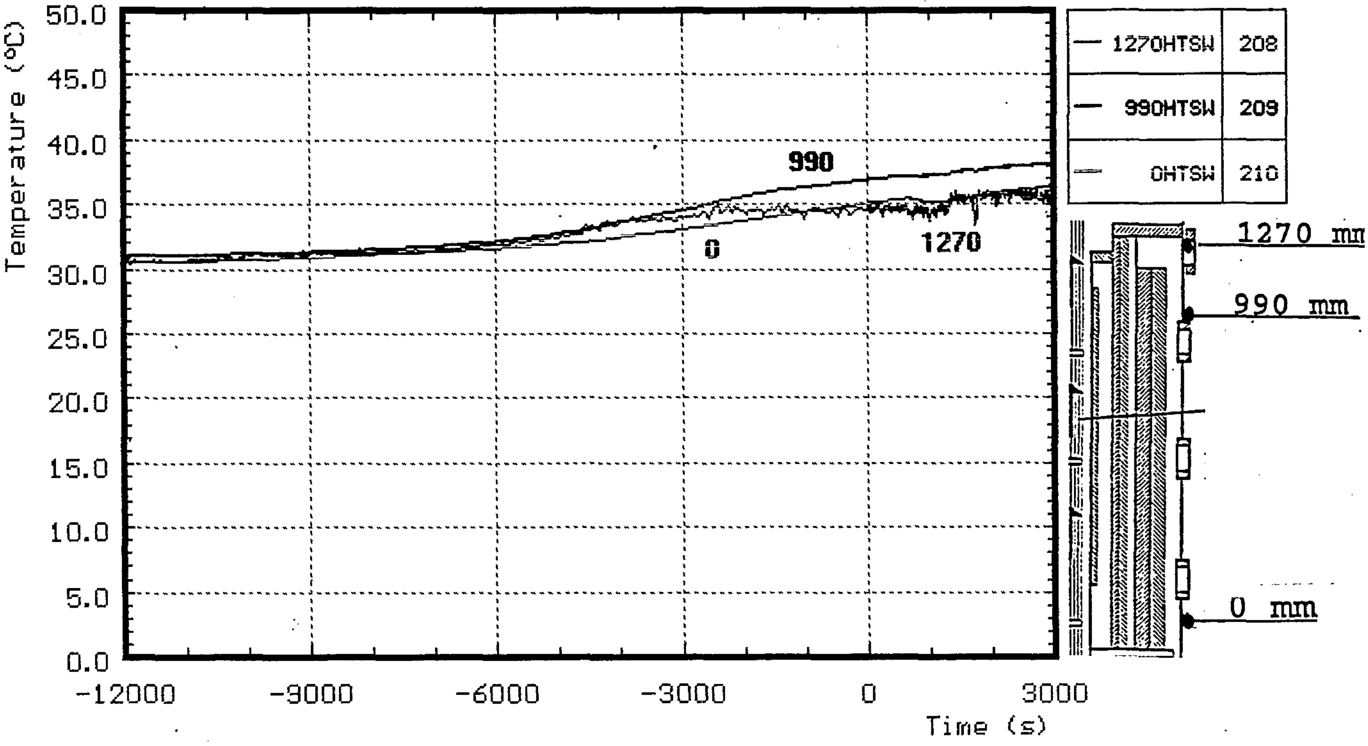

Fig. A32: CORA-28; pre-heating phase temperatures on outer surface of HTS at 380 mm radius

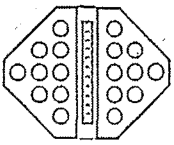

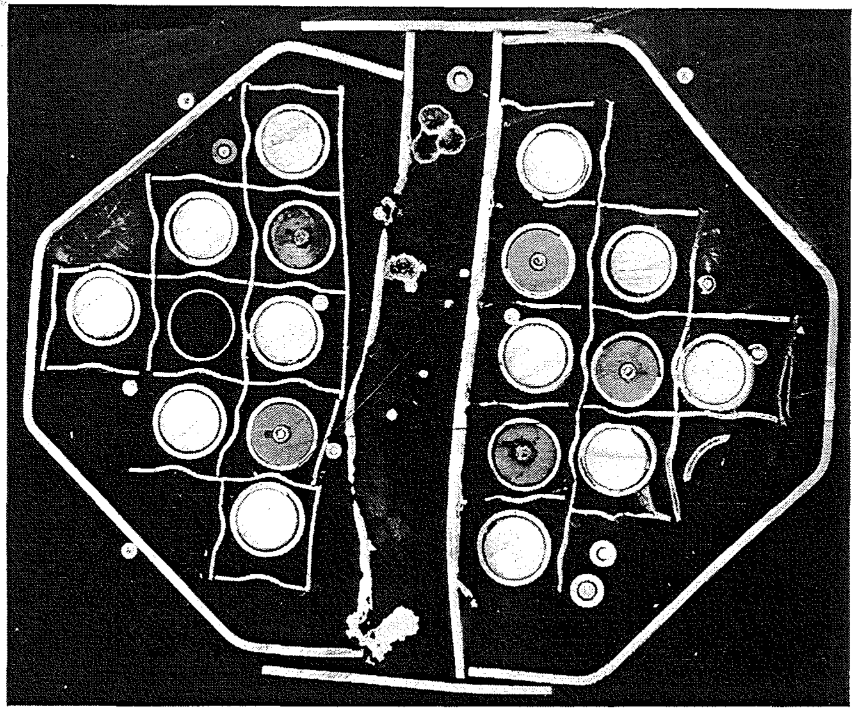

1157 mm *1620°C*

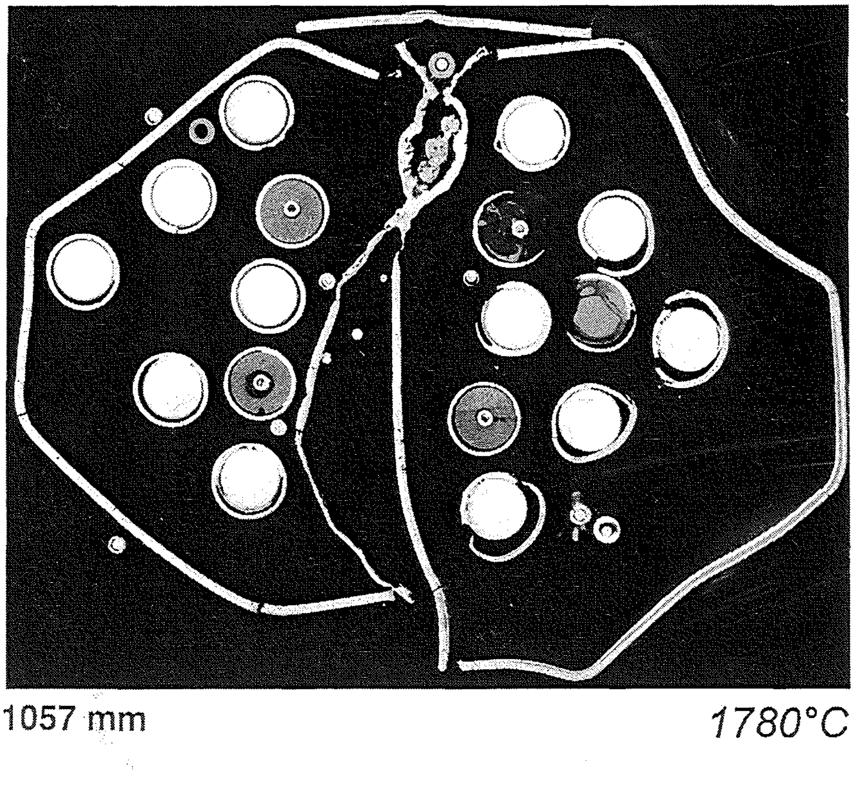

1057 mm *1780°C*

(bottom view)

Fig. A33: Horizontal cross sections of bundle CORA-28 (1157, 1057 mm)

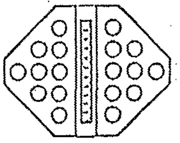

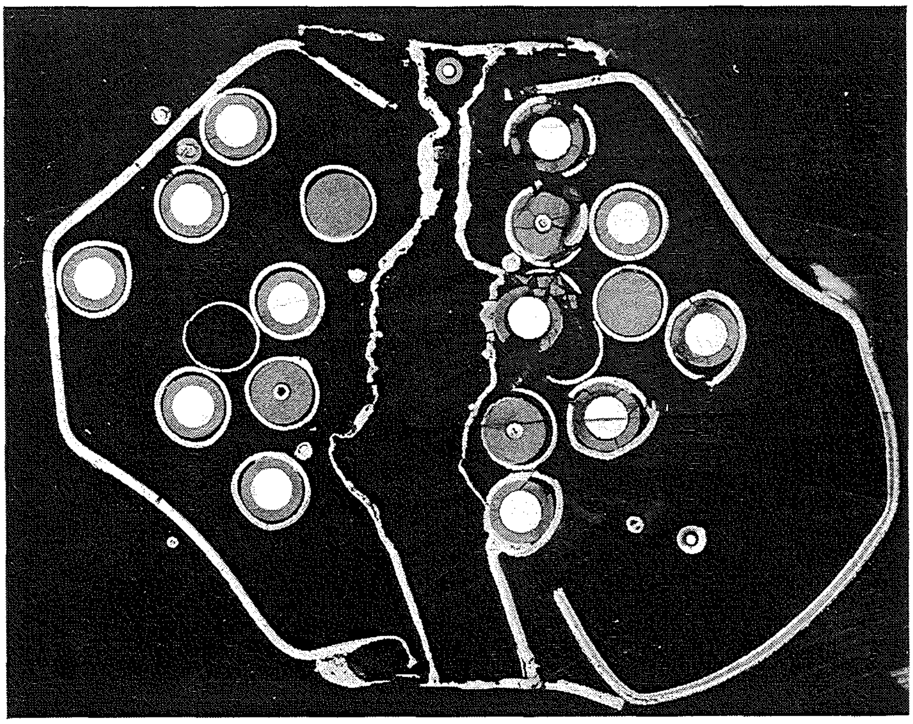

957 mm 1840°C

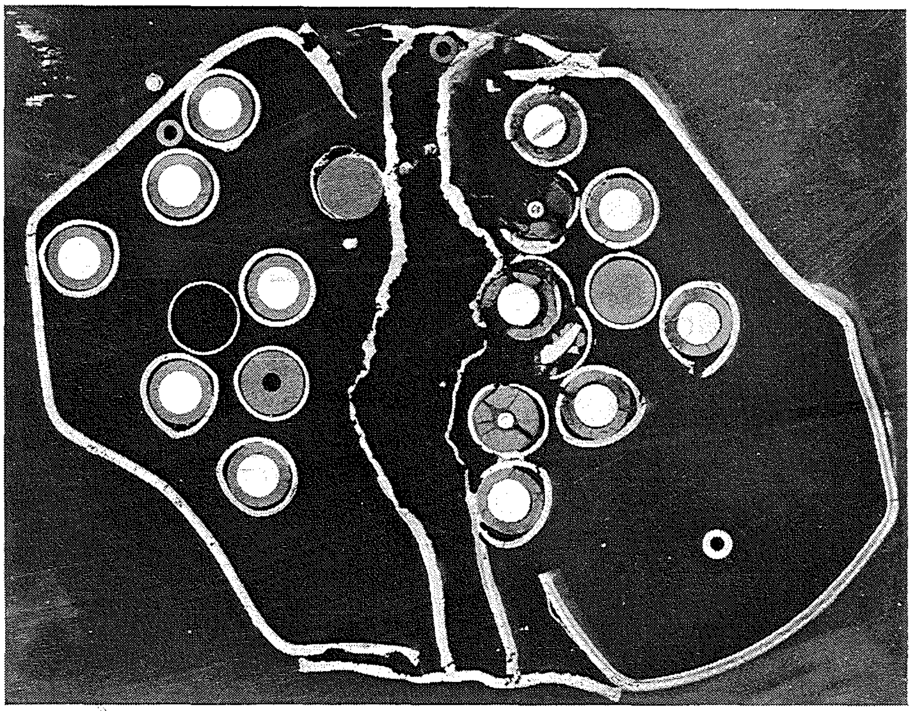

942 mm 1840°C

(bottom view)

Fig. A34: Horizontal cross sections of bundle CORA-28 (957, 942 mm)

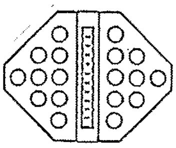

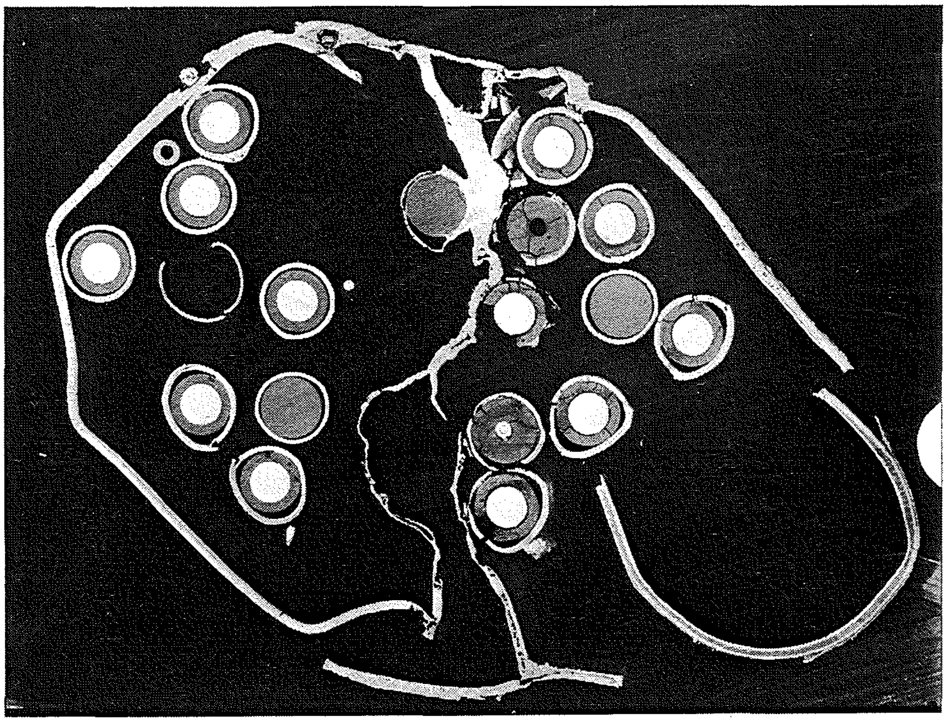

857 mm 1840°C

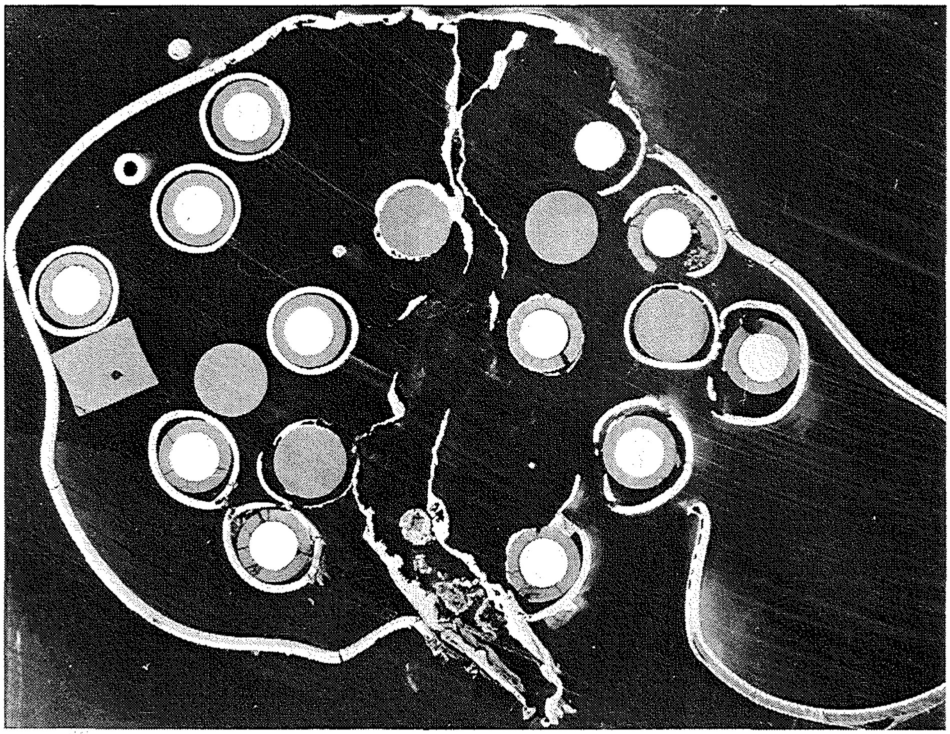

757 mm 1910°C

(bottom view)

Fig. A35: Horizontal cross sections of bundle CORA-28 (857, 757 mm)

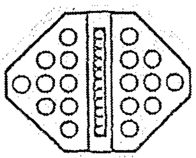

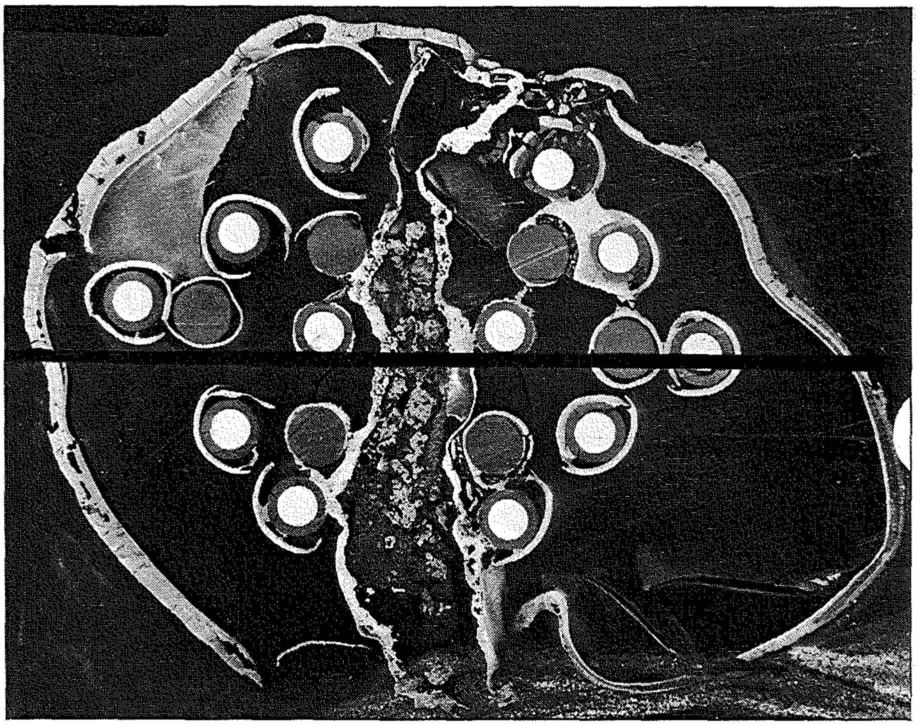

657 mm 1890°C

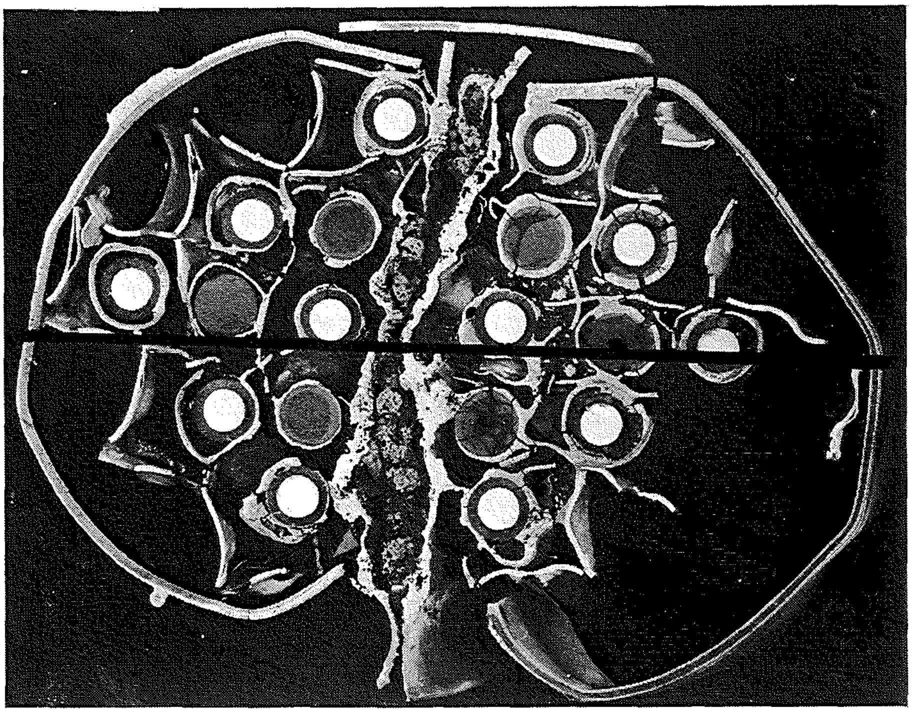

557 mm 1930°C

(bottom view)

Fig. A36: Horizontal cross sections of bundle CORA-28 (657, 557 mm)

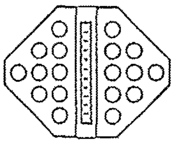

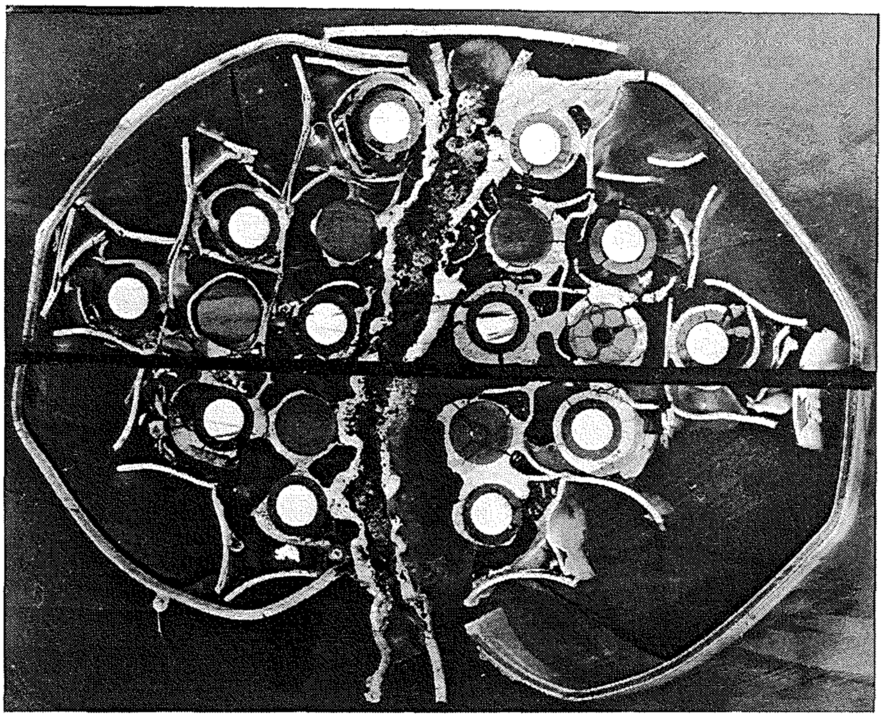

542 mm 1930°C

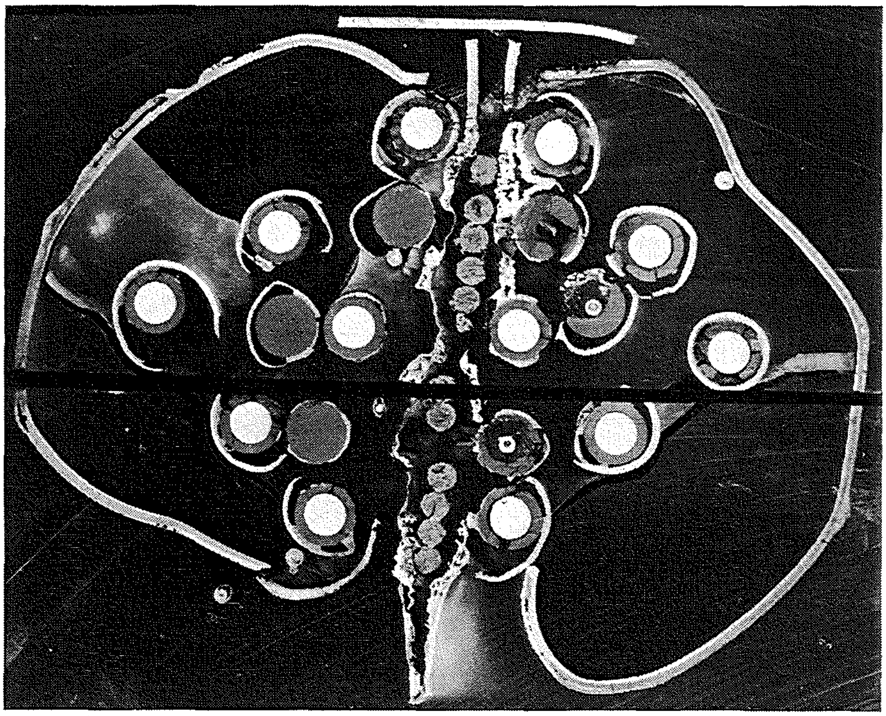

457 mm 1930°C

(bottom view)

Fig. A37: Horizontal cross sections of bundle CORA-28 (542, 457 mm)

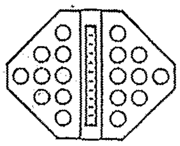

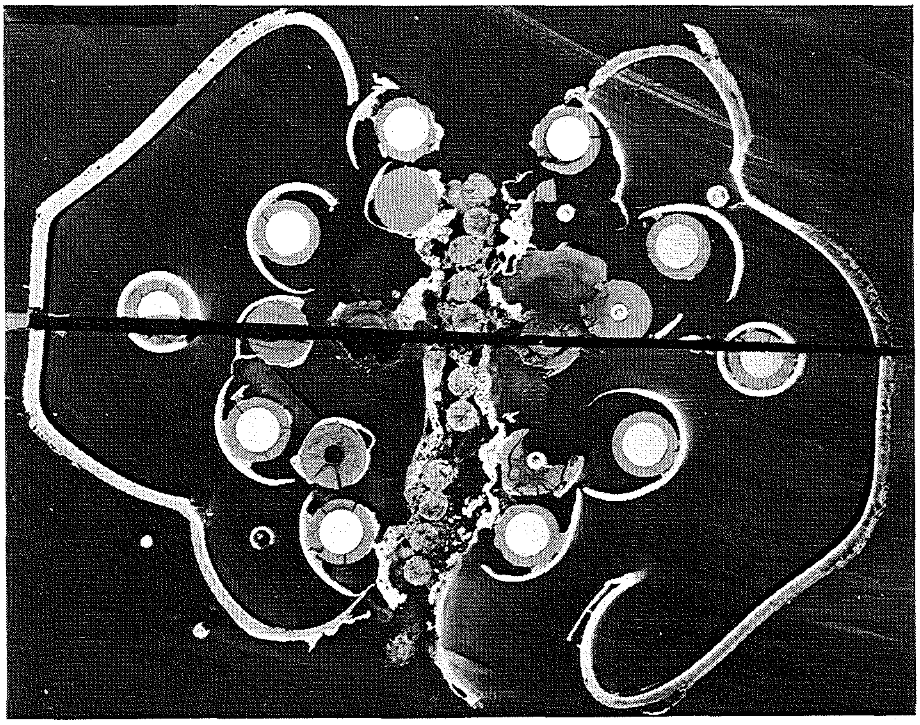

357 mm 1960°C

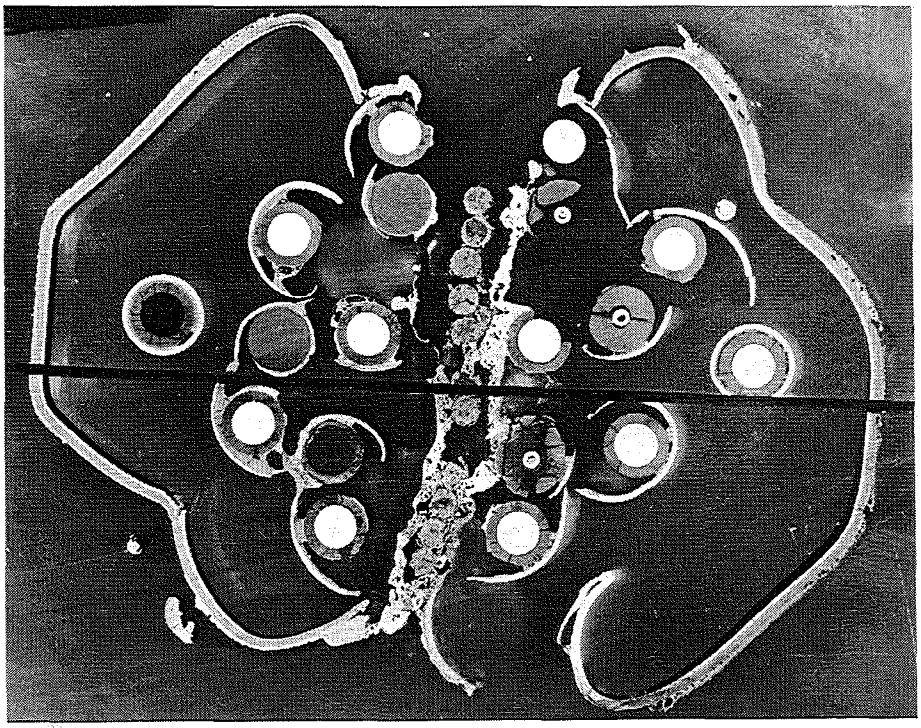

342 mm 1960°C

(bottom view)

Fig. A38: Horizontal cross sections of bundle CORA-28 (357, 342 mm)

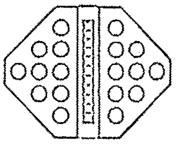

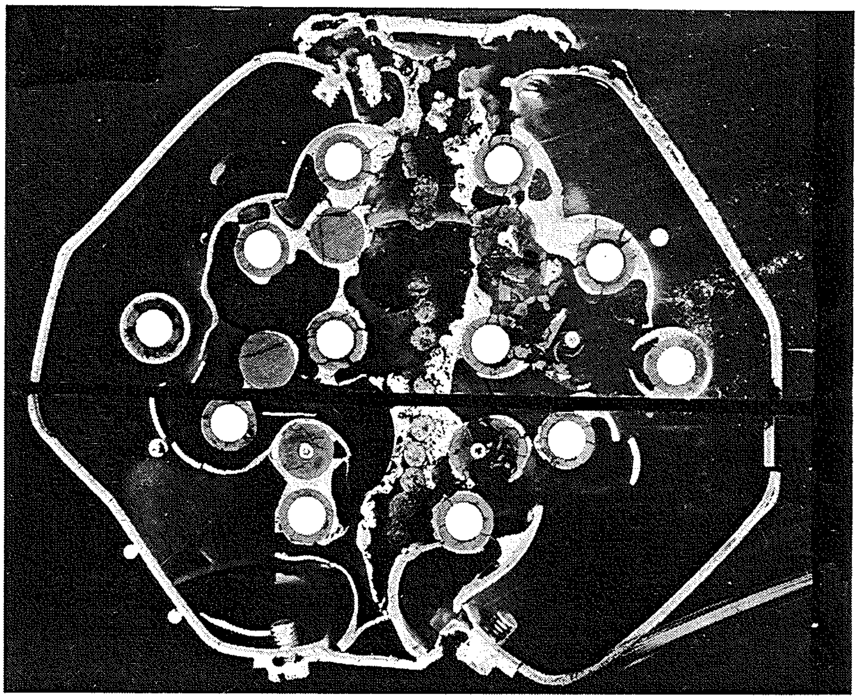

257 mm *1920°C*

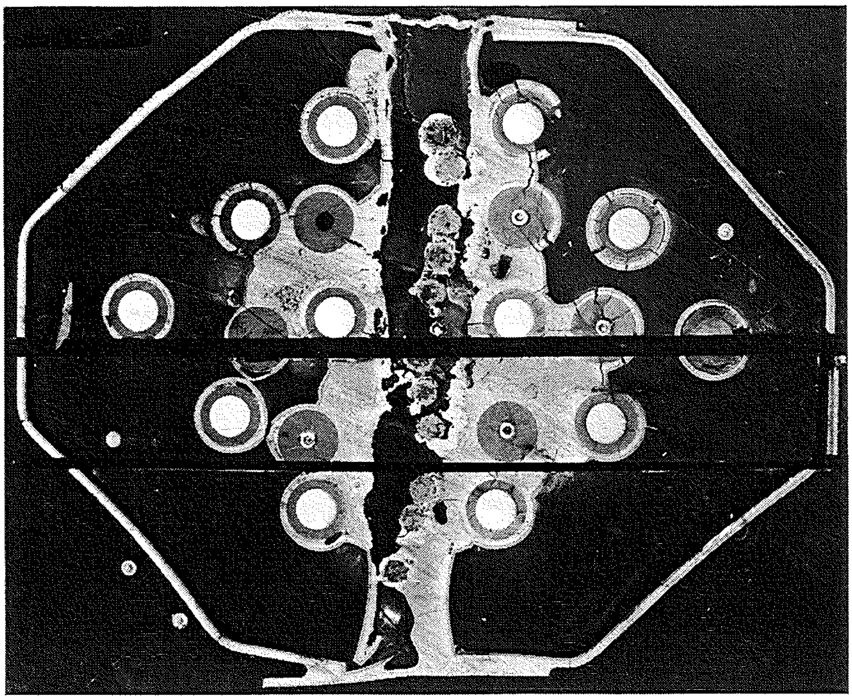

157 mm *1460°C*

(bottom view)

Fig. A39: Horizontal cross sections of bundle CORA-28 (257, 157 mm)

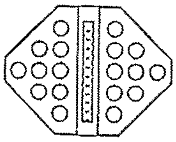

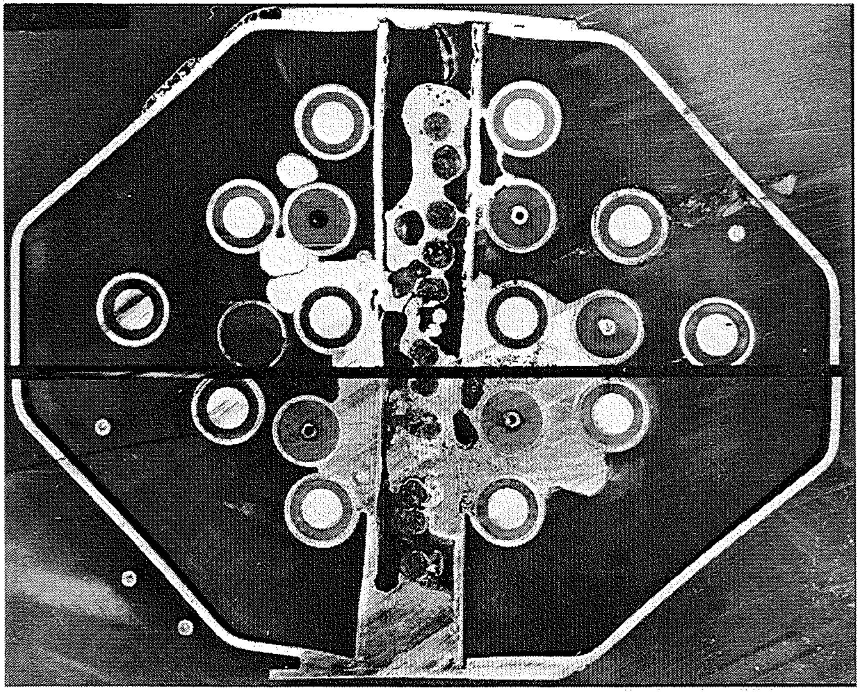

142 mm 1440°C

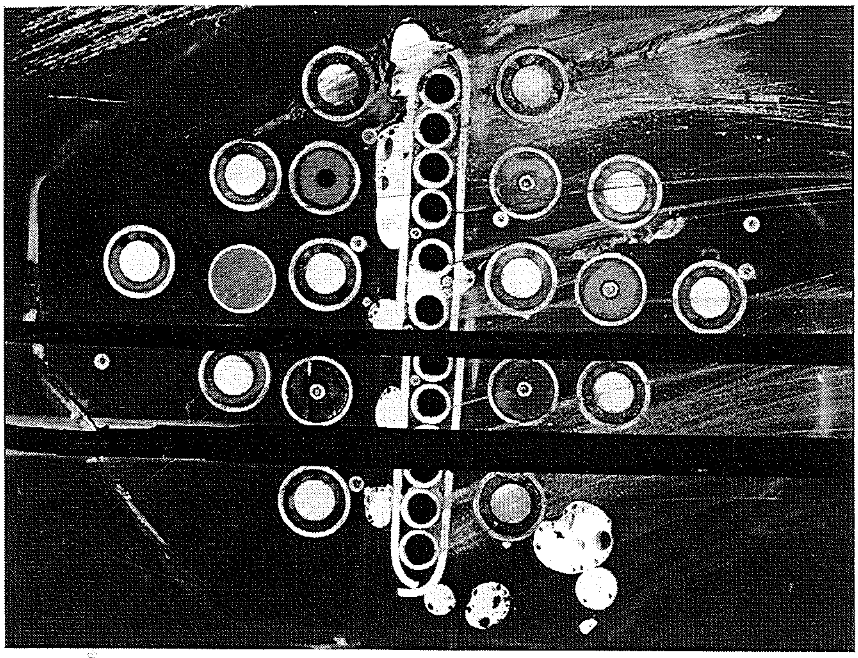

57 mm 800°C

(bottom view)

Fig. A40: Horizontal cross sections of bundle CORA-28 (142, 57 mm)

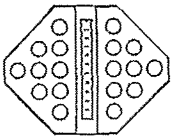

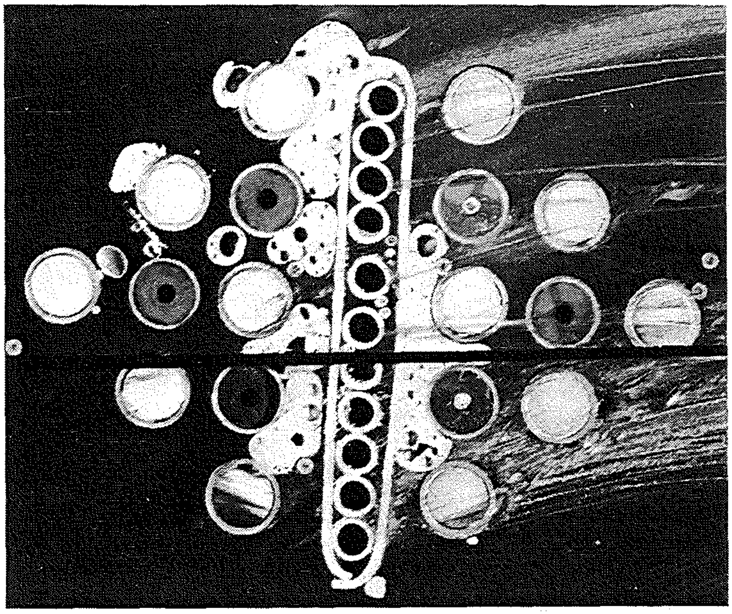

-43 mm

480°C

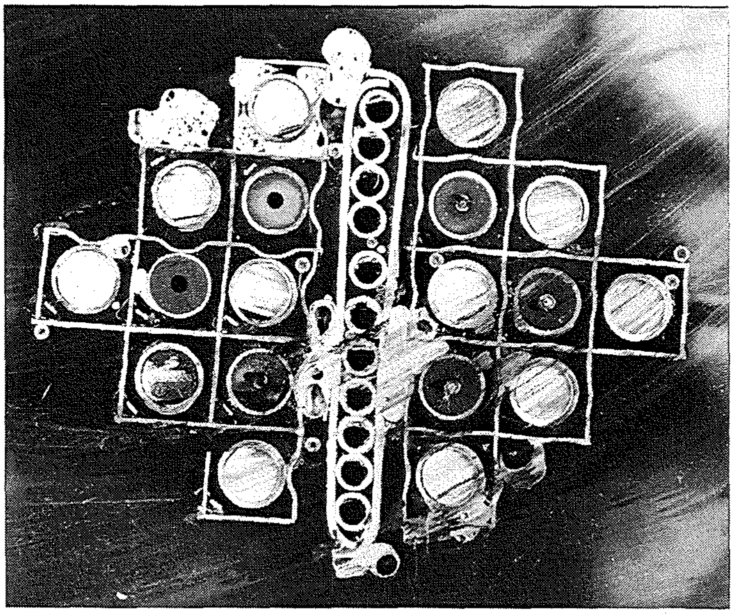

-58 mm

460°C

(bottom view)

Fig. A41: Horizontal cross sections of bundle CORA-28 (-43, -58 mm)

APPENDIX B

Test data of pre-oxidaiton

Figures: B1 - B18

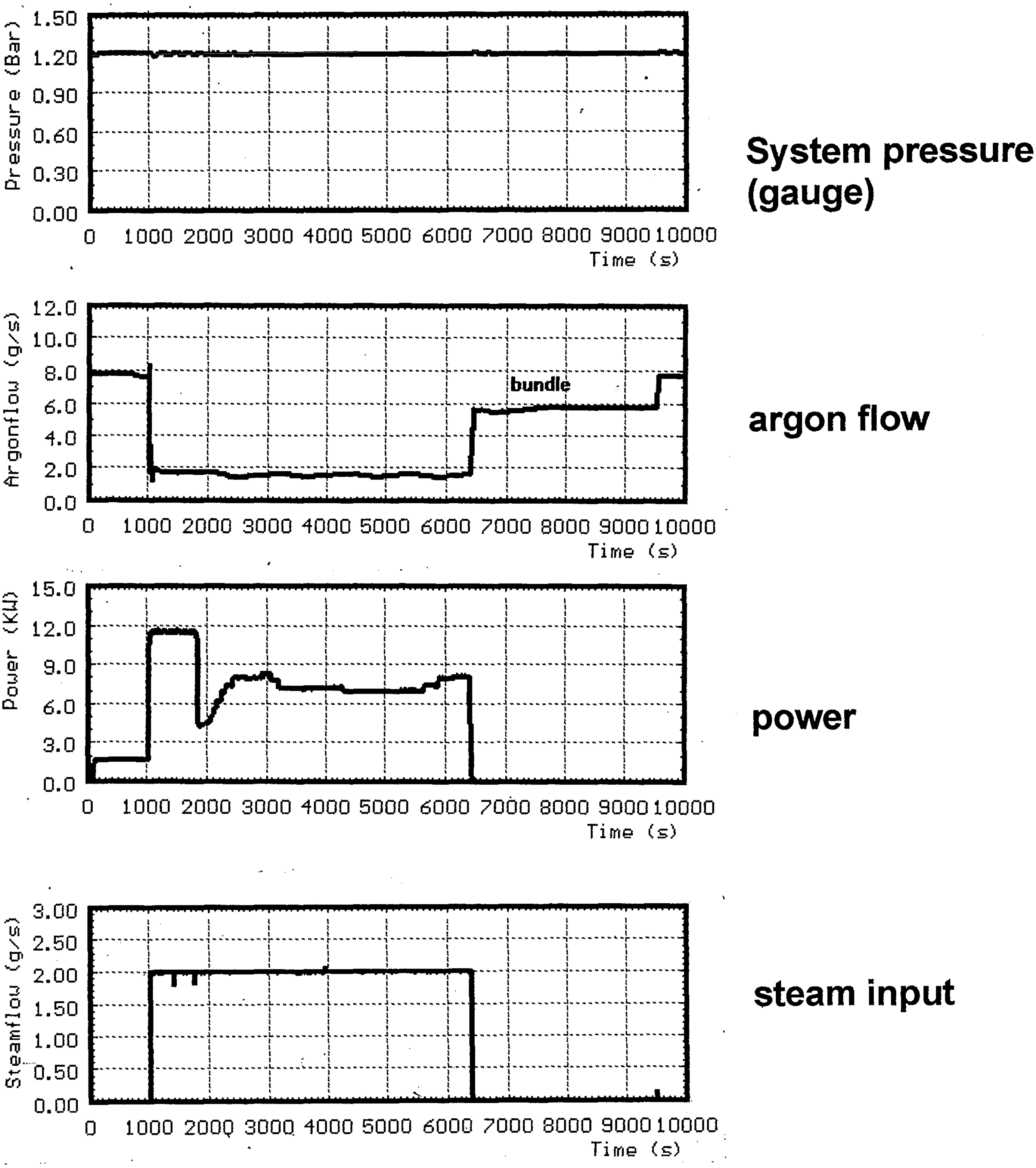

Fig. B1: First preoxidation CORA-28; system pressure, argon flow, steam input and power

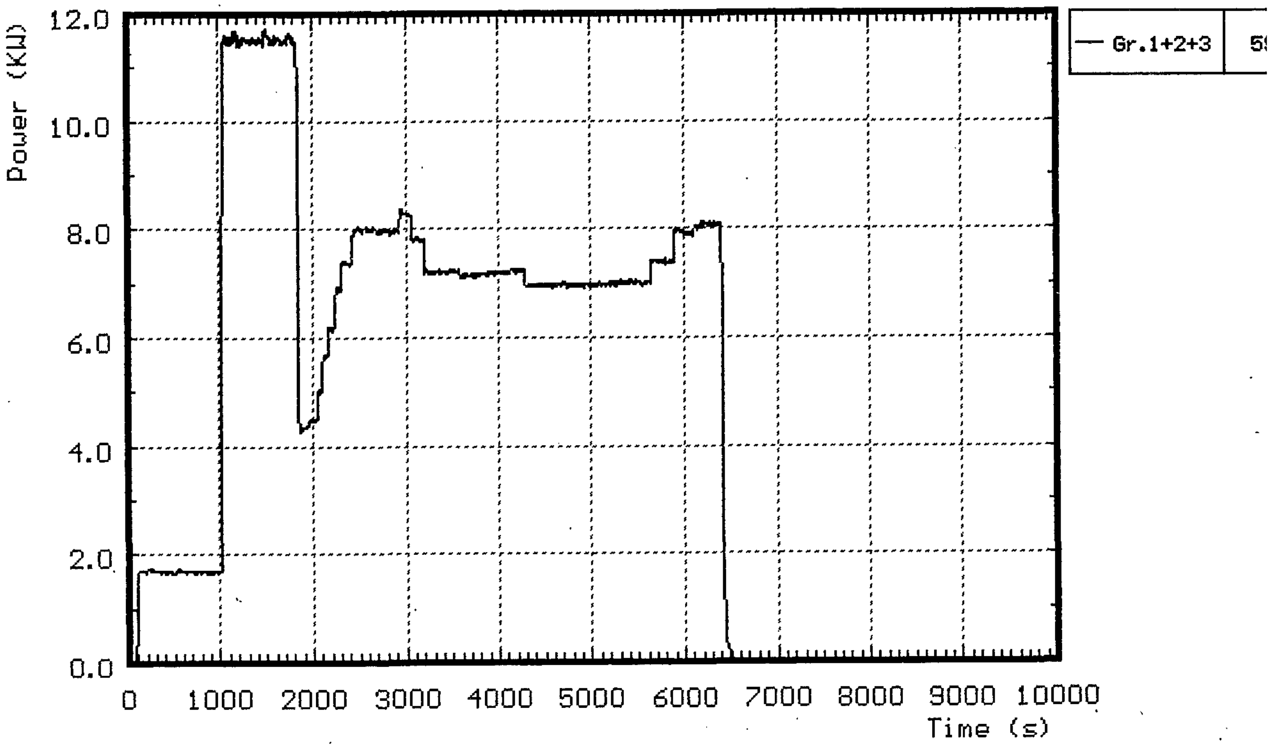

Fig. B2: First preoxidation CORA-28; electric power input

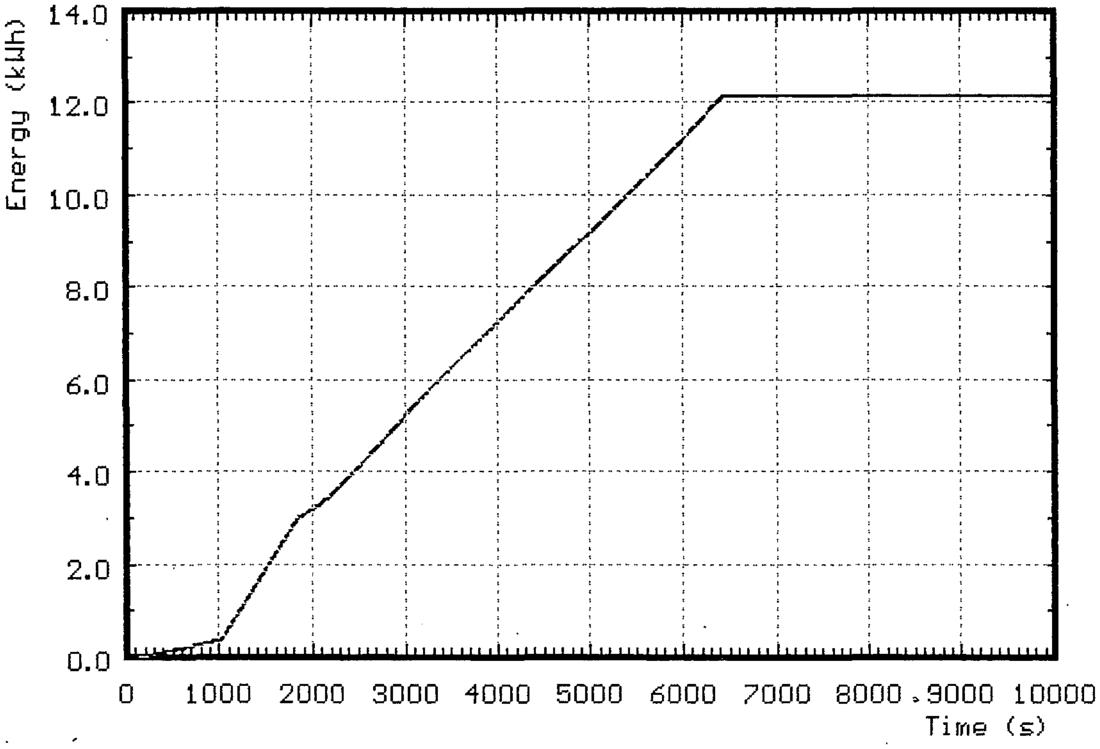

Fig. B3: First preoxidation CORA-28; total energy input

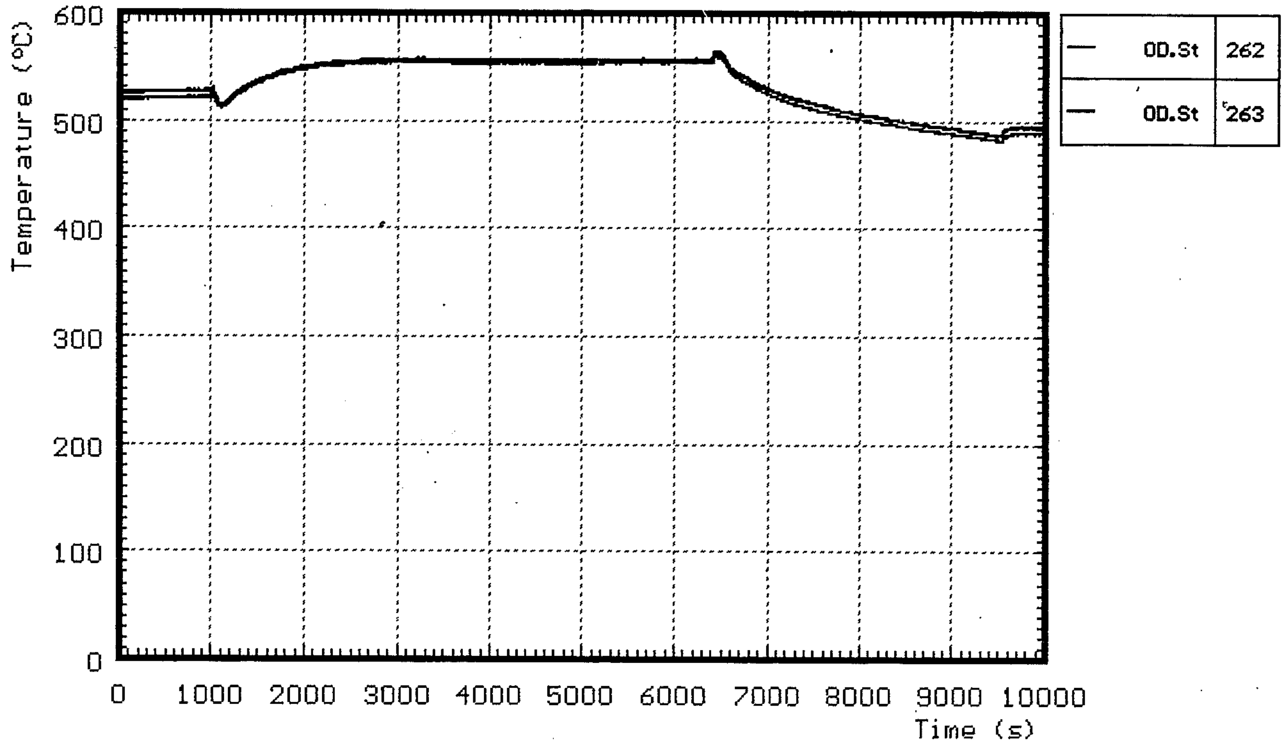

Fig. B4: First preoxidation CORA-28; temperatures at the bundle entrance

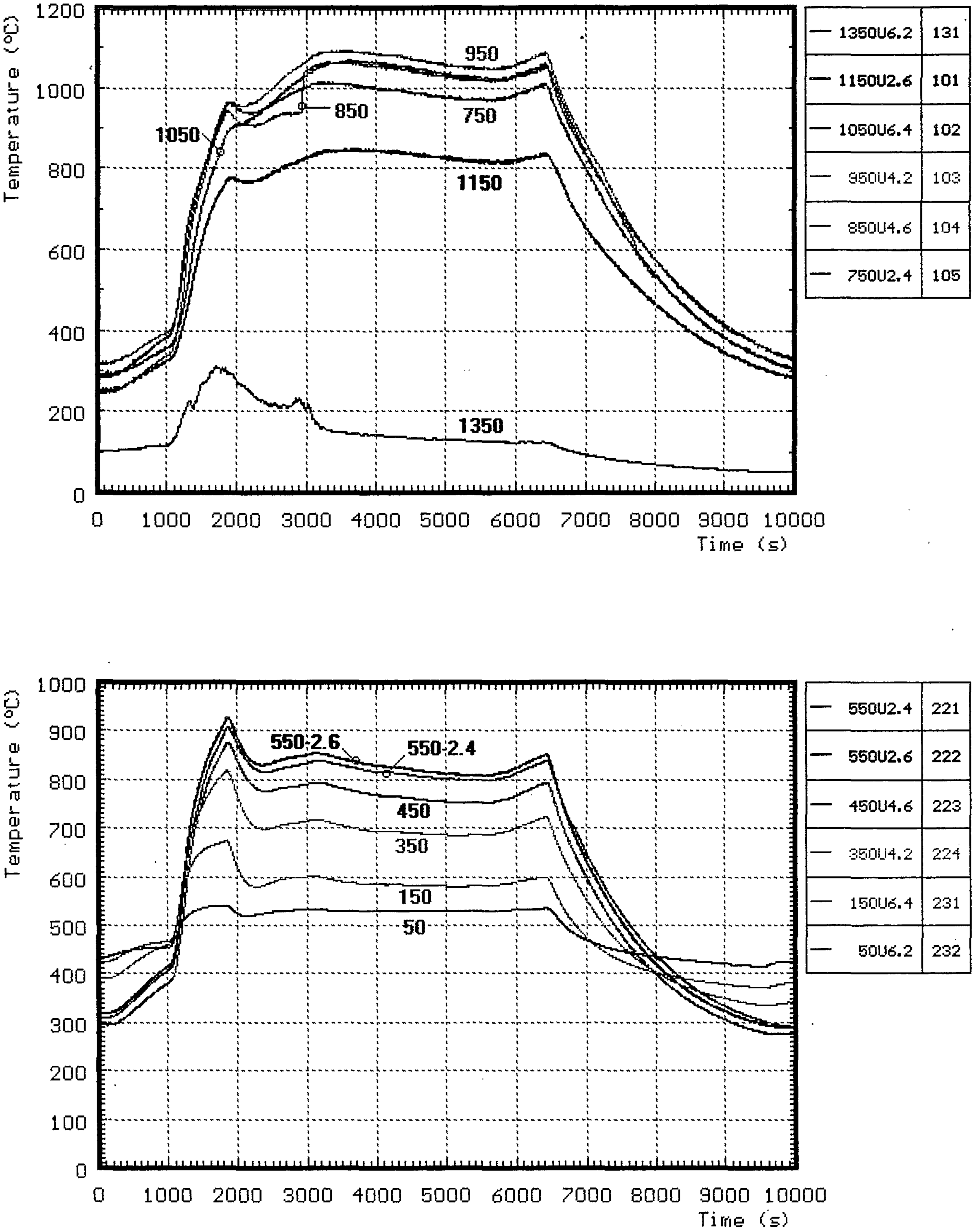

Fig. B5: First preoxidation CORA-28; temperatures of the unheated rods

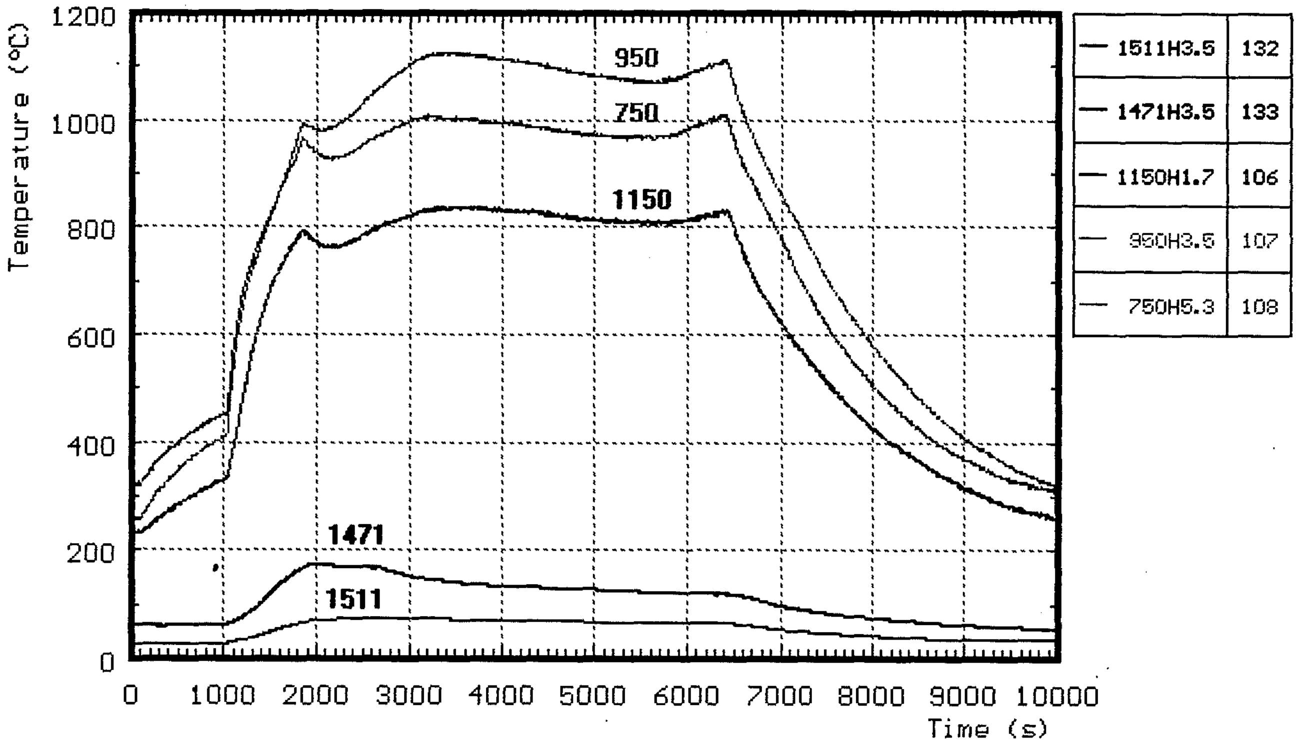

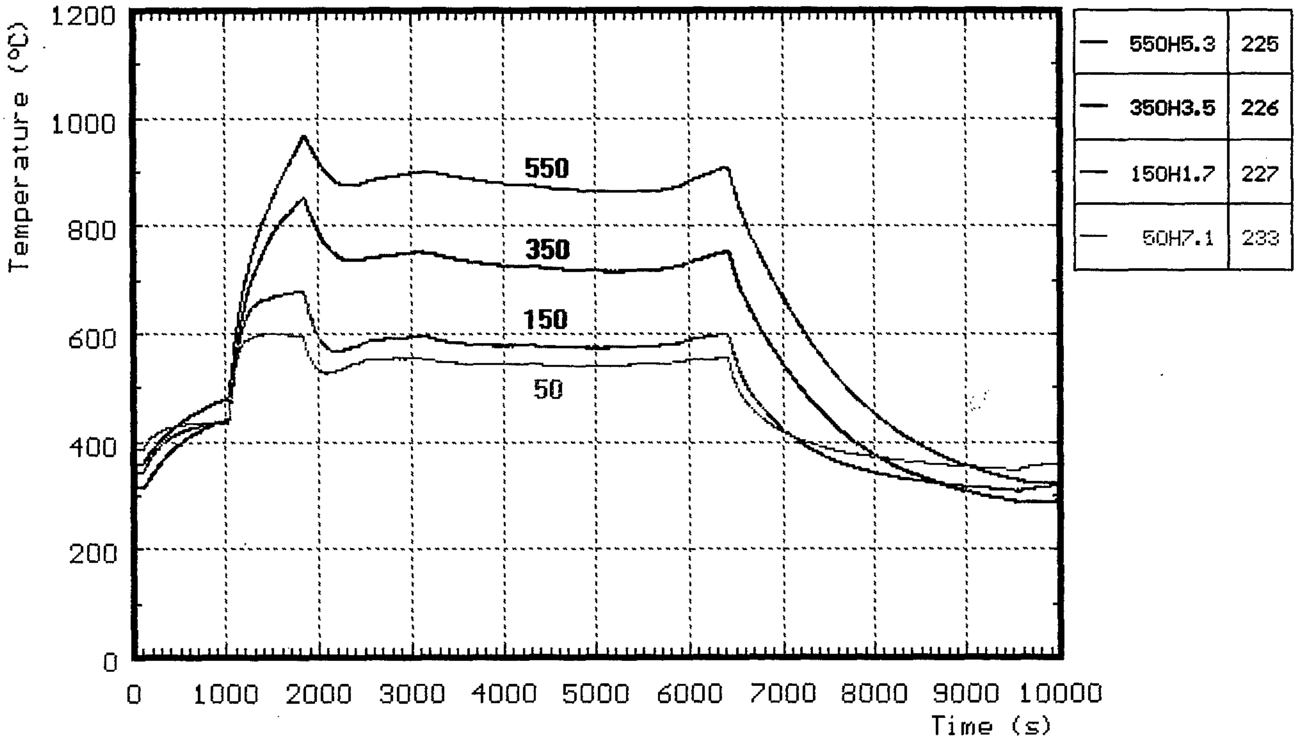

Fig. B6: First preoxidation CORA-28; temperatures of the heated rods

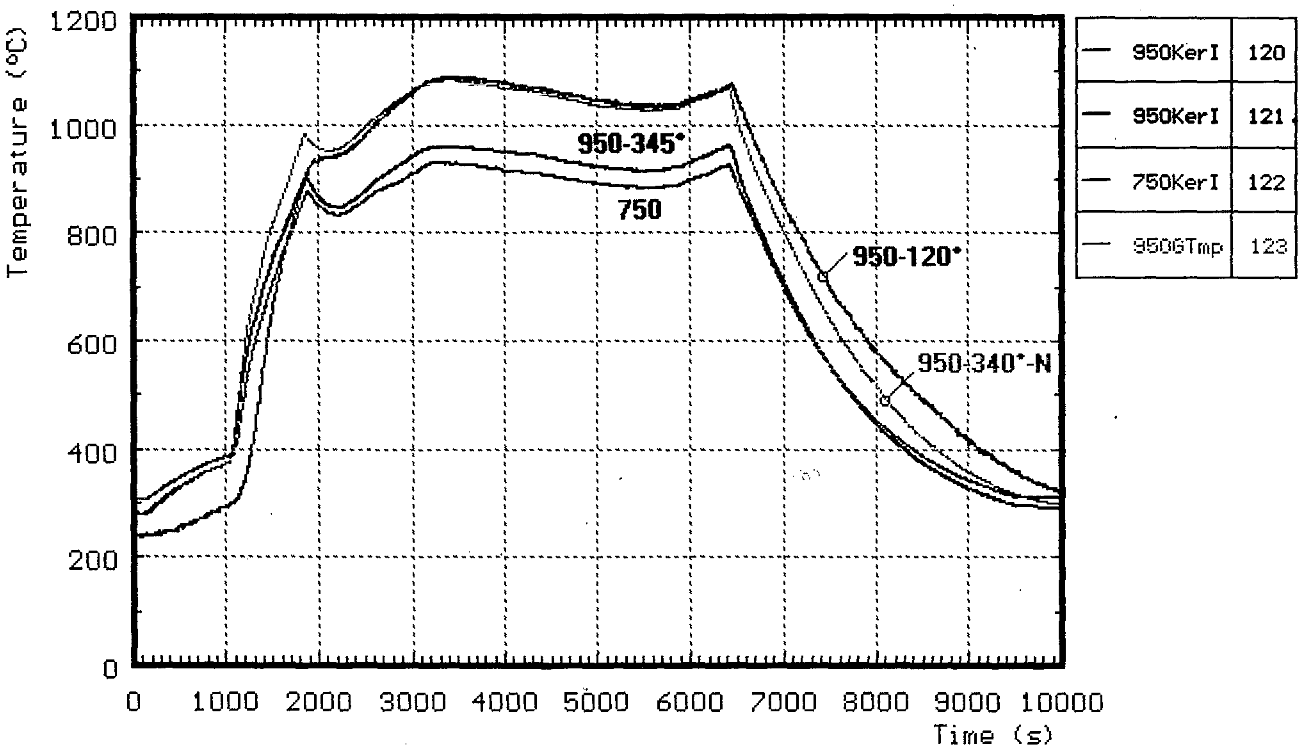

Fig. B7: First preoxidation CORA-28; temperatures with ceramic-protected thermocouples

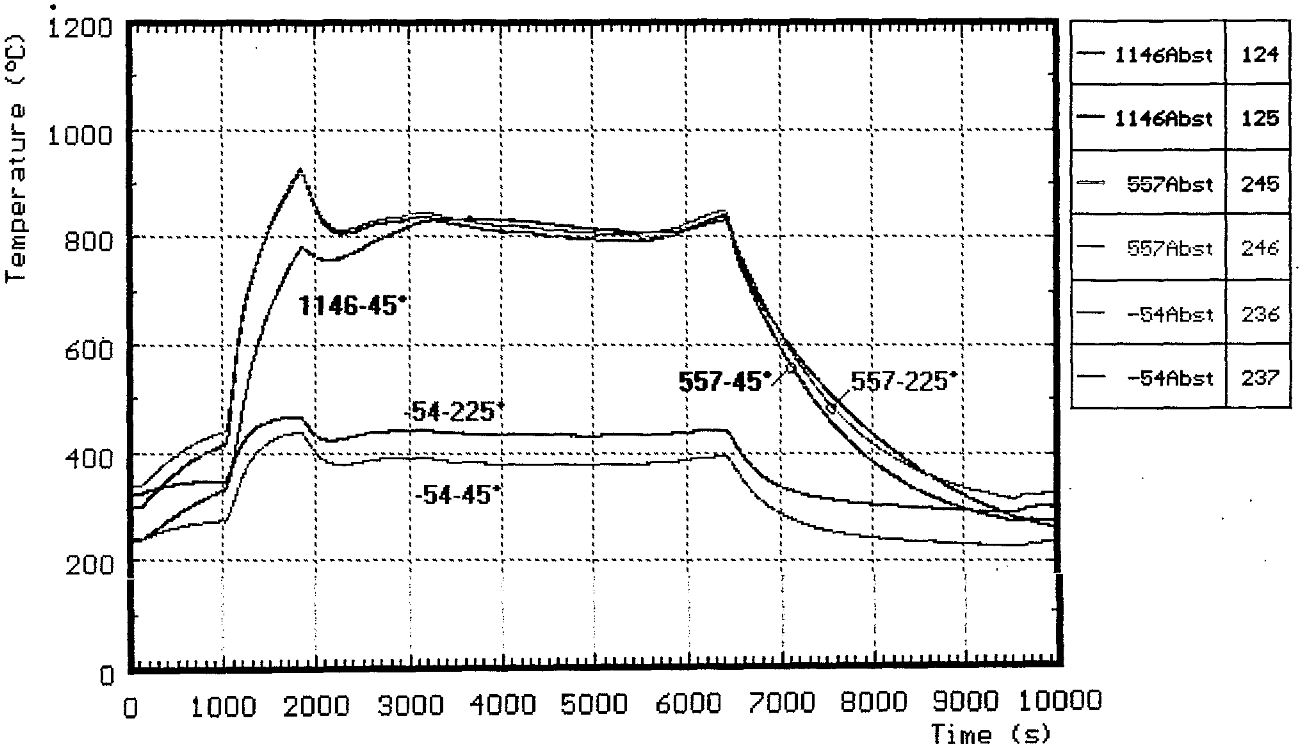

Fig. B8: First preoxidation CORA-28; Temperatures of the spacer

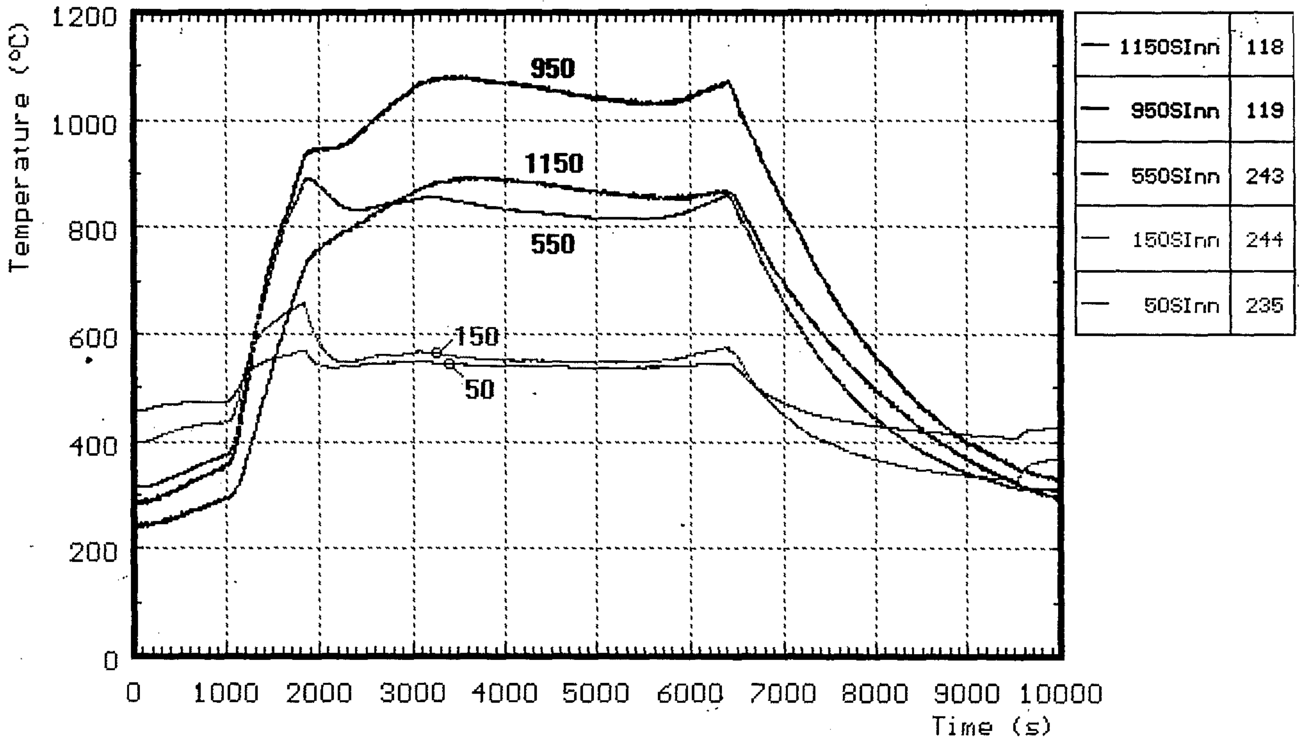

Fig. B9: First preoxidation CORA-28; Temperatures of the channel box wall

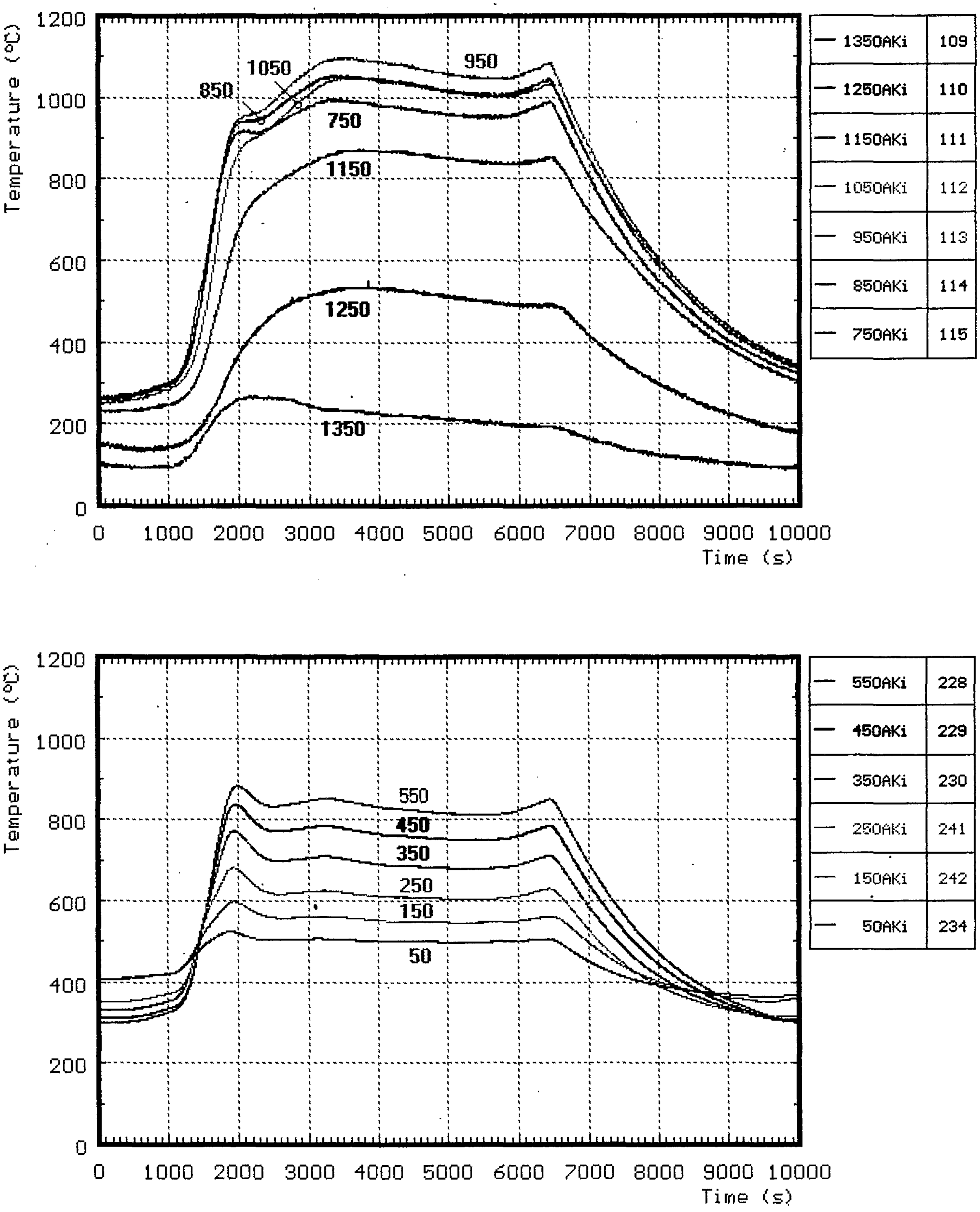

Fig. B10: First preoxidation CORA-28; temperatures of the absorber blade

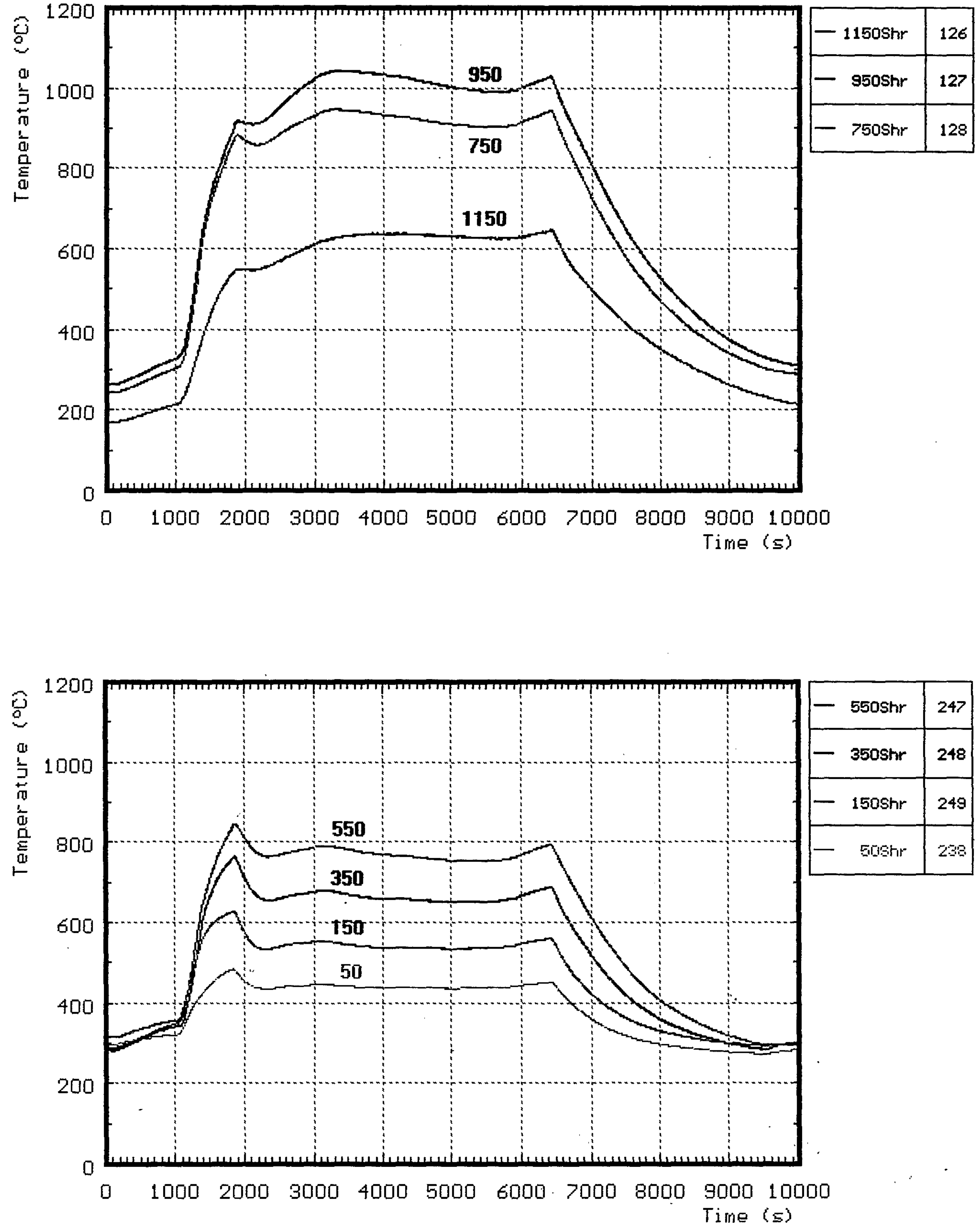

Fig. B11: First preoxidation CORA-28; temperatures of the shroud

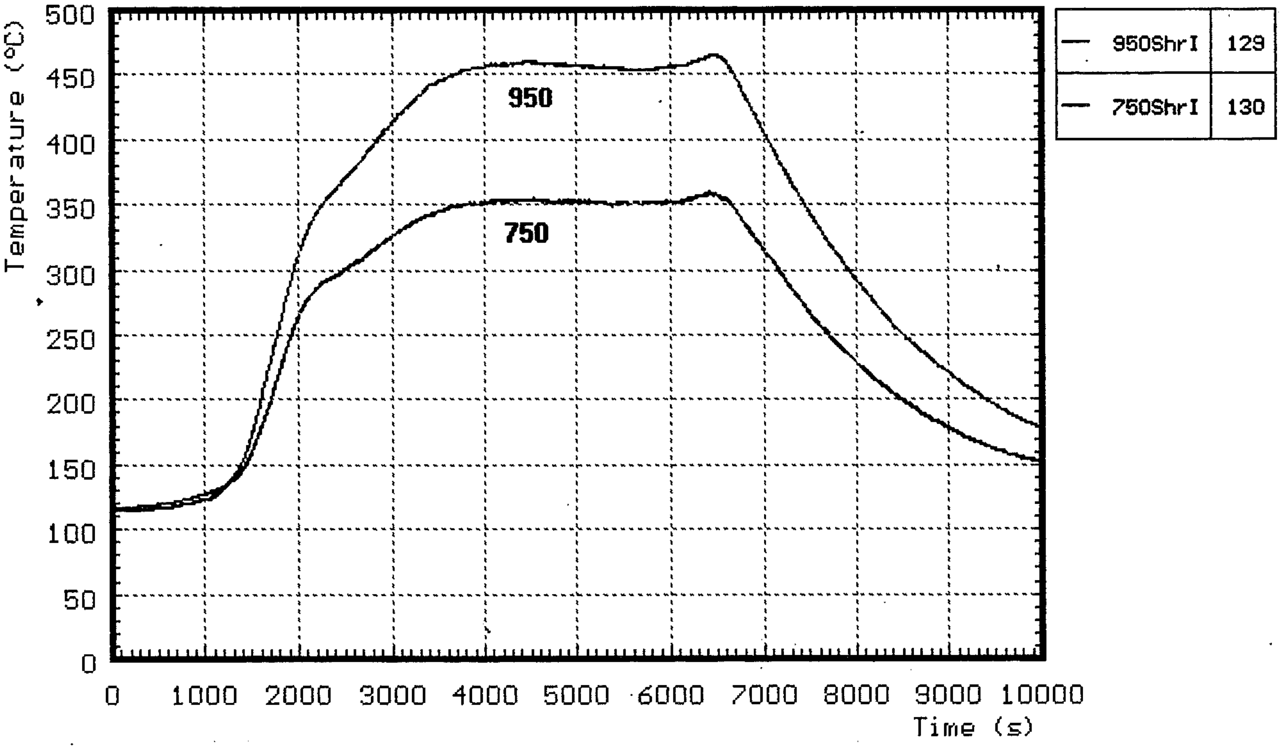

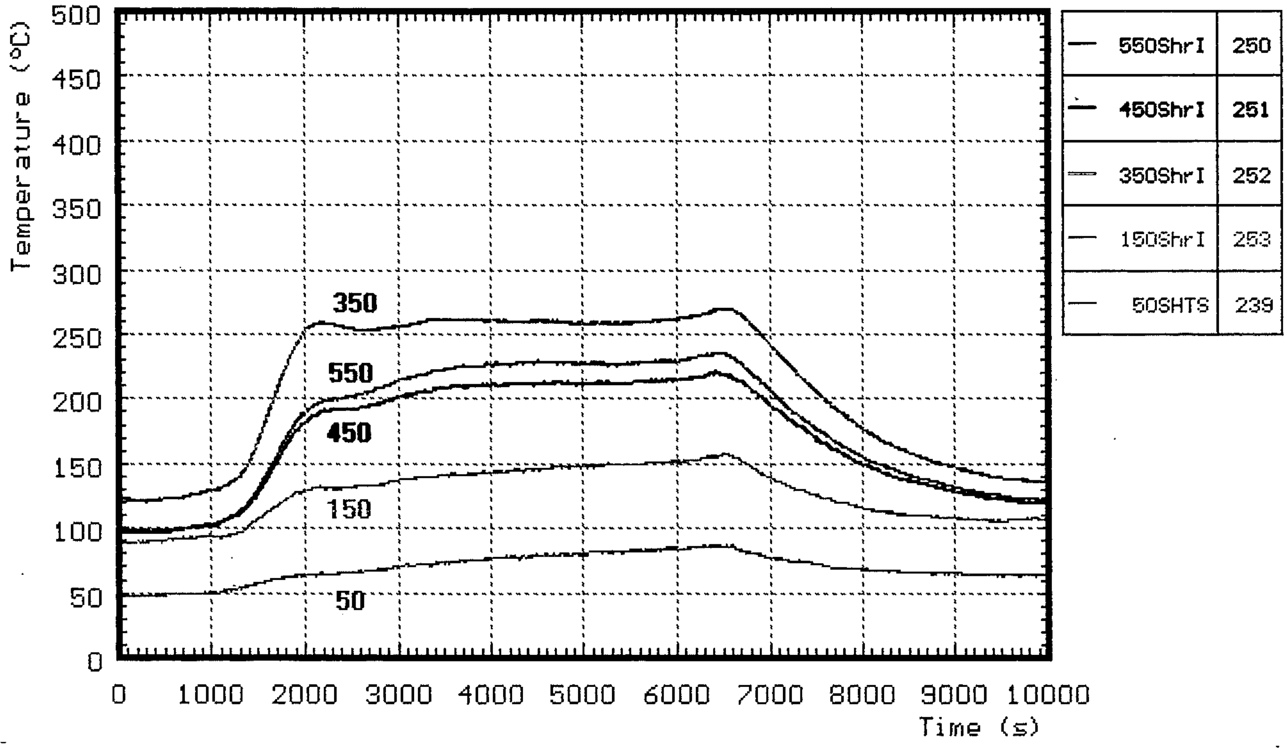

Fig. B12: First preoxidation CORA-28; temperatures of the shroud insulation

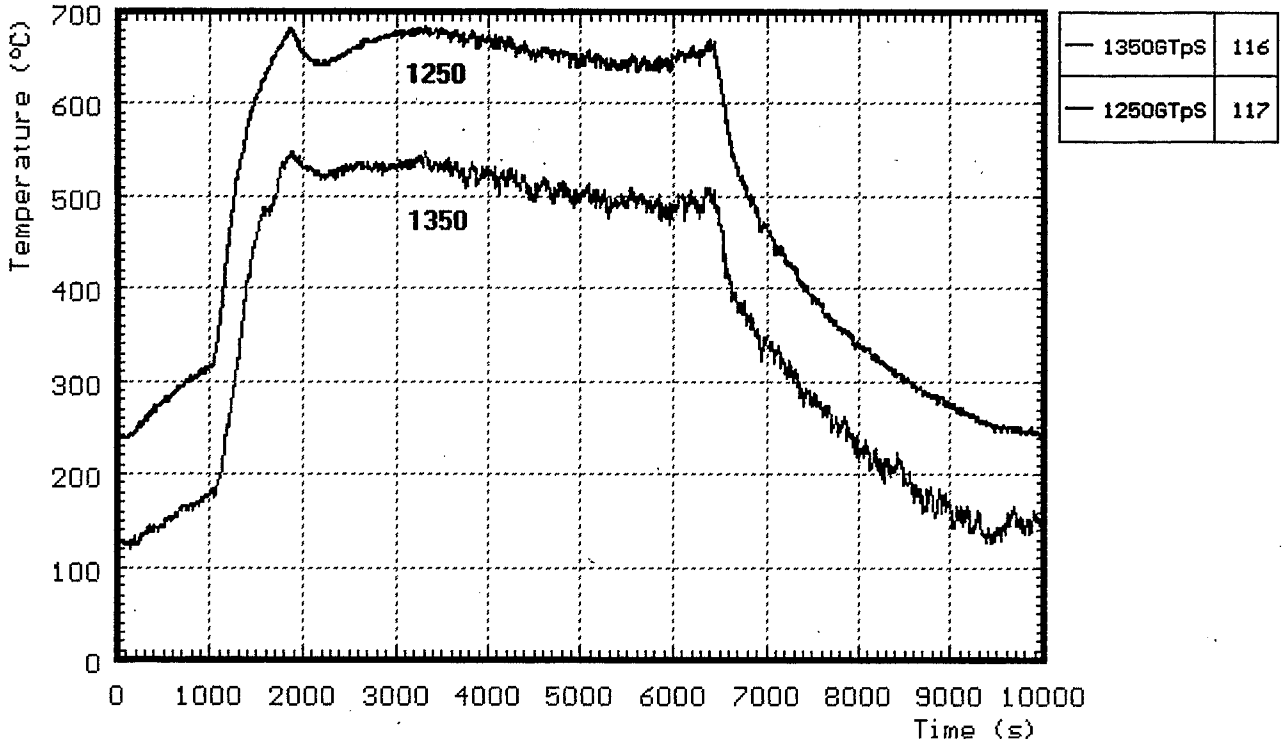

Fig. B13: First preoxidation CORA-28; "gas temperature" measured above the shroud

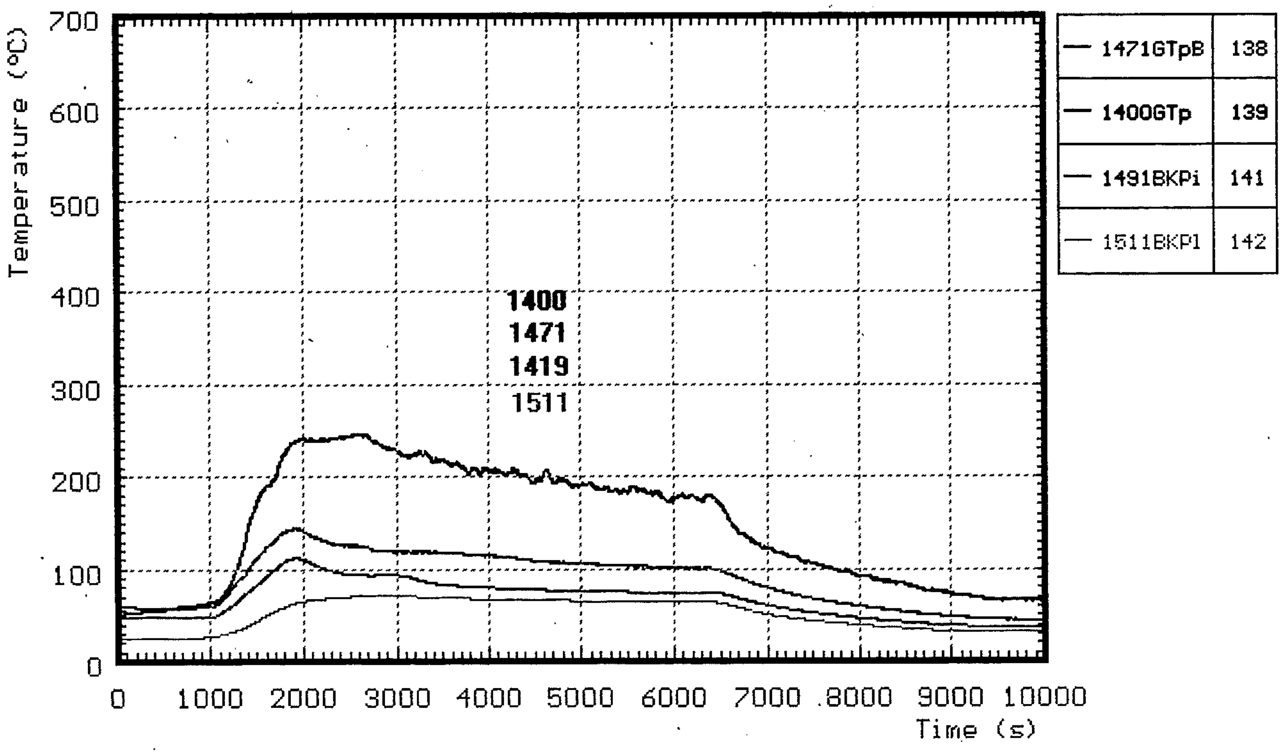

Fig. B14: First preoxidation CORA-28; temperatures in the upper part of the bundle

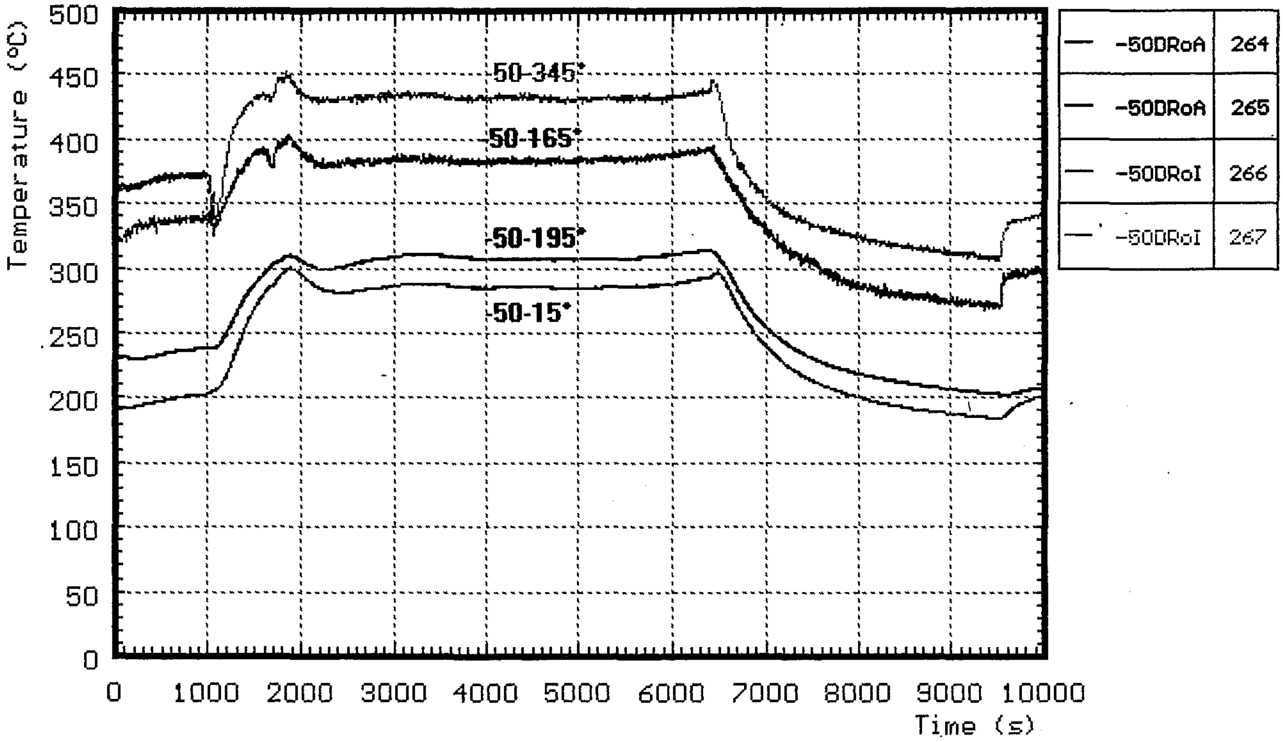

Fig. B15: First preoxidation CORA-28; temperatures of the water in the quench cylinder

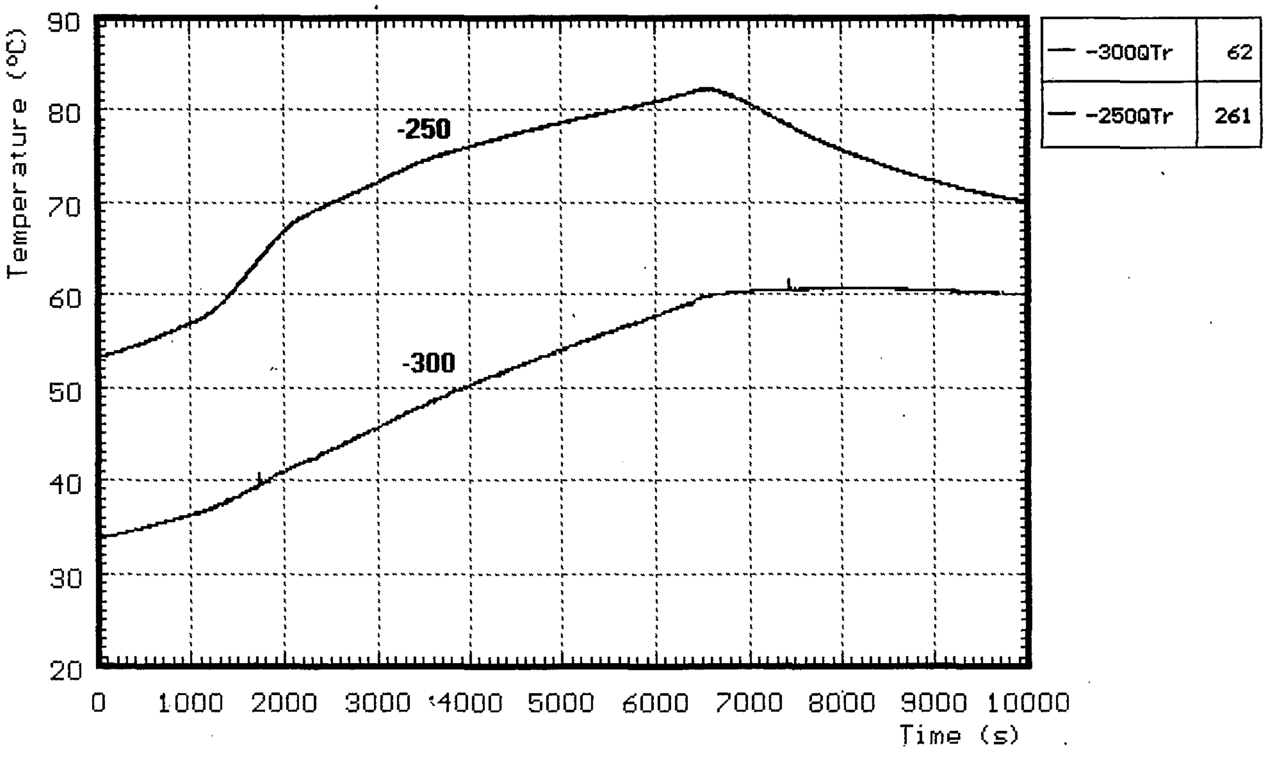

Fig. B16: First preoxidation CORA-28; temperatures at -50 mm at the steam distribution tube

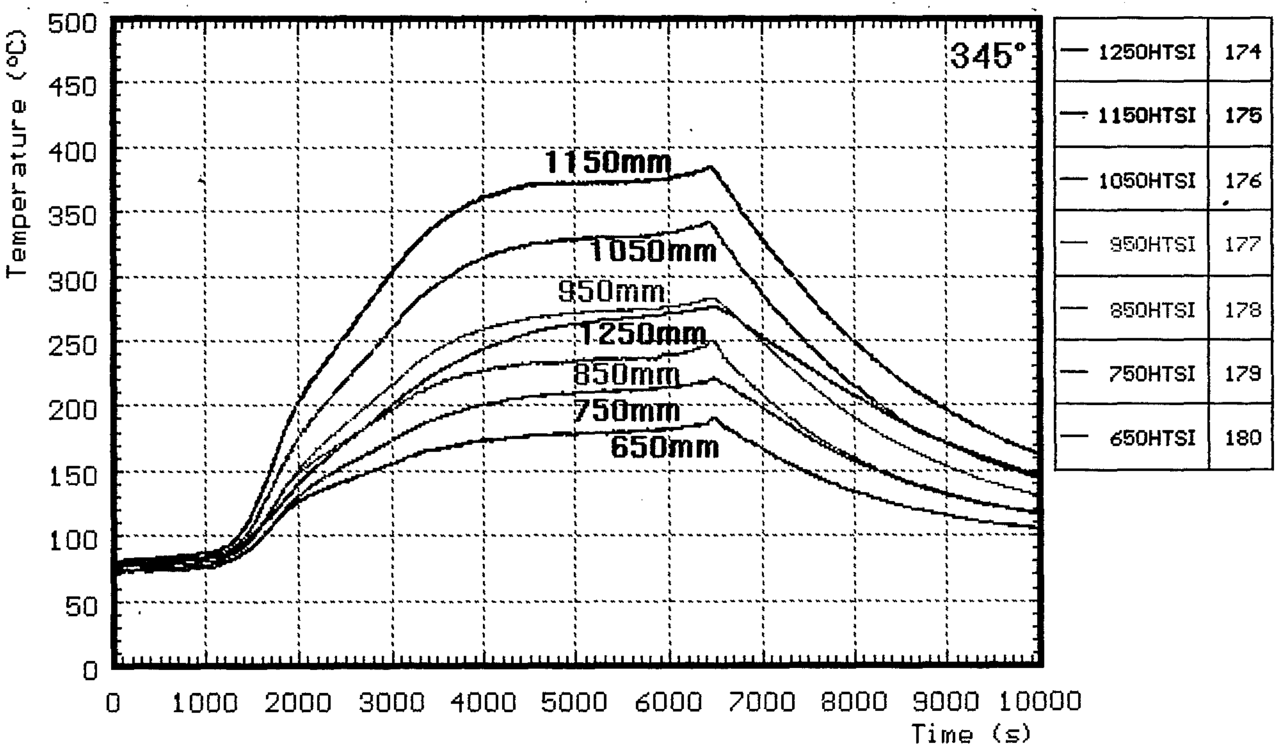

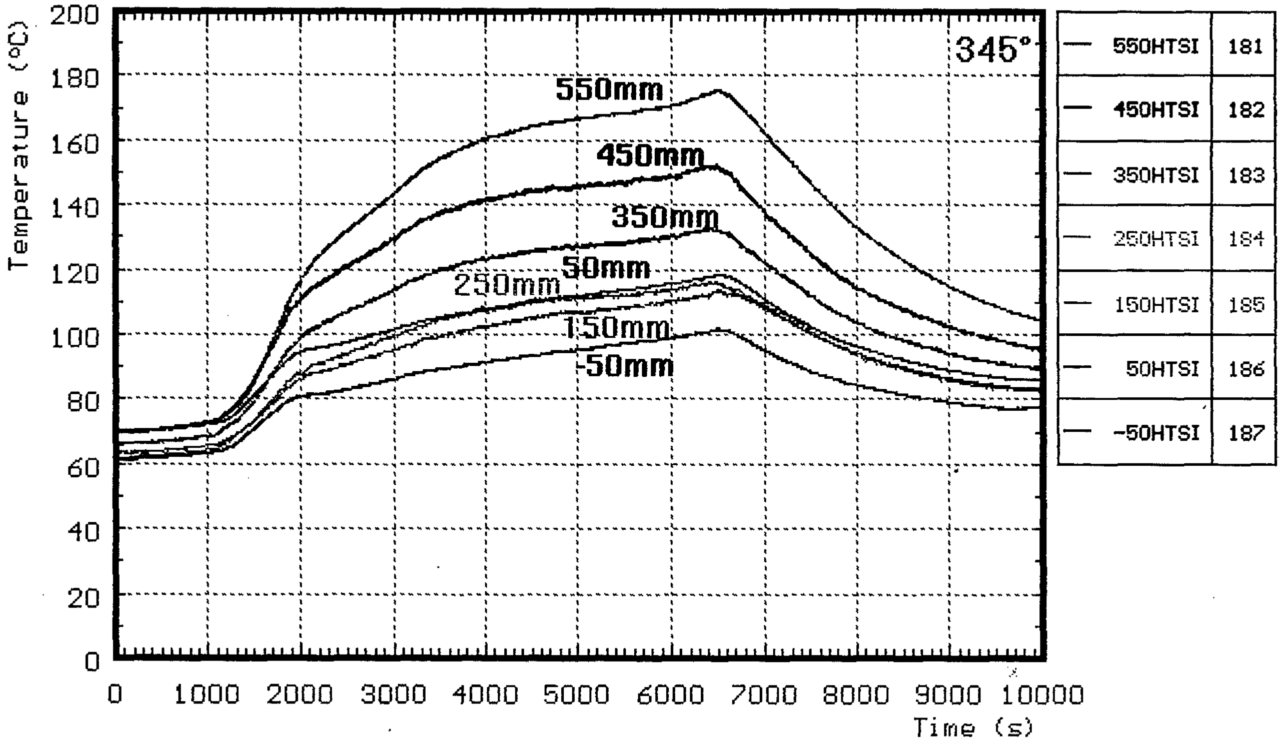

Fig. B17: First preoxidation CORA-28; temperatures of inner surface at 153 mm radius

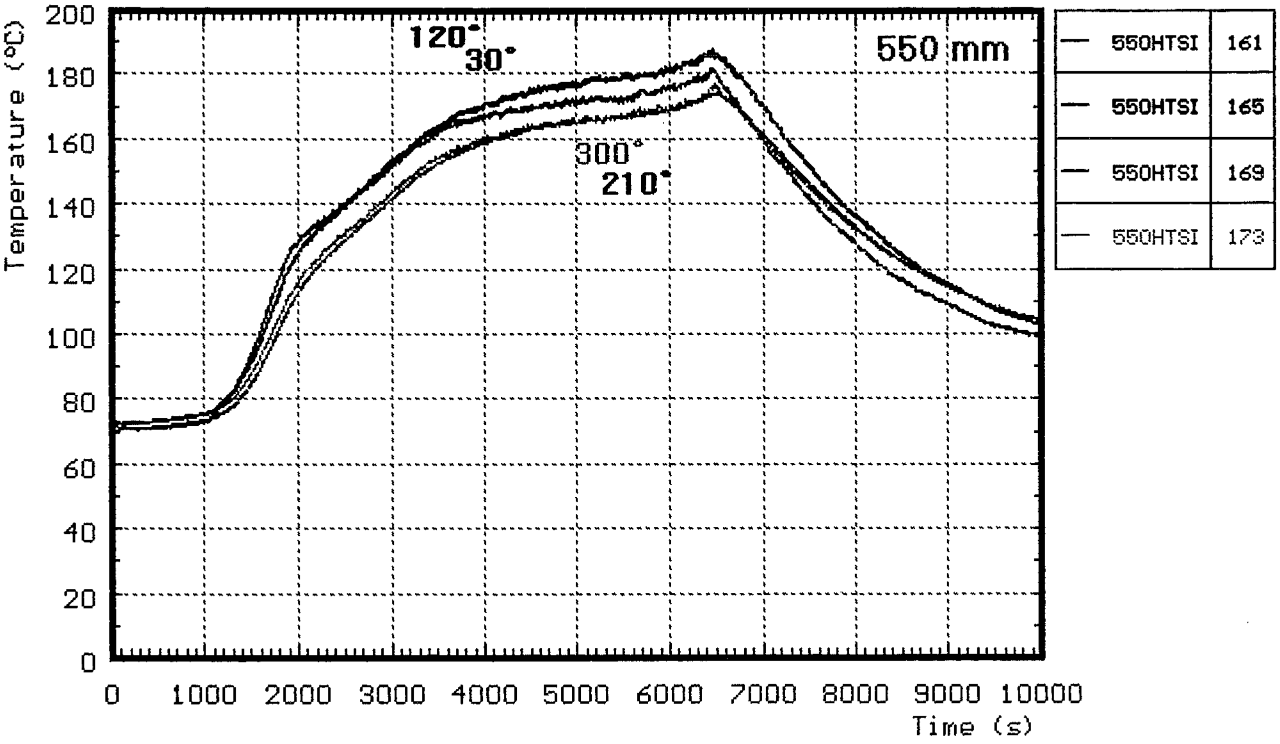

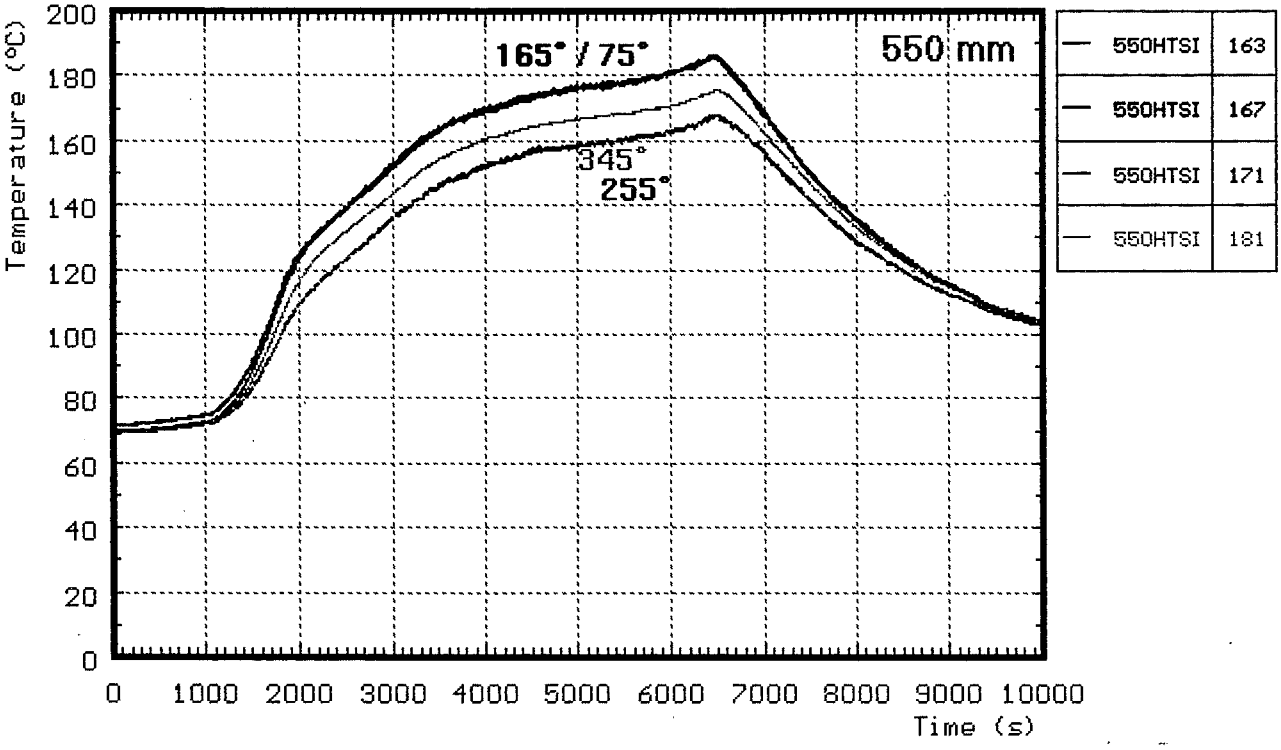

Fig. B18: First preoxidation CORA-28; comparison of temperatures of inner surface at 153 mm radius